JUNE 1956
Copy 1

A.I.Ch.E. JOURNAL

Published by the American Institute of Chemical Engineers

CONTENTS

ALLOY FOR
NON-FERROUS METALS

PHARMACEUTICALS

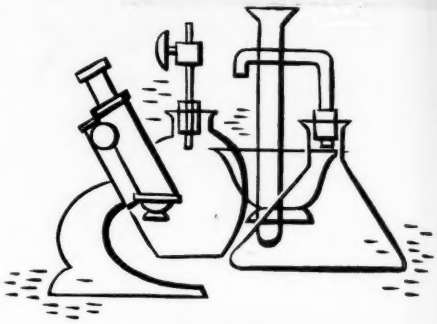

ORGANIC
SYNTHESIS

Foote
LITHIUM METAL

Investigate the potentialities of lithium metal and its derivatives. Write for information.

METAL SCAVENGER
and DEGASSIFIER

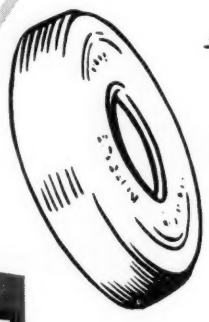

SYNTHETIC
RUBBER

Unpublished
Applications

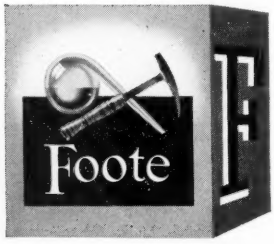

FOOTE MINERAL COMPANY
448 Eighteen W. Chelten Building, Philadelphia 44, Pa.
RESEARCH LABORATORIES: Berwyn, Pa.
PLANTS: Exton, Pa.; Kings Mountain, N.C.; Sunbright, Va.; Knoxville, Tenn.

A.I.Ch.E. JOURNAL

JUNE 1956 · VOL. 2, NO. 2

The A. I. Ch. E. Journal, an official publication of the American Institute of Chemical Engineers, is devoted in the main to theoretical developments and research in chemical engineering and allied branches of engineering and science. Manuscripts should be submitted to the New York office.

Publication Office, Richmond, Virginia. Published quarterly in March, June, September, and December by the American Institute of Chemical Engineers, 25 West 45 Street, New York 36 New York. Manuscripts and other communications should be sent to the New York office. Correspondence with the editor may be addressed to him at Yale University, 225 Prospect Street, New Haven 11, Connecticut. Statements and opinions in the *A.I.Ch.E. Journal* are those of the contributors, and the American Institute of Chemical Engineers assumes no responsibility for them. Subscriptions: one year, member $4.50, nonmember $9.00; two years, member $7.50, nonmember $16.00; additional yearly postage, Canada 50 cents, Pan American Union $1.50, other foreign $2.00 (foreign subscriptions payable in advance). Single copies: $3.00. Second-class mail privileges authorized at Richmond, Virginia.

A.I.Ch.E. JOURNAL

Nuclear Engineering and the Unit Operations

This issue of the A.I.Ch.E. Journal is devoted in large part to certain papers presented at the Nuclear Engineering and Science Congress in Cleveland, Ohio, from December 12 to 16, 1955. Only a relatively small number of the papers presented at Cleveland can be given here, but an attempt has been made to include most of those which appeared to be of greatest appeal to the readers. This is the first issue of the Journal in which there has been a concentration on one particular and rather limited aspect of chemical engineering. It is hoped that it will be successful and that there will be many more special issues as the publishing program expands.

Nuclear engineering has come to the fore in recent years at a rate far exceeding that at which any other branch of engineering has advanced. In view of the necessary secrecy attending its development and a rather restricted publication policy, this speedy progress is all the more remarkable. There are many reasons for it, of course, among which are the vast financial backing of government, the promise and prospect of a new and potentially enormous source of energy, and the appeal of its startling novelty. Also, the possibility that the standard of living throughout the world may be significantly increased has kindled special enthusiasm among nuclear scientists and engineers. However important such reasons may be, this enormous progress of nuclear engineering could not have occurred through them alone. The basic source of strength behind this wonderful achievement is, in the opinion of the editor, the good preparation of our engineering profession and the fact that we were ready for this development.

When one reads the papers of this issue of the Journal, he is compelled to recognize the brilliance of the invention of the unit operations. While a few papers are devoted to the technology of nuclear engineering, the majority of them are simply the application of our unit operations—heat transfer, fluid flow, diffusion, and the like—to a new problem. It is inconceivable that William H. Walker and Arthur D. Little could have visualized this whole field of nuclear development when the idea of unit operations was born, but what greater tribute to their invention can be found? We must also acknowledge the contribution of teachers of chemical engineering, particularly the earlier ones, and the writers of text books who recognized the great merits of this idea and who gave it the wide currency enjoyed today. The concept of unit operations is still the backbone of chemical engineering education, and it is a very sturdy one.

Today nuclear engineering can be advanced and brought to a point of extraordinary achievement through unit operations. Tomorrow it may be the utilization of solar energy, the gasification and liquefaction of coal, the direct conversion of fossil fuel to electric energy, or the demineralization of sea water to which we must apply ourselves. But whatever it is, we shall find, as we have here, that the application of unit operations to the problem will be enormously fruitful.

We chemical engineers may feel justifiably proud of the Nuclear Engineering and Science Congress and of the part played there by individuals and by the American Institute of Chemical Engineers. Most of all, however, we should take pride in the profession itself, in the educational philosophy which has done so much to give substance and vitality to our work, and in the demonstrated ability of our professionals to apply themselves so successfully to the new and wonderful field of nuclear engineering.

H.B.

Hydraulic Analysis of Sudden Flow Changes in a Complex Pumping Circuit

GEORGE E. ALVES

E. I. du Pont de Nemours and Company, Inc., Wilmington, Delaware

A problem arose as to what would happen if there were sudden failures of power to one or more pumps of a large-scale complex pumping circuit composed of several individual pumping systems. This paper describes the application of several published methods of hydraulic transient analysis to the problem. The performance of the system computed under several assumptions is discussed, and a comparison is made with experimentally determined values.

In the design and operation of most process pumping systems, consideration is given only to the normal steady state conditions; that is, based on continuous uninterrupted operation, the pump, motor, and piping are specified for the given process flow rate and pressure. However, there are a few process pumping systems in which sudden flow changes would cause damage to the pumping facilities or adversely affect the process. This was the case on a problem involving a large-scale, complex pumping circuit.

The pumping circuit, Figure 1, consists of several individual pumping systems in parallel between a large suction header and a large discharge header. Each individual pumping system contains a suction line; a large double-suction, double-volute, high-capacity, high-head centrifugal pump with a flywheel, driving motors, and a brake; and a discharge line with a valve and a piece of process equipment. Two electric motors are used to power the pump; one is an a.c. motor for normal operation at design speed, and the other is a d.c. motor with power supplied by a motor-generator set for emergency operation at reduced capacity at one third of design speed. In the event of failure of a driving motor, the flywheel extends the pumping time while the circuit is being shut down.

Use of a tilting-disk check valve in the discharge line of each system was contemplated to prevent reverse flow in the line in case of failure of power to a pump. However, a question arose as to what might happen if the check valve did not operate properly. When power to a pump fails, the check valve could "hang up," allowing an appreciable backflow to build up, and then close suddenly, causing a high-pressure surge which could rupture the line. If there is no check valve, a considerable backflow could follow such a failure, thus producing a further decrease in flow through the discharge header. Also the high torque on the pump could produce reverse rotation of the d.c. motor, thereby causing damage, if d.c. power is on, to the motor-generator set (powered by a Diesel engine).

To answer such a question, an analysis was required. Several published methods were applied to determine possible pressure buildup if check valves were used and to determine in the absence of check valves the flow through the circuit and the torque on the pump-motor unit as a function of time for various abnormal operating conditions. Owing to the lack of assurance of the various methods of analysis and to the importance of the problem, some of the computed values were verified by tests. The results of the analysis led to the decision not to install check valves but to use brakes or nonreversing clutches to protect the systems from the consequences of running the pumps as turbines.

That the methods of analysis have been verified for a large-scale, complex pumping circuit may be of interest to designers faced with the necessity of conducting similar hydraulic-transient analyses. This paper presents a summary of the methods of computation and a comparison of the computed and experimental results.

DISCUSSION

In the hydraulic analysis of pumping systems involving sudden flow changes, consideration must be given to the effect of slowing down the mass of fluid flowing in the line and the effect of the rotating parts, such as pump impeller, flywheel, and motor rotors.

Water Hammer

When a column of flowing fluid is suddenly stopped, a pounding of the line is observed. This pounding of the line is commonly known as *water hammer*. As the flowing fluid is decelerated, pressure waves are set up owing to the inertia of the fluid in the line.

A brief discussion of water-hammer theory will be presented here as background for the discussions of check-valve operation and hydraulic transients. For sudden flow stoppage, the pressure rise due to the deceleration of a truly incompressible fluid in a nonexpandable pipe would be infinite; that is, all the fluid in the line would behave as a "plug" and the pressure rise would be that corresponding to the inertia effects of this plug. Experiments in pipe lines, however, have shown that there is a finite maximum pressure change, because part of the kinetic energy of the moving fluid in the pipe is expended in stretching the pipe walls and compressing the fluid. The equation for the maximum pressure rise produced by a sudden flow change can be derived from Newton's second law, relating force to the rate of change of momentum. The resulting equation is referred to in the literature as the Joukowsky, or water-hammer, equation and is given as

$$h_{wh} = a(\Delta V)/g_c \qquad (1)$$

where

$$a = \left\{1 \Big/ \left[\frac{\rho}{g_c}\left(\frac{1}{k} + \frac{D}{bE}\right)\right]\right\}^{1/2} \qquad (2)$$

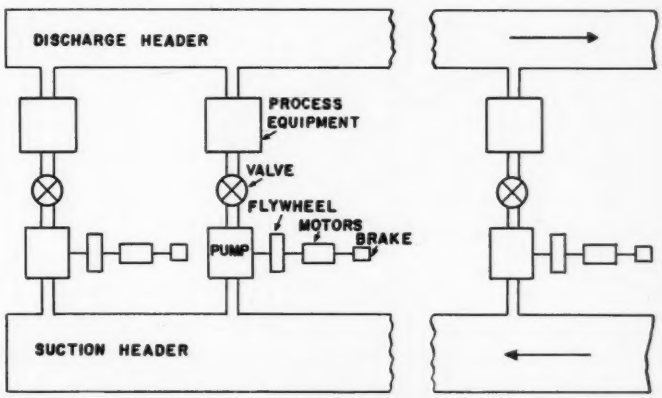

Fig. 1. Pumping circuit.

The maximum pressure rise given by Equation (1) can also be developed if the flow is changed within the time it takes the pressure wave to travel from the point of stoppage to the end of the pipe or to the point of total wave reflection and return; that is, within one pipe period, as given by

$$\tau = \frac{2L}{a} \qquad (3)$$

For example, the discharge piping between the pump and the piece of process equipment and between the piece of process equipment and the discharge header may be considered:

$$a \cong 3{,}800 \text{ ft./sec.} \qquad (4)$$

$$h_{wh} \cong 120\Delta V, \text{ ft.} \qquad (5)$$

$$\tau \cong 0.01 \text{ sec.} \qquad (6)$$

If the time of flow stoppage is somewhat longer than one pipe period, the pressure rise will not be so great as that given by Equation (1) as part of the direct pressure waves will be canceled by the reflected pressure waves. The actual pressure rise can be determined by use of the Allievi equations or charts, which are solutions of the wave equations (*1, 2, 4, 10*).

The foregoing analysis also applies to the pressure reduction for the reflected wave or on acceleration of flow. If the pressure reduction results in a static pressure at any point in the line below the vapor pressure of the fluid, the fluid in the line will separate or pull apart as the pressure wave passes that location. The pipe might collapse as the fluid separates; or, barring that, it might burst as the fluid rejoins, provided there are no protective devices such as relief valves to admit air when the fluid separates and to release the air and some fluid when the fluid rejoins.

Additional details on water-hammer theory can be obtained from references *2, 3, 4, 5, 10,* and *12*.

Check Valves

If a check valve in the discharge line from the pump were closed within one pipe period or 0.01 sec., the maximum pressure rise in the line could be calculated from Equation (5):

$$h_{wh} \cong 120V_0, \text{ ft.} \qquad (7)$$

If the check valve were to "hang up" for a time, with a resulting backflow through the system, and then slam shut, the maximum pressure rise in the line would be

$$h_{wh} \cong 120V_b, \text{ ft.} \qquad (8)$$

Information on closing time of check valves (*8*) indicates that the normal closing time of tilting-disk check valves would be about 0.5 sec. With this length of time the backflow could build up to be between 30 and 60% of the normal forward flow, as will be evident later on in this discussion.

Pump Performance

It should be noted that in normal operation, conditions in the system will be unchanging. However, in the event of a power failure, the pump impeller will gradually slow down. Then when the torque supplied by the inertia of the rotating parts is insufficient to pump fluid, the flow in the line will reverse direction and the pump impeller will keep on rotating and slowing down in the normal direction of rotation; that is, the pump acts as a brake or energy dissipator. Finally the pump impeller will reverse direction of rotation and the pump will operate as a turbine with no load. For a constant head on the pump the flow in the reverse direction will increase to a maximum and then decrease somewhat to a constant value at the point of turbine operation with no load. Thus, for the study of hydraulic transients or unsteady state operation in pumping systems, a complete set of pump-performance data, commonly referred to as "complete pump characteristics," is required—complete in the sense that data on head, capacity, speed, and torque are required for the pump in normal or pump operation, as an energy dissipator, and in turbine-type operation.

A typical manufacturer's pump-performance curve for the double-suction, double-volute pump is shown in Figure 2. However, complete pump characteristics were not available from the manufacturer for the actual pumps or even from the literature for any double-suction, double-volute pump. At the time that the computations were made, complete pump characteristics were available for other types of centrifugal pumps namely, single-suction, single-volute (*6, 7*), single-suction, double-volute (*7*), and double-suction, single-volute (*6, 11*). A comparison of these curves indicated that for constant capacity and speed, the variations in head and torque between the different designs were only about 10 to 20%; therefore, as shown in Figure 3, the plot of the data for the double-suction, single-volute pump presented in reference *11* was used in the computations.

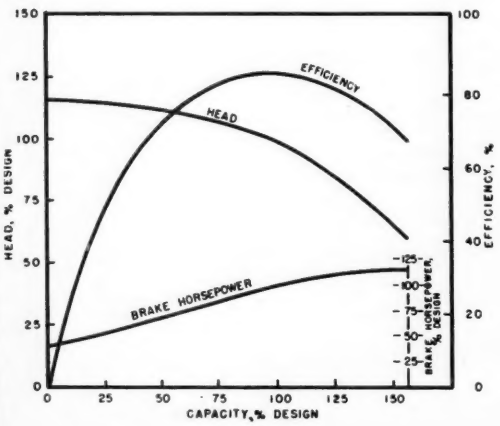

Fig. 2. Typical pump performance curves for a double-suction, double-volute pump.

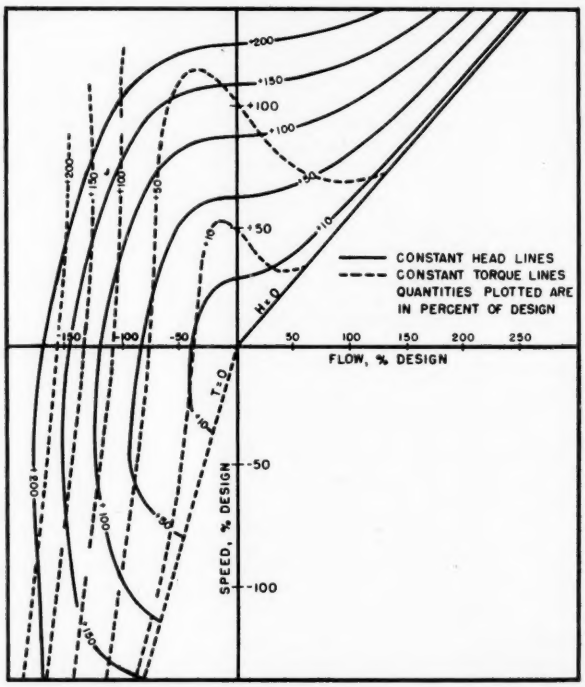

Fig. 3. Complete pump characteristics for a double-suction, single-volute pump.

Hydraulic Transients

Hydraulic transients or unsteady state phenomena considered herein include the flow through the circuit and, for the pumps with sudden power failures, the flow through the pump, the speed of the pump, and the torque on the pump-motor unit. All these transients are considered as a function of time for various types of power failure. The pump undergoing a sudden power failure will be referred to as the *idle* pump.

There are several methods of computing the foregoing information by the application of the various water-hammer equations, complete pump characteristics, and the equation of motion of a rotating system. In addition, there is a method which does not take into account the water-hammer effects. The several methods of computation are described below.

Water-hammer Effects Neglected

A simple method neglecting water-hammer effects is the graphical integration of the equation of motion of a rotating system (*6*).

The equation of motion of a rotating system

$$t = -(I/g_c)(d\omega/d\theta) \qquad (9)$$

is integrated and then the units are changed to those customarily used, to give

$$\theta_{n+1} - \theta_n = -[(\pi I n_0)/(30 g_c t_0)] \int_{N_n}^{N_{n+1}} (dN)/T \qquad (10)$$

Equation (10) can be solved by a graphical integration. First a plot is made of (constant)/T vs. N and then the time is determined from the area under the curve. The constant is the term in brackets in Equation (10). Values of N and T are obtained from the complete-pump-characteristics plot, Figure 3, for an assumed flow and computed head, with the notation that

$$H = h/h_0 \qquad (11)$$

$$Q = q/q_0 \qquad (12)$$

$$N = n/n_0 \qquad (13)$$

$$T = t/t_0 \qquad (14)$$

When two or more pumps are in operation and power to one pump fails, the pressure in the discharge header will drop and the flow from the idle pump will decrease. After a length of time there will be backflow through the idle pump. Therefore, in the foregoing computations the head on the idle pump should be corrected for both discharge-header pressure reduction and flow through the idle pump. Assuming a flow, either in the normal direction or in the reverse direction, depending upon the time, through the idle pump at a given speed, one can compute the head on the idle pump and then check on the complete-pump-characteristics plot; the correct value of the flow is thus found by trial and error. Finally the value of torque T on the idle pump is read from the complete-pump-characteristics plot by use of the foregoing determined values of head, flow, and speed. From these values and the application of Equation (10), the time-vs.-speed curve for the idle pump can be obtained; and from the values of the flow through the idle pump and the flow delivered by the other pumps, a plot of flow through the discharge header vs. time can be made.

This method was applied to two cases of power failure, and the results were verified experimentally in order to assure the reliability of the computational procedure.

Case 1. Sudden Failure of One Pump with A.C. Power Remaining on the Other Pumps

Principal attention was given to the condition in which both a.c. and d.c. power would fail simultaneously. Consideration also had to be given to the possibility of a shaft breakage between the impeller and the flywheel. For the latter condition the reduction in the moment of inertia had to be considered.

On the basis of the method described above and the assumption of a constant discharge-header pressure at the design value, since this would give conservative results, values of $(\pi I n_0)/(30 g_c t_0 T)$ were plotted against N, as shown in Figure 4, for the condition of simultaneous failure of both a.c. and d.c. power. By a graphical integration of the area under the curve the values of time required to retard the impeller of the idle pump to given speeds were determined. Figure 5 shows curves of the flow through the idle pump and the speed of the idle pump as a function of time. Note that the flow through the idle pump decreases rapidly to zero; then the flow reverses direction and gradually increases to a maximum corresponding to the lowest point in Figure 5; and finally the flow decreases to a steady state value at the terminal or steady state reverse speed of the idle pump.

A comparison of the computed values with the experimental results showed good agreement, as indicated in Table 1.

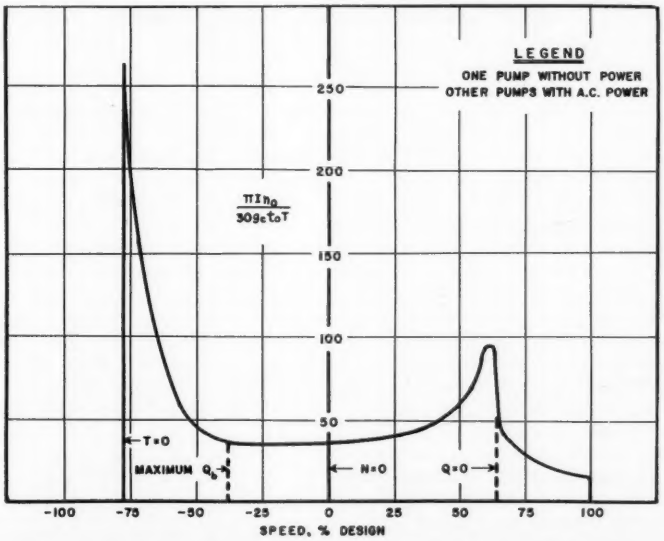

Fig. 4. Graphical integration of the equation of motion of rotating masses.

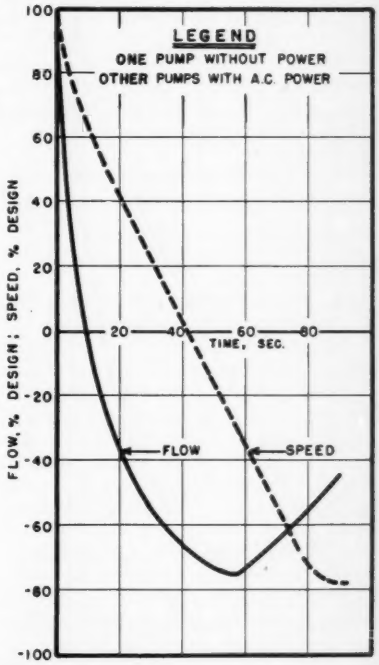

Fig. 5. Flow and speed vs. time for the idle pump.

An interesting note is the surprisingly short interval of time that would be required for the pump impeller to change direction of rotation in case the shaft should break between the impeller and the flywheel. In a practical case the moment of inertia of the impeller might well be about 1% of the combined moment of inertia of the impeller, flywheel, and motor rotors. If this were the case, the time for the impeller to change from design speed in the normal direction to about 80% of design speed in the reverse direction would be less than 1 sec. It can be seen that such a short time interval would preclude the possibility of experimental verification because of the probability of damage to the installation.

Case 2. Sudden A.C. Power Failure on All Pumps with Sudden D.C. Power Failure on the Majority of the Pumps

The computations were performed for sudden d.c. power failure on the majority of the pumps. For the retardation from 100 to 33.5% design speed, the contribution of the operating d.c. motors was neglected. From 33.5% design speed to zero the contribution of flow from the pumps with d.c. power had to be taken into account. The same procedure applied to Case 1 was used to compute the times.

Table 2 presents the results obtained both by the computation described above and by experiment for d.c. power failure on all pumps. Little difference in time would be expected for the retardation from 100 to 33.5% design speed, since comparatively little contribution to the torque would be made by the few operating d.c. motors. For retardation below 33.5% design speed the time for the computed case would be expected to be greater than for the case with d.c. power failure on all pumps.

Allowance for Water-hammer Effects

This method takes into account the raising or lowering of the pressure at the pump discharge owing to surges or water hammer.

There are two methods of attacking the problem: (*a*) arithmetic and (*b*) graphical. The arithmetic method is tedious and involves a trial-and-error procedure. This method is adequately described in the literature (*10*) and will not be discussed here. However, the graphical counterpart is only briefly described in the literature (*2, 5, 9, 10, 12*), and an outline of this method will be given.

Graphical Procedure. The graphical procedure is essentially a solution of Equation (10), with Equation (1) being incorporated for the change in head on the idle pump due to surges or water hammer. A coordinate system is prepared of head vs. flow in the discharge line (Figure 6). Added then are the curve of pump performance for 100% design speed and the curve of the pumping-system friction. A *surge-characteristic* line having a slope of (aV_0/g_ch_0) [*see* Equations (1) and (11) and note that the velocity at any time is equal to QV_0] is drawn downward from the intersection of the pump-performance curve and the system-friction curve until it meets the pump-performance curve for the speed existing after a retardation time of one pipe period. This pump-performance curve for a retarded speed is computed from the pump-performance curve at 100% of design speed and the following pump relations (*11*):

$$H = H_a(N/N_a)^2 \qquad (15)$$

$$Q = Q_a(N/N_a) \qquad (16)$$

The speed is determined by application of Equation (10) for a small interval of

Table 1. Retardation Times

Sudden Failure of One Pump with A.C. Power on Other Pumps

Flow, % design	Speed, % design	Time, sec. Power failure, a.c. and d.c. Experimental	Power failure, a.c. and d.c. Computed for constant discharge-header pressure	Broken shaft at pump (no flywheel) Computed for constant discharge-header pressure*
Zero flow				
			8.7	0.09
0	64.7			
	70.1	11		
Zero speed				
−67.7	0		41.2	0.41
	0	45		
−66.1	0 (Brake)	Experimental		
−55.1	0 (Brake)	Computed, allowing for decrease in discharge-header pressure		
Zero torque (terminal speed)				
−44.9	−78.2		89.2	0.89
−36.6	−80.2	120		

*Moment of inertia of the pump impeller assumed as 1% of the combined moment of inertia of the rotating masses.

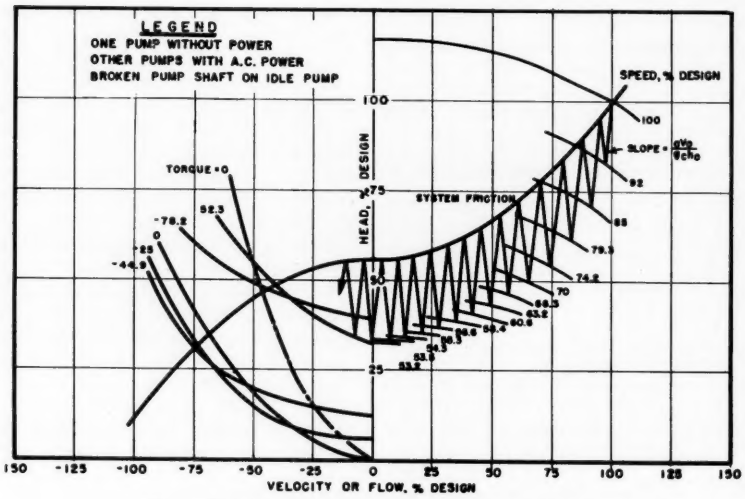

Fig. 6. Graphical procedure for hydraulic transients.

Table 2. Retardation Times

A.C. Power Failure on All Pumps and D.C. Power Failure as Indicated

Speed, % design	Time, sec. Power failure, d.c., on all pumps, experimental	Power failure, d.c., on majority of pumps, calculated
100 (initial)	0	0
33.5	33.5	29.2
0	390	453

time:

$$(T_n + T_{n+1})/2 = [(\pi I n_0)/(30 g_c t_0)] \cdot [(N_n - N_{n+1})/(\theta_{n+1} - \theta_n)] \quad (17)$$

where

$$\theta_{n+1} - \theta_n = 2L/a \quad (18)$$

This involves a trial-and-error solution to determine with accuracy the point of intersection. However, where the interval of time is very small and the moment of inertia is large, Equation (17) can be approximated to serve as a practical check on the other methods and to eliminate the trial-and-error solution by replacing $(T_n + T_{n+1})/2$ with T_n.

The *reflected-surge-characteristic* line is then drawn upward with a slope of $-aV_0/g_c\ h_0$ to the system-friction curve. The process is repeated until the point of zero flow is reached. After this point the procedure is the same except that the plot of complete pump characteristics is used instead of the normal pump-performance curve and the pump relations. From the plot of complete pump characteristics, data are obtained for the pump with reverse flow and positive speeds. Maximum reverse speed (negative speed at zero torque) is approximately the negative speed at which the surge-characteristic line crosses the zero-torque curve when being drawn to the system-friction curve or the pump-performance curve for the next highest negative speed.

After the point of zero flow is reached for a system with a very small pipe period and a large moment of inertia of the rotating elements, there may be a large number of pipe periods of time to be considered before the point of maximum reverse speed (zero torque) is reached. An approximation can be made for the number of intervals of time from zero flow to zero speed and from zero speed to maximum reverse speed by use of an approximation of Equation (10):

$$T_{avg} = [(\pi I n_0)/(30 g_c t_0)] \cdot [(N_n - N_{n+1})/(\theta_{n+1} - \theta_n)] \quad (19)$$

an inspection of the construction shown in Figure 6, and the plot of complete pump characteristics, Figure 3. First an average head can be obtained by inspection of the construction and then, by use of this average head and the points of zero flow and zero speed, or zero speed and estimated maximum reverse speed, an average value of the torque is read from the plot of complete pump characteristics. Thus the difference in time is obtained from Equation (19) and the number of pipe periods obtained by dividing this time by the length of time of 1 pipe period.

Figure 6 is the construction for the case of a possible sudden shaft failure on one pump and a.c. power on the other pumps (*see* case 1). For the idle pump to decelerate from 100% of design speed to a speed corresponding to zero flow, a time of 14 pipe periods would be required. From zero flow to zero speed, the time was approximated, because of the large number of pipe periods required, as follows. Inspection of Figures 3 and 6 shows that $30\% < H < 55\%$, $0\% < N < 55\%$, and $T_{avg} \cong 25\%$; thus from Equation (19) $\Delta\theta = 0.27$ sec., or 27 pipe periods. From zero speed to maximum reverse speed, the same procedure as above was applied: $30\% < H < 45\%$, $-80\% < N < 0\%$, and $T_{avg} \cong 35\%$; thus $\Delta\theta = 0.29$ sec., or 29 pipe periods.

A summary of times is as follows:

	Time, sec.
100% Speed to zero flow	0.14
Zero flow to zero speed	0.27
100% Speed to zero speed	0.41
Zero speed to maximum reverse speed	0.29
100% Speed to maximum reverse speed	0.70

These values compare favorably with those given in Table 1. Thus it is indicated again that the simple graphical integration of the equation of motion of a rotating system, neglecting water-hammer effects, is of sufficient accuracy for these problems on unsteady state flow.

Charts. For the quick estimation of various hydraulic transients in pumping systems, Parmakian (*9*) has presented charts based upon experience gained on large pumping installations of the United States Bureau of Reclamation. However, it is believed that at those installations the system friction was negligible compared with the pumping head, and therefore for systems with considerable friction the charts would indicate times appreciably shorter than those computed by the methods previously discussed.

For the case of a possible shaft failure (*see* case 1), the times obtained from the charts are from 15 to 50% of those given in Table 1.

CONCLUSIONS

1. The graphical integration of the equation of motion of a rotating system, water-hammer effects neglected, is a rapid method of computing hydraulic transients in a pumping system.

2. The periods given by the charts prepared by Parmakian were considerably shorter than those obtained by computation. The charts probably do not apply to systems having high friction losses.

3. The agreement was good between the computed and experimental values of the hydraulic transients.

4. This analysis led to the decision not to install check valves but to employ brakes or nonreversing clutches to protect the systems from the consequences of running the pumps as turbines.

NOTATION

- a = velocity of wave propagation, ft./sec.
- b = pipe-wall thickness, ft.
- D = pipe inside diameter, ft.
- E = modulus of elasticity of pipe wall material, lb. force/sq. ft.
- g_c = conversion factor, 32.2 (lb./lb. force)(ft./sec.^{2})
- H = h/h_0
- h = head, ft.
- I = moment of inertia = WR^2, lb.-ft.^{2}
- k = bulk modulus of elasticity of the fluid, lb. force/sq. ft.
- L = length of pipe from the location of flow stoppage to the location of total wave reflection (used in water-hammer computation), ft.
- N = n/n_0
- n = rotational speed, rev./min.
- Q = q/q_0
- q = rate of flow, cu. ft./sec.
- R = radius of gyration, ft.
- T = t/t_0
- t = torque, lb. force-ft.
- V = velocity, ft./sec.
- ΔV = change in velocity, ft./sec.
- W = weight of rotating element, lb.
- θ = time, sec.
- ρ = fluid density, lb./cu. ft.
- τ = $2L/a$ = pipe period, sec.
- ω = rotational speed, radians/sec.

Subscripts

- 0 = initial steady state or design condition
- a = normal operation at 100% design speed
- avg = average
- b = backflow
- n = any point
- wh = water hammer

LITERATURE CITED

1. Allievi, L., "Theory of Water-Hammer," translated by E. E. Halmos, Riccardo Garroni, Rome (1925).
2. Angus, R. W., *Proc. Inst. Mech. Engrs. (London)*, **136**, 245 (1937).
3. ———, "Hydraulics for Engineers," Pitman and Sons, Toronto (1943).
4. "A.S.M.E. – A.S.C.E. Symposium on Water Hammer, 1933," published by Am. Soc. Mech. Engrs.
5. Kerr, S. Logan, *Trans. Am. Soc. Mech. Engrs.*, **72**, 667 (1950).
6. Knapp, R. T., *loc. cit.*, **59**, 683 (1937).
7. *Ibid.*, **63**, 251 (1941).
8. Parmakian, John, *Memo.*, U. S. Bur. Reclamation, Denver, Colo. (April 26, 1949).
9. ———, *Trans. Am. Soc. Mech. Engrs.*, **75**, 995 (1953).
10. Rich, G. R., "Hydraulic Transients," McGraw-Hill Book Company, Inc., New York (1951).
11. Stepanoff, A. J., "Centrifugal and Axial Flow Pumps," John Wiley and Sons, New York (1948).
12. ———, *Trans. Am. Soc. Mech. Engrs.*, **71**, 515 (1949).

Presented at Nuclear Engineering and Science Congress, Cleveland

Flooding Characteristics of a Pulse Extraction Column

R. B. EDWARDS and G. H. BEYER

Iowa State College, Ames, Iowa

An investigation using the hexone-water system was made of flooding in a 1-in.-diam. ten-plate pulse column. An analysis of column operation led to the derivation of an equation for predicting conditions of inadequate pulsation and for establishing the amount of liquid recycled under any operating conditions.

In recent years liquid-liquid extraction has become increasingly important, and considerable attention has been given to the development of more efficient types of extractors. One important way of improving extraction efficiency is to pulse the fluid contents of sieve-plate and packed extraction columns.

Pulsed sieve-plate extraction columns are called *pulse columns*. The plate perforations in a pulse column are usually so small that counterflow of the two liquid phases due to density difference does not occur. However, application of a cyclical pulsation to the column provides the additional energy necessary to force the liquids through the plates. The small plate perforations of a pulse column provide high fluid velocities and small drops and thus create the turbulence and transfer area necessary for high extraction rates.

The height of column and the maximum allowable column throughput are quantities required in designing a pulse column for a specific extraction operation. Some studies have dealt with the extraction efficiency, which controls the height of a column, but little attention has been given to the limiting conditions of flow in a pulse column. The limiting conditions of flow are identified by flooding—defined as the entrainment of light-liquid phase with heavy-liquid effluent, or vice versa. This latter aspect of column design was the principal subject of this investigation.

The general performance characteristics of pulse columns were presented by Sege and Woodfield (*4*), who observed the relationship, illustrated in Figure 1, between certain types of phase dispersion, pulse frequency (at constant amplitude), and total column throughput. The various regions of pulse-column operation were designated as follows:

A. Flooding region due to insufficient pulsing.

B. Mixer-settler region, characterized by separation of phases into clear layers between plates during the quiescent portions of the pulse cycle.

C. Emulsion-type region, characterized by fairly uniform dispersion of the discontinuous phase and little change in phase dispersion throughout the pulse cycle.

D. Unstable region, characterized by local flooding and irregular dispersion at operation near the flooding point.

E. Flooding region due to excessive pulsation.

Sege and Woodfield stated that at low frequencies the capacity of the column is equal to the *pulsed volume velocity* (the pulse amplitude-frequency product). Thus the flooding curve at low frequencies was shown as a straight line through the origin. At higher frequencies the flooding curve began to deviate from the pulsed-volume-velocity line, first passing through a maximum and then decreasing. Finally a limiting frequency (or amplitude-frequency product) was reached, above which no countercurrent flow through the column was possible. Other investigators (*3, 5*) also reached the conclusions illustrated in Figure 1.

At a given throughput, flooding of a pulse column can be caused by either inadequate or excessive pulsation. Decreasing the pulse frequency causes flooding when the pulsation becomes insufficient to pass the feed streams through the column. Increasing the pulse frequency causes flooding when the pulsation causes emulsification, or the rate of countercurrent flow decreases because of small drop size.

These two types of flooding were also described in a study by Cohen and Beyer (*1*), who presented a simplified analysis of the operating mechanism of a pulse column for conditions of inadequate pulsation, in which the effect of the flow of light-liquid phase to the column was considered. Conditions of vigorous pulsing were shown to be accompanied by a definite amount of recycle, or back mixing, within the column. Their work indicated that the simple relationship between total throughput and pulsed volume velocity indicated in Figure 1 is an oversimplification.

The major purpose of this investigation was to initiate a systematic study of the pulse-column operating variables which influence flooding. The operating variables considered were pulse frequency, pulse amplitude, light-liquid flow rate, and heavy-liquid flow rate. An equation is developed for predicting conditions of inadequate pulsation. Experimental data are presented in support of this equation.

APPARATUS AND PROCEDURE

A 1-in.-diam. ten-plate pulse column with a 2-in. plate spacing was used. The column consisted of stacked glass sections with gaskets and plates inserted between the glass sections as shown in Figure 2. Four tie rods surrounding the glass sections placed the entire assembly in compression. The contacting section of the column was 18 in. high and consisted of nine sections of heavy-walled glass tubing, each 1-in. I.D. and 1⅞ in. high. End sections of the column were made from 2-in.-long sections of 3-in. I.D. glass tubing fitted to 2-in.-long conical glass sections which reduced the diameter of the end sections to the diameter of the column. A 1-in. length of 1-in. I.D. tubing was fitted to the conical section, giving a total over-all length of 5 in. for the end section. The plates were made from 2-in. squares of 26-gauge stainless steel sheets perforated with 1/32-in.-diam. holes punched on staggered centers 0.055 in. apart, providing 25% free area. The 1/16-in. Teflon gaskets located on each side of each plate were punched with a 1-in.-diam. hole to match the inside diameter of the glass sections.

The schematic flow diagram presented in Figure 3 illustrates pulse-column assembly and operation. The hexone-water system was selected for this investigation; no solute was used, as flooding, rather than extraction, was studied.

Pulsation of the fluid contents of the column was introduced through a chamber located at the base of the column. A glass check valve was installed in the aqueous effluent line to eliminate backflow in the flexible leg during the downsurge of the pulse. As the top of the column was open to the atmosphere, only liquid in the column and in the pulse line between the pulse generator and the bottom of the column was pulsed. Pulsation was produced either by a duplex diaphragm proportioning pump with the check valves removed or by a reciprocating brass bellows. Both pulsators possessed sinusoidal variation of displacement with time.

Amplitude, frequency, and wave form are necessary to identify the characteristics of a pulse. A sinusoidal pulse wave form was used in this investigation, as well as in the majority of pulse-column studies reported by other workers. The *pulse amplitude* was defined in this investigation as the total linear displacement of the fluid contents in the column cross section from one extreme position to the other. The product of the

R. B. Edwards is at present with Eastman Kodak Company, Rochester, New York, and G. H. Beyer with the University of Missouri, Columbia, Missouri.

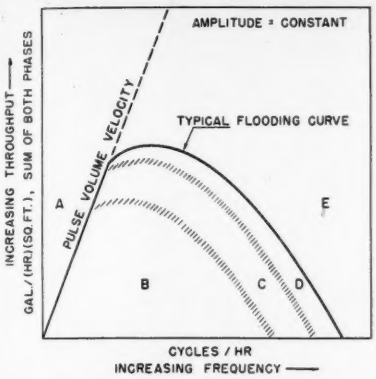

Fig. 1. Pulse-column operating characteristics.

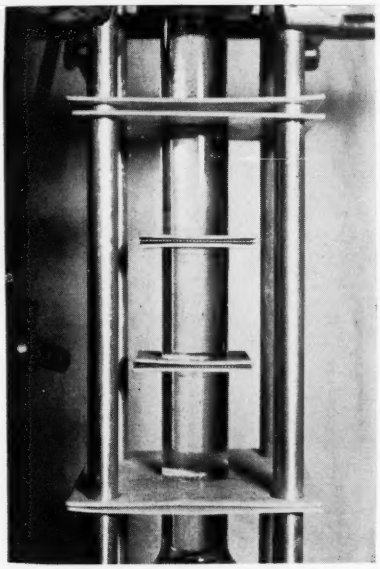

Fig. 2. Close-up photograph showing stacked-column construction.

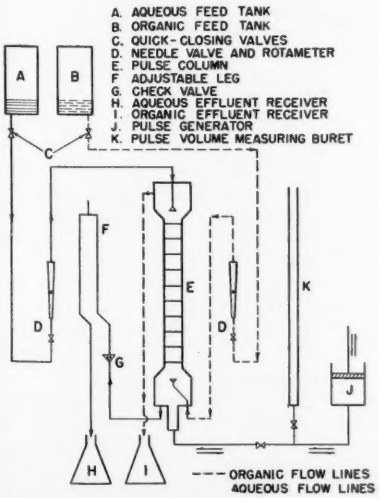

Fig. 3. Schematic flow diagram of pulse column and auxiliary equipment.

pulse amplitude and the column cross-sectional area was equal to the pulse volume.

Two methods of measuring pulse amplitude (or volume) were used. At low pulse frequencies and amplitudes, the pulse volume was measured by the variation in height of a column of fluid in a burette. The second method of measuring pulse amplitude consisted of measuring the total linear displacement of the fluid directly in the column. A sharply pointed probe attached to a micrometer was mounted at the top of the pulse column, as shown in Figure 4. Raising the point of the probe until it just broke free from the liquid surface at the bottom of the downsurge and lowering it until it just made contact with the liquid surface at the top of the upsurge made possible a measurement of the fluid displacement. The effect of surface tension tended to prevent the liquid from breaking free from the point of the probe and so necessitated a static correction.

The pulse frequency was determined by a visual count of the number of pulses occurring during a known interval of time. A sufficient number of pulses was observed so that the frequency might be calculated with an error of less than 0.1 cycle/min.

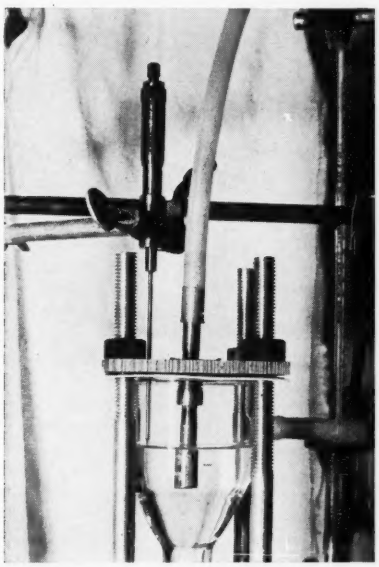

Fig. 4. Micrometer probe used to measure pulse volume.

Before any column runs were made, the aqueous and organic phases were mutually saturated by pumping both phases through the column several times. The pulse column was usually placed in operation at a given pulse frequency, with flow rates adjusted to the desired values by the needle valves and rotameters. The principal interface was maintained at the top of the column by the flexible leg.

After the flow rates and the interface level were constant for a period of at least a half hour, the column was assumed to be at steady state in the normal operating region (areas B and C in Figure 1). At a given organic flow rate, pulse frequency, and aqueous flow rate, the amplitude was gradually decreased until flooding was observed. After each decrease of the pulse amplitude, the column was allowed to return to steady state operation unless flooding occurred. The transition from normal operation to flooding was usually well defined by an uncontrollable rising of the interface at the top of the column. Simultaneously, a buildup of an organic phase layer in the end section beneath the bottom plate was observed. At incipient flooding, the flow rates were measured by collecting the effluent streams during three consecutive 5-min. increments of time and measuring these volumes. Column operation was then interrupted to measure the pulse volume.

INVESTIGATION

Flooding Caused by Inadequate Pulsation

For mixer-settler type of operation, a definite minimum rate of pulsation exists which is just sufficient to push upward the amount of light liquid fed and to pull downward the amount of heavy liquid fed. Flooding caused by inadequate pulsation is not governed by hydrodynamic considerations; it is caused by the inability of the pulse to pass the desired amount of fluid through the plates.

An equation will now be derived from an analysis of column operation at inadequate pulsation. In the following derivation, operation will be considered at the bottom section of the column immediately below the lowest plate, as indicated by the level P in Figure 5. It will be assumed that the organic and aqueous phases are both fed continuously to the column at constant rates, but that organic and aqueous effluent streams both leave the column only during the pulse upsurge. It will also be assumed that the pulse wave form is sinusoidal.

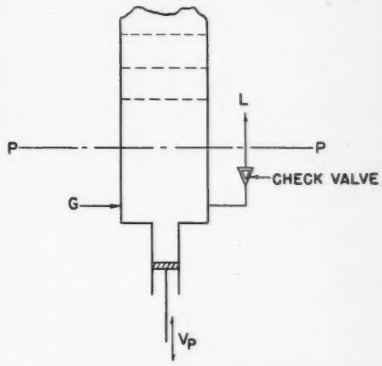

Fig. 5. Schematic illustration of bottom of pulse column.

If the upward flow of fluid at P is considered as positive, then

$$Q = \frac{v}{2}\sin(2\pi ft) + Gt \qquad (1)$$

and

$$V_p = vf \qquad (2)$$

where

V_p = pulsed volume velocity, cc./min.

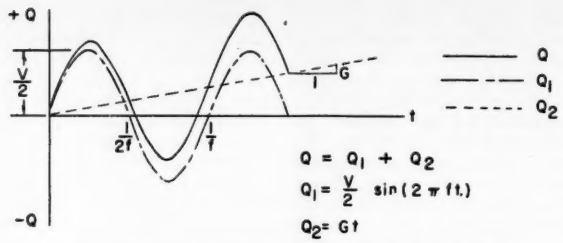

Fig. 6. Q vs. t at level P for a sine-wave pulse form.

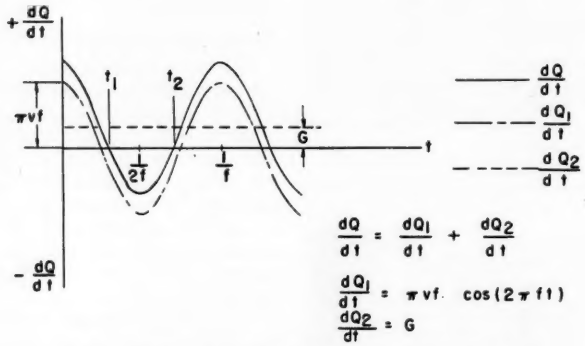

Fig. 7. dQ/dt vs. t at level P for a sine-wave pulse form.

In Equation (1) the quantity Gt represents the amount of fluid which has passed P as a result of the continuous feed of organic phase into the bottom of the column. Likewise the quantity $v/2 \sin(2\pi ft)$ represents the amount contributed by the sinusoidal pulse. Equation (1) is illustrated in Figure 6.

Differentiation of Equation (1) with respect to time gives the velocity past P at any time.

$$dQ/dt = \pi vf \cos(2\pi ft) + G \quad (3)$$

Equation (3) is illustrated in Figure 7.

The fluid volume that is pulled down the column on each downsurge q_d is obtained by integrating Equation (3) between the limits of t_1 and t_2, where t_1 and t_2 are the first and second roots, respectively, of Equation (3) when the velocity is zero, as shown in Figure 7. Thus

$$q_d = -\int_{t_1}^{t_2} [\pi vf \cos(2\pi ft) + G]\, dt \quad (4)$$

or

$$q_d = v \cos\phi + (2\phi - \pi)G/2\pi f \quad (5)$$

where

$$\phi = \arcsin(G/\pi vf) \quad (6)$$

Because of the check valve located in the aqueous effluent line, no backflow is assumed to exist in the flexible leg, and so the downward movement of fluid occurs only in the column.

The rate at which fluid flows down the column is then obtained from the product of the pulse frequency and q_d as given by Equation (5). The rate of downward flow must be at least equal to the aqueous flow rate L, as the aqueous phase will be drawn down through the column only when the fluid velocity is negative at P. If the rate of downward flow is greater than the aqueous flow rate, a condition will exist in which liquid in the column is recycled. Recycle, or back mixing, represents the return of fluid to its source. When recycle is present, therefore, some fluid can be expected to pass through a single plate more than once, and some cocurrent flow will be superimposed upon the net countercurrent flow of both phases.

For the general case, with V_r representing the recycle rate in cc./min.,

$$\frac{V_r + L}{f} = v \cos\phi + (2\phi - \pi)G/2\pi f \quad (7)$$

or

$$V_r = V_p \cos\phi + G\phi/\pi - G/2 - L \quad (8)$$

When $V_r > 0$, back mixing exists in the column. When $V_r = 0$, no recycle is present and the pulsation is just adequate to pass L cc./min. of aqueous phase down the column. When $V_r < 0$, the pulsation is not adequate to pass the required amount of aqueous phase down the column and flooding occurs.

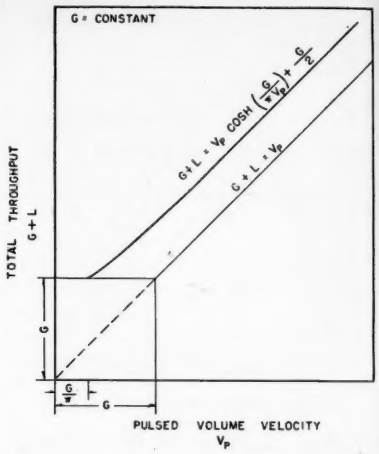

Fig. 8. Comparison of flooding equations.

A similar analysis of column operation considering the upsurge also results in Equation (8), indicating that the recycle on the upsurge is equal to the recycle on the downsurge. On the upsurge, fluid flows not only upward through the column, but also upward through the aqueous effluent line. Thus aqueous phase leaves through the flexible leg, and organic phase plus recycled fluid flows up the column.

Equation (8) represents an exact expression of the flow behavior of a pulse column, but it is cumbersome to use in the form given. Through the use of a series expansion of Equation (8), it may be shown (*2*) that an excellent approximation of it is given by

$$V_r = V_p(\cosh\theta) - G/2 - L \quad (9)$$

where

$$\theta = G/\pi V_p \quad (10)$$

At incipient flooding where $V_r = 0$, rearrangement of Equation (9) gives

$$\pi L/G + \pi/2 = (\cosh\theta)/\theta \quad (11)$$

Equation (11) is a convenient expression for predicting conditions of flooding due to inadequate pulsation. The left side of the equation is a function of only the flow-rate ratio, a quantity usually established by the stage requirements of a given extraction problem. With the flow-rate ratio known, the value of θ may be determined and the minimum pulsed volume velocity necessary for any value of G thus established. It should be noted that when the quantity $\pi L/G + \pi/2$ is greater than the quantity $(\cosh\theta)/\theta$, negative recycle, or flooding, exists. When the reverse is true, normal operation accompanied by recycle occurs.

Equation (11) indicates that total throughput is inadequate for describing the conditions of flooding caused by inadequate pulsation. Instead each indi-

TABLE 1. INADEQUATE PULSATION STUDIES AT DIFFERENT PULSE FREQUENCIES

Nominal Aqueous Flow Rate = 100 cc./min.

Run	v	V_p	G	L	θ	cosh θ	(cosh θ)/θ	$\pi L/G + \pi/2$	V_r
Pulse frequency = 72.6 cycles/min.									
NG-15	2.25	163.4	114.0	98.5	0.222	1.0248	4.62	4.28	11.9
HG-1-R	1.6	116.2	17.0	103.6	0.046	1.0011	21.76	20.71	3.2
HG-2-R	1.7	123.4	41.3	99.9	0.106	1.0055	9.48	9.17	3.6
HG-3-R	3.4	246.8	257.7	99.1	0.332	1.0556	3.18	2.78	32.6
HG-4-R	2.6	188.8	141.7	103.4	0.239	1.0287	4.30	3.86	20.0
HE-5-R	2.3	167.0	137.7	98.8	0.262	1.0345	3.95	3.83	5.2
HE-6-R	5.6	406.6	654.7	100.9	0.512	1.1340	2.21	2.06	32.8
HE-7-R	2.0	145.2	103.3	98.9	0.226	1.0257	4.54	4.58	− 1.6
HE-8-R	1.9	137.9	78.8	100.8	0.182	1.0166	5.58	5.56	0.9
HE-9-R	2.9	210.5	204.0	98.9	0.308	1.0478	3.40	3.10	19.7
HE-10-R	4.9	355.7	504.3	102.4	0.451	1.1035	2.45	2.21	37.9
HE-11-R	3.9	283.1	369.5	102.1	0.415	1.0874	2.63	2.44	20.9
Pulse frequency = 59.9 cycles/min.									
WG-31-R	3.64	217.7	234.2	103.6	0.342	1.0591	3.10	2.96	9.9
WG-32-R	4.30	257.1	333.3	103.0	0.413	1.0865	2.63	2.54	9.7
WG-33-R	2.63	157.3	122.5	99.9	0.248	1.0309	4.16	4.14	1.1
WG-34-R	5.11	305.6	443.3	101.3	0.462	1.1087	2.40	2.29	15.9
WG-35-R	5.70	340.9	524.4	101.6	0.490	1.1225	2.29	2.18	18.9
WG-36-R	5.77	345.0	527.8	99.7	0.487	1.1210	2.30	2.16	23.1
EG-53-R	2.26	135.3	90.0	98.7	0.212	1.0225	4.82	5.02	− 5.4
Pulse frequency = 35.7 cycles/min.									
EG-5	8.9	317.7	498.0	103.0	0.499	1.1271	2.26	2.22	6.1
HE-16-R	3.3	117.8	66.5	98.4	0.180	1.0162	5.64	6.22	−12.9
HE-17-R	9.3	332.0	432.9	99.5	0.415	1.0874	2.64	2.29	45.1
WE-46-R	7.81	278.8	382.4	98.8	0.437	1.0971	2.51	2.38	15.9
WE-47-R	7.80	278.5	370.3	98.9	0.423	1.0908	2.58	2.41	19.7
EE-52-R	3.78	134.9	91.8	103.0	0.217	1.0236	4.72	5.10	−10.8
Pulse frequency = 17.5 cycles/min.									
HE-12-R	7.0	122.5	43.7	101.7	0.114	1.0065	8.83	8.88	− 0.2
HE-13-R	8.2	143.5	77.3	103.3	0.171	1.0147	5.93	5.77	3.7
HE-14-R	9.1	159.2	117.0	98.5	0.234	1.0275	4.39	4.22	6.6
HE-15-R	13.8	241.5	266.6	100.1	0.351	1.0623	3.03	2.75	23.1

vidual flow rate must be considered. To compare Equation (11) with the flooding relation presented in Figure 1 by earlier workers, Equation (11) can also be written as

$$G + L = V_p(\cosh \theta) + G/2 \quad (12)$$

It may be recalled that the equation of the inadequate pulsation line illustrated in Figure 1 is

$$G + L = V_p \quad (13)$$

Equations (12) and (13) may be compared by plotting $G + L$ against V_p at constant G, as shown in Figure 8.

Figure 8 predicts that throughputs greater than the pulsed volume velocity should be possible. Equation (12) is represented in Figure 8 by a slightly curved line which nearly parallels the straight line of Equation (13). Because $\theta \leq 1$, the line representing Equation (12) terminates at an abscissa of $V_p = G/\pi$; the ordinate for this point is G. When the total throughput is G, the minimum ordinate for both flooding lines in Figure 8, Equation (13) predicts that a pulsed volume velocity equal to G will be necessary to avoid flooding. However, the flooding line given by the theoretically derived Equation (12) predicts that a pulsed volume velocity of only G/π will be required. Such a low pulsed volume velocity is possible because the organic feed entering the bottom of the column enhances the pulse upsurge. Thus the volume pushed upward through a plate is larger than that due to pulsation alone.

To test Equation (11) experimentally, a series of flooding runs was made at an aqueous flow rate of 100 cc./min. and pulse frequencies of 17.5, 35.7, 59.9, and 72.6 cycles/min. The results are given in Table 1. The data, compared with Equation (11) in Figure 9, substantiate the conclusion that flooding due to inadequate pulsation is indeed a function of the pulsed volume velocity rather than of pulse volume and pulse frequency acting independently of one another.

The data shown in Figure 9 indicated a tendency for flooding to occur with a slight amount of recycle present, so that the column appeared to flood at higher pulsed volume velocities than predicted. One possible explanation of why a slight recycle would be present was the existence of a condition which may be designated as "forced recycle"—the inability of a droplet forming on the surface of a plate to break free before being sucked back through the perforation on the reverse pulse surge. Also the check valve failed to close immediately as the pulse began its downsurge, thereby allowing some fluid to be pulled back into the bottom of the column from the flexible leg. The agreement of the data with the equation, however, was sufficiently good so that additional modification of the equation was considered unnecessary.

In addition to the flooding studies made at an aqueous flow rate of 100 cc./min., runs were made at nominal aqueous flow rates of 50, 200, and 300 cc./min. The experimental results are given in Table 2, and the data are compared in Figure 10 with the theoretical relation. Fair agreement of the data with the equation existed, although most of the points fell slightly below the line as described above. However, several flooding points for runs at high aqueous flow rates were above the line in the region where flooding should occur, indicating that operation with negative recycle was possible without flooding. In these runs at high aqueous flow rates the check valve was observed not to close on the pulse downsurge, and so the aqueous effluent flowed from the column continuously instead of leaving only on the upsurge, as assumed in the derivation of the flooding equation. Apparently in these runs such a low flexible-leg position was used that fluid could flow from the column simply owing to the effect of gravity, without the aid of pulsation.

The theoretical analysis presented here may also be used to calculate the amount

Table 2. Inadequate Pulsation Studies at Different Aqueous Flow Rates

Run	f	v	V_p	G	L	θ	cosh θ	(cosh θ)/θ	$\pi L/G + \pi/2$	V_r
Nominal aqueous flow rate = 50 cc./min.										
HE-18-R	72.6	1.3	94.4	81.7	51.3	0.275	1.0381	3.77	3.54	5.9
HE-19-R	72.6	2.7	196.0	256.0	49.3	0.416	1.0878	2.61	2.17	35.9
HE-20-R	72.6	2.2	159.7	165.3	48.2	0.329	1.0450	3.18	2.49	36.1
HE-21-R	72.6	4.6	334.0	575.1	46.9	0.548	1.1540	2.10	1.83	50.9
HE-22-R	72.6	1.15	83.5	20.5	47.4	0.078	1.0031	12.86	8.83	26.2
HE-30-R	72.6	3.9	283.1	440.3	50.8	0.495	1.1251	2.27	1.93	47.5
WG-37-R	59.9	2.05	122.8	120.5	49.9	0.312	1.0490	3.36	2.87	18.7
WG-38-R	59.9	2.51	150.3	205.5	51.5	0.435	1.0961	2.52	2.36	10.4
WG-39-R	59.9	3.16	189.3	302.0	51.0	0.508	1.1318	2.23	2.10	12.2
WG-40-R	59.9	4.04	242.0	447.5	50.7	0.588	1.1780	2.00	1.93	10.6
WG-41-R	59.9	4.35	260.6	495.8	49.9	0.606	1.1893	1.96	1.89	12.1
EE-54-R	17.5	5.42	94.8	90.7	50.3	0.304	1.0465	3.44	3.31	3.5
Nominal aqueous flow rate = 200 cc./min.										
EE-55-R	72.6	2.67	193.8	86.8	193.7	0.142	1.0101	7.11	8.58	−41.3*
WG-50-R	59.9	3.43	205.4	101.6	200.1	0.157	1.0123	6.45	7.76	−43.0*
WG-51-R	59.9	5.79	346.6	302.9	205.2	0.278	1.0389	3.74	3.70	3.5*
Nominal aqueous flow rate = 300 cc./min.										
HE-25-R	72.6	3.0	217.8	52.5	288.7	0.077	1.0030	13.02	18.85	−96.5*
HE-26-R	72.6	5.2	377.8	104.6	299.1	0.088	1.0039	11.41	10.55	27.6
HE-28-R	72.6	2.95	214.2	34.2	291.0	0.051	1.0014	19.64	28.30	−93.6*

*Check valve not seated; so continuous flow of aqueous effluent existed.

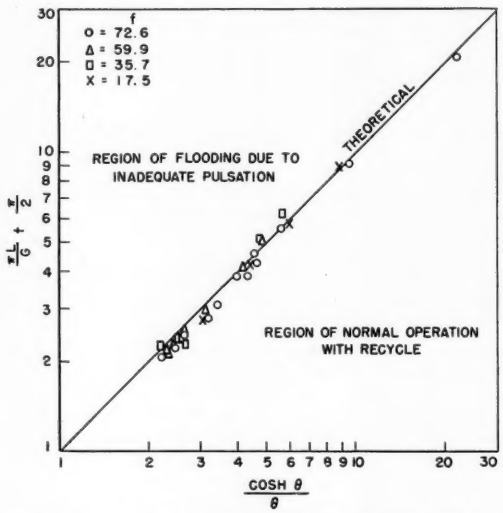

Fig. 9. Comparison of theoretical flooding equation with experimental results obtained at four frequencies and an aqueous flow rate of 100 cc./min.

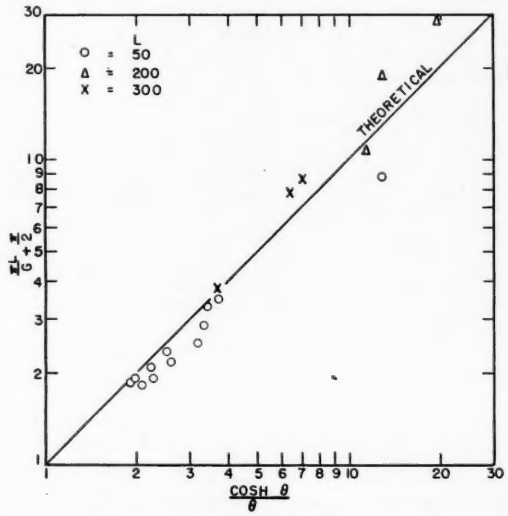

Fig. 10. Conditions at incipient flooding due to inadequate pulsation observed for three different aqueous flow rates.

of recycle for various conditions of operation. Recycle represents a deterioration of true countercurrent operation. The recycle rate V_r might prove useful as a correlating device for pulse-column-extraction studies.

NOTATION

Q = net quantity of fluid in cc. which has flowed upward past level P (*see* Figure 5) at any time t in min. from the time $t = 0$.
t = time, min.
G = light-phase (organic) flow rate, cc./min.
L = heavy-phase (aqueous) flow rate, cc./min.
f = pulse frequency, cycles/min.
v = pulse volume, the volume displaced during the pulse movement of the fluid contents of the column from one extreme position to the other, cc./cycle
V_p = pulsed volume velocity, cc./min, $v \times f$
q_d = fluid volume pulled down the column on each downsurge, cc./cycle
V_r = recycle rate, cc./min.
ϕ = arcsin $(G/\pi v f)$
θ = $G/\pi V_p$

ACKNOWLEDGMENT

The authors wish to express their appreciation to the Ames Laboratory of the Atomic Energy Commission and to the Institute for Atomic Research, Iowa State College, for support of this project.

LITERATURE CITED

1. Cohen, R. M., and G. H. Beyer, *Chem. Eng. Progr.*, **49**, 279 (1953).
2. Edwards, R. B., Ph.D. thesis, Iowa State College Library, Ames, Iowa (1954).
3. Griffith, W. L., G. R. Jasny, and H. T. Tupper, U. S. Atomic Energy Commission *Rept. AECD-3440* (1952), declassified.
4. Sege, G., and F. W. Woodfield, *Chem. Eng. Progr.*, **50**, 396 (1954).
5. Wiegandt, H. F., and R. L. Von Berg, *Chem. Eng.*, **61**, 183 (July, 1954).

Presented at Nuclear Science and Engineering Congress, Cleveland.

Purity Control in Sodium-cooled Reactor Systems

WARREN H. BRUGGEMAN

Knolls Atomic Power Laboratory, Schenectady, New York

Recent advances in purity control in sodium systems are covered. Emphasis is placed on results from the prototype S.I.R. system as well as other unpublished data. Included are chemical and nuclear activation analyses of sodium, filtration data, and details and operation of cold traps and plugging indicators.

The development of sodium as a coolant for nuclear reactors has given rise to many interesting problems. One such area of interest is associated with purity control of the sodium. During the past months several (*1, 2*) informative papers have been published on the subject. The present paper is an attempt to bring the reader up to date in the field of sodium-purity control. Emphasis is placed not only on previous unpublished work but also on experience gained in preliminary operation of the sodium-cooled submarine intermediate reactor (S.I.R.) project.

SODIUM SUPPLY

Sodium, available commercially from three American manufacturers: duPont, Ethyl Corp., and U. S. I. Chemical Corp., is produced electrolytically from salt and is extremely pure. A typical analysis of commercial sodium is given in Table 1. This assay represents an average of sixteen individual samples of sodium supplied by duPont for the S.I.R. Mark A power plant, a prototype of the power plant of the U.S.S. *Seawolf* (SSN575).

Because the Mark A plant was designed prior to widespread use of cast-drum sodium, its sodium charge was purchased in the form of 12½-lb. bricks. The principal impurities controlled in the purchase specification were calcium, to less than 400 p.p.m., and chlorine, to less than 50 p.p.m. Although not critical, these impurities were designated to assure a product consistent with that normally used in prior-development systems.

A special request was placed on the sodium supplier to provide sodium which was "cast dry," i.e., cast without the use of kerosene as a mold-release agent. In addition, it was requested that stop-cock valves not be heavily greased prior to running the Mark A order. This was done to assure absence of hydrocarbons. It is felt that the hydrocarbons in excess will decompose and carburize the stainless steel components of a sodium system (*3*). At Knolls Atomic Power Laboratory, carburized layers of approximately 1-mil thickness have been observed in tests up to 1,000°F. Although not excessively deep, such carburization is thought to weaken thin reactor parts which may be subjected to cyclic strains.

Because of a faint kerosenelike odor in sodium supplied to Mark A, careful analyses were made for hydrogen and carbon. Analysis of the molten metal indicated 50 and 100 p.p.m. respectively. The value of 100 p.p.m. carbon is felt to be well below that amount which would cause carburization. Analyses were performed by procedures outlined in references *4* and *5*.

As a remaining check on the impurity content in the Mark A sodium charge, samples were inserted for nuclear reactivity measurements in a thermal critical assembly. Results were in arbitrary units (cents of reactivity/g.) which, when converted, indicated that total parasitic absorption due to impurities was less than 18 p.p.m. boron or equivalent. As such, the nuclear poisoning effect of the impurities is less than 10% of the value calculated for pure sodium. Samples of Ethyl and U.S.I. sodium, tested in a similar manner, gave results identical to those from the duPont metal.

Substantiation of the purity of commercial sodium is available from recent radioactive decay data on Mark A sodium. After a period of 100-hr. operation the S.I.R. reactor was shut down and the sodium activity observed. The sample decayed for 13 days at the expected 15-hr. half-life. The impurity activity controlling after the thirteenth day leveled out at 27 days to a value 9 decades below the saturated Na^{24} level. Although this is a significant reduction in activity, it points up the need for complete system drainability of the sodium system. This is particularly true if maintenance is to be readily obtained on high-power-level reactor systems.

FILTRATION

Although the analysis of sodium indicates that the material is pure, it is advisable to filter the metal prior to introduction into a reactor system. Such filtration removes sodium oxide and also any insoluble foreign matter which may find its way into the commercial sodium.

In Mark A S.I.R. the brick sodium was melted in 900-lb. batches and forced through a filter into a transfer tank operating under vacuum. A second filter is located in this tank. The batches of sodium were transferred by positive pressure through this second filter to the system storage tank. The filters used in both tanks were sintered stainless steel with an average pore size of 5μ. Both

Table 1. Analysis* of S.I.R. Mark A Sodium

Element	P.p.m.	Method‡
Ag	< 1	S
Al	7.7	C
B	4	S
Ba	2	S
Be	< 1†	S
Bi	< 10†	S
Ca	191	C
Cd	< 1	S
Ce	2	S
Cl	30	C
Co	2	S
Cr	< 1	C
Cs	< 5	C
Cu	2	S
Fe	2.4	C
Hg	< 4†	S
In	< 2†	S
K	<100	C
Li	17	C
Mg	< 5	C
Mn	< 2	S
Mo	< 2†	S
Ni	0.5	C
P	< 10	C
Pb	1.1	C
Pd	< 5	S
S	14	C
Si	< 0.5	C
Sn	< 10†	S
Sr	5	S
Ti	< 10†	S
U	< 5	C
V	< 5	S

*Sodium supplied by E. I. duPont de Nemours & Co. in 1954. Analysis of "as received" bricks performed by General Analytical Unit, Knolls Atomic Power Laboratory, L. P. Pepkowitz, Manager.
†None detected; value listed represents expected sensitivity of spectrographic detection.
‡S = spectrographic; C = wet chemical.

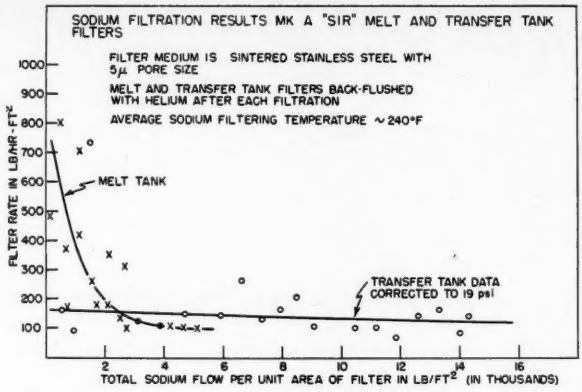

Fig. 1.

filters were back flushed with helium after each transfer.

As expected, heavy accumulations of sodium oxide occurred in the melt tank owing to the oxidized skin on the brick sodium. This necessitated the changing of filters and puddling and removing the oxide dross at approximately 6,000-lb. intervals. The filtration rate averaged 248 lb./(hr.)(sq. ft.) at an average temperature of 236°F. with a 19 lb./sq. in. differential.

The difficulties resulting from the excess dross on brick sodium points up the desirability of procuring sodium in rail car lots or in the cast in drum form. Even in using these forms, a filter is advisable. Filtration data taken on the Mark A transfer-tank filter would be applicable in these cases since the sodium filtered was relatively free of oxides. The average filter rate from the Mark A transfer tank was 177 lb./(hr.)(sq. ft.) at an average differential of 20.0 lb./sq. in. at 245°F.

Figure 1 plots data for the melt- and the transfer-tank filters. To allow comparison of the two operations, the transfer-tank-filter results were corrected to a 19 lb./sq. in. differential by use of a ratio of pressures. There is no obvious explanation for the absence of high filtration rates during initial operation of this filter. It is expected that oxide deposition within the filter pores plays an important role in the results. The inconsistency in data may occur since the transfer-tank filter was original equipment and may have been exposed to sodium for a long period of time prior to use. On the other hand, data plotted on the melt-tank filter represent runs on the second and third filter replacements.

A chemical analysis after filtration indicated that of the impurities listed in Table 1 the only element which experienced a significant reduction was calcium. This decreased from 191 to less than 40 p.p.m. Calcium reduction results from its oxidation with the excess sodium oxide present in the brick melting tank.

CALCIUM IN SODIUM

If the sodium had been supplied in oxide-free tanks, such oxidation of calcium would not be expected to occur immediately upon charging. The possibility is therefore raised of admitting soluble, unoxidized calcium into a reactor coolant system. Subsequent oxidation would result in the formation of calcium oxide, which is insoluble and hence could cause hydraulic or mechanical difficulties.

The decrease of free calcium in sodium systems has been observed at Knolls for several years. The impurity tends to accumulate on the walls of the pipe and at low-velocity regions. In one experiment calcium was added to a flowing system equipped with a restricted-passage orifice plate. This plate, perforated with 50-mil-diam. holes, was intended to simulate the small flow passages in a power reactor. The loop was charged with sodium containing sufficient sodium oxide to cause sodium oxide plugging of the plate when the loop temperature was lowered to 525°F. On the addition of calcium to provide 500 p.p.m. calcium in sodium, the flow decreased to 84% of the original value. When enough calcium was added

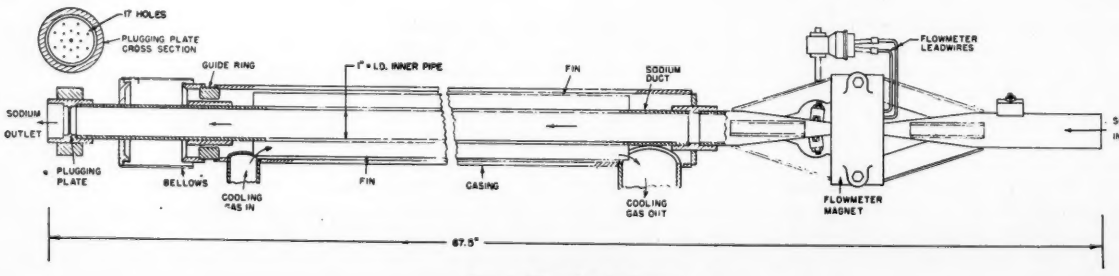

Fig. 2. Plugging indicator.

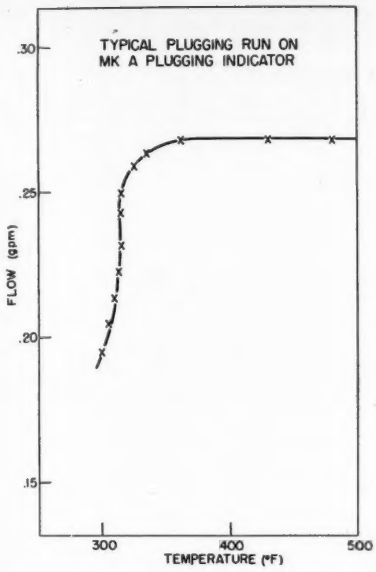

Fig. 3.

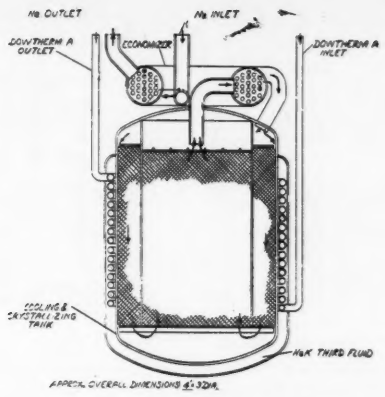

Fig. 4. Cold trap.

to raise the concentration to 675 p.p.m., flow decreased to 13% of normal. Subsequent dissection of the loop showed a calcium build-up of 1.5% at the perforated plate. Although solubility at loop temperatures is in excess of 1% calcium, a sample of the bulk sodium indicated only 2 p.p.m.

In view of the potential difficulties which may result from free calcium in sodium, caution should be exercised in the use of sodium which is received completely unoxidized.* Treatment by bubbling air through the molten fluid is one possible way of oxidizing, and thus removing, the calcium. An alternative is to purchase low-calcium sodium from the manufacturers. Although this is relatively new, as of this writing, two of the three sodium manufacturers can supply metal in tank-car lots with less than 50 p.p.m. calcium. The added cost for this product does not appear to be significant.

OXYGEN DETECTION

The principal impurity of concern in a sodium system is oxygen. The effect of the oxide on system pluggage, corrosion, and radioactive steel transport is discussed in the "Liquid Metals Handbook" (*1*). In order to monitor for oxygen in a sodium system, a plugging indicator can be used. Details of this instrument are discussed by Voorhees and Mausteller (*1*).

Figure 2 illustrates the plugging indicator used in Mark A S.I.R. Rated sodium flow is 0.3 gal./min. and the restricted passage consists of a thin plate with seventeen holes, each 0.046 in. in diameter.

Figure 3 shows a typical plugging run obtained by use of this unit. The break in the curve is distinct to within 35°F., resulting in accurate oxygen determination. With greater oxide concentrations, the knee in the curve would be even sharper. During the run shown, the plugging plate was cooling at a rate between 5° and 10°F./min.

The need for oxygen detection and control even after a system is carefully charged is illustrated by recent Mark A S.I.R. experience. The sodium was, as discussed above, double filtered at low temperature into the system storage tank. The storage tank and associated piping had been evacuated several times to a vacuum of 50μ. After each evacuation the system was repressurized to above atmospheric pressure with pure helium which had been further purified by passing through sodium potassium bubblers. The reactor-coolant system proper was also treated in a similar manner.

Despite the foregoing precautions, the oxygen content upon filling assayed at 0.019% O_2. It is probable that the total system oxide content was even higher, as only the oxide in solution can be detected. This excess above solubility was substantiated by a longer than usual cold-trapping time required to effect a reduction in the oxygen level.

Unfortunately, from a data standpoint, the initial operation was made with a sampler equipped for oxide determination by the conventional mercury-extraction technique (*6*). The device used was shielded evolution of the K.A.P.L. type II sampler (*7*). Somewhat later the system was fitted with a plugging indicator, thereby permitting very accurate oxygen control.

Recent data indicate that even after several months of operation, oxide is still building up at a rate of 7 g. of oxygen/day. Since no appreciable repairs have been undertaken and, further, since only a small fraction of this amount could be explained as oxygen from the inert gas, it is concluded that the oxygen is still being leached out as original impurities from the system. It must be stated, however, that "first time" caution has caused careful control of oxygen at levels (0.002% O_2) which are considered substantially lower than will ultimately be found necessary.

OXYGEN REMOVAL

The high degree of oxygen control in Mark A is readily maintained by use of a cold trap. The design of this unit is shown in Figure 4. It consists of a cooler-crystallizer section and a regenerative heat exchanger. Sodium, at a flow of 12 gal./min., is cooled in the regenerator from 600° to 750°F. The Dowtherm jacket in the crystallizer lowers the temperature an additional 70° to 300°F. This Dowtherm cooler assures that the lowest temperature exists in the crystallizer, thus providing for oxide accumulation in this region. In addition, the heat removed in the crystallizer provides the thermal driving force for operation of the regenerator. A more detailed description of the design features of this type of cold trap is found in reference *1*.

The crystallizer region of the Mark A cold trap is packed with a knitted stainless steel wire of 4 to 5 mils diam., packed to a density of 20 lb./cu. ft. This packing provides for the growth and support of the oxide crystals. The packing is a continuous strand of wire, considered necessary to prevent slivers of wire fiber from disengaging and causing mechanical difficulties in an otherwise clean reactor system. The volume of the crystallizer is approximately 80 gal. Aside from a capacity consideration, the volume provides approximately 5 to 6 min. holdup, which assures maximum efficiency in the crystallizer region.

*Similar plugging difficulties may occur owing to formation of Mg^{24} from the decay of Na^{24}. Magnesium will oxidize in preference to sodium, forming insoluble magnesium oxide. For example, magnesium build-up in a sodium system which has a saturated activity of 1 curie/g. will be 46 p.p.m./yr.

The crystallizer size of the mark A cold trap was based on some unpublished studies conducted by B. G. Voorhees and the author on a small ½-in. piping loop equipped with a test cold trap. The cold-trap crystallizer was 4 in. in diam. and 20 in. long and was packed with stainless steel wool. The loop was equipped with a perforated plate which served as a plugging indicator.

Residence time in the crystallizer was varied by varying the sodium flow rate. The results are plotted in Figure 5 as oxygen concentration in the loop as a function of number of times the system volume was passed through the cold trap. The flow volume passed through the unit is thus a measure of cold-trap efficiency. It is seen from Figure 5 that an appreciable gain in efficiency results from increasing crystallizer hold time from 2½ to 5 min. These data indicate that little is gained in efficiency when residence time is increased from 5 to 10 min.

A subsequent run was made on a comparable size of cold trap in which the steel-wool packing was removed. Although the unit was effective, the rate of removal was considerably less than the units which employ the steel-wool packing.

An estimate of the capacity used to design the Mark A cold trap was also determined by Voorhees and the author. Runs were conducted in a cold trap employing a 15-gal. steel-wool–packed crystallizer. Oxygen, added as Na_2O and Na_2O_2, was permitted to reach equilibrium with the test-system sodium before the cold trap was activated. The test was carried out until 35 wt. % Na_2O was accumulated in the crystallizer region. No increase in pressure drop was detected when the test system was secured for other reasons.

The Mark A cold trap is used on an intermittent basis in purifying the sodium charge. A typical operating run in purifying the S.I.R. sodium is shown in Figure 6. A comparison of these data was made with the theoretical reduction possible, based on ideal mixing in the system. This analysis* indicated that the cold-trap discharge was saturated at the lowest cold-trap temperature and hence was 100% effective.

In discussing cold traps, the author emphasizes that units of the Mark A type are designed for high efficiency and with considerable emphasis on total radioactive-shield weight. Cold traps for central-station nuclear plants can be less complex if allowed to be larger or of lower efficiency. For example, data above indicate that packing is not absolutely essential; likewise, the regenerative heat exchanger could be eliminated. A simple cold trap, particularly well suited to small test systems, is the natural-circulation type described in reference *1*.

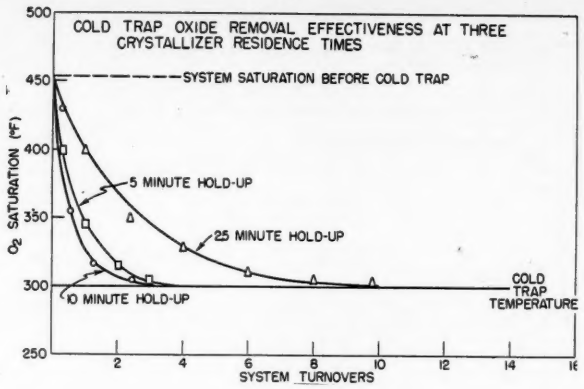

Fig. 5.

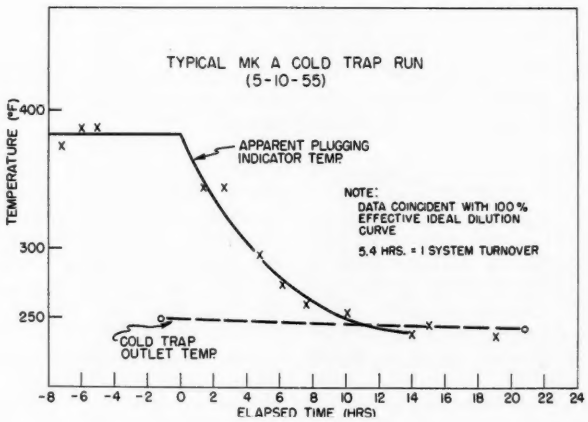

Fig. 6.

CONCLUSION

With time the technology of the use of sodium as a reactor coolant is becoming even more highly developed. It is significant that in the operation of the S.I.R. Mark A plant, purity-control considerations have worked out as anticipated. In general, this operation substantiates the author's belief that the purity considerations in using sodium are simple and no more complex than those involved in the use of other coolant fluids.

ACKNOWLEDGMENT

The author wishes to acknowledge the contributions of personnel in the Knolls Atomic Power Laboratory General Analytical Activity, S.I.R. Reactor Operations, and S.I.R. Coolant Testing. Individual contributors were B. G. Voorhees, W. W. Kendall, and A. A. Abbatiello. The able assistance of I. C. Chouinard in preparing the manuscript is appreciated.

LITERATURE CITED

1. Jackson, C. B., et al., Sodium-NaK Supplement, "Liquid Metals Handbook," 3d ed., U.S. Gov't Printing Office, Washington 25, D. C. (July, 1955).
2. Trocki, T., W. H. Bruggeman, and F. E. Crever, *Trans. First United Nations Sponsored Conference on Nuclear Energy* (August, 1955).
3. Brush, E. G., Knolls Atomic Power Laboratory, private communication.
4. Pepkowitz, L. P., and E. R. Proud, *Anal. Chem.*, **21**, 1000 (1949).
5. Pepkowitz, L. P., Knolls Atomic Power Laboratory, private communication.
6. ———, and W. C. Judd, *Anal. Chem.*, **22**, 1283 (1950).
7. Bruggeman, W. H., and G. Billuris, "Sampling of High Temperature Alkali Metals," Industrial Laboratories Publishing Company, Chicago (January, 1953).

Presented at Nuclear Science and Engineering Congress, Cleveland

*The analysis was based on:

$$\frac{C - C_t}{C_s - C_t} = e^{-V_s}$$

where

C = instantaneous oxide concentration in the system
C_t = theoretical minimum oxide concentration at the cold-trap discharge
C_s = system oxide saturation at start of the cold-trap run
V_s = number of times the system volume was passed through the cold trap

Oscillatory Behavior of a Two-phase Natural-circulation Loop

EUGENE H. WISSLER, H. S. ISBIN, and N. R. AMUNDSON

University of Minnesota, Minneapolis, Minnesota

A natural-circulation loop with water as the circulating fluid was studied for a range of operation covering two-phase flow. The work reported in this paper is concerned with the periodic oscillations of the flow rate and fluid temperature. The oscillations occurred even with constant heat input and constant cooling-water properties for the heat exchanger. The analytical approach includes a theoretical analysis of an open-ended system and numerical solutions obtained with an analogue computer for a simplified loop system. Also presented are the equations of motion, continuity, and energy, which were developed for a transient two-phase flow model for adaptation to more detailed numerical evaluations.

A program of study of the transient operation of natural-circulation loops has been underway at the University of Minnesota (*1*) and this paper is concerned with the oscillatory behavior of a two-phase natural-circulation loop. These studies are of interest for the emergency cooling of nuclear reactors and in the design of boiling-water reactors. The literature survey pertaining to the transient operation of a natural-circulation loop is given by Alstad, Isbin, Amundson, and Silvers (*1*), and a survey of two-phase flow literature is given by Isbin, Moen, and Mosher (*2*).

EXPERIMENTAL LOOP

Figure 1 is a schematic diagram of the natural-convection loop which was studied. The loop was constructed primarily of 16-gauge, 1-in. O.D. (0.872-in. I.D.) hard-drawn brass tubing. The major features of the loop are described in reference *1*. During a natural-circulation run the flowrators were by-passed and only the electromagnetic flow meter was used. Normally the surge tank, E_1, was not used for two-phase natural-circulation runs. For those runs in which the pressure at one point in the loop was held constant, the gate valve between the surge tank E_2 and the loop was opened; for the constant-volume run, the gate valve was closed. A heater and pump were installed to maintain the cooling-water supply at 5 gal./min. and at 130°F.

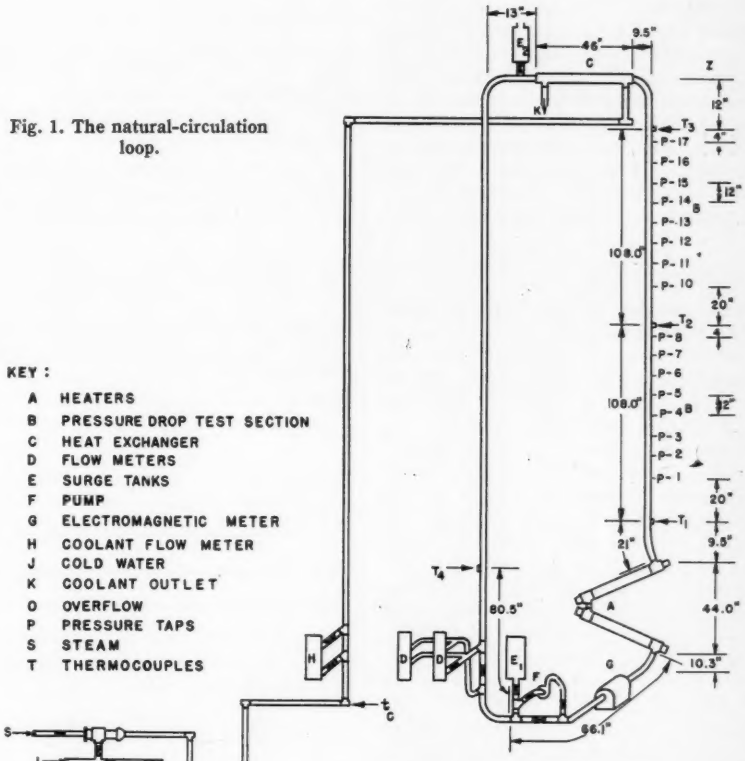

Fig. 1. The natural-circulation loop.

THEORETICAL ANALYSIS

General Equations

The continuity equation, the equation of motion, and the energy equation for a viscous fluid flowing in a region of general geometry were formulated for a phase having continuous properties. A similar set of equations was derived for flow across a surface of discontinuity. The combination of these two sets of equations gave the equations for the two-phase flow. If these equations are applied to flow through a pipe of uniform cross section in which the steam and water phases are assumed to be in equilibrium (that is, p and T correspond to the saturation pressure and temperature), the continuity equation may be written as

$$A\frac{\partial \rho}{\partial t} = -\frac{\partial W}{\partial x} \qquad (1)$$

The equation of motion for upward flow through a pipe becomes

$$\frac{1}{g_c}\frac{\partial W}{\partial t} + \frac{1}{g_c}\frac{\partial (W\phi_1 V)}{\partial x} = -A\frac{\partial p}{\partial x} - A\frac{g}{g_c}\rho z' - AF_f \qquad (2)$$

E. H. Wissler is at present stationed at the Army Medical Research Laboratory, Fort Knox, Kentucky.

Finally the energy equation is

$$A\frac{\partial(\rho\epsilon)}{\partial t}+\frac{\partial(W\phi_2\epsilon)}{\partial x}-\frac{A}{J}\frac{\partial p}{\partial t} \qquad (3)$$
$$=Q+\frac{\partial}{\partial x}\left[(k_wA_w+k_sA_s)\frac{\partial T}{\partial x}\right]$$

The terms ϕ_1 and ϕ_2 represent the ratio of the true rate of transport to the rate of transport of the mean flow for momentum and energy respectively. If both phases have the same linear velocity, ϕ_1 and ϕ_2 are unity.

The three functions ϕ_1, ϕ_2, and F_f were determined experimentally from steady state data. It was found that ϕ_1 and ϕ_2 could be correlated as functions of ρ alone and that

$$F_f=a(\rho)W^{1.79} \qquad (4)$$

where $a(\rho)$ is a function of ρ. Figures 2, 3, and 4 illustrate the variation of ϕ_1, ϕ_2, and $a(\rho)$ with ρ. Equations (1) through (4) have been applied to a natural-circulation loop in the form of finite-difference equations. The discussion of these equations is not included in this paper as the numerical calculations by means of the S.E.A.C. (National Bureau of Standard's digital computer, Standard's Eastern Automatic Computer) have not been successfully completed. The pressure-drop data will be reported separately.

STABILITY ANALYSES

An insight into the factors which determine the stability of a natural-convection system is gained through the analysis of an open-ended loop, such as the one shown in Figure 5. The fluid entering the heater always has the constant temperature T_0, and the velocity of the stream is fixed by the density difference between the fluid in the hot and cold legs. For any constant heat input, one may define a state of equilibrium in which the difference in weight of the two legs is just equal to the frictional resistance to flow. Under certain conditions this system may be unstable; that is, a small deviation from the equilibrium temperature distribution or the equilibrium flow may be propagated in space or time with increasing amplitude. The problem is to determine those conditions under which a flow perturbation of the form $\epsilon_V \sin \omega t$ can cause a sufficiently large change in the external force acting on the system to sustain or increase the flow perturbation. The problem has been treated analytically for a one-phase fluid (*3*), and the following conclusions were obtained:

1. If an oscillatory flow rate is to be possible, the force cannot be generated in the heater; it must be generated in the vertical riser.

2. The product of the coefficient of expansion of the fluid and the vertical height of the riser must exceed a certain value (defined by an analytical expression) if the flow perturbation is to be sustained.

3. The period of oscillation will be approximately equal to the residence time of the fluid in the heater and the vertical riser.

In order to predict the period for a closed loop, a problem was solved on a Reeves Electronic Analog Computer. The number of nonlinear terms was limited to sixteen, and the model used was necessarily a simple one. The computer could handle only ten subdivisions, with the driving force expressed as a linear function of all ten enthalpies and the frictional force as a quadratic function of the velocity. The number of available summing amplifiers limited the problem to the case in which boiling occurred only at the top subdivision of the vertical riser. The loop equations used were derived as noted in reference *1*.

The energy equation has been simplified in the following manner:

1. $\epsilon \simeq H$. The kinetic- and potential-energy terms were always less than 0.5% of the corresponding enthalpy terms.

2. $\dfrac{\partial}{\partial x}\left[(k_wA_w+k_sA_s)\dfrac{\partial T}{\partial x}\right]$

omitted. The axial conduction term was always less than 0.001% of the term $\partial/\partial x\,(W\phi_2H)$.

3. $\dfrac{A}{J}\dfrac{\partial p}{\partial t}$

omitted. An error of less than 0.004% is caused by the omission of this term.

4. $\phi_2 = 1$. The analysis was restricted to a simple model. With these conditions, Equation (3) reduces to

$$\frac{\partial H}{\partial t}=-\frac{V}{A}\frac{\partial H}{\partial x}+\frac{Q}{A\rho} \qquad (5)$$

The integration of the equation of motion [Equation (2)] around the loop leads to

$$\frac{dV}{dt}=\frac{-\oint\frac{g}{g_c}\rho z'\,dx-\oint F_f\,dx}{\oint\frac{\rho}{A}\frac{dx}{g_c}} \qquad (6)$$

with the added restriction that $\phi_1 = 1$.

Equations (5) and (6) were applied as

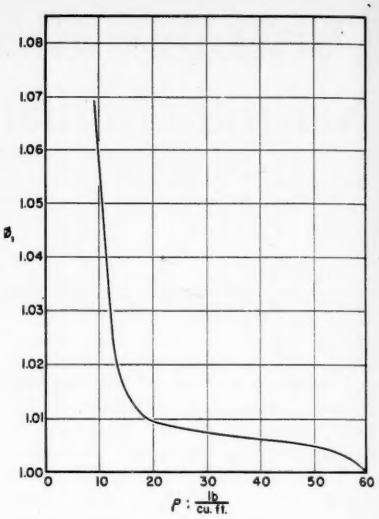

Fig. 2. The momentum-transport coefficient, ϕ_1.

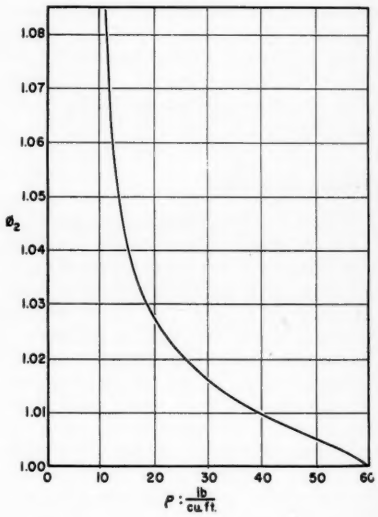

Fig. 3. The energy-transport coefficient, ϕ_2.

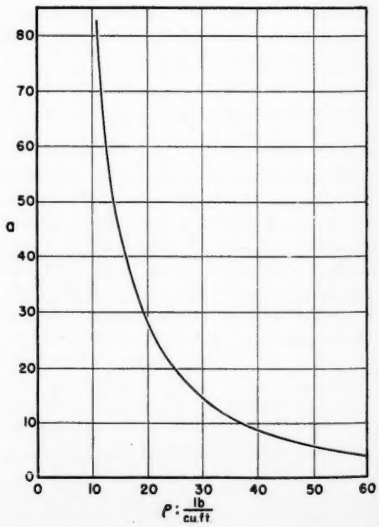

Fig. 4. The friction coefficient, $a(\rho)$.

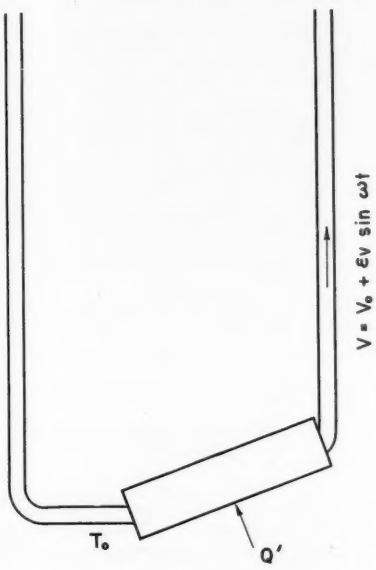

Fig. 5. The stability model.

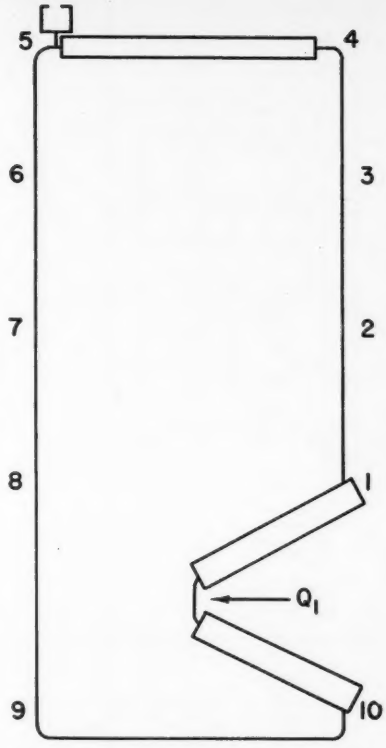

Fig. 6. Subdivisions for the analogue-computer problem.

TABLE 1. DATA FOR THE ANALOGUE COMPUTER

n	$(A\,\Delta x)_n$, cu. ft.	H_{n_0}, B.t.u./lb.	ρ_{n_0}, lb./cu. ft.	α_n, lb./(cu. ft.)(B.t.u./lb.)	z_n, ft.
1	0.23000	182	59.781	−0.024	3.7084
2	0.02387	182	59.781	−0.024	6.5278
3	0.02387	182	59.781	−0.024	6.5278
4	0.02387	182	37.500	−9.500	6.5278
5	0.01749	153	60.477	−0.024	0
6	0.02387	153	60.477	−0.024	−6.5278
7	0.02387	153	60.477	−0.024	−6.5278
8	0.02387	153	60.477	−0.024	−6.5278
9	0.01356	153	60.477	−0.024	−3.7084
10	0.04504	153	60.477	−0.024	0

Energy equation:

$$\frac{dH_n}{dt} = -\frac{V}{(A\,\Delta x)_n}(H_n - H_{n-1}) + \frac{Q_n}{A_n\bar{\rho}_n}$$

Flow equation:

$$\frac{dV}{dt} = \frac{-\frac{g}{g_c}\sum \bar{\rho} z_n'\,\Delta x - F}{\frac{1}{g_c}\sum \frac{\bar{\rho}_n\,\Delta x_n}{A_n}}$$

$$\bar{\rho}_n = \tfrac{1}{2}(\rho_n + \rho_{n-1})$$

$Q_1 = 3.16$ B.t.u./sec.; $Q_2 = Q_3 = Q_4 = 0$

$Q_5 = -25.0V[((H_5 + H_4)/2) - H_c]$ for the cooler. The heat transfer coefficient was taken to be a linear function of the flow rate, and the temperature driving force was approximated by the enthalpy differences.

A Taylor series was used for the approximation of the frictional force:

$$F \simeq F_0 + \frac{1.8F_0}{V_0}(V - V_0) + \frac{0.72F_0}{V_0^2}(V - V_0)^2$$

differential-difference equations and the loop was subdivided as shown in Figure 6. Table 1 summarizes the equations and data used for the analogue-computer problem.

The density at point n was written as

$$\rho_n = \rho_{n_0} + \alpha_n(H_n - H_{n_0}) \qquad (7)$$

and the mean density of the nth subinterval was set equal to the average of the densities at n and $n - 1$. A stable solution was found if the coefficient of expansion of water was used for all values of α_n. An oscillatory solution, Figure 7, was obtained if vaporization to a few per cent quality was assumed in the top section of the vertical riser.

RESULTS

Two steady-equilibrium modes of operation are possible when the pressure at one point in the loop is held constant (surge tank E_2 open to the atmosphere). For a very low heat input the water temperature in the riser never exceeds the boiling point and a state of stable equilibrium may be defined. For a very high heat input, the entire riser contains both steam and water, and a maximum flow rate is obtained. Oscillatory modes of operation result for the intermediate heat inputs. The manner in which the period and amplitude depend on the heat input is illustrated by Figures 8 to 12. The period and amplitude of the oscillations are determined by the mean temperature level of the fluid in the vertical riser.

The period is inversely proportional to the mean velocity provided that some steam is in the riser at all times. When the system does not contain some steam during most of the cycle, the period is considerably longer than that predicted by the extrapolation of the higher flow-rate periods.

In the analogue-computer problem $Q_1 = 3.16$ B.t.u./sec. and the period is 149 sec., which is about 21 sec. less than the experimentally observed value for the lowest flow rate. The computed period would be expected to be less than the observed value since the density function used in the top subinterval of the riser was a two-phase density function which implied that the system contained some steam during all the cycle. Further the density function used for the boiling subinterval was linear, and it was not possible to exclude densities greater than the density of saturated water. A special nonlinear element would be required to generate a density function with the correct properties. As a result, the computed mean flow rate is less than that which could actually exist; however, the flow-rate curve and enthalpy curves have essentially the same shape as the experimentally determined ones. A larger com-

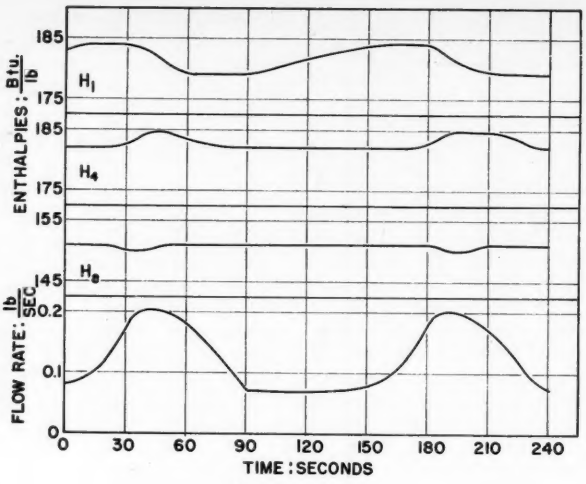

Fig. 7. Solution of the analogue-computer problem.

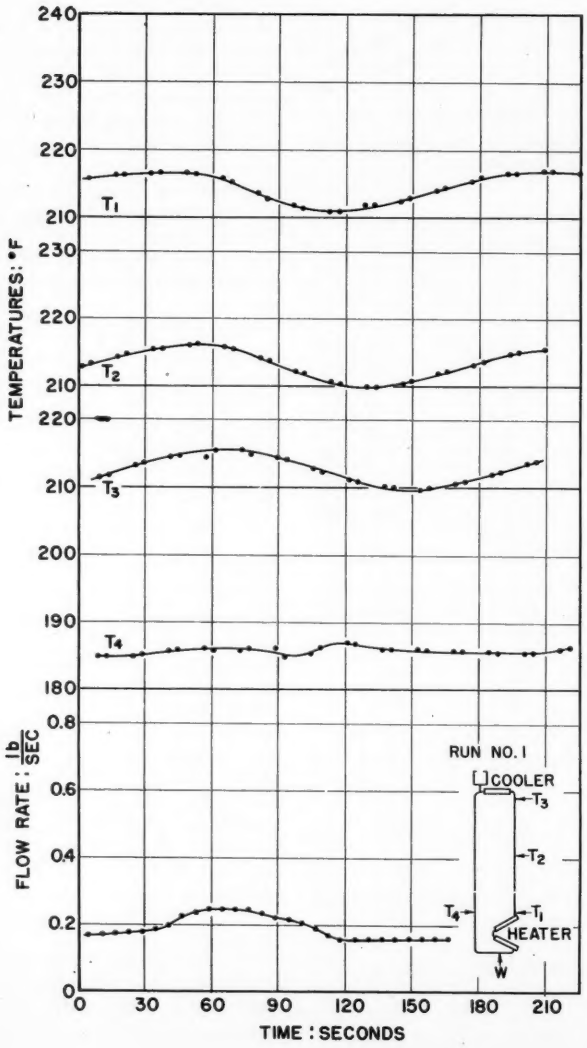

Fig. 8. Flow and temperature oscillations with a low heat input (Q = 5.84 B.t.u./sec.; surge tank open to atmosphere).

puter would be required for solving the stability problem at the higher heat fluxes.

CONCLUSIONS

A natural-circulation loop can be made unstable in the sense that a small displacement from the equilibrium state leads to undamped oscillations. Stable operations result when the fluid temperature in the riser is restricted to values less than the boiling point and when the heat input reaches a value such that the frictional force changes more rapidly than the driving force. The theoretical treatment of an open-ended natural-circulation system and the solution of a simple problem by means of an analogue computer have lent support to the general conclusions of the stability analyses.

ACKNOWLEDGMENT

The work described in this paper was made possible by a contract, No. AT(11-1) 211, between the Atomic Energy Commission and the Chemical Engineering Department of the University of Minnesota.

NOTATION

$a(\rho)$ = an empirically defined function for Equation (4)

A = cross-sectional area for flow; A_w = cross-sectional area for water-phase flow; A_s = cross-sectional area for steam-phase flow

g = local acceleration of gravity

g_c = conversion factor in Newton's law of motion

F_f = frictional force of the wall per unit length; F = loop resistance at flow rate V; F_0 = loop resistance at flow rate V_0

H = specific enthalpy of fluid; H_c = specific enthalpy of the cooling water

J = mechanical equivalent of heat

k_w = thermal conductivity of water; k_s = thermal conductivity of steam

p = fluid pressure

Q = linear rate of heat input to the fluid; Q_n = heat input per subdivision

t = time

T = fluid temperature

u = mean linear velocity; u_w = mean linear velocity of water phase; u_s = mean linear velocity of the steam phase

$$u = \frac{A_w \rho_w u_w + A_s \rho_s u_s}{A \rho} = \frac{W}{A \rho}$$

V = mean volumetric flow rate; V_0 = initial or equilibrium volumetric flow rate in loop; $\epsilon_V \sin \omega t$ = perturbation in the flow rate

W = total mass flow rate

x = distance along stream line

z = vertical height; z' = slope of pipe at x

α = coefficient of expansion used in Equation (7); the enthalpy difference was used to approximate the temperature difference

ϵ = specific fluid energy =

$$H + \frac{u^2}{2g_cJ} + \frac{g}{g_c}\frac{z}{J}$$

with subscripts s and w designating steam and water phases; mean specific fluid energy

$$\epsilon = \frac{A_w\rho_w\epsilon_w + A_s\rho_s\epsilon_s}{A\rho}$$

ρ = mean fluid density; ρ_w = density of water phase; ρ_s = density of steam phase;

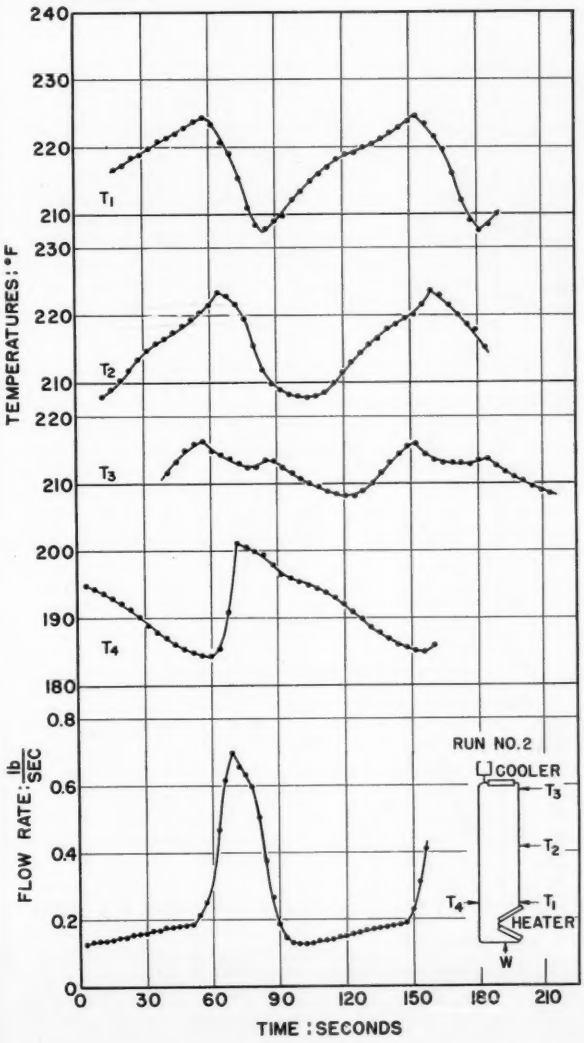

Fig. 9. Flow and temperature oscillations (Q = 7.75 B.t.u./sec.; surge tank open to atmosphere).

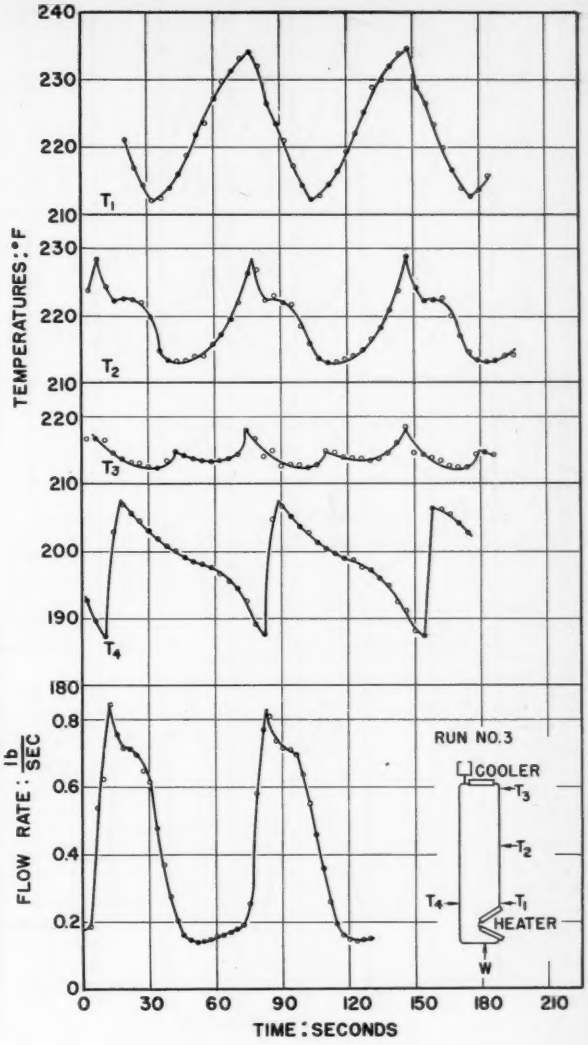

Fig. 10. Flow and temperature oscillations (Q = 9.44 B.t.u./sec.; surge tank open to atmosphere)

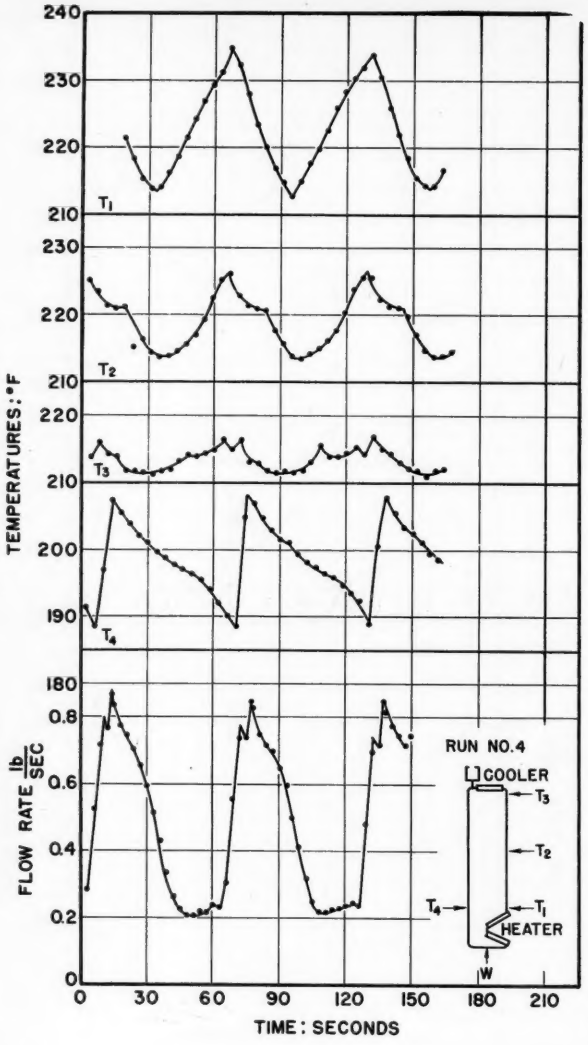

Fig. 11. Flow and temperature oscillations (Q = 11.80 B.t.u./sec.; surge tank open to atmosphere)

$$\rho = \frac{1}{A}(A_w\rho_w + A_s\rho_s)$$

$$\phi_1 = \frac{A_w\rho_w u_w^2 + A_s\rho_s u_s^2}{Wu}$$

$$\phi_2 = \frac{A_w\rho_w u_w\epsilon_w + A_s\rho_s u_s\epsilon_s}{W\epsilon}$$

Subscripts

n = subdivision number
s = steam phase
w = liquid-water phase
0 = initial conditions

LITERATURE CITED

1. Alstad, C. D., H. S. Isbin, N. R. Amundson, and J. P. Silvers, *ANL*-5409 (in preparation for distribution to A.E.C. depository libraries); *A.I.Ch.E. Journal*, **1**, 417 (1955).
2. Isbin, H. S., R. H. Moen, and D. R. Mosher, *AECU*-2994 (November, 1954).
3. Wissler, Eugene H., Ph.D. thesis, Univ. Minnesota, Minneapolis, Minn. (June, 1955).

Presented at Nuclear Science and Engineering Congress, Cleveland.

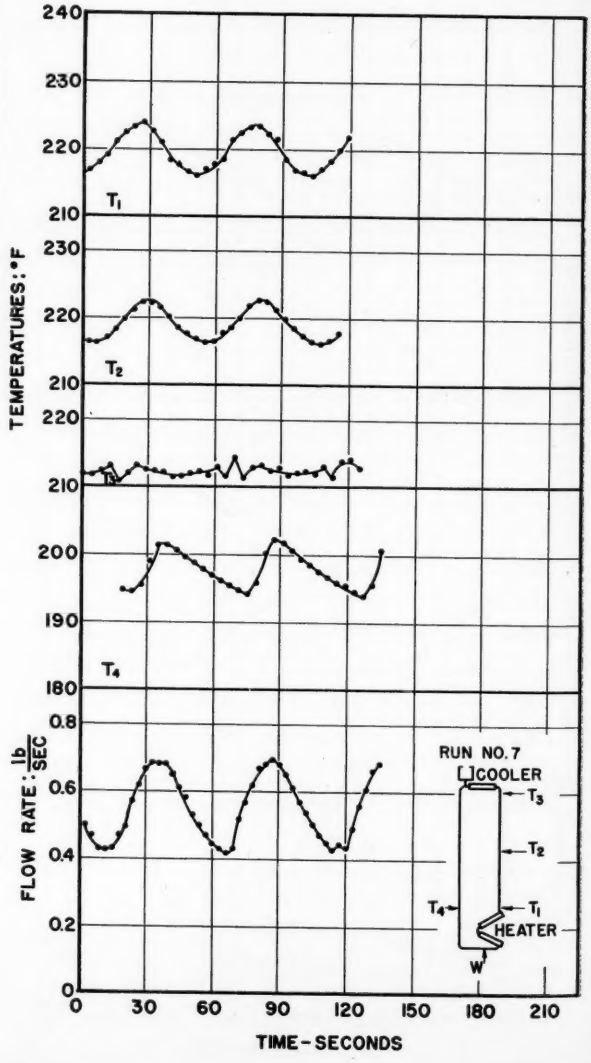

Fig. 12. Flow and temperature oscillations (Q = 12.70 B.t.u./sec.; surge tank open to atmosphere)

Process for Fission-product Removal from Uranium-bismuth Reactor Fuels by Use of Fused-salt Extraction

O. E. DWYER

Brookhaven National Laboratory, Upton, New York

The liquid-metal–fuel reactor under development at the Brookhaven National Laboratory uses a fuel which is a solution of U^{233}, Mg, and Zr in liquid bismuth. For a power-breeder thermal reactor, high neutron economy is essential, and this calls for low concentrations of those fission products in the fuel which are high neutron capturers. Roughly 45% by weight of the fission products can be continuously removed from the fuel by salt extraction with alkali and alkaline-earth fused-salt mixtures. These fission products contain the highly "poisonous" rare earths. This paper will present a discussion of process-design considerations and proposed flow sheets.

The L.M.F.R. (liquid-metal–fuel reactor) being developed for power purposes at the Brookhaven National Laboratory is a thermal breeder reactor and uses as a fuel a dilute solution of uranium-233, magnesium, and zirconium in liquid bismuth. The breeding is done in a blanket surrounding the core of the reactor, the most promising blanket material being a thorium-bismuthide slurry in bismuth. Since the η value for U^{233} at thermal energies is only 2.31, it is necessary to maintain low concentrations of fission products in the fuel in order to breed with g values significantly greater than unity. The L.M.F.R. can also operate as a converter, "burning" U^{235} and producing U^{233}. The η for U^{235}, 2.08, is even lower than that for U^{233}, indicating that if the L.M.F.R. were to operate as a converter, neutron economy would possibly be even more critical.

For the low fission-product concentrations desired in the L.M.F.R. the rate of fuel processing is necessarily high when one thinks in terms of the pounds of fuel which must be handled per day; but for a high-density liquid fuel such as uranium bismuth, where continuous operation can be used, actual flow rates are estimated to be less than 1 gal./min. for reactors having heat rates as high as 1,000 Mw. In other words, L.M.F.R. economics are apparently such that the concentration of fission products in the fuel will be low.

In the L.M.F.R. the fission products can be divided arbitrarily into three groups: (*a*) those elements, or compounds formed from fission-product elements, which are appreciably volatile at operating temperatures; (*b*) nonvolatile elements which form chlorides more stable thermodynamically than UCl_3 and elements which, as anions, form salts; and (*c*) nonvolatile elements which form chlorides less stable than UCl_3. For convenience, the names of these three groups have been abbreviated to F.P.V., F.P.S., and F.P.N., respectively. As reactor poisons, the first two groups are by far the worst, the first because of Xe^{135} with its 2.7×10^6—barn cross section, and the second because of the rare earths, particularly Sm^{149}, with its 47,000-barn cross section. The fission products in the third group, owing to their low poisoning effect, can be allowed to build up to considerably higher concentrations in the fuel with less frequent processing of the fuel for their removal. It is proposed to remove the F.P.V.'s by a volatilization process, either gas sparging or simple desorption, the latter carried out under low pressure conditions if necessary. It is the F.P.S.'s with which the present paper is concerned—their poisoning capacity and their continuous removal from the fuel.

In a commercial L.M.F.R. the individual concentrations of the three groups of fission products would, of course, be determined by economic considerations; however, it is felt that their combined poisoning effect would probably be less than 5%; i.e., they would absorb less than one twentieth as many neutrons as the uranium.

POISONING EFFECT OF F.P.S.'S

The method of determining the poisoning effect of this group of fission products will be described. The fission products extractable as chlorides by fused salts are rubidium, strontium, ythrium, cesium, barium, lanthanum, cerium, praseodymium, neodymium, promethium, samarium, europium, and gadolinium. In addition, iodine and bromine, as salts, would presumably transfer to the salt with very high partition coefficients. Table 1 gives the yields (for U^{235}) of the fission products for the pertinent chains and the estimated atom fraction of each chain which is removed from the fuel with the F.P.S. group.

Although the L.M.F.R. is nominally a thermal breeder, such reactors would have to operate for some years as converters. For this reason, the treatment given below is based on the use of U^{235}, and not U^{233}, as the fissile material.

With reference to Table 1 again, in estimating the fraction of certain chains leaving the fuel stream as F.P.S.'s, it was assumed arbitrarily that 10% of the iodine and bromine left the fuel with the F.P.V. group. From the figures in Table 1, the average mass number of the F.P.S.'s is calculated to be 128.0, and their weight percentage of the total fission products turns out to be 43.2.

There are eight nuclides which are particularly bad poisons—Sr^{89}, I^{131}, Nd^{143}, Nd^{145}, Sm^{149}, Sm^{151}, Eu^{155}, and Gd^{157}, and they must be given special consideration. As a result, there will be three subgroups of the F.P.S.'s—group A, consisting of the chains listed in Table 1 minus chains 89, 131, 143, 145, 149, 151, 155, and 157; group B, consisting of chains 89, 131, 143, 145, 149, 151, 155, and 157 minus the eight high-cross-section nuclides listed above; and group C, consisting of the eight nuclides. Group A is shown in Table 2. Many of the cross-section values used in this paper were taken from a recent Brookhaven Laboratory report (*3*).

From the figures given in Table 2, the average cross section for group A is calculated to be 7.9 barns. The poisoning effect of this group is relatively

Table 1. Fission Chains from U^{235} Relative to F.P.S.'s

Mass	% Yield	Estimated fraction in F.P.S.'s	Mass	% Yield	Fraction in F.P.S.'s
81	0.18	0.90	142	5.68	1.00
83	0.62	0.05	143	5.35	1.00
85	1.55	0.05	144	4.75	1.00
87	2.80	0.25	145	4.00	1.00
88	3.64	0.20	146	3.15	1.00
89	4.40	1.00	147	2.45	1.00
90	5.13	1.00	148	1.85	1.00
91	5.60	0.95	149	1.28	1.00
92	5.73	0.05	150	0.82	1.00
127	0.21	0.90	151	0.49	1.00
129	1.08	0.90	152	0.26	1.00
131	3.0	0.50	153	0.11	1.00
133	6.74	0.05	154	0.05	1.00
137	6.15	0.90	155	0.03	1.00
138	6.36	0.80	156	0.02	1.00
139	6.34	1.00	157	0.01	1.00
140	6.23	1.00	158	0.002	1.00
141	6.00	1.00			

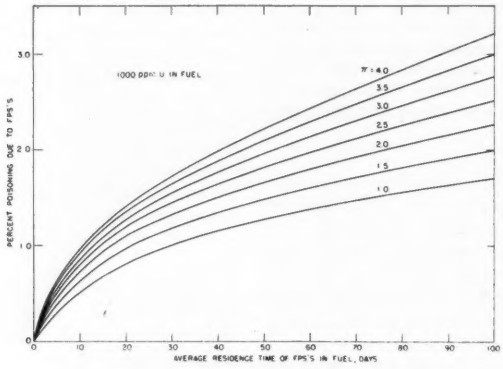

Fig. 1. Poisoning effect of F.P.S.'s in L.M.F.R.

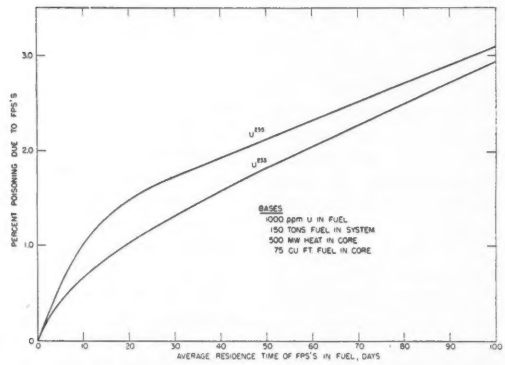

Fig. 2. Comparison of U^{233} and U^{235} with respect to F.P.S. poisoning effect.

small and assumed to be the same for all conditions of reactor operation. The poisoning effects of the other two groups varies appreciably with operating conditions, and the methods used in estimating them will be explained. The following treatment is based on the continuous removal of the F.P.S.'s, the existence of steady state conditions, and the assumption that all the F.P.S.'s transfer from the metal to the salt phase to the same degree.

The concentration of a given nuclide in the fuel stream depends upon a number of processes which govern its rate of formation and its rate of disappearance from the system. The following rates are involved, expressed in atoms/sec.:

Table 2. F.P.S.'s in Group A

Mass	(% Yield) × (fraction in F.P.S.'s)	Cross section, barns
81	0.16	2.6
83	0.03	10.0*
85	0.08	0.9
87	0.70	0.14
88	0.73	0.005
90	5.13	1.0
91	5.32	1.52
92	0.29	1*
127	0.19	6.1
129	0.97	11.0
133	0.34	29.0
137	5.53	2.0
138	5.08	0.6
139	6.34	8.4
140	6.23	1.0*
141	6.00	10.0*
142	5.68	1.8
144	4.75	5.0
146	3.15	9.8
147	2.45	60.0
148	1.85	3.3
150	0.82	2.9
152	0.26	150
153	0.11	420
154	0.05	5.5
156	0.02	750
158	0.002	4.0

*Assumed.

1. Rate of formation from fission

$$= N^{235} V_c \sigma_{5f} \phi f \qquad (1)$$

2. Rate of formation resulting from neutron capture

$$= N_t V_c \sigma_t \phi \qquad (2)$$

3. Rate of formation resulting from decay of parent

$$= \lambda_p N_p V_t \qquad (3)$$

4. Rate of disappearance by decay

$$= \lambda N V_t \qquad (4)$$

5. Rate of disappearance by neutron capture

$$= N V_c \sigma \phi \qquad (5)$$

6. Rate of disappearance by extraction in fused salt

$$= \frac{W_s k N}{\rho_s} = \frac{V_t N}{t_r} \qquad (6)$$

Of course, not all the foregoing processes apply in a particular case. In fact, for practical purposes process 2 can be neglected entirely, because it so happens that none of the really serious poisons have significant rates of formation as a result of neutron capture, owing to the low cross sections of the neutron-capturing species.

From the foregoing equations, the steady state concentration of a chain-initiating nuclide or a nuclide whose precursors have negligibly short half-

lives is found to be expressed by the equation

$$N = \frac{N^{235} V_c \sigma_{5f} \phi f}{\lambda V_t + V_c \sigma \phi + \frac{W_s k}{\rho_s}} \quad (7)$$

which can be converted to the more convenient form

$$N = \frac{f}{\frac{\left(\lambda + \frac{1}{t_r}\right) V_t}{3.15 \times 10^{16} P} + \frac{\sigma}{\sigma_{5f} N^{235}}} \quad (7a)$$

For a nuclide inside the chain ends, the corresponding equations are

$$N = \frac{\lambda_p N_p V_t}{\lambda V_t + V_c \sigma \phi + \frac{W_s k}{\rho_s}} \quad (8)$$

and

$$N = \frac{\lambda_p N_p}{\lambda + \frac{1}{t_r} + \frac{3.15 \times 10^{16} \sigma P}{V_t \sigma_{5f} N^{235}}} \quad (8a)$$

and for a chain-terminating nuclide, the two equations are

$$N = \frac{\lambda_p N_p V_t}{V_c \sigma \phi + \frac{W_s k}{\rho_s}} \quad (9)$$

and

$$N = \frac{\lambda_p N_p}{\frac{1}{t_r} + \frac{3.15 \times 10^{16} \sigma P}{V_t \sigma_{5f} N^{235}}} \quad (9a)$$

In the foregoing equations the factor 3.15×10^{16} represents the number of fissions per second per megawatt of heat release.

By use of the preceding equations, say (7*a*), (8*a*), and (9*a*), the concentration of each of the nuclides in the eight chains containing the high-cross-section species can be determined. From this point on, in illustrations of the method of determining the poisoning effect, the calculations will be based on the following set of typical operating conditions:

1,000 p.p.m. U^{235} in fuel
300 tons fuel in system
500-Mw. (heat) reactor
20-day residence time for F.P.S.'s in fuel

For these conditions, Tables 3, 4, and 5 summarize the calculated results. Tables 3 and 4 present the results for groups *B* and *C*, respectively, and Table 5 shows a comparison of all three groups. The average cross section of 40 barns for group *B* is very much of a guess, as it is based primarily on the assumed cross sections shown in Table 3; but since this group contributes less than 1% of the total F.P.S. poisoning effect, the uncertainty of its average cross section does not have a significant effect on the results. It will be noticed that, for the conditions considered, the eight nuclides of group *C* account for 96.3% of the F.P.S. poisoning effect, and it is interesting to note that one of these (Sm^{149}) alone accounts for 70.5%. The rare earths, as a group, account for 93.5%. The reactor poisoning due to the F.P.S.'s, expressed on a percentage basis, will be

$$p = \left(\frac{\sum (N\sigma)}{N^{235} \sigma_{5a}}\right) 100 \quad (10)$$

In the present case N^{235} and σ_{5a} are 2.51×10^{19} atoms/cc. and 687 barns, respectively, which makes p equal to 1.02. Thus for every 100 neutrons absorbed by the U^{235}, 1.02 will be captured by the F.P.S.'s. It is felt that this would be a typical figure for an eventual commercial L.M.F.R. power breeder with fully integrated fuel processing. For the conditions of the foregoing example, the concentration of the F.P.S.'s would be 16.85 p.p.m. This would seem a very low concentration upon which to base a continuous-extraction process, but for a high-temperature liquid-metal–fused-salt system such as the one under consideration here, it is more than adequate.

Figure 1 shows a family of curves presenting the poisoning effect of the F.P.S.'s as a function of their average residence time in, and the power density of, the reactor system. Offhand, one might expect the poisoning effect to be proportional to the power density π because of the direct effect of concentration; i.e., for a fixed residence time and total heat rate, when π is doubled and V_T is halved, then the concentration must be doubled. But the average cross section of the F.P.S.'s does not remain the same, owing to the fact that the more concentrated the F.P.S.'s, the less the relative concentrations of the high-cross-section nuclides. The concentrations of such nuclides, owing to the fact that their disappearance is due primarily to neutron capture, tend to remain constant.

Figure 2 shows a comparison of U^{235} and U^{233} with respect to the poisoning effects of their respective F.P.S.'s. It is seen that, other things being equal, the poisoning effect with U^{235} is appreciably greater than that with U^{233}; for example, for 1% poisoning, under the conditions of the plot, the average residence times for the F.P.S.'s from U^{235} and U^{233} are 10 and 19 days respectively. Or, in other words, the concentrations would be 18 and 34 p.p.m., respectively. The considerably greater poisoning effect of the F.P.S.'s from U^{235} is due to the much higher fission yields of the rare earths from this isotope.

The power figures in the foregoing discussion are on a *total* basis; i.e., they include all the heat obtainable from the radioactive decay of the fission products.

Table 3. F.P.S.'s in Group B for U^{235}

Nuclides	Calculated fraction of total chain	Chain yield, %	Cross section, barns
89 chain minus Sr	0.208	4.40	1.4
131 chain minus I	0.000	3.00	
143 chain minus Nd	0.548	5.35	50*
145 chain minus Nd	0.018	4.00	10*
149 chain minus Sm	0.380	1.28	50*
151 chain minus Sm	0.000	0.49	
155 chain minus Eu	0.000	0.03	
157 chain minus Gd	0.351	0.01	1,000*

*Assumed.

Table 4. F.P.S.'s in Group C for U^{235}

Nuclide	*N*, atoms/cc.	σ, barns
Sr^{89}	3.39×10^{16}	110
I^{131}	1.07×10^{16}	600
Nd^{143}	2.33×10^{16}	290
Nd^{145}	3.81×10^{16}	52
Sm^{149}	2.65×10^{15}	47,000
Sm^{151}	3.22×10^{15}	7,200
Eu^{155}	1.56×10^{14}	13,000
Gd^{157}	7.93×10^{12}	160,000

CHEMISTRY

The use of fused chlorides for extracting fission products from a uranium-bismuth reactor fuel was first proposed by Winsche and studied experimentally by Bareis at Brookhaven. Equilibrium results on some of the rare earths in the U–Bi/LiCl–KCl system were shown by Wiswall to be consistent with the postulation that the transfer of the rare earths from metal to salt was due to their selective oxidation, the degree of transfer being determined by the limitations of chemical equilibrium. An article by these three workers recently appeared in the unclassified literature (*4*).

Table 5. Poisoning Effects of F.P.S. Subgroups for U^{235}

Group	ΣN, (atoms/cc.)10^{-17}	$\bar{\sigma}$, barns	$[(\Sigma N)\bar{\sigma}] \times 10^{-20}$	% of F.P.S. poisoning
A	6.27	7.88	0.0494	2.8
B	0.394	40	0.0158	0.9
C	1.120	1,518	1.700	96.3
Total F.P.S.'s	7.78	225	1.765	100.0

Table 6. Free Energies of Formation of Certain Chlorides at 500°C.

Compound	$-\Delta F$, kcal./g. atom Cl	Compound	$-\Delta F$, kcal./g. atom Cl
$EuCl_2$	90.5	$CeCl_3$	70
$BaCl_2$	87.5	$PmCl_3$	69
KCl	87	$NdCl_3$	67
$SmCl_2$	85	$GdCl_3$	65.5
RbCl	85	YCl_3	65
CsCl	85	$MgCl_2$	61.5
$SrCl_2$	84	$ZrCl_2$	59
LiCl	83.5	UCl_3	58
$CaCl_2$	82	$CrCl_2$	35.5
NaCl	81	$FeCl_2$	29
$LaCl_3$	70	$NiCl_2$	24
$PrCl_3$	70	$BiCl_3$	18.5

Table 6 presents free-energy-of-formation values for the rare earths, alkali metals, and certain other metals of particular interest in the present discussion. These figures are for 500°C., on the basis of an atom of chlorine, and were obtained principally from two sources (*1*, *2*). They give a direct measure of chemical stability or tendency to chloride formation. It is seen that the free energy of formation of UCl_3 is well below that for any of the rare earths and the fission products in groups *IA*, *IIA*, and *IIIA* of the Periodic Table, indicating that it should be possible to oxidize these elements out of a uranium-bismuth solution without materially affecting the uranium. There are two approaches to accomplishing this. One involves the use of a buffer system, and the other is based on the use of the so-called "stoichiometric" method.

The only buffer system which has thus far shown promise of success is the Mg^{++}–Mg system. From the free-energy values in Table 6, one would predict that if a salt mixture of KCl–NaCl–$MgCl_2$ were contacted with a metal phase consisting of U–Bi–Sm, the Sm would reduce the $MgCl_2$ and transfer from the metal to the salt phase, according to the equation

$$MgCl_2 + Sm \rightarrow Mg + SmCl_2$$

It is assumed, of course, that the solubilities would be such that the reduced Mg would transfer quantitatively to the metal phase and the $SmCl_2$ to the salt phase. Moreover, the degree of separation achieved would depend on the "activities" of the reacting components in the two phases, besides the question of the extent of approach to equilibrium. The Mg in the metal phase would buffer the uranium, tending to prevent it from being oxidized. The oxidation-reduction potential of this type of system is not affected by small changes in concentration of the $MgCl_2$ in the salt or Mg in the metal and therefore can be easily controlled. The concentrations of the Mg and $MgCl_2$ will always be greatly in excess of those of the F.P.S.'s in the two phases. With the system KCl–NaCl–$MgCl_2$/–Bi–U–R.E.*, separation factors in the order of 100 have been obtained. The separation factor is defined by the relation

$$\frac{\text{(p.p.m. F.P.S. in salt)/(p.p.m. U in salt)}}{\text{(p.p.m. F.P.S. in metal)/(p.p.m. U in metal)}}$$

Appreciably increasing or decreasing the concentration of Mg in the metal will make the system more or less reductive, respectively, even though the separation factor remains substantially constant. With the eutectic mixture KCl–NaCl–$MgCl_2$ (m.p. 396°C.) the Mg concentration in the metal should be no more than about 100 p.p.m.

The stoichiometric method involves the use of a relatively strong oxidant in the salt mixture, like UCl_3 or $BiCl_3$, in concentrations just great enough to remove the greater portion of the F.P.S.'s from the fuel stream without oxidizing an appreciable amount of the uranium.

With UCl_3 as the oxident, uranium is added to the metal, which means that in actual practice this method of F.P.S. removal has the advantage of adding uranium make-up to the fuel. The stoichiometric relationships are such, however, that the F.P.S.'s will not transfer sufficient uranium to replace that which is consumed. The additional uranium can be transformed with magnesium.

Bismuth chloride is a very strong oxidizing agent, and one which does not add a solute to the fuel. It must, of course, be added to the carrier salt in just the right amount to extract the F.P.S.'s and not the uranium. It should give separation factors at least as great as those obtainable with $MgCl_2$. The F.P.S.'s are, as it were, titrated out. It is evident that this method has the disadvantage of requiring very careful control of the oxidant in the salt stream. On the other hand, the buffer system described above may work only when the Mg concentration is below that desired in the fuel for inhibiting corrosion and mass transfer. For this reason, the stoichiometric method appears more promising. In such a system the salt mixture carrying the oxidant could be any satisfactorily low-melting mixture of chlorides with individual salts at least as stable as magnesium chloride.

*R.E. = Rare earth.

PROCESS DESIGNS FOR F.P.S. REMOVAL

The flow sheets described below are not based on the results of continuous pilot plant operation but are proposed for such on the basis of small batch-type experiments.

Use of Buffer System

A flow sheet, with typical numerical values, explaining the removal of F.P.S.'s from the L.M.F.R. fuel and based on the "buffer" chemical system described above, is shown in Figure 3. The flow rates, concentrations, and equilibrium stages indicated on this diagram are based on a total heat rate of 570 Mw. and a F.P.S. concentration in the fuel of 15 p.p.m. For a U^{235} concentration of 600 p.p.m. and a representative fuel inventory of 300 tons, or a π of about 2, this would amount to about 1.0% reactor poisoning. The numerical values in the flow sheet are based on the following four assumptions: (*a*) there is no entrainment; (*b*) partition coefficients for F.P.S.'s and U between salt and metal phases are constant over concentration ranges involved; (*c*) all F.P.S.'s have the same partition coefficients; (*d*) the separation factor, as defined above is the same for all extraction columns and equals 100. The individual values for the F.P.S. and U partition coefficients between salt and metal phases depends on the buffering action, and therefore the concentration, of the magnesium in the metal. The process outlined in Figure 3 does not represent a careful optimization of the several operating variables but is nevertheless believed to be typical as far as indicated sizes, concentrations, and flow rates are concerned.

Columns 1, 2, and 3 are countercurrent extraction columns of 3.9, 4.1, and 4.5 equilibrium stages, respectively. They could all be spray columns in which the liquid-metal fuel fell in the form of fine droplets through the slowly rising salt. The columns should preferably contain some baffling to prevent vertical mixing of the salt. Viscosity, interfacial tension, and density conditions are such as to make the bismuth-salt system a good one for this type of operation. Carryover, or entrainment, as judged on the basis of small-scale laboratory experiments, should be negligible. The relative velocity of the falling metal with respect to the rising salt should be about 2 ft./sec. This, together with the fact that the flowing streams are very small, means that the diameters of the columns are also very small. For example, column 1, the largest, would need to be no more than 3 or 4 in. in diameter. The heights of the columns will depend on their efficiencies and the separations required, but in any case it is expected that they would not need to be much taller than 3 ft. The height of column equivalent to a theoretical stage has not been experimentally determined but has been estimated on the basis of mercury-water heat transfer in spray columns, use being made of the analogy between heat and mass transfer. Rates of approach to equilibrium in bismuth-salt systems at 500°C. are found to be extremely rapid in small-scale batch experiments. Generally speaking, diffusivities in liquid-metal and fused-salt

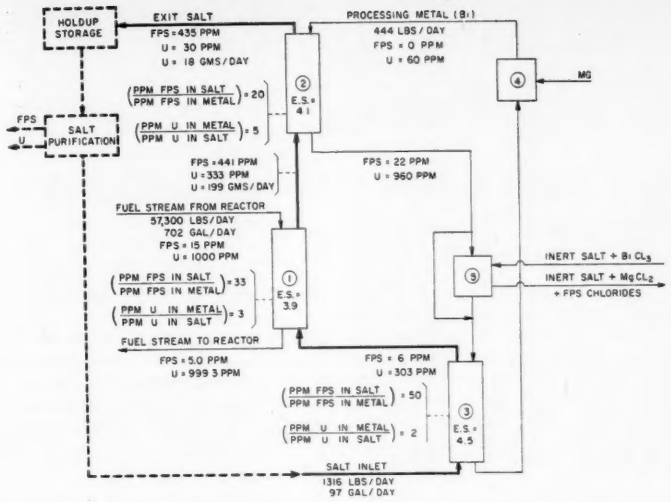

Fig. 3. Proposed flow sheet for F.P.S. removal from L.M.F.R. fuel by use of buffer method.

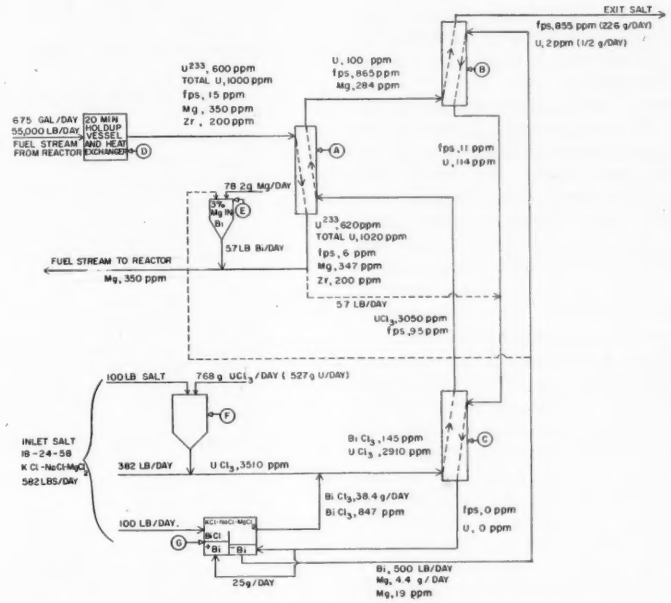

Fig. 4. Proposed flow sheet for F.P.S. removal from L.M.F.R. fuel by use of stoichiometric method.

systems at this temperature are high in comparison with those in ordinary liquids.

In column 1 the fission products are extracted from the fuel; in column 2 the uranium is recovered from the salt leaving column 1; and in column 3 the uranium is recovered from the processing metal stream by the incoming salt. The same salt stream passes through all three columns. The partition coefficients, indicated on the flow sheet, are varied among all three columns by changing of the oxidation-reduction potential in each by variation of the Mg concentration in the metal phase. It is estimated that the Mg concentrations in columns 1, 2, and 3 should be about 50, 65, and 35 p.p.m., respectively. Column 2 is more reductive than 1 to promote transfer of uranium to the metal phase, and column 3 is more oxidative than 1 to promote transfer of uranium to the salt. Units 4 and 5 on the flow sheet are for adding Mg to, and removing Mg from, the processing metal stream, respectively, to give the desired partition coefficients in columns 2 and 3. The Mg could be added by means of an electrochemical cell in which Mg and Bi are the anode and cathode, respectively, and in which the salt bridge could consist of the ternary KCl–NaCl–$MgCl_2$. Or the Mg could be added mechanically in the form of a bismuth solution. Item 5 is a salt-metal contactor in which sufficient $BiCl_3$ is added to the carrier salt to oxidize the desired fraction of the magnesium without oxidizing a significant amount of uranium. This operation would probably be done on a batch basis, owing to the very small flow rate of the processing metal stream.

After leaving column 1, the salt must be cooled to remove decay heat; but heat exchangers have not been included in the figure for the sake of simplicity. Heat release from the F.P.S.'s will be discussed briefly in a later section. The dashed portion of the flow sheet in Figure 3 is simply a schematic representation of the salt-decontamination step as it relates to the main processing plant.

Use of the Stoichiometric System

A second flow sheet for a proposed L.M.F.R. fuel-processing plant, based on the stoichiometric chemical system, is shown in Figure 4. From an engineering standpoint, the two flow sheets are similar. The second flow sheet is based upon a 500-Mw. heat rate with U^{233} as the fissile material.

With reference to the figure, the fuel from the reactor is first held up in a heat exchanger *D* to allow the fission products to "cool off" before flowing through extraction column *A*. In this column approximately two thirds of the F.P.S.'s are removed from the fuel; but before it is returned to the reactor, its Mg concentration is brought up to its original value by the addition about once daily of a 3% solution of Mg in bismuth. The UCl_3 carried in the salt from column *A* is nearly all recovered in column *B* by contacting the salt with a Mg–Bi solution. The uranium, accompanied by a small amount of F.P.S.'s, is recovered from the metal stream leaving column *B* by contacting it with the incoming salt in column *C*. The electrochemical cell *G* introduces $BiCl_3$ into the inlet salt stream and magnesium into the processing metal stream in the proper stoichiometric quantities to accomplish the two-step transfer of the uranium from the out-going salt to the in-going salt. Uranium chloride is added to the salt stream from mixing tank *F* at the required rate to supply the necessary U make-up to the fuel stream. In other words, UCl_3 as the oxidant in the salt simultaneously removes the fission products from, and adds U to, the fuel. The stoichiometric quantities are such that a small amount of Mg must be oxidized along with the F.P.S.'s in order to add the required amount of uranium. The UCl_3 addition of 768 g./day does not include the U make-up required for neutron capture by the U. If it is not desired to add the uranium to the fuel by this method, then the oxidant would be $BiCl_3$.

In the stoichiometric system a typical carrier salt would be the NaCl–KCl–$MgCl_2$ eutectic. The salt stream, of course, becomes very radioactive and must be cooled. As in

Figure 3, the heat exchangers for this have been omitted. It is pointed out again that the numerical values shown in Figure 4 are not the result of careful economic optimization but are nevertheless believed to be fairly representative of commercial operation.

It will be noticed that the flow rates shown in Figures 3 and 4 are very small, an indication that the equipment is correspondingly small. The largest conduit lines need to be no greater than ¼ in. in diameter and the largest contactor column 3 in. in diameter. The small equipment, which is mainly a consequence of the facts that the operation is continuous and that the chemistry is nonaqueous, means that the shielding required, though thick, is not expensive. From the standpoint of investment costs, instrumentation and control equipment will be major items. It is expected that electrochemical cells can be used for adding small amounts of solutes to both salt and metal streams and that electromotiveforce cells can be used for control of concentrations of critical materials. At Brookhaven both the austenitic type-347 and the ferritic 400-series stainless steels have been used with good success, as long as the systems are quite oxygen free. As Table 6 shows, the chlorides of iron, chromium, and nickel are at the bottom of the list, an indication of their relatively low tendency of formation. Pretreatment and conditioning of equipment before use includes such operations as electropolishing, degassing under high vacuum at temperatures in the neighborhood of 800°C., and contacting with magnesium–bismuth solutions. It is essential that the equipment and piping be absolutely gas tight. This calls for either canned-rotor or canned-motor pumps and bellows-sealed valves and pressure transmitters.

Since the average residence time of the F.P.S.'s in the reactor would probably be only a few days, they are very radioactive at the time of their removal and provide an excellent source of high-intensity ionizing radiation. For an average residence time of 20 days, it is estimated that the specific activity of the F.P.S.'s may be as high as 50,000 to 100,000 curies/g., depending upon their holdup time after removal. The radiation capacity associated with the F.P.S.'s dissolved in the fused salt in a large L.M.F.R. plant, say one of 500 to 1,000 Mw. heat rate, could be as great as several million curies. Moreover, since the F.P.S.'s are dissolved in the molten salt, they are in an easily handlable form. Thus, it is assumed that high-intensity gamma-radiation facilities would be an integral part of a commercial L.M.F.R. power plant.

After a suitable storage period, the salt can be purified for reuse. Complete decontamination, however, is unnecessary. The F.P.S.'s can be removed from the salt by contacting it with liquid lead containing a strong reductant like magnesium or calcium and they can then be removed from the lead by direct oxidation with an air stream. Alternatively, they may be left in the lead for indefinite storage.

Presumably, in the stoichiometric scheme the salt could be used over and over again with just "cooling" between cycles. What limits the concentration of F.P.S.'s in the salt during each pass through the plant is simply the resulting heat-generation rate per unit volume of salt.

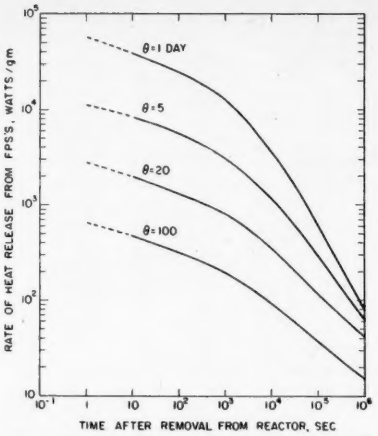

Fig. 5. Energy release from F.P.S.'s.

HEAT RELEASE FROM FISSION PRODUCTS

An important consideration in the design of processes and equipment for handling radioactive fission products is the problem of heat removal. This is particularly true in the present case, because of the relatively short age of the fission products at the time of their extraction from the fuel. However, heat removal from fused salts does not present a difficult problem.

Figure 5 shows a family of curves giving the specific heat rates for the F.P.S.'s as a function of average residence time in the reactor and time after removal therefrom. The curves were calculated from fission-product heat-release data obtained from the Argonne National Laboratory (*5*). Extrapolations to short decay times were made with the aid of the Way-Wigner (*6*) expression for fission-product-decay heat.

In Figure 4 the exit salt from Column *A* contains 865 p.p.m. of F.P.S.'s which have been held up 20 min. after removal from the reactor. Assuming a typical fuel inventory of 300 tons, the average residence time of the F.P.S.'s in the fuel will be about 18 days. From Figure 5 it is seen that the specific heat release for the F.P.S. under these conditions will be about 850 watts/g. This amounts to a total energy release of about 130,000 B.t.u./(hr.)(cu. ft. of salt). Had the F.P.S. concentration in the fuel been 5 p.p.m., the corresponding figure would be about 400,000 B.t.u./(hr.)(cu. ft. of salt). The energy will be divided about equally between beta and gamma radiation. The former energy will be liberated as heat at essentially the point of liberation, but the fraction of the gamma energy converted to heat in the heat exchanger will depend upon design of the exchanger and density of the coolant.

ACKNOWLEDGMENT

The author gratefully acknowledges the assistance of Elizabeth A. Carruthers and Donald F. Molino with the calculation work for Figures 1, 2, and 5.

NOTATION

f = fraction of uranium atoms fissioning to a particular mass chain
g = breeding ratio, atoms of fissile material produced per atom of fissile material burned
k = (atoms F.P.S./cc in exit salt)/(atoms F.P.S./cc. in fuel)
N = concentration of a given nuclide in fuel, atoms/cc.
N_p = concentration of parent nuclide in radioactive decay, atoms/cc.
N_t = concentration of target nuclide in neutron capture, atoms/cc.
N^{235} = concentration of U^{235}, atoms/cc.
p = percentage of poisoning, defined by Equation (10)
P = thermal power of reactor, Mw.
t = time, sec.
t_r = average residence time of N in fuel, sec.
V_c = fuel volume in core, cc.
V_t = fuel volume in reactor system, cc.
W_s = salt flow rate, g./sec.
η = number of neutrons produced per thermal neutron absorbed in uranium
θ = average residence time in fuel, days
λ = radioactive decay constant for N, $sec.^{-1}$
λ_p = radioactive decay constant for parent nuclide, $sec.^{-1}$
π = power density, Mw. of heat per ton of fuel
ρ_s = salt density, g./cc.
σ = thermal-neutron cross section for N, barns
σ_t = thermal-neutron cross section for target nucleus, barns
σ_{5a} = thermal-absorption cross section for U^{235}, barns
σ_{5f} = thermal-fission cross section for U^{235}, barns
ϕ = thermal-neutron flux, neutrons/(sq. cm.)(sec.)

LITERATURE CITED

1. Brewer, L., personal communication to H. M. Clark, Rensselaer Polytechnic Institute, Troy, N. Y. (July 19, 1954).
2. Glassner, A., *Argonne Natl. Lab. Rept.* ANL-5107 (August, 1953).
3. Hughes, D. J., and J. A. Harvey, *Brookhaven Natl. Lab. Rept.*, BNL-325 (July 1, 1955).
4. Bareis, D. W., R. H. Wiswall, and W. E. Winsche, *Chem. Eng. Progr. Symposium Series*, **50**, No. 12, 228 (1954).
5. Steinberg, E. P., Argonne Natl. Lab., Lemont, Ill., private communication to O. E. Dwyer (May 13, 1955).
6. Wigner, E. P., and K. Way, "Paper 43," *National Nuclear Energy Series*, Div. IV, Vol. 9, McGraw-Hill Book Company, Inc., New York (1951).

Presented at Nuclear Science and Engineering Congress, Cleveland.

Liquid-metal Extraction for Processing of Spent Fuel

A. F. VOIGT, A. H. DAANE, E. H. DEWELL, R. G. CLARK, J. E. GONSER, J. F. HAEFLING, AND K. L. MALABY

Iowa State College, Ames, Iowa

Plutonium and the fission products can be removed from irradiated uranium by liquid-metal extraction by use of another metal immiscible with uranium. Metals studied have been silver, cerium, and lanthanum. Plutonium removal by silver is high, by the rare-earth metals moderate. In all cases volatile elements, including cesium, strontium, and barium, are removed. Rare earths are efficiently removed. Ruthenium and molybdenum are largely unaffected. Experiments with synthetic fuels corresponding to long burn-up periods show improved removal of most elements. Repeated batch extractions indicate that a continuous process separating the fuel into uranium, plutonium, and fission-product fractions could be developed.

As the development of reactors to produce competitive electrical power will require low processing costs, some very different types of processing are being investigated. A successful process may mean the difference between a nuclear power industry which can truly compete in price with other fuels and one which must be subsidized to meet competition.

The basic idea behind the processes under investigation is quite different from that behind the ones that have been used to date. In the conventional process for the clean-up and reuse of nuclear fuel, the fuel metal is dissolved in acid and separated from fission products and other fissionable material (e.g., plutonium) with a high degree of purification before being refabricated into fuel elements. The degree of removal of the intensely radioactive fission products is sufficient to permit direct handling of the fuel elements in the refabrication and hence an elaborately designed fuel element is possible. However, another possible technique would be to provide in the separation only enough removal of fission products to negate any poisoning or impairment of metallic properties for which they might be responsible and at the same time by reforming the metal out of the molten state, to counteract any radiation damage which the metal may have sustained. Refabrication in this case would have to be done as a remote operation, and the fuel-element design would necessarily have to be simple to allow this.

The economic success of such a processing cycle would depend on the relative cost of complete chemical separation and direct refabrication on one hand and less complete, simple separation and remote fabrication on the other. Because there is a strong possibility that the latter alternative may be less costly, the authors have actively investigated simple types of processing.

The processing to be described falls in the general class of so-called "pyrometallurgical" processes. Very early work (*1*) in this laboratory showed that this type of processing could give separations of considerable interest and promise. Renewed work from 1952 on has added much to the early data and carried the program to the stage at which scale-up experiments are in progress.

As has been described (*2*) the work at this laboratory has been concerned with liquid-metal extraction. In the phase systems of a number of metals, including silver, rare earths, magnesium, calcium, thorium, and others, with uranium there is an extensive immiscibility in the molten state. At temperatures just above the melting point the solubility of each phase in the other is a few per cent or less. Consequently a liquid-liquid extraction above the melting point is possible if provision is made for adequate mixing of phases and subsequent separation.

Experiments (*2*) showed that silver, cerium, and lanthanum were some of the metals of choice in such a process. They also indicated that silver was a good extractant for plutonium as well as for many of the fission products, but that cerium and lanthanum extracted less of the plutonium. With all these elements rather large amounts of the important fission products, with the exception of molybdenum and ruthenium, were extracted.

PREPARATION OF MATERIALS

Most of the previously reported experiments were done with irradiated uranium, which contained the fission products and plutonium at rather low concentrations. One of the observations from these experiments was that the concentration of the material extracted affected the extent of the extraction. Since actual power reactor fuels will in all probability be operated to a degree of burn-up quite in excess of any of the irradiated uranium which was available for experimentation, it became necessary to go to artificial fission-product–uranium mixtures, which have been called "fissium."

The composition of the fissium material used was determined by a thorough study of the fission chains and the feasibility of preparing alloys. The possible effect of varying the energy of the neutron spectrum responsible for the fission acts was considered, as were the recent observations on fission yield, fine structure, and the burn-up of materials of high cross section. Calculations for a 30-day irradiation period to 2% burn-up of U^{235} and no cooling gave the values in Table 1 for the atomic percentages of the most important elements resulting from the fission of U^{235}.

A practical artificial spent fuel was made up to be much simpler than this would indicate. The elements xenon, cesium, strontium, barium, krypton, rubidium, and iodine were eliminated from consideration because they are so volatile that their addition would be very difficult, and in any case their removal in any melting operation is easy and complete. In some cases a single rare earth, neodymium, was added to represent all the group, the amount added being equivalent to the sum of all the rare-earth percentages. In other cases cerium was considered separately and neodymium was

TABLE 1. ATOMIC PERCENTAGES OF THE ELEMENTS IN THE FISSION PRODUCTS

Element	At. %	Element	At. %	Element	At. %
Zr	15.0	Sr	6.6	Kr	2.14
Mo	9.20	Ba	4.57	Te	1.60
Xe	9.17	La	3.18	Rb	1.21
Ce	9.00	Tc	3.14	Sm	1.11
Nd	7.90	Nb	2.75	Pm	0.73
Ru	7.88	Y	2.66	I	0.73
Cs	7.83	Pr	2.26	All others	1.45

added equivalent to all the other rare earths. Examination of the table shows that with these reservations, the addition of four or five elements, zirconium, molybdenum, and ruthenium plus the chosen rare earth or earths, would take care of the first ten elements in the table plus a number of others. The elements added amounted to 59% of the total atoms and those known to be volatile amounted to another 32.2%, or a total of 91.2%. The actual composition of the fissium used is given in Table 2.

The fissium was made up as needed with radioactive isotopes of the elements of interest to permit analysis by radiochemical methods. In most of the experiments to be described, the added elements were made radioactive by irradiation in the Argonne National Laboratory CP-5 reactor. As the isotopes producible in cerium and ruthenium by n, γ reactions are less satisfactory for analytical purposes than Ce^{144} and Ru^{106}, which can be obtained as fission products from the Oak Ridge National Laboratory, cerium and ruthenium metals containing these tracers were made by reduction of the salts by the conventional methods. Table 3 lists the properties of the isotopes used.

The fissium was prepared in kilogram quantities by a process involving several steps. The refractory nature of some of the metals made a high-temperature melting process necessary in order to get them into the alloy. This was accomplished by arc melting all the alloying metals with about 100 g. of uranium. The resulting button of concentrated alloy was sectioned into quarters, which were placed in a tantalum crucible about 1 in. in diameter alternately among pieces of uranium metal weighing about 200 g. each. This assembly was melted by induction heating *in vacuo*, removed, inverted, and remelted.

The homogeneity of the samples was checked by means of radioautographs of the resulting cylinders and by scanning with a gamma-ray scintillation spectrometer. The radioautographs showed considerable concentration of some of the fission products at the crucible interface. Removal of the surface by machining removed most of this inhomogeneity, though there was still indication of a nonuniform distribution. The scintillation spectrometer was set at the characteristic gamma-ray energy of the particular nuclide of interest, e.g., 0.72 Mev. for zirconium, and by scanning the length of the cylinder through a collimating system one could observe the distribution of the particular element. Though some lack of uniformity was observed, it did not appear that repeated melting would help the situation, and the samples were used as produced. Other methods of preparing the material, such as a tilting resistance furnace, gave less satisfactory results.

Table 2. Fissium Composition, 2% Burn-up

Element	Atom ratio	Weight %
U	98	99.5
Zr	0.30	0.117
Ru	0.156	0.068
Mo	0.184	0.076
Ce	0.180	0.108
Nd	0.358	0.220

The extraction experiments to be reported were each run with about 150 g. of uranium and an equal volume, roughly half this weight, of the extracting metal. Tantalum crucibles were used for the extractions. The samples were heated inductively *in vacuo* to 1,200° to 1,220°C. for 20 min. in all cases unless otherwise indicated.

The induction heating is known to provide sufficient stirring to mix the lighter metal and uranium phases. It is not known whether this stirring is vigorous enough to permit the system to approach equilibrium in the time taken for the experiments.

Table 3. Isotopes Used for Fissium Analysis

Element	Isotope	Half-life	Radiation energy, Mev.	Remarks
Zr	95	65d	$\beta 0.37, \gamma 0.72$	35-day Nb^{95} daughter introduces problems
Mo	99	66h	$\beta 1.2, \gamma$'s	Short half-life is a severe limit
Ru	103	40d	$\beta 0.22, \gamma 0.5$	Soft β is difficult to measure accurately
Ru	106	1y	$\beta 0.04$ Rh$\beta 3.5, \gamma$'s	Hard β of Rh daughter is easily measured
Ce	141	33d	$\beta 0.58$	Irradiated Ce contains 14-day Pr^{143}, which confuses issue
Ce	144	280d	$\beta 0.3$ Pr $\beta 3.0$	Hard β of Pr daughter is easily measured
Nd	147	11d	$\beta 0.83$	

Table 4. Distribution Coefficients

Fission products	Extractants Ag	Ce	La	Legend Letter	Range
Mo	*B*	*C*	*B*	*B*	0.003–0.03
Ru	*B*	*D*	*D*	*C*	0.03–0.3
Zr	*D*	*D*	*D*	*D*	0.3–3
Nd	*E*	*E*		*E*	3–30
Ce	*D*		*E*		

Table 5. Decontamination

Fission products	Extractants Ag	Ce	La	Legend Letter	Dec. fact.	% removed
Mo	*P*	*P*	*P*	*P*	1–1.3	0–23
Ru	*P*	*Q*	*Q*	*Q*	1.3–1.8	23–45
Zr	*S*	*Q*	*S*	*S*	2.5–5	60–80
Nd	*T*	*U*		*T*	5–10	80–90
Ce	*S*		*S*	*U*	10–50	90–98

Table 6. Forward and Reverse Extractions*

Fission products	Ag For.	Ag Rev.	Ce For.	Ce Rev.	La For.	La Rev.	Legend Letter	Distn. coeff.
Mo	*B*	*D*	*C*	*C*	*B*	*D*	*B*	0.003–0.03
Ru			*D*	*D*	*D*	*D*	*C*	0.03–0.3
Zr	*D*	*D*	*D*	*E*	*D*	*E*	*D*	0.3–3
Nd	*E*	*G*	*E*	*G*			*E*	3–30
Ce	*D*	*G*			*E*	*F*	*F*	30–100
							G	100

*The ranges for the forward extractions are those given in Table 4; those for the reverse extractions represent two runs on each extractant.

ANALYSIS

The original fissium melts were sectioned into samples for extraction, and between each extraction sample a sample was taken for analysis. Radiochemical analysis of these samples showed a non-

Table 7. Distribution Coefficients in Repeated Extractions

Fission products	Extractants: Silver 1	Silver 2	Cerium 1	Cerium 2	Lanthanum 1	Lanthanum 2
Mo	*A*	*A*	*C*	*C*	*B*	*B*
Ru	*A*	*A*	*D*	*D*	*D*	*D*
Zr	*D*	*D*	*C*	*D*	*D*	*C*
Nd	*D*	*E*	*E*	*F*		
Ce	*D*	*D*			*E*	*E*

Legend: Letter	Range
A	0–0.003
B	0.003–0.03
C	0.03–0.3
D	0.3–3
E	3–30
F	30–100

uniform distribution of various activities along the cylinder which did not show up in the homogeneity studies previously mentioned. In general the fission-product content of the extraction samples, the original material for each extraction, was taken as the average between the two adjacent analytical samples, but if one of these appeared out of reason, a weighted average was used.

A decontamination factor was determined for each extraction, defined as the ratio of the amount of the element of interest in the original metal to that of the final extracted metal. For most purposes this is not considered as important a quantity as the distribution coefficient, which in our usage is defined as the ratio of the amount of the element of interest per gram of metal in the extractant phase to that quantity in the uranium phase.

Analyses were by standard radiochemical techniques. In many cases the amount of an element in a particular phase was too small to follow through a chemical procedure without the addition of carrier. In these cases known amounts of carrier were added and the principles of the isotope dilution technique were used.

RESULTS

It was found that the reproducibility of the experiments was rather poor by the standards which are accepted for aqueous solution chemistry. The trends and orders of magnitude are, however, clearly established and the tables of data have been arranged to show the trends by indicating ranges of values rather than actual values. In the extraction and decontamination experiments summarized in Tables 4 and 5 an average of six determinations is represented by each given range.

Table 8. Decontamination in Repeated Extractions

Fission products	Extractants: Silver 1	Silver 2	Silver Overall	Cerium 1	Cerium 2	Cerium Overall	Lanthanum 1	Lanthanum 2	Lanthanum Overall
Mo	*P*	*P*	*P*	*P*	*P*	*P*	*P*	*P*	*P*
Ru	*P*	*P*	*P*	*P*	*Q*	*R*	*Q*	*P*	*Q*
Zr	*S*	*S*	*T*	*R*	*Q*	*S*	*R*	*S*	*S*
Nd	*S*	*T*	*U*	*T*	*U*	*V*			
Ce	*S*	*U*	*V*				*S*	*S*	*T*

Legend

Letter	D.F.	% rem.	Letter	D.F.	% rem.
P	1–1.3	0–23	*T*	5–10	80–90
Q	1.3–1.8	23–45	*U*	10–50	90–98
R	1.8–2.5	45–60	*V*	>50	>98
S	2.5–5	60–80			

In these first experiments in a new field it has not been possible to find the reasons for the lack of reproducibility and to obtain improvement. However, the principal cause of the lack of agreement is probably the sampling. It is quite possible that small particles of one phase may remain suspended in the other after the induction furnace has been turned off. As soon as the induction heating is stopped, the stirring ceases and settling begins. Cooling starts at the same time, however, and is fairly rapid and so the phases may not have time to separate completely. To remedy this situation a procedure has been initiated of reheating the melt in a resistance furnace to allow complete phase separation after the melt is removed from the induction furnace.

In order to ascertain whether or not the extraction represented equilibrium conditions, the extractant metal phase from some extractions was reextracted with inactive uranium. The results of these experiments (Table 6) show that in some cases distribution coefficients in the same range were obtained independently of the direction of approach, for example, in the extraction of ruthenium into cerium or lanthanum. More frequently, however, the reverse-direction extraction showed a higher value of the distribution coefficient than the forward extraction, which can be explained by a lack of attainment of equilibrium in the system. More vigorous stirring or longer heating was a possible aid in the solution of this difficulty.

Another series of experiments was designed to determine whether initial decontaminations and distributions could be duplicated in a second extraction of the uranium phase with the same metal. Two parallel runs were made for each extractant, and the results for distribution coefficient and decontamination are given in Tables 7 and 8, respectively. It can be seen that similar distributions and decontaminations were obtained in the first and second extractions. Comparison of duplicate runs shows that consecutive extraction experiments give just as good agreement as duplicate runs. The indication is that scale-up to continuous or repeated batch extraction would be possible.

The fissium used in these experiments did not contain plutonium and no plutonium data are available from these experiments, but a restatement of the earlier runs on plutonium is important in order to consider the process as a whole. Table 9 contains a summary of the plutonium data (*2*) at two levels of plutonium content: medium, about 18 mg. of plutonium/kg of uranium, and high, about 230 mg. of plutonium/kg. of uranium. The distribution coefficients for silver are high enough to indicate complete removal if the process is repeated a small number of times. With cerium, a number of repetitions would be necessary; with lanthanum, removal of plutonium would be difficult. Somewhat lower removal by lanthanum would allow its use to remove fission products while leaving the plutonium in the fuel, but with the removal as large as is indicated, this would probably give too large a loss of plutonium to be feasible.

Table 9. Plutonium Extraction

Extractant	Distribution coefficient: Medium level	Distribution coefficient: High level	Decontamination factor: Medium level	Decontamination factor: High level
Ag	4.6	7.0	3.7	5.1
Ce	0.95	1.02	1.50	1.58
La	0.65	0.56	1.28	1.22

TREATMENT OF THE EXTRACTANT PHASE

Removal of fission products and plutonium from uranium by such an extraction process must be followed by a step to clean up the extractant phase if the process is to be of much value in a fuel

cycle. Methods of cleaning up the extractant phases have been under investigation for some time with particular emphasis on the silver phase resulting from extraction of uranium with silver.

Some of the procedures tried to clean up the silver have been electrorefining with an aqueous bath, electrorefining with fused salt baths, and treatment with molten salts containing silver chloride. In the electrorefining experiments the contaminated silver is made the anode and a silver rod is used as the initial cathode. As the electrolysis progresses the cathode grows at the expense of the anode. A silver cathode which is decontaminated from those impurities which were present in the silver anode is obtained as a result either of lack of oxidation of the impurities at the anode leaving them in the form of a sludge or lack of reduction at the cathode leaving them in the electrolyte. Large decontamination factors were obtained from both of the electrorefining procedures, but the aqueous studies were abandoned. The aqueous bath required to obtain a smooth adherent deposit was so filled with complexing agents and other reagents that its stability toward the radiation which it would receive in actual use appeared highly problematical.

The fused-salt electrorefining studies are continuing with quite promising results. However, problems exist. Deposits tend to be crystalline and to form long streamers from the electrode. Owing to the large surfaces of these crystalline deposits the amount of adsorption and trapping of the electrolyte within the cathode deposit is considerable. Solutions of these problems appear to be at hand to permit further studies on decontamination.

The direct treatment of the contaminated silver with molten silver chloride has difficulties also, particularly in the choice of materials for use as containers. Glass is unusable at the temperature of molten silver, and metals are rapidly chlorinated by hot silver chloride. Silica crucibles have been found to hold the mixture and these are at present in use. Decontamination results are not available for many elements as, for example, so little ruthenium or molybdenum go into silver that their removal is hardly a problem. Results for fission-product cerium, which does extract into silver, indicate a removal of 97 to 99.6% in a single heating with silver chloride or silver chloride–sodium chloride mixtures containing 10 to 90 mole % silver chloride. Results for zirconium similarly indicate removal of 96 to 99.9% of the fission product from silver in such extractions. Thus it appears that the silver layer can be freed of at least some of its fission-product load after the silver extraction of uranium.

CONCLUSIONS

In estimating the value of this type of processing it is important to review the reasons for reprocessing fuel. Foremost for many reactors will be the cure of radiation damage. Changes occur in thermal conductivity, strength, and even shape of solid fuel elements in which fission is occurring at a high rate. These make it necessary to limit the time of exposure of the fuel elements and to reprocess at shorter intervals than would be required for any other reason. The fission products which in being slowed down give rise to this radiation damage may also just by their presence in the metal change its strength or other metallic properties or its resistance to radiation damage. Hence, their removal may be essential. Little is known about this aspect of the problem as it involves studies on complex alloys with small amounts of many elements very uniformly mixed through the alloy, a highly complicated system which it has not been possible to duplicate.

A third reason for reprocessing is the removal of fission products because of their neutron-absorbing tendency. The urgency for this depends on the type of reactor in question, as the neutron absorption by different fission-product nuclides is highly dependent on the neutron energy. Thus for a thermal reactor, removal of certain poisons may be of prime importance while for a fast reactor there are no nuclides of particularly serious poisoning ability. The reprocessing step should also provide for the replenishment of the used fissionable material in the fuel element, for example, by allowing the addition of highly enriched U^{235} to a fuel mixture of moderate enrichment.

Most of these ends can be accomplished by pyrometallurgical processing. The healing of radiation damage in a solid fuel can certainly be done by a melting and recasting process provided the fuel element is of such design that it can be fabricated remotely. Since the resistance of an alloy to radiation damage depends on its microstructure, it is also essential that the most resistant microstructure be obtainable by remote fabrication.

It is not known which of the fission-product elements may impair the structure of the metal and its resistance to radiation damage, which ones will have no effect, and which ones may actually improve the metal. It would be expected, however, that the presence of a nonmetal atom like xenon or a large atom like cesium would tend to impair rather than to improve. Thus the rare gases, the alkali and alkaline earth elements, may be the most important elements to remove from the standpoint of metallic structure. These, as it has been noted, are the particular elements that are removed by volatility in pyrometallurgical processing. Experiments not reported here (*2*) show that the decontamination factor for cesium and strontium in a single liquid-metal extraction step is of the order of 500 to 10,000 at the highest fission-product concentrations in which the process was tested, a level which corresponded to a burn-up of about 0.03%. Since these decontamination factors were considerably higher at high concentrations than at low, it would be logical to assume even better decontamination factors if the experiments could be run at a level corresponding to 2% burn-up.

Those elements which are removed specifically by extraction rather than volatilization, particularly the rare earths, might or might not be harmful to the metallic properties. At the present time too little is known about this to permit even a guess. Those elements which are not removed, such as ruthenium and molybdenum, might at low concentrations actually improve the metal. At least there is no information either of a practical or theoretical nature which would indicate that they have a large adverse effect on the metal. The radii of these atoms are such that they might fit into the uranium lattice without producing excessive distortion.

Thus, although the evidence is still meager it appears that pyrometallurgical processing would remove those fission-product impurities most likely to distort the uranium lattice by their presence. Those elements which it does not remove would be expected to have much less deleterious effect and possibly even to be beneficial.

As far as poisoning by neutron absorption is concerned, in a thermal reactor a very large part of this is in Xe^{135}, which is transitory and of minor importance in a processing cycle. Except xenon, most of the poisoning is in the rare earths, samarium, gadolinium, neodymium, and europium, and in iodine. Of these elements the rare earths are extracted to a large extent in the liquid-metal process and the iodine would in all probability be lost by decomposition of uranium iodides at the temperature of the extraction. The next group of fission products in order of decreasing importance as poisons in a thermal reactor are cadmium, strontium, cesium, rhodium, and krypton. By this time the contribution of each element to the poisoning is small. The authors have no information about cadmium and rhodium, but the rest of this group is completely removed by volatility.

In a fast reactor the problem of fission-product poisoning is minor and is a much less urgent reason for reprocessing than it is in a thermal reactor. The major contributors to poisoning in this case are elements which have been found to be fairly difficult to remove, such as zirconium, ruthenium, and molybdenum. However, enough of the zirconium is removed along with those elements which contribute less but still appreciably to the poisoning effect so that this effect is reduced to approximately half of its original value by a single extraction step.

It is clear that while a metal is in the molten condition additional fissionable material could be added and distributed uniformly through the metal.

Thus pyrometallurgical processing, though in its very early development stages compared with more conventional types, seems to have promise of accomplishing the goals of a processing cycle at potentially less cost. To achieve the final development of such a process will require a prolonged effort on the part of metallurgists, chemical engineers, and chemists. Effort in this laboratory is continuing with experiments on scaling up and on the development of continuous extractors to operate at this temperature.

The results with the artificial fissium mixtures are not very satisfying owing to the lack of agreement in the results. Unless some improvements are made in this agreement, it may be necessary to go back to real fuels of lower burn-up and to extrapolate to the expected burn-up or to wait until fuels of high burn-up are available and have decayed to a level of radioactivity which will permit laboratory handling. Other techniques of making fissium may be more successful and will also be tried.

Before closing, it would be well to point out that this type of processing is also uniquely adapted to use with a liquid-metal fuel reactor. If the other problems which are peculiar to the use of liquid-metal fuels are solved, it is probable that there will be a strong future for pyrometallurgical processing in the reprocessing cycle of a liquid-metal reactor.

LITERATURE CITED

1. F. H. Spedding, *et al.*, *Atomic Energy Commission Reports CN-1058*, 11/43, and CN-1199, 12/43, now declassified.
2. Voigt, A. F., *Proc. Intl. Conf. on Peaceful Uses of Atomic Energy, Geneva, 1955*, 9, 591.

Presented at Nuclear Science and Engineering Congress, Cleveland.

Use of Zirconium in Liquid-sodium Systems

F. E. BOWMAN and D. D. CUBICCIOTTI

Atomics International, Canoga Park, California

The attractive nuclear properties of zirconium make it a highly desirable core material for sodium-cooled reactors. The elevated temperature strength while low is sufficient for certain applications. Development of higher strength alloys is underway. Sodium in itself is completely compatible with zirconium; however, the nonmetallic contaminants, namely oxygen, hydrogen, and nitrogen, can effect serious damage. The primary problem in the use of zirconium in a sodium system, then, lies in controlling these impurities in the sodium.

In surveying the field of materials possessing potentialities in nuclear reactor construction, one is immediately attracted to zirconium because of its low capture cross section for thermal neutrons. The fact that during the initial period of reactor design and construction metallic zirconium was essentially a laboratory curiosity resulted in the use of aluminum as the primary metallic nonfuel core material. However, with the advent of the submarine reactor and the necessity for higher operating temperatures for feasible power production, the limitations of aluminum were exceeded. Neutron economics then demanded that the application of zirconium be completely investigated. The success of this investigation and the subsequent development program is amply demonstrated by a survey of the literature.

As the primary objective of the zirconium development program was the Submarine Thermal Reactor, or S.T.R., it was natural that water-corrosion resistance was of the utmost importance. As a consequence, until very recently essentially all processing and fabrication developments have been directed toward eliminating those impurities found to be detrimental with respect to corrosion. The fundamental objective of the alloy-development program also was the compensation for those deleterious impurities which cannot conveniently be removed.

The current interest in nuclear station-

ary power plants has prompted a re-evaluation of power reactors primarily promoted by the economic factors imposed by nonmilitary applications. Here neutron economy is of even greater importance, as is core life. In addition power costs are directly related to the temperatures involved in the heat transfer system and hence to the reactor-core operating temperature. Because of the advantages to be gained by increasing the temperatures in the reactor an evaluation of the over-all problem at North American Aviation, Inc., has resulted in the decision that sodium-cooled reactors have advantages over water-cooled systems in that the opportunities for development in the direction of increased operating temperatures are much more broad. For this reason, efforts have been concentrated upon the sodium-cooled graphite-moderated reactor for the production of power.

In selecting the core materials for a reactor of this type there are three essential requirements, (1) low thermal neutron capture cross section, (2) satisfactory elevated-temperature properties, and (3) compatibility. Breaking down the second and third requirements into further details, the materials must possess satisfactory elevated-temperature mechanical strength; have reasonable heat transfer characteristics; be capable of fabrication into relatively complex configurations; be dimensionally stable; be resistant to attack by sodium; and be able to exist in contact, either direct or through sodium, with the inevitable dissimilar materials.

The austenitic stainless steels are the obvious choice of available material based upon a precursory survey of the problem. They satisfy the mechanical-property requirements and have been found to be capable of satisfactory operation in sodium at the temperatures under consideration. The cross section, approximately 3 barns, is however a decided disadvantage, and in the interest of neutron economy the investigation of other materials was warranted.

Here again from the nuclear standpoint zirconium appears most attractive. The neutron cross section of zirconium (0.18 barn) is slightly smaller than that of aluminum (0.22 barn) and decidedly more favorable than the cross sections of the stainless steels (about 3 barns). The ability of this material to fulfill the other requirements may be evaluated from a brief survey of its pertinent characteristics.

PHYSICAL PROPERTIES AT ELEVATED TEMPERATURES

The properties of zirconium at both room and elevated temperatures are significantly affected by the impurity level and hence by the method of production. For the purposes of this discussion, those properties resulting from the current production method, arc-melted sponge, will be considered. Figure 1 indicates the strength characteristics vs. temperature of this material, in the form of 0.035-in. sheet taken from a production run. The rather serious temperature limitations imposed by unalloyed zirconium are readily apparent. If one considers that most elevated-temperature applications must be designed on the basis of creep strength rather than yield or ultimate strength, this limitation becomes even more severe.

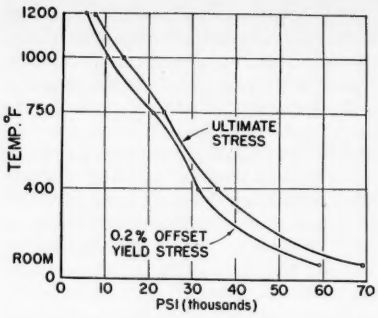

Fig. 1. Temperature dependence of strength of zirconium.

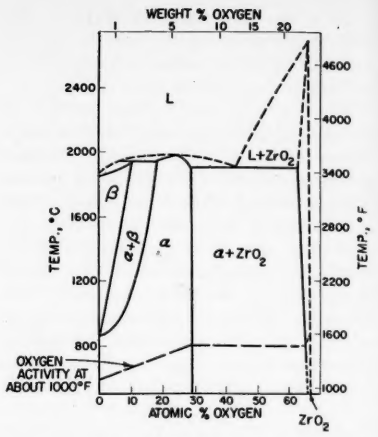

Fig. 2. Partial diagram of the zirconium-oxygen system.

For some time a program directed toward improving the elevated-temperature strength of zirconium without seriously sacrificing its nuclear advantages has been underway. To date this program has had the additional goal of providing resistance to hot-water corrosion, a fact which has restricted its value to the sodium problem to some extent. However a few values obtained by Schwope and Chubb (*1*) indicate the potentialities of further work. Table 1 contains the strength data at 500°C. of several experimental alloys reported by the authors. For comparison purposes the yield stress of type 347 stainless steel may be taken as 31,000 lb./sq. in. at 500°C. The favorable comparison of this with the listed values for the zirconium alloys indicates the possibilities in the development of zirconium alloys for elevated-temperature applications.

FABRICATION POTENTIALITIES

Zirconium and a majority of its alloys which exhibit promising elevated-temperature properties have without serious difficulty been rolled into plates and sheets, the starting material for most reactor-component fabrication. Seamless tube drawing has presented difficulties, primarily because of die seizure. However, it has been found that proper lubricants can overcome this disadvantage. In fact, 0.750-in.-diam. tubing with 0.010-in. wall thickness has been drawn in lengths up to about 14 ft.

Zirconium is probably one of the easiest of the metals to weld if the necessary precautions are taken. In the molten state and at very high temperatures in the solid state the metal is exceedingly reactive with both oxygen and nitrogen. Both of these gases form compounds which are detrimental to the ductility of the contaminated metal. As a result, it is essential that the weld be well shielded with an inert gas. Zirconium welding was developed by use of a dry-box technique, which seriously limited the operations that could be performed. Recently, however, at North American Aviation a program to develop techniques for the automatic welding of relatively large components from thin sheets of zirconium, 0.035 in., has been successfully carried out. By proper torch design and suitable welding fixtures butt welds up to 10 ft. long have been made by modified heliarc methods. Standing lip welds in various configurations have also been successfully accomplished by hand welding. Tensile tests of welded coupons indicate that the welds are superior in strength to the parent metal. Ductility, as measured by bend tests, is superior in the weld metal as compared with the parent material. Care must be taken, however, to avoid an embrittled heat-affected zone. This can largely be taken care of by proper surface preparation prior to welding. The production of large-diameter thin-walled tubing is apparently no problem as this has been and is being done essentially on a commercial scale. In most cases zirconium can be formed cold; however, some of the higher strength alloys require heat to facilitate the operation. These materials can be worked in air for short times at temperatures up to about 600°C. without seriously impairing the properties. It has been noted, however, that working at from

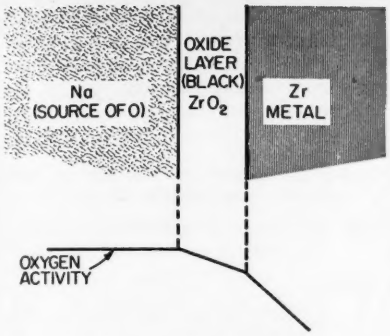

Fig. 3. Schematic diagram of zirconium-sodium interface during rapid transfer of oxygen. Lower curve shows relative oxygen activities.

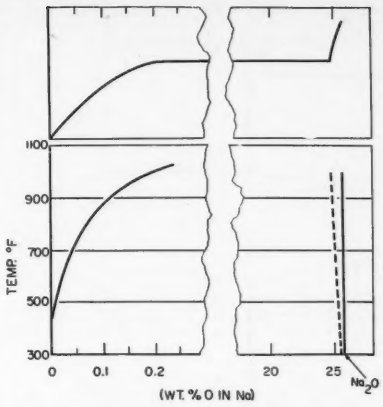

Fig. 4. Schematic representation of oxygen activity in sodium at 1,000°F. (upper curve) compared with solubility curve.

100° to 200°C. will appreciably reduce the work-hardening rate and thus permit a greater amount of essentially "cold" work.

Zirconium has the serious disadvantage of forming brittle intermetallic compounds with practically all the conventional structural materials. This complicates its use in applications which require the metallurgical bonding of zirconium to these other materials as part of the structure. It has been found, however, that flash welding produces a joint, with considerable strength and some ductility, between zirconium and the stainless steels, both ferritic and austenitic. Such joints are essential in many designs calling for a closed cooling system, as zirconium is much too expensive to permit its use external to the reactor core, where the nuclear advantages are unimportant.

COMPATIBILITY

With regard to the behavior of zirconium and its alloys in dynamic sodium it would perhaps be well to consider briefly liquid-metal corrosion in general. Miller (*2*) lists the following mechanisms by which liquid metals can react with certain materials:

1. Solution attack
2. Direct alloying
3. Intergranular penetration
4. Corrosion by contaminants
5. Corrosion erosion
6. Facilitation of self-welding
7. Mass transfer

At temperatures up to 600°C. sodium apparently has no significant solubility for zirconium. The reverse of this is also true, and so the first two methods of possible attack can be eliminated. Sufficient stress-rupture work with zirconium and its alloys has been carried out to indicate that intergranular penetration is not a problem. Such tests are more conclusive for this type of corrosion as grain boundary attack is usually accelerated by the application of stress.

Corrosion by contaminants is the principal means by which sodium affects zirconium as well as many other materials.

Zirconium is a very reactive metal at high temperatures. It readily takes nonmetals (oxygen, nitrogen, hydrogen, carbon) away from other metals and for that reason has often been used as a getter. In the structural applications of zirconium these nonmetals are harmful and act as corroding agents.

In the sodium-cooled graphite-moderated reactor system under study at North American Aviation, the zirconium cans of the moderator are in contact with molten sodium at high temperatures. The zirconium is thus susceptible to corrosion by any nonmetals that get into the sodium-coolant stream, and so the effect of such corrosion and the means of controlling it are being studied.

THE ZIRCONIUM-OXYGEN SYSTEM

Because quite a lot is known about the effects of oxygen on zirconium, it is used as a typical nonmetal for this discussion. Oxygen is very soluble in alpha zirconium to form a solid solution. Domagala and McPherson (*3*) have reported the phase diagram shown in Figure 2. Under equilibrium conditions at 1,000°F. the solubility of oxygen in alpha zirconium is about 29 atom %. When more oxygen is added, it reacts to form the new phase, zirconium dioxide. An estimate of the activity of the oxygen in zirconium-oxygen mixtures is given by the dotted line. However if oxygen is added too rapidly for equilibrium to be attained, then the situation will probably be as shown in Figure 3. There the oxygen has not been able to diffuse into the metal rapidly and a layer of zirconium dioxide had formed before the entire metal phase became saturated with oxygen. Therefore in practice the relative rates of diffusion of oxygen in the metal and diffusion of oxygen from the sodium to the zirconium are important because they determine whether or not a layer of zirconium dioxide will form on the metal. These properties are currently being studied.

THE SODIUM-OXYGEN SYSTEM

The solubility of oxygen in liquid sodium is small, the limits being shown in Figure 4 (*4*). As oxygen is added to sodium, it dissolves until the solubility limit is reached and then sodium monoxide begins to precipitate. The activity of oxygen dissolved in sodium at 1,000°F. is given in a general way by the curve at the bottom of the figure.

The state of the oxygen dissolved in the sodium is not as Na_2O but probably as $O^=$. In zirconium metal the dissolved oxygen is also $O^=$. Therefore the transfer of oxygen from sodium to zirconium probably does not involve any change of the state of the oxygen.

When liquid sodium and zirconium are put in contact, the oxygen will transfer from one metal to the other until the oxygen activity is equalized in the two metals. In Figure 5 a schematic comparison of the oxygen pressure in equilibrium with sodium-oxygen and zirconium-oxygen mixtures is given. As the oxygen pressure over a mixture of sodium and zirconium at 1,000°F. is increased, oxygen dissolves in both metals, but to a greater extent in zirconium. At a certain pressure (roughly 10^{-30} atm.) zirconium dioxide begins to form, and at slightly higher pressures all the zirconium is in the form of zirconium dioxide, while only a fraction of a per cent of oxygen is in the sodium. Further increases in oxygen pressure eventually convert the sodium to sodium monoxide (complete at about 10^{-20} atm.).

The significant feature of this diagram is that the zirconium system is far below the sodium system. To maintain the oxygen concentration in zirconium at

TABLE 1. TENSILE PROPERTIES OF SOME ZR ALLOYS AT 500°C.

Composition	0.2% Offset yield stress, lb./sq. in.	Ultimate stress, lb./sq. in.	Elongation, %
Zr	16,000	24,000	30
2 wt. % Al	32,000	46,000	25
1.2 wt. % Mo	35,800	48,010	44
2.2 wt. % Nb	35,000	43,000	9
10.4 wt. % Ti	41,200	58,300	33
3.9% Ti + 1.9% Mo	37,600	52,500	30
4.6% Ti + 0.8% Al	32,000	46,800	23

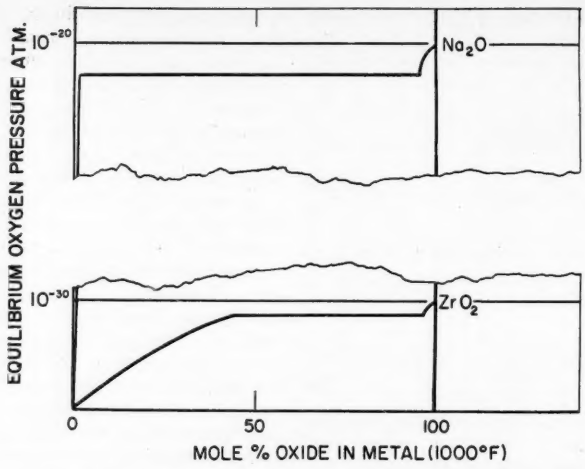

Fig. 5. Comparison of oxygen pressure in equilibrium with sodium-oxygen and zirconium-oxygen mixtures.

an arbitrary low value, it is necessary to hold the oxygen in the sodium to an extremely low value; for example, to hold the oxygen in zirconium to 0.5 wt. %, the oxygen in sodium must be kept below 10^{-10} wt. % or so. These estimates are open to a great deal of uncertainty, but the over-all principle is apparent.

It must be remembered, however, that thermodynamic considerations forecast equilibrium conditions. The rate at which these conditions are realized must be determined by other means. It is obvious that oxygen contents of the order of 10^{-10} % in sodium cannot be attained. The life, then, of zirconium in a sodium system is necessarily determined by (1) maximum tolerable concentration of the nonmetallic in zirconium based on its effect on physical properties and (2) the rate at which this concentration level is reached. This rate is determined by one of two diffusion processes: the diffusion of O^- in zirconium or in ZrO_2. Fundamentally it would be interesting to know the conditions under which each process becomes dominant but practically it is the end effect that is of utmost importance.

The experimental effort, therefore, has been directed primarily toward obtaining strictly engineering data. It has been found that with oxygen levels in sodium above about 0.005 wt. % the rate of weight gain with zirconium is essentially independent of the level. This amounts to approximately 0.50 mg./(sq. cm. of surface area) (month). The data appear to follow a parabolic rate law. In addition to the weight gains noted, evidence of diffusion of oxygen into the metal is given by a definite increase in surface hardness as determined by microhardness measurements. The depth of penetration as measured by this technique appears to proceed at about 0.0015 in./month at 1,000°F. There are, as yet, insufficient data to establish the actual oxygen concentration gradient represented by this hardness change. A serious loss in room-temperature ductility in this hardened layer is, however, indicated. Such embrittlement results in a serious loss in fatigue strength in a notch-sensitive material such as zirconium. Fortunately this hardening and embrittling effect disappears for oxygen contents encountered this far at the elevated temperatures contemplated for the applications. However, in view of the relatively high solubility of oxygen in zirconium it is apparent that with time the oxygen level could reach the point when the effect of temperature is no longer so pronounced and serious trouble could be anticipated.

It is, then, obvious that in reactor systems, in which the occasional introduction of contaminants such as oxygen is an inherent possibility, provision must be made for maximum protection for the zirconium. In order to provide such protection two possible approaches are available. The concentration of oxygen (and other nonmetals) in the sodium must be reduced to and maintained at a minimum. A nonreactive and impenetrable barrier may be applied to the zirconium.

The concentration of oxygen in sodium can be reduced by (*a*) cold trapping and (*b*) gettering. Cold trapping works on the principle that cooling the sodium will precipitate out sodium oxide. In Figure 3 one sees that the solubility of oxygen in sodium decreases rapidly as the temperature is lowered. The lowest temperature that can be used is the melting point of sodium, and there the solubility is 0.003 wt. % oxygen. However, as we have seen, to protect zirconium a much lower oxygen concentration is required. An alternate method is to introduce a more reactive metal than zirconium to getter the oxygen. A number of getters in small-scale capsule tests have been investigated. The results with these are given in Table 2. Zirconium-titanium alloy seems most promising at present. In the future it is planned to run a sodium loop with a hot section containing this alloy to test its effectiveness.

Table 2. Getters for Protecting Zirconium from Oxygen in Sodium

(All tests made at 1,200°F. in stainless capsules for 1 month)

Getter	Effect
Al	Alloyed with Zr and attacked it badly
Mg	Alloyed—some attack
Ca	Alloyed—seemed to protect Zr slightly
Th	Seemed to protect—no apparent effect on Zr
Zr–Ti	Seemed to protect—no apparent effect on Zr

The other method mentioned for protecting the zirconium is to provide a barrier that will prevent the oxygen from contacting the zirconium. Such a barrier might be a metal plating or a nonmetal layer of some sort. A useful plate would have to be insoluble in the zirconium as well as in the sodium so as to remain on the surface. A metal plating would therefore have to be of a nonalloying metal. Alternately, a nonmetal coating would have to be nonreactive. For instance, zirconium dioxide would not do, as the oxygen would diffuse into the zirconium. Very little has been done in this area.

To summarize briefly, it appears that the nuclear advantages of zirconium can be utilized in sodium-cooled reactors if proper provisions are made to accommodate for the nonmetallic impurities. Oxygen and hydrogen in particular are readily introduced into sodium and are readily removed by solution in any contacting zirconium at elevated temperature. A serious loss in physical properties is possible if such a reaction is permitted to proceed to any extent. Contaminant removal from the sodium by proved trapping methods and the possibility of barrier coatings on the zirconium promise to guarantee a satisfactory life for zirconium components of systems now contemplated.

LITERATURE CITED

1. Schwope, A. D., and W. Chubb, *J. Metals*, **4**, 1138 (1952).
2. Miller, E. C., "Liquid-Metals Handbook," 2d ed., U. S. Gov't. Printing Office, Washington, D. C. (1952).
3. Domagala, R. F., and D. J. McPherson, *J. Metals*, **6**, 238 (1954).
4. Jackson, C. B., and R. M. Adams, "Liquid-Metals Handbook," 2d ed., U. S. Gov't. Printing Office, Washington, D. C. (1952).

Presented at the Nuclear Science and Engineering Congress, Cleveland.

Estimation of Heat Sources in Nuclear Reactors

LLOYD G. ALEXANDER

Oak Ridge National Laboratory, Oak Ridge, Tennessee

Knowledge of local heating rates is needed for estimation of operating temperatures, thermal stresses, and cooling requirements in nuclear reactor components. Heat is liberated by the dissipation of the energy of fission fragments, beta particles, fast neutrons, and gamma photons. Heating rates are formulated in terms of either neutron or gamma flux densities, the corresponding collision probabilities, and appropriate energy transfer coefficients, the forms of which are given. Special methods of estimating the flux densities are discussed. The data on the magnitudes of the various energy sources are reviewed.

The designer of nuclear reactors needs to know the local rates of heat liberation in the various reactor components in order to estimate temperatures, cooling requirements, thermal stresses, corrosion rates, radiation-damage annealing rates, and temperature-dependent reactivity changes. The heat-liberation rates can be formulated in terms of the local neutron and gamma fluxes, ϕ_n and ϕ_γ. Admittedly, values of these are not easily come by; nevertheless, recent progress in neutron- and gamma-particle transport theories makes it possible to treat many systems of interest to engineers. It is the purpose of this paper to formulate the heat-liberation rates and to indicate methods of estimating the fluxes.

ENERGY SOURCES AND MODES OF LOCAL DEPOSITION OF HEAT

Heat is liberated in reactors by the dissipation of the kinetic energy of fission fragments, beta particles, gamma photons, and neutrons. These particles, in penetrating matter, collide with electrons and atomic nuclei and impart energy to them. In some collision processes part of this energy is reradiated, but for the most part it is rather rapidly degraded into thermal motion of nuclei and electrons in the macroscopically near vicinity of the collision.

Fission fragments, primary gamma photons, and neutrons result directly from fission. Fission fragments emit beta particles and gamma photons by radioactive decay. Neutrons diffuse through the reactor and generate gamma photons by inelastic collisions with and absorptions in various nuclei. Photons arising from all these processes may experience many scattering collisions, losing all or part of their energy at each collision.

Fission-fragment and Beta-decay Energy

According to Shapiro (*18*), two and occasionally three heavy particles result from the fission of U^{235} by thermal neutrons. Hanna (*11*) critically examined the data as of 1950 and concluded that the most probable value for the average kinetic energy of the fission fragments E_{ff} lies in the range 168 ± 5 mev./fission.

Because of their high charge, fission fragments have short ranges (*18*). Accordingly, from a macroscopic point of view their energy is dissipated at the point of fission.

Way (*23*) estimated the energy released by the beta decay of fission fragments $E_{ff\beta}$ to be 7 mev./fission. Effective ranges are of the order of 1 mm. or less in reactor materials; hence, the beta energy is also liberated very near the point of fission.

The sum E_f of the fission-fragment and beta-ray energies is thus about 175 mev./fission. The heat-release rate is proportional to the number of fissions per unit volume per unit time and may be formulated as follows:

$$(G_{ff} + G_{ff\beta}) = \int_{E_n=0}^{E_n=\infty} \Sigma_f(E_n)\phi_n(E_n)E_f \, dE_n \quad (1)$$

Here $\phi_n(E_n)$ represents the energy-dependent neutron flux density, i.e., total path length (cm.) traversed by neutrons having energy E_n (mev.) per unit volume (cc.) per unit time (sec.) per unit energy range (mev.), and $\Sigma_f(E_n)$ is the probability, per centimeter of travel, that a neutron of energy E_n will experience a collision resulting in fission. The integration is carried over all energies; however, there are negligibly few neutrons having energies greater than 7 mev. In thermal reactors the great majority of the flux is concentrated into a narrow band around the temperature of the medium. Furthermore, the fission cross section $\Sigma_f(E_n)$ decreases rapidly with increasing neutron energy. Accordingly, in thermal reactors the integral is approximated very well by the product of the thermal flux (say, the flux lying between 0.0 and 0.1 ev.) and the fission cross section evaluated at the temperature of the medium. The thermal flux may be denoted by $\phi_n(th)$, whence

$$\phi_n(th) = \int_{0.0}^{0.1\text{ev}} \phi_n(E_n)\, dE_n \quad (2)$$

Using Equation (2) and converting to B.t.u./(hr.)(cu. ft.) gives Equation (1) in the form, for thermal reactors,

$$G_f = (G_{ff} + G_{ff\beta}) \frac{\text{B.t.u.}}{(\text{hr.})(\text{cu. ft.})} = 2.70 \times 10^{-6}\Sigma_f(th)\phi_n(th) \quad (3)$$

Neutron Energy

Three processes by which neutrons impart kinetic energy to atomic nuclei are (*a*) absorption, (*b*) elastic scattering, and (*c*) inelastic scattering.

In an absorption collision the neutron enters and combines with the target nucleus N, forming the next higher isotope N'. The nucleus is "knocked on,"

and its velocity is readily calculated from a simple momentum balance.

Defining δ_{nc} as the average fraction of the kinetic energy of the incident neutron appearing as kinetic energy of the target nucleus after a capture collision, one has

$$\delta_{nc} = \overline{E_{N'}/E_n} = m/(M + m) \quad (4)$$

where m denotes the atomic mass of the neutron, M the atomic mass of the target nucleus, and $\overline{E_{N'}}$ the average postcollision kinetic energy of the nucleus.

The remainder of the neutron kinetic energy plus the binding energy is released in the form of a series of so-called "capture" gamma photons of decreasing energy. The N' isotope may be radioactive and may decay by beta-gamma emission. Later sections deal with heat release from these sources.

The local heating effect due to the capture of fast neutrons is thus

$$G_{nc} = \int_{E_0}^{\infty} \delta_{nc} E_n \Sigma_{nc}(E_n) \phi_n(E_n)\, dE_n \quad (5)$$

where E_n denotes the energy of the neutrons and where Σ_{nc} is the so-called "macroscopic" neutron-capture cross section. It is the probability that a neutron will experience a capture collision per unit length of travel. The lower limit of integration, E_0, is chosen sufficiently high so that Equation (5), derived on the assumption that the energy of the target nucleus prior to the collision is negligible in comparison with the initial neutron energy, remains valid but also sufficiently low so that only a negligible portion of the neutron energy remains to be transferred at energies less than E_0.

The transfer coefficient δ_{nc} of Equation (4) is small except in materials having low atomic mass. Moderator materials have low atomic mass (12 or less), but they are selected, for reasons of neutron economy, from among materials having low capture cross sections in comparison with their scattering cross sections. For all materials the capture cross sections tend to become small at high neutron energies, while at low neutron energies, where the cross sections may be appreciable, the energy available for transfer is small. Thus it turns out that the contribution G_{nc} of neutron capture to the local heating rate is always small compared with the heat released by neutron elastic scattering and the dissipation of gamma energy. Neutron captures cannot be neglected, however, because of the accompanying emission of high-energy "capture" gammas, which will be considered in a later section.

In elastic collisions the neutron does not react with the nucleus, and both momentum and kinetic energy are conserved. The appropriate balances are most conveniently formulated in the center-of-mass system of coordinates. By combining these and transforming the results to the laboratory system of coordinates, Glasstone and Edlund (*7*) obtained a result that may be put into the form

$$E_n'/E_n = \frac{M^2 + 2Mm\cos\theta + m^2}{(M + m)^2}$$

where E_n' is the postcollision neutron energy and θ is the angle of scattering in the center-of-mass system. Since kinetic energy is conserved in the collision, it follows that

$$E_N/E_n = 1 - E_n'/E_n$$

where E_N is the postcollision energy of the target nucleus.

The scattering is usually isotropic in the center-of-mass system; hence the probability $P(\theta)\, d\theta$ that a neutron will be scattered elastically through an angle θ into angle $d\theta$ is related (*7*) to the angle θ by

$$P(\theta)\, d\theta = \sin\theta\, d\theta/2.$$

By definition the average fraction δ_{ne} of neutron energy E_n converted into kinetic energy E_N of the target nucleus is given by the integral

$$\delta_{ne} = \int_0^{\pi} (E_N/E_n) P(\theta)\, d\theta$$

which leads to the simple result that

$$\delta_{ne} = (1 - \alpha)/2 \quad (6)$$

where

$$\alpha = [(M - m)/(M + m)]^2$$

The elastic-collision heating rate is formulated similarly to Equation (5):

$$G_{ne} = \int_{E_0}^{\infty} \delta_{ne} E_n \Sigma_{ne}(E_n) \phi_n(E_n)\, dE_n \quad (7)$$

The lower limit E_0 may be taken at about 0.01 mev. G_{ne} must be summed with respect to all kinds of atoms present in the medium.

If the compound nucleus formed by the interaction of a neutron with a target nucleus decomposes by the emission of another neutron, the net result is equivalent to the scattering of the incident neutron. The nucleus however is left in an excited state, kinetic energy is not conserved, and the scattering therefore is inelastic.

The neutron energy may be reduced severalfold as a result of the collision. The major portion of this energy loss appears as energy of excitation of the nucleus and is rather quickly radiated in the form of "inelastic-scattering" gammas. The kinetic energy acquired by the nucleus is generally less than that which it would have received by capture of the neutron. This kinetic energy, which is the only part of the energy transferred that appears locally as heat, is small in comparison with that released by dissipation of gamma energy for the same reasons that the corresponding contribution from neutron capture is small, except that the cross sections for inelastic scattering may be larger than for capture. At present writing it is not clear that the local contribution to the heating rate of the inelastic-scattering process is always negligible. In any event, the process cannot be neglected because of the accompanying emission of gamma rays, which sometimes makes the single most important contribution to the local heating rate (*26*). This aspect of the process is considered further in a later section.

Energy Release by Beta Decay of Activated Nuclei and Related Processes

Nuclei rendered unstable by the capture of a neutron may emit alpha, beta, or other particles as well as gamma photons. Beta emission is the most common mode of decay. For a given transition the beta particles are emitted with energies ranging continuously from zero up to some characteristic maximum $E_\beta(\max)$ which is the most commonly tabulated value (*12, 14*). As the contribution to the local heating from beta decay of activated nuclei is usually small compared with other contributions, it is generally sufficiently precise (*12*) to take the average electron energy to be $\frac{1}{3}\ E_\beta(\max)$. Thus the local heating rate due to "capture" betas becomes

$$G_{nc\beta} = \int_0^{\infty} \Sigma_{nc}(E_n)\phi_n(E_n)\, dE_n \cdot \sum_i N_i E_{\beta i}(\max)/3 \quad (8)$$

where N_i is the number of betas of characteristic energy $E_{\beta i}(\max)$ emitted per neutron capture in the decay chain involving i groups of betas. The decay process may proceed through several isomeric states and atomic numbers. It should be noted that the contribution from "thermal" neutrons in Equation (8) may be large and override the contribution from fast neutrons.

The contribution of beta decay to the local heating rate is negligible in all moderators except possibly light water. It may become appreciable in structural materials, fuel diluents and clad, coolants, and other materials exposed to high thermal neutron fluxes when these have appreciable capture cross sections, as in stainless steels.

The isotopes Li^6 and B^{10} emit alpha particles following capture of neutrons. As the capture cross sections are large and as nearly all the kinetic energy of the incident neutron plus the binding energy appears as kinetic energy of the product nucleus (there being only a weak capture gamma ray emitted by B, none by Li), the local heating may become important if the concentrations of these nuclides become

appreciable. The effect is computed by means of Equation (8), but the summation is replaced by the sum of E_n and the energy equivalent of the mass change, which for Li^6 amounts to 4.78 mev. and for B^{10} to 2.31 mev.

Gamma Heating

Gamma photons penetrating matter exhibit three interaction processes: (*a*) photoelectric effect, (*b*) pair production, and (*c*) Compton scattering.

In the first process a photon transfers all its energy to an electron, which is "knocked on" and dissipates its energy in the immediate vicinity. The probability that a photon will experience such a collision per unit length of travel is denoted by $\mu_{pe}(E_\gamma)$. When the atom from which the electron was ejected acquires another electron in its place, an X ray of low energy is emitted; however, about 95% of these are reabsorbed inside the atom, and an Auger electron of low energy is ejected from among the outer valance electrons. This electron also dissipates its energy in the vicinity. Various other energy-"dribbling" processes may occur, but the net effect is that all the energy of the primary gamma photon is dissipated as heat in the vicinity of the collision. Thus the fraction $\delta_{\gamma pe}$ of initial gamma energy E_γ dissipated is unity. Consequently the heating rate due to photoelectric collisions of gamma photons is given by

$$G_{\gamma pe} = \int_0^\infty E_\gamma \mu_{pe}(E_\gamma)\phi_\gamma(E_\gamma)\, dE_\gamma \quad (9)$$

where E_γ denotes the energy of the gamma photon and $\phi_\gamma(E_\gamma)$ denotes the energy-dependent gamma flux.

Photons having energies in excess of 1.02 mev. may interact with the coulomb field of a nucleus and produce an "electron pair." The probability of pair production per unit length of travel is denoted by $\mu_{pp}(E_\gamma)$. The resulting particles dissipate their kinetic energy near the point of production. The positron ultimately combines with an electron forming two photons having energies approximately 0.51 mev. each. These may penetrate some distance from the point where the pair production occurred. The nucleus involved in the collision also acquires some energy. The net result is that $(E_\gamma - 1.02)$ mev. of energy is dissipated at the point of collision. Thus $\delta_{\gamma pp}$, the fraction of photon energy E_γ dissipated locally, becomes

$$\delta_{\gamma pp} = (E_\gamma - 1.02)/E_\gamma; \qquad E_\gamma \geq 1.02 \quad (10)$$

The heating rate due to pair production takes the form

$$G_{\gamma pp} = \int_0^\infty \delta_{\gamma pp} E_\gamma \mu_{pp}(E_\gamma)\phi_\gamma(E_\gamma)\, dE_\gamma \quad (11)$$

The lower limit is taken as zero for later convenience, but $\mu_{pp}(E_\gamma)$ is zero for E_γ less than 1.02 mev.

Compton scattering is the scattering resulting from an elastic collision of a photon with an electron. For this process Compton derived the following relation between the scattering angle θ and the energies E_γ and E_γ' of the photon before and after collision:

$$E_\gamma'/E_\gamma = \frac{1}{1 + E_\gamma(1 - \cos\theta)/(mc^2)} \quad (12)$$

Since the collision is elastic, kinetic energy is conserved, and

$$\frac{E_\beta}{E_\gamma} = \frac{E_\gamma - E_\gamma'}{E_\gamma} = 1 - \frac{E_\gamma'}{E_\gamma} \quad (13)$$

where E_β is the energy of the electron. The probability that a photon will be scattered through an angle θ into angle $d\theta$ is given by the Klein-Nishina formula (*10*), which may be put into the form

$$P(\theta)\, d\theta = K(E_\gamma'/E_\gamma)^2[(E_\gamma/E_\gamma') + (E_\gamma'/E_\gamma) - \sin^2\theta]\sin\theta\, d\theta \quad (14)$$

where K is a normalization constant such that

$$\int_0^\pi P(\theta)\, d\theta = 1$$

The fraction $\delta\gamma_c(E\gamma)$ of the energy of the incident photon that appears as kinetic energy E_β of the beta particle is given by

$$\delta_{\gamma c}(E_\gamma) = \int_0^\pi (1 - E_\gamma'/E_\gamma)P(\theta)\, d\theta \quad (15)$$

The integral has not been reduced to a convenient algebraic form but has been evaluated. (*See* Equations (18) ff.).

The energy deposition due to Compton scattering may be formulated as follows:

$$G_{\gamma c} = \int_0^\infty \delta_{\gamma c}(E_\gamma)\mu_c(E_\gamma)E_\gamma\phi_\gamma(E_\gamma)\, dE_\gamma \quad (16)$$

Summing the gamma heating contributions given by Equations (9), (11), and (16) gives

$$G_\gamma = \int_0^\infty (\delta\gamma_{pe}\mu_{pe} + \delta_{\gamma pp}\mu_{pp} + \delta_{\gamma c}\mu_c)E_\gamma\phi(E_\gamma)\, dE_\gamma \quad (17)$$

where the E_γ's have been omitted in the parenthesis for brevity. Substituting from Equation (10) and rearranging, while keeping in mind that μ_{pp} vanishes for energies less than 1.02 mev. and that μ_{pe} is unity, one finds

$$G_\gamma = \int_0^\infty \mu_e(E_\gamma)E_\gamma\phi_\gamma(E_\gamma)\, dE_\gamma - \int_{1.02}^\infty 1.02\mu_{pp}\phi_\gamma(E_\gamma)\, dE_\gamma \quad (18)$$

where

$$\mu_e(E_\gamma) = \mu_{pe} + \mu_{pp} + \delta_{\gamma c}\mu_c \quad (19)$$

The quantity $\mu_e(E_\gamma)$ appearing in the left-hand integral, divided by the density of the medium, has been graphed by Snyder and Powell (*20*) as a function of E_γ for various materials. Their coefficient $\mu - \sigma_s$ is identical with $\mu_e(E_\gamma)$. It is called the energy absorption coefficient. If the so-called "annihilation photons," resulting from the neutralization of the positron, are assumed to be absorbed in the vicinity of the point of pair production, one may neglect the right-hand integral provided the annihilation photons are not included in the gamma flux $\phi_\gamma(E_\gamma)$.

NEUTRON FLUX DISTRIBUTION

The neutron diffusion and transport theories yield descriptions of the spectral and spatial distributions of the neutron fluxes $\phi_n(E_n)$. These theories have been discussed elsewhere (*7*) and will not be considered here in detail. A one- or two-group diffusion calculation will suffice to describe the "gross" variation of the thermal flux in many thermal reactors with sufficient precision for calculations of G_f. If $\phi_n(th, o)$ is the flux at some reference point in a homogeneous reactor (say the center) and $f(r)$ denotes a function, obtained from diffusion theory, describing the spatial variation of $\phi_n(th, r)$ where r denotes the radius vector from the reference point, such that

$$\phi_n(th, r) = \phi_n(th, o)f(r) \quad (20)$$

by Equation (3) it follows [by use of the notation of Equation (20)] that

$$G_f(r) = A\phi_n(th, o)f(r)\Sigma_f(th, r) \quad (21)$$

where A is a proportionality factor. The heat output from the reactor due to fission fragments Q_f is obtained by integrating $G_f(r)$ over the volume of the fuel-bearing part of the core.

TABLE 1

Geometry	$f(r)$	G_0/G_{avg}
Sphere of radius R	$\sin(\pi\rho/R)/(\pi r/R)$	3.29
Cube of side A	$\cos(\pi x/A)\cos(\pi y/A)\cos(\pi z/A)$	3.64
Right cylinder of radius R	$J_0(2.405\rho/R)\cos(\pi z/2R)$	3.87

$$Q_f = \int_{V_f} G_f(r)\, dV$$

where V_f denotes the volume of the fuel region. Substituting from Equation (21) and solving for $A\phi_n(th, o)$ gives

$$A\phi_n(th, o) = \frac{Q_f}{\int_{V_f} f(r)\Sigma_f(th, r)\, dV}$$

Replacing this in Equation (21) gives

$$G_f(r) = \frac{Q_f f(r)\Sigma_f(th, r)}{\int_{V_f} f(r)\Sigma_f(th, r)\, dV} \qquad (22)$$

The energy available from fission fragments (kinetic and beta decay) is about 175 mev./fission. The total energy per fission is about 200 mev. Thus Q_f is about 87% of the total reactor heat output, Q_t. The balance of Q_t is generated by fission gammas (7.5 mev.), fission-fragment-decay gammas (6 mev.), fast neutrons (5 mev.), capture gammas and betas (7 mev.). The particles bearing this energy (about 25 mev.) tend to leak out of the fuel-bearing zones and to liberate heat in the coolant, reflector, thermal shield, pressure shell, and biological shield. However, in the designing of the fuel-bearing core, it is sufficient and conservative to assume that all the reactor heat Q_t of a reactor is realeased in the fuel and that it has the same spatial distribution as Q_f.

The function $f(r)$ has been evaluated by Glasstone and Edlund (7) for certain bare, homogeneous, thermal reactors of simple shape, with $\Sigma_f(th, r)$ uniform.

Integrating the given functions over the corresponding geometric forms readily yields the ratio of the maximum heat-release rate G_0 to the average rate G_{avg}. Values are listed in Table 1. The presence of moderating reflectors, control elements, structural materials, coolants, ducts, and nonuniform loading (variable Σ_f) modify these simple distributions. Space does not permit treatment of these effects, but it is important to reduce G_0/G_{avg} so that a larger fraction of the core may operate at or near the limiting conditions and so that burn-up of nuclear fuel and accompanying effects will be more uniform.

Glasstone and Edlund point out that the functions $J_0(x)$ and $(\sin x)/x$ are rather similar to $\cos x$ and may to a good first approximation be replaced by $\cos x$.

In order to increase resonance escape in low-enrichment uranium reactors, the fuel is sometimes segregated from the moderator. Fast neutrons, released by fission in the fuel, have a high probability of escaping into the moderator, where they are quickly slowed down without exposure to resonance absorption in U^{238}. In the O.R.N.L. graphite reactor this result is achieved by use of metallic fuel rods about 1 in. in diameter arranged in an 8-in. square array in a matrix of graphite. The fuel has negligible moderating properties; neutrons are "thermalized" almost entirely in the graphite and diffuse thence back into the fuel, there causing further fissions. As a result, there is a local gradient in the flux density both in the moderator and in the fuel superimposed on the gross flux distribution of Equation (20). Some reactors, which are heterogeneous from a phase standpoint, such as the M.T.R., are really homogeneous from a nuclear standpoint, there being negligible local gradients in the neutron flux in the moderator and fuel.

Neutron-diffusion theory has been employed in the calculation of thermal flux distributions in fuel elements in heterogeneous reactors (7). The basic equation is

$$D\nabla^2\phi_n(th, \rho) - \Sigma_a\phi_n(th, \rho) + S_n(th, \rho) = \partial n/\partial t$$

where n is the number of thermal neutrons per cubic centimeter, S_n is the volume source of thermal neutrons (due to slowing down of fast neutrons) in neutrons per cubic centimeter per second, D is the neutron-diffusion coefficient, Σ_a is the neutron-absorption coefficient (the so-called "macroscopic" absorption cross section), and t denotes time. In the steady state $\partial n/\partial t$ is zero; in the fuel S_n is zero. The solution, in polar coordinates (corresponding to the case of an infinitely long fuel rod immersed in a uniform external flux), is

$$\phi_n(th, \rho) = BI_0[\rho(\Sigma_a/D)^{1/2}] \qquad (23)$$

where ρ is the distance from the axis of the fuel rod and B is an arbitrary constant whose magnitude is proportional to the power level at which the reactor is operating and which may be evaluated by multiplying the gross flux distribution, $f(r)$ of Equation (20), by the local variation $\phi_n(th, \rho)$ and proceeding through the operations indicated in Equation (22) to evaluate the product $AB\phi_n(th, o)$ in terms of Q_f.

Using Equation (23), Alexander (2) calculated the temperature distribution in fuel rods and plates and compared the results with temperature distributions calculated from flux distributions measured experimentally by Woods and Biehl (24). As expected, the agreement is only fair, since diffusion theory applies poorly in cases where the neutron mean free path is appreciable compared with the dimensions of the system being studied.

In the design of fuel elements it is customary and conservative practice to assume that all the fission energy (200 mev./fission) is released in the fuel. In estimating heat release in moderator, coolant, pressure shell, and shield, however, it is necessary to estimate the leakage out of the fuel zone of energy associated with fast neutrons and gamma rays. A fair estimate of the fast-neutron spectral distribution as a function of position in the moderator of heterogeneous reactors employing long fuel rods may be had from the "Fermi age" treatment (7) of simple models, e.g., an infinite matrix of line sources with negligible capture of fast neutrons in U^{235} and U^{238} and only weak capture in the moderator. The flux at radius ρ from a single infinite line source of strength S_n nascent neutrons per unit length per unit time immersed in infinite moderator is given by

$$\phi_n(\rho, E_n) = \frac{1}{E_n\xi\Sigma_t} \cdot \int_{E_s=E_n}^{\infty} \frac{S_n P(E_s)p(E_s, E_n)\, dE_s}{4\pi\tau(E_s, E_n)} \cdot \exp\left[-\rho^2/4\tau(E_s, E_n)\right] \qquad (24)$$

where E_s is the energy of the nascent neutrons, $P(E_s)$ their spectral distribution, $p(E_s, E_n)$ the capture-escape probability, and $\tau(E_s, E_n)$ the Fermi age.

$$P(E_s) = 0.484(\sinh\sqrt{2E_s})\exp(-E_s)$$

$$p(E_s, E_n) = \exp\left(-\int_{E_n}^{E_s} \Sigma_a\, dE/\xi\Sigma_t E\right)$$

$$\tau(E_s, E_n) = \int_{E_n}^{E_s} D\, dE/\xi\Sigma_t E$$

Here ξ is the average logarithmic energy decrement of neutrons per collision; D is the diffusion coefficient; Σ_a and Σ_t are the absorption and total cross sections respectively.

The flux at any point in the moderator is constructed by summing the contributions given by Equation (24) for all line sources.

Alternatively the Monte Carlo technique (17) permits treatment of the spatial variation of the fast flux for the case of strong absorption in fuel, moderator, control elements and leakage out of the reactor, provided the fission-rate density in the fuel can be estimated by some means, e.g., by a multigroup diffusion calculation on a "homogenized" model of the core. In the Monte Carlo method the events in a neutron "life history" are selected by random sampling from an appropriate distribution. Initial neutron energies are selected from the fission-neutron spectral distribution, a flight direction is established, the coordinates of the first collision are found, kind of nucleus and type of collision are selected, postcollision neutron energy and new flight direction are determined. The history is followed until the neutron is absorbed or escapes from the reactor. The process is repeated until a sufficiently large number of cases has been obtained to permit a statistical analysis of the spatial and spectral distributions of the fast flux.

The technique is applicable to the calculation of fast fluxes in moderator, core vessels, shields, reflectors, thermal

shields, pressure shells, biological shields, etc. However, unless simplifications are introduced, especially geometric symmetries, the number of histories required may be excessive even for an electronic computer.

GAMMA-RAY–FLUX-DENSITY DISTRIBUTIONS

Compton scattering greatly complicates the estimation of gamma flux densities. The process is not isotropic and the energy decrement of the scattered photon is strongly dependent on the scattering angle. Photons scattered through small angles retain most of their original energy and may penetrate to remote regions of the reactor. Photons scattered through large angles suffer large energy losses, and their penetrating power is greatly reduced.

The important primary gamma sources are the fission process, the decay of fission fragments, neutron captures, inelastic-scattering collisions of neutrons. Compton scattering is the most important secondary source. At many points of interest, indeed at most, the contribution to the gamma flux made by scattered photons is many times greater than that of unscattered photons.

In principle, the gamma flux may be constructed by integration over the gamma sources. The vector coordinates of a point in the reactor may be denoted by r and the gamma flux density in photon centimeters per second per cubic centimeter per mev. by $\phi_\gamma(E_\gamma, r)$, r' denotes another point in the reactor, a volume increment about r' is denoted by dV_γ', and the total gamma source strength in photons per second per centimeter at r' is denoted by $S_\gamma(r')$. $P(E_\gamma, r')\ dV_\gamma'$ may be considered the conditional probability that a photon will be emitted from, or scattered out of, dV_γ' per mev. with energy E_γ. $P(r', r)$ may be considered the probability that the photon will be emitted per steradian in the direction of r. The probability that a photon per centimeter of travel will be removed from the beam, denoted by $\mu_t(E_\gamma)$, is simply the sum of the probabilities of the photoelectric, pair-production, and Compton-scattering collisions.

$$\mu_t(E_\gamma) = \mu_{pe}(E_\gamma) + \mu_{pp}(E_\gamma) + \mu_c(E_\gamma) \quad (25)$$

The probability $P(r' \rightarrow r)$ that a photon will arrive uncollided at r is thus simply (in homogeneous, isotropic media)

$$P(r' \rightarrow r) = \exp\left[-\mu_t(E_\gamma)(|\, r' - r\,|)\right]$$

where $|r' - r|$ denotes the scalar distance between r' and r. It follows that

$$\phi_\gamma(E_\gamma, r) = \int_{V_\gamma} S_\gamma(r') P(E_\gamma, r')\ dV_\gamma' \cdot P(r', r) \exp\left[-\mu_t(E_\gamma)(|\, r' - r\,|)\right] \quad (26)$$

The primary gamma sources are isotropic, and for these $P(r', r)$ has the value of $\frac{1}{4}\pi$ per steradian. In the case of the scattered-gamma source, $P(r', r)$ is a complicated function of the "directed" gamma flux $\phi_\gamma(E_\gamma, \vec{\Omega}, r')$, which is defined as the gamma flux at r' contributed by photons of energy E_γ moving in the direction $\vec{\Omega}$. It has units of photon-centimeter per second per cubic centimeter per mev. per steradian. Thus the construction of the flux $\phi_\gamma(E_\gamma, r)$ at r requires a knowledge of the more complicated flux $\phi_\gamma(E_\gamma, \vec{\Omega}, r')$ everywhere else. Consequently, a general formulation of $\phi_\gamma(E_\gamma, r)$ does not seem feasible.

The Monte Carlo technique may be applied to this problem (*17*). Suppose the histories of a sufficient number of primary photons of energy E_γ' are determined to define $F(E_\gamma'; r' \rightarrow r)$ identified as the average fraction of the energy E_γ' of photons originating at r' that is dissipated at r per cubic centimeter. The heating rate is now readily formulated as follows:

$$G_\gamma = \int_{V_\gamma} \int_{E_\gamma'=0}^{\infty} S_{p\gamma}(r')\ dV_\gamma' \cdot P(E_\gamma')\ dE_\gamma'\ E_\gamma' F(E_\gamma'; r' \rightarrow r) \quad (27)$$

where $S_{p\gamma}(r')$ is the primary gamma-source strength.

In principle, $F(E_\gamma'; r' \rightarrow r)$ may be evaluated for any case howsoever complicated in geometry or heterogeneity, but the sheer magnitude of the computational labor may render the method impractical. The simplest case is that of an infinite, homogeneous, isotropic medium. Life histories are generated in the usual manner and an account is kept of the amount of heat liberated and of the radial distance R of each collision from the point of origin. From these data it is easy to calculate the fraction $f(E_\gamma', R)\ dR$ of the energy E' of the original photons that is released inside a spherical annulus of radius R and thickness dR. The volume of such an annulus is $4\pi R^2\ dR$, from which it follows that $F(E_\gamma'; r' \rightarrow r)$ is given by

$$F(E_\gamma'; r' \rightarrow r) = \frac{f(E_\gamma', |\, r' - r\,|)}{4\pi(|\, r' - r\,|)^2} \quad (28)$$

A general solution of the foregoing case has been obtained by Goldstein and Wilkins (*8*) along lines laid down by Spenser and Fano (*21*). Briefly, the method consists in expanding the directed flux $\phi_\gamma(E_\gamma, \vec{\Omega}, r)$ in a series the terms of which are products of Laguerre and Legendre polynomials. The directed flux is integrated with respect to all directions to remove the angular dependency, then multiplied by the distance from the origin raised to integral powers. The product is integrated over all space to express the spatial dependence in terms of the "moments" of the flux, which are then used to evaluate the arbitrary coefficients in the original series in the usual way by application of the boundary conditions and utilization of the orthogonal properties of the Legendre polynomial. Having constructed the flux $\phi_\gamma(E_\gamma', r)$ due to a monoenergetic unit point source (1 photon/sec. of energy E_γ') at r', Goldstein then computes the fraction of the energy E_γ' released at r. This of course is identical with $F(E_\gamma', r' \rightarrow r)$ defined above. The results are reported in terms of an energy absorption build-up factor $B_a(E_0, \mu_0 r)$, where E_0 is E_γ' in the notation used here, μ_0 is $\mu_t(E_\gamma')$, r is $|r' - r|$, and B_a is defined in such a way that

$$F(E_\gamma', r' \rightarrow r) = \frac{B_a(E_\gamma'; |\, r' - r\,|)}{4\pi(|\, r' - r\,|)^2} \mu_e(E_\gamma') \cdot \exp\left[-\mu_t(E_\gamma')(|\, r' - r\,|)\right] \quad (29)$$

Here μ_e is the energy absorption coefficient defined by Equation (19). Values of B_a as a function of E_γ' and $|r' - r|$ are tabulated for a variety of materials by Goldstein (*8*). Taylor (*22*) has proposed an empirical correlation exponential in $|r' - r|$ which is conveniently applied to problems in gamma heating in pressure shells and thermal shields (*1*).

Conceivably the function $F(E_\gamma', |r' - r|)$ could be evaluated experimentally. Small radiation sources of various energies could be moved about in a mock-up of the system under study and the heat liberation at various points of interest measured. If a direct thermal measurement is made, the measuring instrument would have to be extremely sensitive or else the radiation-source strength would have to be inconveniently large.

The mathematical difficulties in estimating gamma heating may be considerably reduced, albeit at an unknown cost in accuracy, if one is willing to utilize the straight-ahead-scattering approximation, investigated carefully by Hurwitz, et al. (*13*). The assumption is made that photons suffer energy degradations but that the scattered photons fall into one of two classes: (*a*) photons scattered through such small angles that the deviations from the line of flight may be ignored and (*b*) photons scattered through such large angles that the resulting low-energy photons have little penetrating power (high μ_t) and are absorbed near the point of scattering. These assumptions depend upon the following arguments: (*a*) the energy distribution of the scattered photons shows a strong forward component, (*b*) the angular distribution also shows a strong forward component, (*c*) distances of interest in heat-generation calculations are measured in relatively few attenuation lengths from the primary source (and the probability

Table 2. Primary Energy Sources

Source	Energy, mev./fission	Spectral distribution	Ref.
Fission fragments	168 ± 5	———	11
Fission-fragment beta decay	7	———	23
Fast neutrons	5	$P(E_n) = 0.484 (\sinh \sqrt{2E_n}) \exp(-E_n)$	18
Prompt fission gammas	7.5	$P(E_\gamma) = \exp(-E_\gamma)$	6
Fission-fragment gamma decay	6	Fragmentary data	4, 16, 25
Capture gammas	varies, ~7	Fragmentary data	15
Total	200		

that a photon will suffer many scatterings is small), and (*d*) photoelectric absorption increases strongly with decreasing photon energy. For example, of the photons scattered out a beam of 6 mev. photons, those scattered through angles of less than 50° carry 90% of the energy of all the scattered photons.

The approximation is applied by breaking the gamma-source spectrum into a number of energy groups. The group having the highest energy E_1 is attenuated between r' and r by the simple exponential factor $\exp[-\mu_t(E_1')(|r' - r|)]$. The next group loses photons in proportion to $\mu_t(E_2')$ but gains photons from group 1 by Compton scattering; group 3 receives photons from both groups 1 and 2; and so on. The transfer of photons between groups is a function of the energy-widths of the groups and their separation in energy and is computed from the Klein-Nishina relation [Equation (14)]. The differential equations expressing the photon "economy" for each group are integrated successively, giving the flux at r.

Hurwitz, using this multigroup technique, has calculated the energy release at r due to an energy-distributed source at r' having a typical spectrum and found that the results could be expressed in terms of an average "effective" gamma-absorption coefficient $\bar{\mu}_{eff}$, obtained by averaging μ_{eff} over the spectrum of the source.

$$\bar{\mu}_{eff} = \int_{0.5}^{\infty} \mu_{eff}(E_\gamma')P(E_\gamma')\, dE_\gamma' \quad (30)$$

where $P(E_\gamma')$ is the spectral distribution and where

$$\mu_{eff}(E_\gamma) = \mu_e(E_\gamma) + \mu_c'(E_\gamma)$$

Here μ_c' is a term added to the energy-deposition coefficient μ_e to account for the energy release due to gamma photons scattered to energies below 0.5 mev., which are assumed to be absorbed in the near vicinity of their scattering. It is evaluated by integrating the scattered-energy ratio E_γ'/E_γ given by Equation (12) with respect to the angular probability given by Equation (14) as follows:

$$\mu_c'(E_\gamma) = \int_{\theta=0}^{\theta(E_\gamma'=0.5)} (E_\gamma'/E_\gamma)P(\theta)\, d\theta \quad (31)$$

By use of the present notation Hurwitz's results may be put in the form

$$G_\gamma(r) = \int_{V_\gamma} \frac{S_{p\gamma}(r')\, dV_\gamma\, \bar{E}_\gamma \bar{\mu}_{eff}}{4\pi(|r' - r|)^2} \cdot \exp[-\bar{\mu}_{eff}(|r' - r|)] \quad (32)$$

Primary Gamma Sources

The fission gamma and fission-fragment-decay gamma sources are both proportional to the fission density in stationary fuel reactors.

$$S_{p\gamma}(r') = N_\gamma \int_0^\infty \phi_n(E_n, r')\Sigma_f(E_n, r')\, dE_n \quad (33)$$

where N_γ is the number of photons, fission and decay, emitted per fission. Gamble (*6*) reports that 7.5 prompt gamma photons are released per fission, and that these have an average energy of about 1 mev. each. Their spectral distribution is approximately exponential.

$$P(E_\gamma) = \exp(-E_\gamma); \quad 0.1 < E_\gamma < 7 \text{ mev.} \quad (34)$$

This relation does not hold at the extremes of the energy range; however, the contribution from photons with energy above 7 mev. is negligible, while gammas emitted with energies less than 0.1 mev. carry less than 1% of the total energy.

The fission-fragment-decay gamma spectrum could be constructed from a knowledge of the fission yields of the various nuclides, their decay schemes, and the energies of the decay gammas. Moteff (*16*) and Clark (*4*) have tabulated the available data. Moteff listed some nuclides which emit gammas with energies down to 0.04 mev., with half-lives in excess of 30 sec. Clark extended the listing but did not tabulate gammas having energies below 0.1 mev. The sum of the gamma energies of all the nuclides reported was computed by Clark to be a little greater than 1 mev./fission. Since it has been estimated by Way (*23*) on theoretical grounds that the total fission-fragment gamma-decay energy is approximately 6 mev., it appears that there is about 4 to 5 mev. of energy/fission released by gamma emitters having half-lives shorter than 30 sec. The intensity and spectral distribution of the gammas from these short-lived isotopes is currently being investigated at Oak Ridge National Laboratory (*25*).

Day (*5*) has recently tabulated the available data on the cross sections for inelastic scattering of neutrons in various media and the spectra of the resulting gamma photons. Grace et al. (*9*) report some measurements on the scattering of 2.5-mev. neutrons in various materials. Other papers relating to the inelastic scattering of neutrons are listed by Day.

Mittelman (*15*) has tabulated the information available on the spectrum of capture gamma rays as of October, 1953. The strength of this gamma source is proportional to the local neutron flux and to the capture coefficient Σ_c. Equation (33) may be used by replacing Σ_f by Σ_c.

SUMMARY

The local rates of heat release in nuclear reactors have been formulated in terms of the local neutron and gamma fluxes. Certain special methods of estimating these fluxes were indicated and their application to the heating problem was discussed briefly. The data available on neutron- and gamma-source strengths have been reviewed.

There are four and possibly five important sources of heat the distribution of which is directly dependent on the neutron flux distribution. These are (1) fission-fragment energy, (2) fission-fragment beta-decay energy, (3) elastic collisions of fast neutrons, (4) beta decay of nuclei activated by neutron absorption, and (5) inelastic collisions of fast neutrons. Of these, sources 1 and 2 predominate in the fuel region of the heterogeneous reactors; 4 is small but may be appreciable; and 3 and 5 are negligible. In the moderator regions of such reactors, 1, 2, and 5 are negligible, and only source 3 and gamma heating need be considered. In core tanks composed of materials having high atomic numbers, gamma heating will predominate, but source 4 and possibly 5 may be appreciable. This rule applies also to thermal shields and pressure shells. Reflectors composed of materials of low atomic weight may be treated like the moderator and, if the atomic number is high, like a core tank.

Of the sources listed, sources 3 and 5 depend strongly on the distribution of the fast flux; the others may be computed to good approximations from the thermal flux densities.

The gamma-dependent heating rates are conveniently classified according to the source of the gamma rays: (1) prompt fission gammas, (2) fission-fragment-decay gammas, (3) capture gammas, (4) activated-nuclei-decay gammas, and (5) gammas resulting from inelastic scattering of fast neutrons.

In the fuel regions of heterogeneous reactors, heating due to gammas may be appreciable but is small compared with fission-fragment heating. Heating due to class 4 gammas may become appreciable if large amounts of U^{238} or Th^{232} or other material having high cross section for thermal neutrons are present. In the moderator regions of heterogeneous reactors, heating due to

classes 1 and 2 predominates, but contributions from class 3 may be appreciable in regions adjacent to coolants and structural materials having appreciable capture cross sections. In core tanks composed of materials having low capture cross sections, classes 1 and 2 predominate, but 5 may be appreciable, as in zirconium. In iron thermal shields and pressure shells classes 1 and 2 tend to predominate near the inner surface, class 3 at intermediate depths, while class 5 predominates at greater depths (*26*). Class 4 follows class 3 in distribution, but is much less important and can generally be neglected.

ACKNOWLEDGMENT

The encouragement and assistance of F. C. VonderLage, Director of the Oak Ridge School of Reactor Technology, are gratefully acknowledged, as are the comments and suggestions of E. P. Blizard, M. W. Rosenthal, Carl Copenhaver, J. Davis, R. K. Osborn, and others.

NOTATION

B_a = energy-absorption build-up factor, defined by Equation (29), and tabulated in reference *8*.

D = neutron-diffusion coefficient, reference *7*

E = kinetic energy of particle, mev.

E_f = average kinetic energy of fission fragments plus average energy of betas resulting from decay of fission fragments, 187 mev./fission

E_s = energy of nascent neutrons

$f(r)$ = geometric form of neutron-flux-density distributions.

$f(E_\gamma', R)$ = fraction of energy of photon emitted at a point with energy E_γ' that is dissipated in an annular sphere of radius R and thickness dR.

$F(E_\gamma', r' \rightarrow r)$ fraction of energy of photons emitted at r' with energy E_γ' that is dissipated at r per unit volume about r

G = specific rate of heat release due to dissipation of the energy of nuclear radiations, energy units per unit volume per unit time

I_0 = zero-order modified Bessel function of the first kind

m = atomic mass of neutron, $\sim$1 atomic mass units

M = atomic mass of nucleus in atomic mass units

(mc^2) = rest mass of electron. The value in mev. is about 0.51.

n = number of neutrons per unit volume

N_j = number of β particles of characteristic energy $E_{\beta j}$ emitted in decay chain following a neutron capture

N_γ = number of photons (prompt and decay) emitted per fission

$p(E_s, E_n)$ = capture-escape probability

$P(\theta)$ = probability that a neutron or photon will be scattered through an angle θ per unit angle about θ

$P(E_s)$ = spectral distribution of fission neutrons, reference *18*.

$P(E_\gamma, r')$ = probability that a photon having energy E_γ will be emitted or scattered at r', per unit volume about r'

$P(r', r)$ = probability that a photon emitted or scattered at r' will travel in the direction of r per stearadian about that direction

$P(r' \rightarrow r)$ = probability that a photon or neutron at r' traveling in the direction of r will arrive at r without having suffered a collision

$P(E_\gamma)$ = spectral distribution of gamma flux density or the fraction of photons having energy E_γ per unit energy range about E_γ

Q = rate of heat release in nuclear reactor, energy units per unit time

r = radius vector

S = source function, particles generated per unit volume per unit time

th = thermal energy, $\sim$0.025 ev.

V = volume throughout which particle sources are distributed

Greek

α = physical property of nucleus defined by Equation (6)

δ = average fraction of energy of incident particle that is released locally during a collison

θ = angle of deflection in a scattering collision

μ = photon interaction coefficient, probability of a collision of specified type occurring per centimeter of travel, events per photon-centimeter

$\bar{\mu}_{eff}$ = mean effective gamma-absorption coefficient, defined by Equation (30)

μ_a = photon energy-absorption coefficient defined by Equation (19)

μ_t = photon-absorption coefficient defined by Equation (25)

ξ = logarithmic energy decrement, $\xi \cong 2/(M + \frac{2}{3})$ (*See* reference *7*.)

ρ = radial coordinate in cylindrical geometry

Σ = macroscopic cross section, probability of a collision of specified type occurring per centimeter of travel, events per neutron-centimeter

τ = Fermi age, sq. cm.

ϕ = flux density, number of centimeters traversed by neutrons or photons per cubic centimeter per second

∇^2 = Laplacian operator

Subscripts and Superscripts

a = absorption

c = Compton scattering of photons or capture of neutrons

e = elastic scattering of neutrons (*See also* μ_s.)

f = fission (*Also see* E_f.)

ff = fission fragments

$ff\beta$ = beta particles resulting from beta decay of fission fragments

i = inelastic scattering

n = neutrons

N = nucleus

pe = photoelectric

pp = pair production

$p\gamma$ = primary gamma particles

t = total

β = beta particle

γ = gamma particle

$'$ = prime, denotes postcollision condition or energy

$-$ = superbar, denotes average value of variable

LITERATURE CITED

1. Alexander, L. G., *O.R.N.L.*-CF-55-4-150 (1955).
2. *Ibid.*, 10-118 (1955).
3. Bjorklund, F. E., *LRI*-84 (1954), classified.
4. Clark, F. H., *N.D.A.*-27-39 (1955).
5. Day, R. B., Paper 581, International Conference on Peaceful Uses of Atomic Energy (1955).
6. Gamble, R., and J. E. Francis, "Physics Div. Semiannual Progr. Rept.," p. 21, *O.R.N.L.*-1879 (1955).
7. Glasstone, S., and M. Edlund, "Elements of Nuclear Reactor Theory," D. Van Nostrand, New York (1952).
8. Goldstein, H., and J. E. Wilkins, *N.Y.O.*-3075 (1954).
9. Grace, M. A., et al., *Phys. Rev.*, **82**, 969 (1951).
10. Halliday, D., "Introductory Nuclear Physics," John Wiley and Sons, New York (1950).
11. Hanna, G. C., *C.R.R.*-489 (1951), classified.
12. Hollander, J. M., et al., "Reactor Handbook," Vol. 1, Chap. 1.2, Table of Isotopes, *A.E.C.D.*-3645, p. 158 (1953).
13. Hurwitz, H., Jr., et al., *K.A.P.L.*-753 (1952), classified.
14. Marinelli, L. D., et al., *Rev. Mod. Phys.*, **19**, 25 (1947).
15. Mittelman, P., *Nucleonics*, **13**, No. 5, 50 (1955).
16. Moteff, J., *A.P.E.X.*-134 (1953).
17. *N.B.S. App. Math. Ser.*, 12, Natl. Bur. Standards (1955).
18. Shapiro, M. M., "Reactor Handbook," Chap. 1.2, *A.E.C.D.*-3645, p. 68 (1953).
19. Shor, S. W. W., *N.P.*-1361 (1950).
20. Snyder, W. S., and J. L. Powell, *O.R.N.L.*-421, Supp. 1 (1952).
21. Spenser, L. V., and U. Fano, *Phys. Rev.*, **81**, 464L (1951).
22. Taylor, J. J., *W.A.P.D.*-R.M.-217 (1954).
23. Way, K., *MonP.*-192 (1946), classified.
24. Woods, D., and A. T. Biehl, *N.A.A.*-SR-138, Pt. I (1951), Pt. II (1953); private communication (1955), classified.
25. Peelle, R. W., O.R.N.L., private communication (1956).
26. Davis, J. P., Combustion Engineering, Inc., New York, private communication (1956).

Presented at the Nuclear Science and Engineering Congress, Cleveland.

Mass Transfer in Liquid Metals

W. E. DUNN, C. F. BONILLA, C. FERSTENBERG, and B. GROSS

Columbia University, New York, New York

The rate of mass transfer was measured for solid metal shapes dissolving into mercury at room temperature. Sherwood numbers for horizontal tin, cadmium, zinc, and lead cylinders dissolving by natural convection agreed with Nusselt numbers for heat transfer in nonmetallic liquids at the same Rayleigh (Grashof × Prandtl) numbers. Dissolving of zinc tubes by mercury flowing turbulently within them agreed with heat transfer to nonmetals in tubes. Dissolving of random beds of lead spheres by mercury flowing through the bed agreed with similar nonmetal systems. It is concluded that mass transfer processes in liquid metals follow substantially the correlations for other fluids in heat or mass transfer, which with moderate safety factors may thus be used for at least preliminary design purposes.

Cases of mass transfer in liquid metals are becoming more frequent with the increasing popularity of liquid metals as heat transfer media and as solvents. The pyrometallurgical refining of metals has long employed mass transfer between the melted metal and a molten flux, another molten metal, a solid, or a gas. Corrosion of pipes and vessels by contained liquid metals due to temperature differentials plus a variation of solubility with temperature has long been encountered. The purification of molten sodium by the freezing out of sodium oxide is a similar case. Finally, liquid-metal fuel reactors (L.M.F.R.) have been proposed (*20*) which feature mass transfer to accomplish principal objectives. Replenishment of the fissionable element would involve mass transfer, which, however, would be applied principally in the continuous removal of radioactive and neutron-consuming fission products.

In the design of such processes, or in predicting the effect on performance of changes in operating conditions, it is desirable to have available the appropriate dimensionless correlations of mass transfer for each proposed geometry. A few such correlations from studies on nonmetallic liquids have been published. However, before one could confidently employ such correlations for liquid metals it would seem desirable to establish their validity for liquid metals in at least several key geometries. This paper presents the results of such a study employing four binary systems and three rigid geometries. The solids were lead, tin, cadmium, and zinc, and the liquid phase was mercury at room temperature. Natural convection was studied by dissolving horizontal cylinders of all four metals in a stationary pool of mercury, the Grashof × Schmidt number product ranging from 10^7 to 10^9. Forced convection was studied by passing mercury through zinc pipes at Reynolds numbers of 1,200 to 12,000 and through fixed beds of randomly packed lead spheres at void Reynolds numbers of 20 to 1,000. In all cases the Schmidt number was of the order of magnitude of 100.

The differential equations for forced-convection mass transfer with constant physical properties (dilute solutions) are identical with those for heat transfer, provided that the Nusselt and Prandtl numbers in heat transfer are replaced by the Sherwood and Schmidt numbers for mass transfer. It would thus be expected, and has empirically been shown (*1*) *for nonmetals*, that heat transfer correlations obtained for any given geometry are applicable to mass transfer in the same geometry at the same Reynolds numbers when the foregoing replacements are made. Similarly, natural-convection mass transfer would be expected to follow the heat transfer correlations on further replacement of the fractional density change ($\beta\Delta T$) in the Grashof number by the analogous ($\beta_c\Delta c$) for the dissolving of the solute. It is thus additionally desirable to check whether liquid-metal mass transfer obeys the available heat transfer correlations for the same geometries at the same values of the analogous dimensionless ratios. It should be noted that liquid-metal heat transfer results are not helpful in predicting liquid-metal mass transfer because the range of Prandtl numbers for liquid metals is several orders of magnitude smaller than the Schmidt numbers of liquid-metal systems.

PHYSICAL PROPERTIES OF THE SYSTEMS

For reliable correlations it is necessary to employ accurate values of the pertinent physical properties. Thus all the properties were employed as functions of concentration for each solute metal and were taken at the arithmetic-mean film concentration $\bar{c}_f = (c_i + \bar{c}_b)/2$. In the natural-convection tests $\bar{c}_b$ was taken as the calculated instantaneous average concentration of the solute in the bath. In the forced-convection tests the inlet bulk concentration c_1 of solute metal was always zero, and $\bar{c}_f$ was taken as $(c_i/2) + (c_2/4)$.

The density and the coefficient of solution expansion of the amalgams were obtained from Richards (*16*), the viscosity from Von Schweidler (*17*), and the solubility from Hansen (*9*). These properties are all substantially linear over the range of interest and may be linearly interpolated over the concentration and temperature ranges of Table 1. The diffusivities of these amalgams at low concentrations have been tabulated by Furman and Cooper (*5*). These were corrected to the higher concentrations employed by means of the Eyring (*7*) relation:

$$\frac{(D_v)}{(D_v)_0} = 1 + \frac{d(\ln \gamma)}{d(\ln N)} \qquad (1)$$

The activity coefficient γ was obtained (*3*) as a function of atom fraction N from Richards' classic data (*16*) on the potentials of amalgam concentration cells. When the deviation between Richards' observed potential and that of an ideal cell, both having the pure solute metal as one electrode, is plotted against the logarithm of the other concentration, the slope multiplied by vF/RT equals $d(\ln \gamma)/d(\ln N)$ at the other concentration. The ratio $D_v/(D_v)_0$ so obtained is given in Figure 1. The results for zinc agree closely with Weischedel's experimental values (*18*), the only literature data that go to reasonably high concentrations in these systems.

NATURAL CONVECTION AT HORIZONTAL CYLINDERS

There are few, if any, mass transfer results in the literature for natural convection at horizontal cylinders. There

W. E. Dunn is with E. I. duPont de Nemours and Company, Wilmington, Delaware, C. Ferstenberg with E. I. duPont de Nemours and Company, Philadelphia, Pennsylvania, and B. Gross with Dugway Proving Grounds, Dugway, Utah.

Table 1. Physical Properties of Amalgam Systems Studied

Solute	wt. %	Viscosity, μ lb./(ft.)(sec.) × 1,000		Density, ρ, g./cc.		Diffusivity, D_s, sq. ft./(sec.)(10^5)		Schmidt No. ($\mu/\rho D_s$)		Solubility, wt. %		
		20°	30°	20°	30°	20°	30°	20°	30°	20°	25°	30°
Zinc	0	1.06	1.02	13.545	13.542	1.745	1.850	71.8	65.3			
	0.5	1.094	1.056	13.50	13.497	1.630	1.725	79.6	72.7			
	1.0	1.128	1.090	13.46	13.457	1.510	1.602	88.9	81.1	2.00	2.18	2.40
	1.5	1.162	1.124	13.42	13.417	1.396	1.480	99.4	90.8			
Tin	0	1.06	1.02	13.545	13.542	1.755	1.860	71.4	66.0			
	0.2	1.068	1.029	13.528	13.525	1.602	1.699	78.9	71.8			
	0.4	1.077	1.038	13.516	13.513	1.485	1.574	86.0	78.3	0.64	0.71	0.78
	0.6	1.085	1.046	13.504	13.501	1.404	1.488	91.7	83.5			
Lead	0	1.06	1.02	13.545	13.542	1.212	1.296	103.4	93.3			
	0.5	1.082	1.038	13.541	13.538	1.067	1.142	120.0	107.7			
	1.0	1.100	1.057	13.536	13.533	0.909	0.972	143.2	128.9	1.53	1.67	1.84
	1.5	1.116	1.075	13.532	13.529	0.848	0.907	155.8	140.6			
Cadmium	0	1.06	1.02	13.545	13.542	1.575	1.720	79.6	70.3			
	1	1.088	1.049	13.487	13.484	1.605	1.753	80.5	71.2			
	2	1.117	1.077	13.427	13.424	1.630	1.780	81.8	72.3	5.55	6.20	6.85
	3	1.143	1.106	13.369	13.366	1.653	1.806	82.8	73.5			

are, however, some heat transfer results for sizable cylinders (*12*) and also heat and mass transfer results for natural convection at vertical surfaces, which can be altered to apply roughly to horizontal cylinders by Hermann's conclusion (*10*) for streamline natural convection that the average heat transfer coefficient around a cylinder of diameter D is the same as over a vertical surface of height $2.5D$. For these reasons, plus the mechanical convenience of this shape, horizontal cylinders about ⅛ in. O.D. were selected for the experimental study of natural convection.

Natural convection is usually associated with streamline flow, and the correlations that have been proposed are given in Table 2. However, from heat transfer results with the same-sized cylinders (*12*) turbulence might be expected to initiate at $(Gr_m \times Sc) =$ about 10^6 and to start to raise the Sherwood number rapidly at about 10^7 or slightly higher.

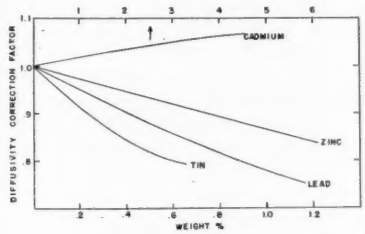

Fig. 1. Diffusivity correction factor for metals in mercury [Equation (1)].

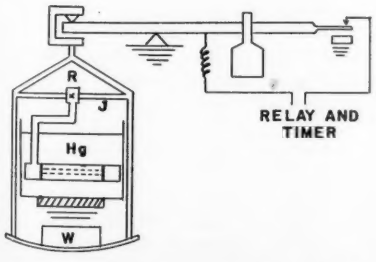

Fig. 2. Schematic diagram of apparatus for mass transfer from a horizontal cylinder by natural convection.

The equipment employed (*3*) is shown schematically in Figure 2. It consisted of a shock-mounted specific-gravity balance sensitive to 0.01 g. modified to support a wire frame. The frame by means of its ballast weight W held the specimen under the surface of the mercury and transmitted changes in the buoyant force to the balance arm. The arm was constrained by set screws to 1/64 in. of movement. An electronic relay indicated the instant that contact was made with the upper set screw.

A run was initiated by rotating the sample around J until it was immersed in the pool of mercury, tightening the set screw R, and setting the weight on the balance to a value slightly above the balancing point. When the sample had dissolved slightly, the buoyancy decreased, the balance arm rose, and, when the relay indicated contact, the time was recorded. The weight was immediately reset in successive small equal increments and the successive times were recorded. The rates of solution were then calculated over each time interval from the change of buoyancy. These rates decreased slowly and linearly with time t, and thus the initial rate of solution was obtained by extrapolation back to $t = C$, as shown in Figure 3*a*. Different driving forces were obtained by allowing solute metal to build up in the bath over a series of runs. After each series the mercury was completely purified by extended bubbling with air followed by sulfuric acid treatment to remove the gross impurity, with vacuum distillation for final purification.

The metal cylinders were prepared in two ways. Zinc and cadmium cylinders were machined down to size from slugs cast in glass. Tin and lead were extruded at 125°C. and upon cooling were cut off into sections. In all cases the ends were then faced off and an axial hole was drilled to hold the iron end pieces, rubber washers, test cylinder, and wire frame all together. All metals were C.P. or better quality. Castings of zinc were made under various cooling conditions to alter the grain size, but there did not appear to be a large variation in initial solution rate from this cause. However, for uniformity, all cast cylinders were allowed to cool slowly in the room.

Table 2. Streamline Natural-convection Mass Transfer Correlations for Horizontal Cylinders

Relation	Origin	Reference
$Sh = 0.53(Gr_m.Sc)^{1/4}$	Heat transfer tests at horizontal cylinders	*12, 13*
$Sh = 0.53[Gr_m.Sc^2/(0.952 + Sc)]^{1/4}$	Heat transfer tests at horizontal cylinders	*12*
$Sh = 0.418(Gr_m.Sc)^{1/4}$	Pohlhausen's theory for vertical plates, with Hermann's modification	*19*
$Sh = 0.525(Gr_m.Sc)^{1/4}$	Wilke's mass transfer tests at vertical plates with Hermann's modification	*19*
$Sh = 0.522(Gr_m.Sc)^{1/4}$	Ostrach's theory for vertical plates at $Sc = 100$, with Hermann's modification	*15*

Note: If the physical properties vary over the boundary layer, as a first approximation they should be taken at its arithmetic-mean concentration.

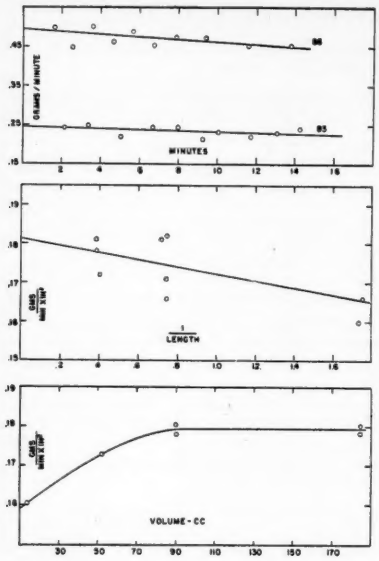

Fig. 3. Effect of time, sample length, and bath volume on the rate of buoyancy decrease of horizontal cylinders in still mercury.

Zinc chill-cast in steel molds, electroplated, or commercially remelted and extruded yielded significantly lower solution rates, owing apparently to traces of iron picked up or to zinc oxide occluded by the metal.

Samples were preamalgamated by being dipped into dilute sulfuric acid to remove the oxide layer and then into mercury. The time elapsed between preamalgamation and the start of the run was found not to affect the rate of solution.

End effects were determined for the most rapidly dissolving metal, cadmium, by varying the length of the samples over the range of ½ to 2½ in. The initial rate of solution was found to increase roughly linearly as $1/L$ decreased, as shown in Figure 3*b*. A 5% increase was obtained by extrapolating to $D/L = 0$ from a cylinder with $D/L = \frac{1}{3}$. All results herein reported were accordingly corrected to the infinite cylinder values. This end-effect correction was assumed proportional to rate of solution. Thus for the more slowly dissolving systems the correction corresponding to cadmium at the desired L/D was decreased proportionally to the rate of solution of the metal, by weight.

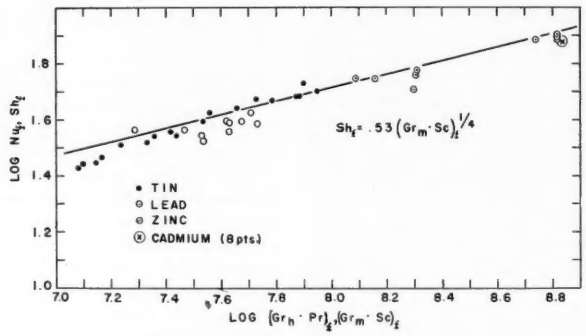

Fig. 4. Correlation of natural-convection mass transfer from horizontal cylinders.

The effect of ambient volume was studied with zinc cylinders. It was found that below 1 kg. of mercury the rate decreased (Figure 3*c*). The amount of mercury used in the runs here recorded was 29 kg., evidently equivalent to an infinite ambient.

One test was carried out to determine whether any appreciable temperature changes occurred at the dissolving surface owing to latent heat effects which might change the solubility c_i. A solid lead bar was bent and one end inserted in a bath of pure mercury and the other in mercury saturated with lead. A copper wire led from each bath to a potentiometer sensitive to 1 μv. The thermoelectric force of this system is roughly 5 μv./°C. There was never any detectable voltage, indicating negligible error due to dissolving.

Typical points are given in Table 3, and all the results are plotted in Figure 4 as the Sherwood number Sh vs. the Grashof number for mass transfer $Gr_m \times$ the Schmidt number Sc. It is seen that the results correlate well among themselves and agree nearly up to $Gr_m \times Sc = 10^9$ with the correlations of Table 2, which agree among themselves.

It should be noted that Sh agreed with the laminar correlations up to (at least) $Gr_m \times Sc$ values of almost 10^9, as contrasted with the observed rapid rise in Nu at $Gr_h \times Pr$ above 10^7, previously mentioned. However, visual inspection of the samples indicated that turbulence had been present at all but the lowest $Gr_m \times Sc$ values. All the zinc and cadmium specimens ($Gr_m \times Sc > 10^9$) showed a highly roughened surface after a test, probably in these cases an effect of crystal orientation. But all the tin and lead specimens—except the four tin specimens of lowest $Gr_m \times Sc$—showed a smooth lower surface but still displayed a roughened top surface (Figure 5*a*), probably because of turbulent eddies downstream of the cylinders. Figure 5*b* shows the smooth surface and "fish-tail" top edge, as might be expected in com-

Table 3. Mass Transfer by Natural Convection for Horizontal Metallic Cylinders in Mercury

Metal	Run	°C.	Initial diam. D, in.	L, in.	Initial rate, g./min.	Buoyancy factor, $\rho/\Delta\rho$	Initial bath conc., wt. %	Solubility, wt. %	End corr.	log Sh_f	log $(GrSc)_f$	Sc_f
Zn	59s	26.7	0.325	1.028	0.1321	1.113	0.000	2.27	1.032	1.464	8.817	80.4
	64	13.3	0.351	2.516	0.0275	1.113	0.957	1.74	1.003	1.709	8.297	97.9
	68	12.8	0.342	2.530	0.0189	1.113	1.236	1.73	1.002	1.748	8.159	101.9
Sn	40	14.5	0.211	1.512	0.0221	1.173	0.0084	0.560	1.003	1.540	7.356	90.5
	44	15.7	0.174	1.281	0.0213	1.173	0.0557	0.578	1.002	1.468	7.168	91.2
	48	15.0	0.350	2.519	0.0166	1.174	0.095	0.567	1.002	1.701	7.948	92.3
	52	14.8	0.293	2.119	0.0142	1.175	0.159	0.564	1.002	1.640	7.656	93.5
	56	15.9	0.350	2.485	0.0124	1.175	0.196	0.581	1.002	1.681	7.870	93.7
Pb	69	13.4	0.350	2.507	0.0581	5.135	0.000	1.290	1.007	1.625	7.709	138
	73	10.8	0.350	2.531	0.0396	5.137	0.1776	1.230	1.005	1.559	7.628	143
	77	11.7	0.350	2.525	0.0258	5.146	0.5390	1.246	1.003	1.563	7.468	149
Cd	80	12.8	0.350	2.523	0.181	1.767	0.000	4.62	1.023	1.882	8.844	83.5
	84	11.9	0.351	0.575	0.158	1.767	0.139	4.53	1.097	1.879	8.838	83.4
	88	13.3	0.348	1.386	0.175	1.767	0.200	4.68	1.039	1.882	8.832	82.3

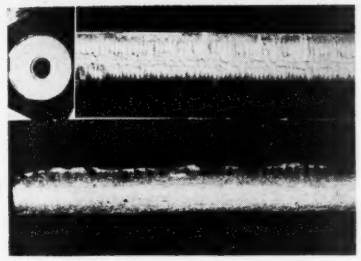

Fig. 5. (*a*) Appearance of top and cross section of horizontal tin cylinder after turbulent natural convection; (*b*) appearance of side of horizontal tin cylinder after streamline natural convection.

pletely streamline flow, which were obtained in the four lowest $Gr_m \times Sc$ tin samples*. These results thus indicate incidence of turbulence at $Gr_m \times Sc =$ 16,000,000 approximately, but no significant deviation from the streamline relation as far up as 650,000,000. There are thus qualitative agreement with the results so far reported for heat transfer to cylinders larger than wires and rough quantitative agreement on the point of incidence or turbulence. It is difficult to assess the significance of the disagreement on the threshold of turbulence and breakaway of the Nu and Sh values from the streamline relation. However, it seems established that laminar natural-convection correlations for any geometry and for either heat or mass transfer will hold for liquid-metal mass transfer in that geometry. It also seems probable, particularly in view of the turbulent forced-convection results to be discussed next, that agreement can also be expected, in general, between the corresponding turbulent natural-convection correlations.

FORCED-CONVECTION FLOW IN PIPES

For turbulent forced-convection flow through pipes, the classic Chilton-Colburn equation for heat transfer (*1*) when modified to mass transfer becomes

$$j_D = (k_D/u)(Sc)_f^{2/3} = 0.023(Re)_f^{-0.2} \qquad (2)$$

For the viscous region the Lévêque equation (*9*) when similarly modified becomes

$$j_D = 1.61(Re)_b^{-2/3}(L/D)^{-1/3} \qquad (3)$$

The only previous work on mass transfer inside of pipes that was found in the literature is that of Linton and Sherwood on the dissolving of cinnamic acid, benzoic acid, and β-naphthol tubes in water; Sc ranged from 1,000 to 3,000. Though the spread of the j_D values was considerable, the results agreed moderately well with Equations (2) and (3).

*Figure 5 illustrates the applicability of mass transfer tests in determining local heat transfer coefficients by measuring the rate of mass removal.

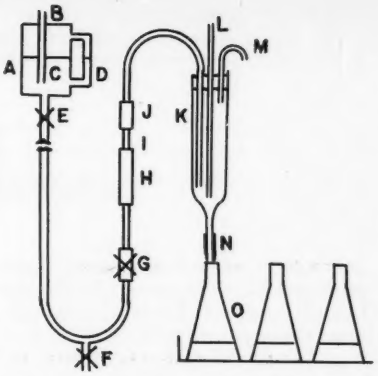

Fig. 6. Apparatus for mass transfer from a zinc tube to mercury.

Various studies on mass transfer wetted-wall columns have shown departures from Equation (2), but this might be expected owing to the motion of the liquid film. It is thus logical to compare liquid metal results in tubes with Equations (2) and (3). Zinc was used for the tubes in this study because it is stronger than the other convenient metals.

The zinc was approximately 99.995% pure, containing roughly equal amounts of bismuth, cadmium, copper, and lead as the principal impurities. After each run the mercury was placed in a suction flask under a layer of 50% sulfuric acid, and room air was bubbled through it from a submerged air-inlet tube by the application of vacuum on top. After an hour or so the acid was decanted and the mercury washed repeatedly with distilled water, trickled through a tall 15% nitric acid tower, washed again, dried in beakers at 120°C., and finally filtered slowly through a dry towel. A bright surface, indicating less than 0.0001% of base metal, was always obtained.

The test apparatus employed (*4*) is shown schematically in Figure 6.

Zinc rods were cast by melting the zinc in an iron crucible, sucking it up into preheated ½-in. Pyrex tubes, and then allowing it to freeze. The rods were cut into 2.1+ in. lengths, drilled through at their axis with an extralong 0.140-in. drill, turned at both ends to a concentric O.D. of 0.350 in., and faced off perpendicular to the axis to a length of 2.1 in. (15 diam.). These specimens (*I* in Figure 6) were forced into heavy-wall steel tubes *H* and *J* having a 0.140-in. bore and a flat-bottomed concentric cup 0.351 in. in I.D. at their nearer ends. Thus the steel-zinc-steel formed a continuous tube of smooth bore. The apparatus contained a closed 3.5-liter steel tank with an air inlet tube *B* to maintain the mercury flow constant during a run, a level gauge *D*, on-off cock *E*, drain pinch clamp *F*, flow-regulating screw clamp *G*, 50-diam.-inlet calming length *J*, glass receiver *K*, thermometer *L*, air vent *M*, and rubber pinch tube *N*. Before a run 30 ml. of 1 *M* hydrochloric acid (more than enough to dissolve the zinc) was added in advance to each of six to ten preweighed sample flasks *O* on a flask holder. A new specimen *I* was next filled and wetted internally with mercury to assure immediate action in the run. It was then inserted between *H* and *J* and the run started at once. Clamp *G* was preset as desired, *E* suddenly opened, and a stop watch started when mercury appeared at *N*. At the end of each preselected time increment (10 to 30 sec. in different runs) *N* was pinched off by hand until the next flask had been slid into position. After the run each flask was weighed to obtain the mercury weight and thus the average flow rate over the interval.

The zinc was dissolved in the hydrochloric acid by placing the flasks around the edge of an electric hot plate so that strong natural circulation occurred without boiling. The solution was completed when hydrogen evolution ceased and a film of HgCl appeared on the mercury on cooling. The solution and washings were collected, exactly neutralized with potassium hydroxide solution to the methyl red end point, and diluted to 1 liter in a volumetric flask, and a 10-cc. portion was diluted to 100 ml. with 0.1 *N* potassium chloride. This solution was then analyzed by either a manual or, preferably, an automatically plotting dropping mercury electrode, previously calibrated with six known solutions prepared from zinc and mercury in the same way. This was by far the most rapid method of analysis available and yielded reasonable accuracy.

For each interval of every run the following average quantities were calculated, corrections being made where pertinent for the change in average I.D. due to the weight of zinc dissolved up to the middle of the interval: diameter, mercury mass velocity, outlet concentration c_2, rate of solution w per unit wall area, mass transfer coefficient $k_D = w/(c_i - c_2/2)$, mass transfer factor j_D, and film concentration Reynolds number Re_f at $\bar{c}_f$. These values of j_D and Re_f computed over each interval were found to agree reasonably well with Equation (2), though averaging 11% higher (*4*). Plotting j_D and Re_f vs. the median time of the interval and extrapolating back to zero time yielded the points listed in Table 4 and plotted in Figure 7. The extrapolated points are slightly lower, as might have been expected because any roughening of the surface, as observed before in natural convection, would thus be eliminated. The average agreement with Equation (2) is accordingly slightly better. Linton and Sherwood found no difference between L/D values of 6 and 21. Therefore Equation (2) may be considered to apply well to liquid-metal turbulent mass transfer in pipes with fully developed velocity distribution for L/D ratios exceeding 6, and probably with adequate accuracy down almost to 0 L/D. Higher j_D values would be expected if the specimen lacked an inlet calming length. The one streamline run obtained agrees well with Equation (3)*, which may undoubtedly also be accepted for liquid metals.

FORCED-CONVECTION FLOW THROUGH PACKED BEDS

Several studies of mass transfer from packed beds to gases flowing through them have been carried out. In most

*This point is plotted against $(Re)_b$, 6.7% larger than $(Re)_f$.

studies the range of Schmidt number was rather limited, and so its effect was difficult to assess. Using the analogous mass transfer definition of j to that found (*1*) for heat transfer inside of tubes, Hougen and coworkers (*11*) have adopted $(Sc)^{2/3}$, as in Equation (2). Denton (*2*) deduced a slightly higher power of Sc, that is, 0.72.

Experiments with liquid solvents can cover much wider ranges of Sc and thus should be more reliable in yielding a general correlation. Gaffney and Drew (*6*) used beds of succinic and salicylic acid pellets of various quasispherical shapes dissolving in *n*-butanol, benzene, and acetone. They also took into account the β-naphthol–water data of McCune and Wilhelm (*14*). The total $(Sc)_f$ range thus covered was 160 to 13,000. Reasonable variations of fractional voids X in the bed were included in a single correlating curve by basing the Reynolds number on the average velocity in the voids, that is, by utilizing $(Re_p)_f/X$, where $(Re_p)_f$ is based on the superficial velocity V. The best exponent of $(Sc)_f$ was obtained as 0.58 and the final correlation is shown as the solid line in Figure 8. $(Re_p)_f/X$ ranged from 1 to 5,000 and D_p from 0.01 to 0.042 ft. It seems logical to compare any liquid-metal results with this correlation.

In this study (*8*) the mercury was purified after each run by agitating it with air in a Bethlehem Oxifier, allowing it to stand overnight, and running it through a Bethlehem gold disk "filter." The mercury was then tested with HNO_3 and $K_2Cr_2O_7$ solution as a check that the lead had been completely removed. The spheres were high-sphericity antimony-free No. 8 lead shot from National Lead Co. and No. BB from Remington Arms Co. and were 99.85% or higher in metallic-lead content. The shot was amalgamated within 30 min. before each run by being mixed with 1*N* HNO_3 and mercury and drained on a screen with the aid of a suction probe. The shot was weighed beforehand to compute the number for calculating surface area and porosity, but the average diameter was obtained by calipering a number of pellets after amalgamation.

The apparatus was similar to that of Figure 6 but employed a thick-walled gauge-glass column between end plates in place of items *H*, *I*, and *J*. The column had seven to ten horizontal thicknesses of 14- and 24-mesh 0.02-in. iron wire cloth at both top and bottom, to distribute the flow and to hold the bed compact by its elasticity. The procedure also was similar to that of the previous test. Five time intervals, usually of 10 sec. each, were employed in most runs. The sample flasks in this case contained 50 or 100 ml. (excess) of 50% by volume glacial acetic acid. After weighing, the flasks were loosely stoppered and gently shaken for over 6 hr. to dissolve the lead totally. The lead was determined gravimetrically in the solution and wash waters by the usual chromate method. The constant conditions of each run and the observed results are given in Table 5. In the last three runs, at low Re, the total change in average shot diameter was under 1%, and average results for the run are reported. Over the first three runs the change in average diameter was 6, 7, and 2% respectively, and all results reported were obtained by extrapolation back to zero time.

The number of transfer units N.T.U. was calculated as $c_2/(\Delta c)_{lm} = \ln [c_i/(c_i - c_2)]$, from which the height of a transfer

Table 4. Mass Transfer in Forced Convection of Mercury Through Zinc Tubes

Run	°C.	Tube length L, ft.	Initial diam. D, ft.	Sc_f	Initial solution rate, g./sec.	Solubility, wt. %	Initial efflux conc., wt. %	$j_D \times 10^3$	$(Re)_f$	Initial mass velocity G, lb./(hr.)(sq. ft.)
4	25.0	0.176	0.0120	83.9	20.6	2.18	0.0183	2.95	4,560	22,767
5	23.0	0.182	0.0120	83.1	70.0	2.11	0.0275	5.25	1,140	7,624
6	24.7	0.182	0.0118	82.6	53.6	2.17	0.0235	3.00	12,400	58,400
7	24.6	0.187	0.0119	82.7	36.5	2.17	0.0264	4.30	7,890	39,190
8	24.8	0.184	0.0117	82.5	14.5	2.18	0.0310	4.57	3,350	16,530
9	24.1	0.186	0.0117	82.7	48.6	2.15	0.0302	4.00	11,120	53,790
11	23.4	0.186	0.0118	83.1	37.5	2.13	0.0279	4.00	8,620	42,110

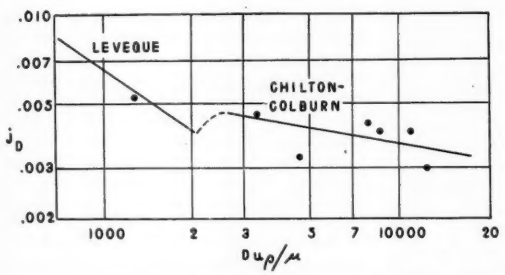

Fig. 7. Correlation of mass transfer in a tube with forced convection.

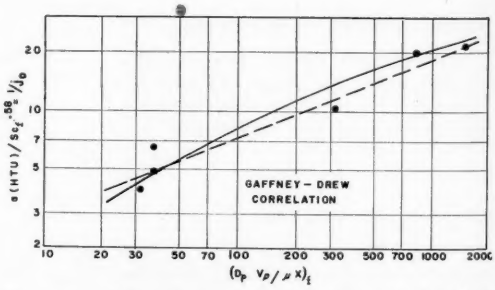

Fig. 8. Correlation of mass transfer from a bed of lead shot to flowing mercury.

Table 5. Mass Transfer in Forced Convection of Mercury Through Packed Beds of Lead Spheres

Run	°C.	Efflux conc., wt. %	Solubility, wt. %	Transfer units, N.T.U.	Bed ht., ft.	H.T.U., ft.	Superficial velocity V, ft./sec.	Fractional voids, X	Shot diam., in.	Bed diam., in.	Re/X	Sc_f	$1/j_D$	$\frac{D_c}{D_p}$	$\frac{H}{D_p}$
1	26.5	0.341	1.721	0.2215	0.164	0.740	0.0721	0.499	0.0825	0.76	820	124.1	19.8	9	24
2	27.8	0.346	1.771	0.2167	0.174	0.803	0.1246	0.486	0.0845	0.76	1498	123.5	21.5	9	25
3	24.0	0.571	1.642	0.428	0.156	0.364	0.0242	0.446	0.0853	0.76	314	127.0	10.2	9	22
4	29.7	1.255	1.833	1.155	0.223	0.193	0.00325	0.507	0.0840	1.02	36.9	133.2	4.82	12	32
5	29.5	1.527	1.829	1.805	0.510	0.283	0.00371	0.555	0.0807	1.02	36.7	136.3	6.53	13	76
6	29.1	1.444	1.813	1.593	0.512	0.321	0.00134	0.498	0.1721	1.43	31.5	135.7	3.95	8	36

unit H.T.U. is obtained as H./N.T.U. Then j_D by the Gaffney and Drew definition was computed as $(Sc)_f^{0.58}/(a$ H.T.U.), which equals $(k_D/V)(Sc)_f^{0.58}$. For consistency with usual practice, the physical properties are taken at $\bar{c}_f$ rather than $\bar{c}$, though Gaffney and Drew did not correct to $\bar{c}_f$.

The agreement between these results and the Gaffney and Drew correlation is seen in Figure 8 to be roughly within the accuracy of the results. The dashed line, which would be more convenient for mathematical manipulations and should be adequately reliable, at least for liquid metals from $(Re_p)_f/X$ of 20 to 2,000, has the equation

$$j_D = \frac{k_D}{V}(Sc)_f^{0.58} = \frac{(Sc)_f^{0.58}}{a \times \text{H.T.U.}} = 0.87\left(\frac{(Re_p)_f}{X}\right)^{-0.40} \quad (4)$$

No significant effect of column diameter D_c seems to be present. The points at the two highest D_c/D_p values (the two upper points at low Re/X in Figure 8) lie above a smooth curve through the other points, but that is opposite to the expected deviation. Thus these correlations should be suitable for D_c/D_p down to somewhat below 8 with reasonable accuracy. The beds were at least twenty-two particles thick, and the results should be applicable to any bed thicknesses above a few particles.

CONCLUSIONS

1. Experiments on the dissolving of horizontal metal cylinders by mercury in natural convection and of zinc tubes and beds of lead shot by mercury in forced convection agreed within the experimental uncertainty with the best available dimensionless correlations for mass transfer in nonmetals under the same conditions (Figures 4, 7, and 8 respectively).

2. The logical supposition that mass transfer in all liquid-metal systems follows the same correlations as in nonmetals is strongly corroborated.

3. Under all the conditions investigated, mass transfer in liquid-metal systems follows, within the experimental uncertainty, the same correlations as does heat transfer in nonmetals, provided that the analogous mass transfer quantities are substituted for the heat transfer quantities (Schmidt number for Prandtl number, Sherwood number for Nusselt number, and solution expansion for thermal expansion in the Grashof number).

4. A preliminary acid treatment and amalgamation is in general desirable to eliminate surface oxide films and to obtain immediate uniform wetting of base metals by mercury at room temperature; otherwise consistent mass transfer results are not obtained.

5. With well-wetted metal surfaces there is no surface or "chemical" transfer resistance in addition to the usual liquid-phase transfer resistance.

ACKNOWLEDGMENT

This study is contribution No. 63 from the Chemical Engineering Laboratories, Engineering Center, Columbia University and includes work carried out in the Department of Chemical Engineering, The Johns Hopkins University. Support by the Atomic Energy Commission under contract AT (30-1)1100 for parts of this study is gratefully recognized. The Belmont Metal and Smelting Company provided many of the metal samples used.

NOTATION

a = surface area per unit volume of packed bed, sq. ft./cu. ft.
c = concentration of solute, lb./cu. ft.
C = specific heat, B.t.u./(lb.)(°F.)
d = differential operator
D_v = diffusivity, sq. ft./sec. except where noted
D = diameter, ft.
F = the faraday, coulombs/g. equivalent
g = acceleration of gravity, ft./sec.²
h = heat transfer coefficient, B.t.u./(hr.)(sq. ft.)(°F.)
H = height of bed, ft.
H.T.U. = height of 1 transfer unit, ft.
k = thermal conductivity, B.t.u./(sq. ft.)(hr.)(°F.)
k_D = mass transfer coefficient, ft./sec.
L = length, ft.
N = atom fraction
N.T.U. = number of transfer units
R = the gas constant, joules/°R.
t = time
T = absolute temperature, °R.
u = average velocity, ft./sec.
v = valence
V = "superficial" velocity through a packed bed, ft./sec.
w = rate of solution per unit area, lb./(sec.)(sq. ft.)

Greek Letters

β = coefficient of thermal expansion, °F.$^{-1}$
β_c = coefficient of volumetric expansion due to solution, cu. ft./lb.
γ = activity coefficient of a solute
Δc = concentration driving force, lb./cu. ft.
ρ = density, lb./cu. ft.
μ = viscosity, lb./(ft.)(sec.) or lb./(ft.)(hr.), as required in the dimensionless ratio

Dimensionless Groups

Gr_h = Grashof number for heat transfer $(D^3g\beta\Delta T\rho^2)/\mu^2$
Gr_m = Grashof number for mass transfer $(D^3g\beta_c(c_i - c)\rho^2)/\mu^2$
j_D = j factor for mass transfer, $Sh(Sc^{1/3}Re)^{-1}$
Nu = Nusselt number hD/k
Pr = Prandtl number $C\mu/k$
Sc = Schmidt number $\mu/\rho D_v$
Re = Reynolds number $Du\rho/\mu_{(pipes)}$ or $D_pV\rho/\mu X$ (packed beds)
Sh = Sherwood number k_DD/D_v
X = fractional voids

Subscripts

b = ambient or bulk average
c = column
f = film
h = heat transfer
i = interface
m or D = mass transfer
p = packing particles
0 = zero solute concentration
1 = inlet stream
2 = outlet stream

LITERATURE CITED

1. Chilton, T. H., and A. P. Colburn, *Ind. Eng. Chem.*, **26**, 1183 (1934).
2. Denton, W. H., "General Discussion on Heat Transfer," British Sect. IV, p. 29, Inst. Mech. Eng., London (1951).
3. Dunn, W. E., Jr., Ph.D. dissertation, Johns Hopkins Univ., Baltimore, Md. (1950).
4. Ferstenberg, C., M.S. thesis, Columbia Univ., New York (1951).
5. Furman, N. H., and W. C. Cooper, *J. Am. Chem. Soc.*, **72**, 5667 (1950); **74**, 6183 (1952).
6. Gaffney, B. J., and T. B. Drew, *Ind. Eng. Chem.*, **42**, 1120 (1950).
7. Glasstone, S., K. J. Laidler, and H. Eyring, "The Theory of Rate Processes," McGraw-Hill Book Company, Inc., New York (1941).
8. Gross, B., M.S. thesis, Columbia Univ., New York (1953).
9. Hansen, M., "Der Aufbau der Zweistofflegrerungen," Julius Springer, Berlin (1936).
10. Hermann, R., *Z. angew. Math. Mech.*, **13**, 433 (1933).
11. Wilke, C. R., and O. A. Hougen, *Trans. Am. Inst. Chem. Engrs.*, **41**, 445 (1945); Gamson, B. W., G. Thodos, and O. A. Hougen, *loc. cit.*, **39**, 583 (1943).
12. Hyman, S. C., C. F. Bonilla, and S. W. Ehrlich, *Chem. Eng. Progr., Symposium Series* No. 5, **49**, 21 (1953).
13. McAdams, W. H., "Heat Transmission," 3d ed., McGraw-Hill Book Company, Inc., New York (1954).
14. McCune, L. K., and R. H. Wilhelm, *Ind. Eng. Chem.*, **41**, 1124 (1949).
15. Ostrach, S., *Natl. Advisory Comm. Aeronaut. Tech. Note* 2645 (February, 1952).
16. Richards, T. W., *Carnegie Inst. Wash. Publ. No.* 118 (1909).
17. Von Schweidler, A., *Sitzber. Akad. Wiss. Wien, Math. naturw. Kl.*, 2A BD, 104 (1895).
18. Weischedel, F., *Z. phys. Chem.*, **85**, 29 (1933).
19. Wilke, C. R., C. W. Tobias, and M. Eisenberg, *Chem. Eng. Progr.*, **49**, 663 (1953).
20. Williams, C., *et al.*, *Nucleonics*, **12**, No. 7, 11 (July, 1954); *Chem. Eng. Progr. Symposium Series* No. 12, **50**, 153 (1954).

Presented at Nuclear Science and Engineering Congress, Cleveland.

Continuous Dissolution of Uranium-aluminum Reactor Fuels

A. F. BOEGLIN, J. A. BUCKHAM, I. CHAJSON, R. B. LEMON, D. M. PAIGE, and C. E. STOOPS

Phillips Petroleum Company, Idaho Falls, Idaho

Extensive pilot plant studies of the continuous, mercury-catalyzed nitric acid dissolution of uranium-aluminum alloy materials similar to possible reactor fuel elements were carried out. Marked differences were observed in the dissolution rates of cast and wrought alloys. Optimum feed-acid concentrations varied with the type of alloy. At constant acid feed conditions dissolving rates varied approximately with the cube root of catalyst concentration up to a limiting concentration. The metal dissolving rate was proportional to the 0.8 power of the nitric acid feed rate. A general empirical correlation was developed.

Nuclear reactor fuels are periodically processed to separate the fissionable material from alloying elements and from fission products which may "poison" the reactor if they are not removed. Many reactors use uranium-aluminum–alloy fuel elements of various compositions and shapes, the spent fuels being processed by batchwise mercury-catalyzed dissolution in nitric acid followed by separation of uranium from aluminum and fission products by solvent extraction. It was anticipated that operating simplifications could be achieved by continuous, as opposed to batch, dissolution. Consequently, extensive pilot plant studies of the continuous dissolution of uranium-aluminum alloys containing up to about 10 wt. % uranium were undertaken. Data and correlations are given for the portion of these investigations pertaining to the important process relationships in continuous dissolution.

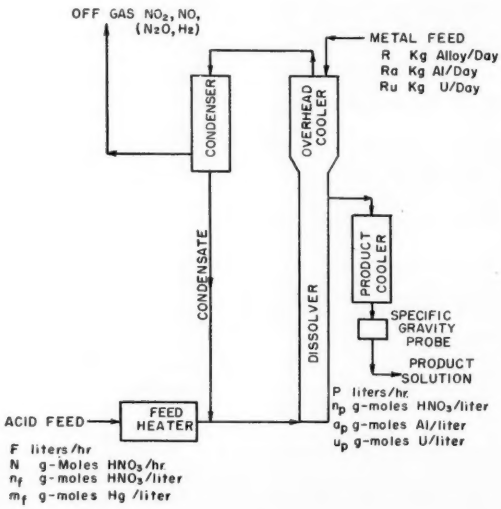

Fig. 1. Schematic drawing of continuous dissolver.

TEST EQUIPMENT AND MATERIALS

The continuous dissolver used in the experimental work was a tall 2-in. I.D. type-347 stainless steel pipe with a cooling section at the top. This overhead cooling section and a down-draft condenser of standard design were used to condense the steam in the off-gas rising from the dissolver solution. The acid feed was continuously steam heated to near-boiling temperatures; the product was water cooled and then collected in a stainless steel drum placed on a platform scale. The acid feed rate was controlled with a rotameter and measured by liquid-level readings on the feed tank. Instrumentation for measuring the feed and product specific gravities and temperatures at various locations was available.

The reactor fuel material to be dissolved was simulated by using cylindrical slugs about 1½ in. in diameter and 8 in. long. Although not representative of M.T.R.-type fuel plates, in that the surface-to-volume ratio of such bars is much lower than that of plates, this form of material was a convenient and economical choice. Extruded 2S aluminum-bar stock and cast and extruded uranium-aluminum–alloy slugs were used in the experimental work. The slugs were loaded periodically through a pair of gate valves located at the top of the dissolver.

GENERAL CONCEPTS

A schematic diagram of the continuous dissolver and the important auxiliary equipment is shown in Figure 1. The symbols defined on this diagram represent the important process variables and are used throughout this paper.

The nitric acid solution and mercuric nitrate catalyst solution (a separate

stream if so desired) are fed at the bottom of the dissolver, and uranium-aluminum slugs are charged intermittently into the top of the vessel. The acid dissolves the slugs as it flows countercurrent to the bed of metal, and the product solution is withdrawn through an overflow pipe. At constant feed rates for slugs, acid, and catalyst the metal level will seek an equilibrium value, and a steady dissolution rate and uniform product composition should be obtained. The system is then inherently stable in that minor process fluctuations will be compensated by changes in the slug level and, hence, the surface area available for dissolution.

When slugs are added at the desired dissolution rate, the equilibrium metal level is dependent upon the quantity of acid fed and the catalyst concentration. The amount of acid fed may differ from that stoichiometrically equivalent to the metal feed rate, and the extent of this difference will be reflected in the product composition. Hence the acid feed rate required for a given dissolution rate is determined by the product composition needed for satisfactory performance in the subsequent process steps. The concentration of the acid in the feed also restricts the product composition to definite ratios of aluminum, uranium, and acid concentration. The mercuric-ion (catalyst) concentration in the feed might also be expected to affect the reaction kinetics. The effects of these three parameters (acid feed rate, feed acid concentration, and catalyst concentration) on dissolution rate are the most important dissolver process relationships that were investigated.

DISSOLVER PROCESS RELATIONSHIPS

General Discussion

In a correlation of the effects of the process variables aluminum dissolving rate R_a (kg./24-hr. day) has been used as the major parameter. This quantity has been selected because it links results obtained with the specific uranium-aluminum alloy used in the experimental work with quantities predictable for alloys of other compositions. The alloy used in this work was approximately 10 wt. % uranium, or about 99 mole % aluminum, and so the reaction is essentially the dissolution of aluminum. In order to obtain the uranium dissolving rates for an alloy of similar composition and metallurgical characteristics from the aluminum dissolving rates presented in the subsequent correlations, one need only multiply by the ratio of percentage of uranium to percentage of aluminum.

The product nitric acid concentration is used in all correlations as an index of product composition. This property is related to the aluminum concentration by stoichiometry and can be readily converted by use of the relationships discussed below.

Stoichiometry

A general discussion of the material-balance relationships and the reaction stoichiometry will clarify subsequent correlations of the effect of each of the process variables.

Samples of the continuous dissolver off-gas were analyzed in a number of runs. Table 1 shows the average analysis, the reactions indicated, and the calculation of the average moles of acid consumed

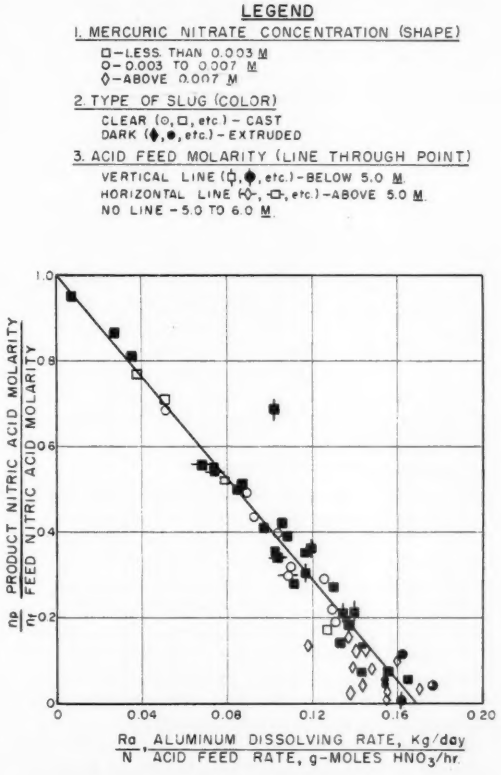

Fig. 2. Stoichiometric correlation of data.

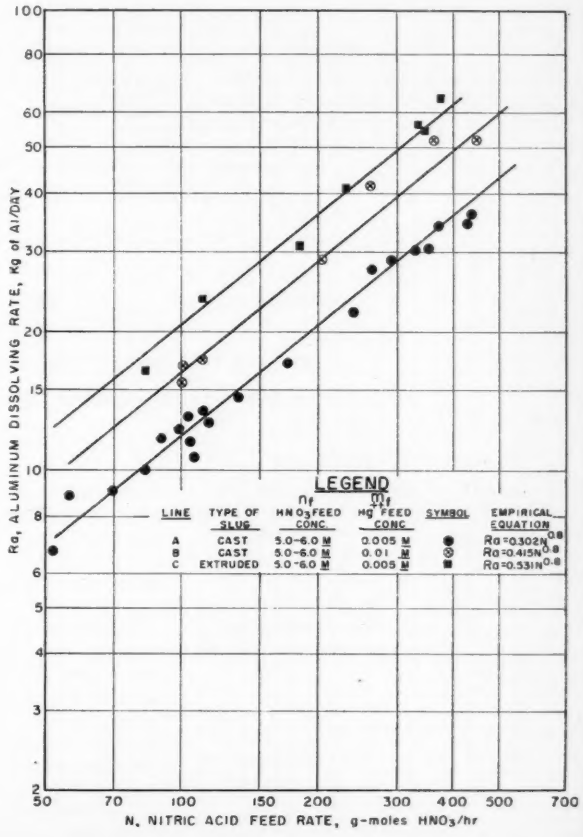

Fig. 3. Variation of dissolution rate with acid feed rate.

Table 1. The Mercury-catalyzed Dissolution of Aluminum in Nitric Acid

Assumed reaction	Moles of acid consumed/ mole Al dissolved	% of Al dissolved through reaction shown*
$Al + 6\ HNO_3 = Al(NO_3)_3 + NO_2 + 3\ H_2O$	6.00	1
$Al + 4\ HNO_3 = Al(NO_3)_3 + NO + 2\ H_2O$	4.00	52
$8\ Al + 30\ HNO_3 = 8\ Al(NO_3)_3 + 3\ N_2O + 15\ H_2O$	3.75	46
$2\ Al + 6\ HNO_3 = 2\ Al(NO_3)_3 + 3\ H_2$	3.00	1
Calculated weighted-average acid consumption = 3.85		

*These values are calculated from the following average of dissolver off-gas samples: $NO_2 = 4\%$, $NO = 70\%$, $N_2O = 23\%$, $H_2 = 3\%$.

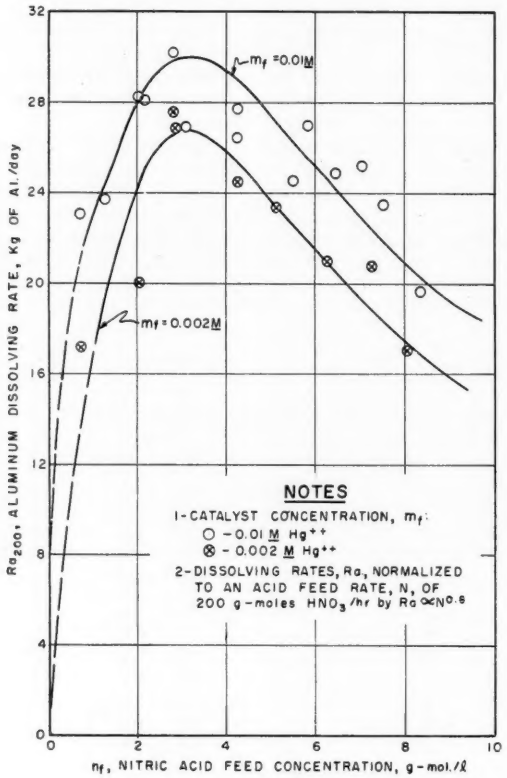

Fig. 4. Effect of feed acid concentration for cast slugs.

for each mole of aluminum dissolved; the small mole fraction of uranium in the alloy is neglected. Using this calculated value of 3.85 for the average acid consumption ratio, in conjunction with a nitric acid material balance around the dissolver, one obtains the following equation for the ratio of product acidity (n_p) to feed acidity (n_f):

$$\frac{n_p}{n_f} = 1 - 5.94\,\frac{R_a}{N} \qquad (1)$$

where N is the acid feed rate in gram-moles per hour and R_a is the kilograms of aluminum dissolved per day. In the derivation of Equation (1) the ratio of volumetric product rate P to volumetric feed rate F was set equal to 1. This is considered valid because experimental data showed that the maximum error introduced by this assumption is less than 1%.

Equation (1) is shown graphically in Figure 2, along with experimental data from a large number of pilot plant runs. The data are seen to agree closely with the line representing Equation (1). It is important to note that data from runs with wide variations in feed mercuric ion concentration, feed acid concentration, and metallurgical properties of the alloy are randomly distributed in Figure 2, showing that the reaction stoichiometry is not significantly influenced by these variables.

The nitric acid consumption for all runs averaged 4.0 moles per mole of alloy dissolved and was within 10% of this value for 85% of the runs. This further shows the validity of Equation (1) as an average representation of the reaction stoichiometry.

Effect of Metallurgical Properties

Metallographic examination of the cast and extruded uranium-aluminum slugs used in these studies revealed significant differences in crystalline structure. The cast slugs consisted of relatively large dentrites of primary aluminum (first to freeze during solidification) surrounded by networks of eutectic of UAl_4 and aluminum. Examination of extruded slugs of the same composition showed a fairly uniform distribution of aluminum and intermetallic compound, with the eutectic network broken and less pronounced.

As might be expected, slugs showing such dissimilarities in alloy structure had different dissolving characteristics. At a constant feed acid composition and catalyst concentration extruded uranium-aluminum slugs dissolved about twice as fast as comparable cast material.

A number of runs were carried out with lengths of extruded aluminum rod. It was found that 2*S* aluminum rod dissolved at a rate very slightly lower than that for extruded uranium-alloy slugs; consequently, the runs made with the former material were considered representative of the behavior of extruded uranium-aluminum slugs. Furthermore, as the uranium contained in the extruded alloy has little effect on the dissolution rate, it may be concluded that extruded alloys of a composition somewhat different from the slugs used in this study will dissolve at comparable rates.

Differences in fabrication histories for a given alloy, however, would be expected to give significant differences in dissolution rate corresponding to differences in alloy structure. Consequently, the numerical dissolution-rate relationships presented in this paper must be considered applicable only to the specific materials used in this study. Furthermore, the effects of irradiation were not investigated.

Effect of Acid Feed Rate

Several series of runs were made at constant feed acid and catalyst concentrations and varying acid feed rates. The results are shown in Figure 3, which is a logarithmic plot of the dissolving rate R_a against the acid feed rate N. The slope of each of the lines is 0.8, which indicates that the dissolving rate is proportional to the 0.8 power of the acid feed rate at all conditions tested. This relationship appears to be quite general, and through its use the results from many runs have been "normalized" to a single acid feed rate to facilitate other correlations.

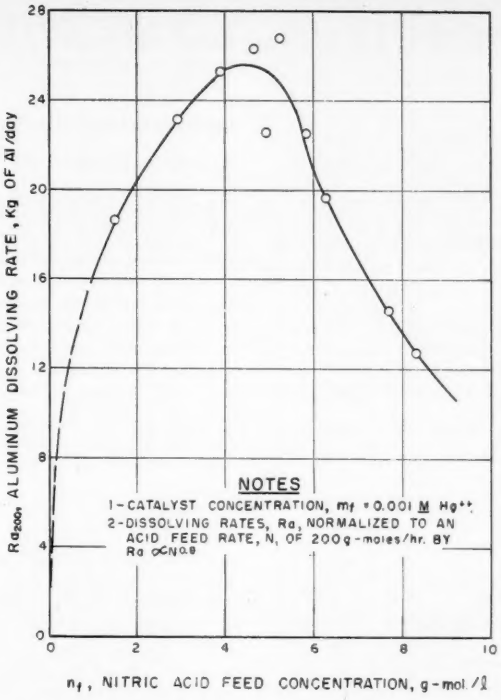

Fig. 5. Effect of feed acid concentration for extruded slugs.

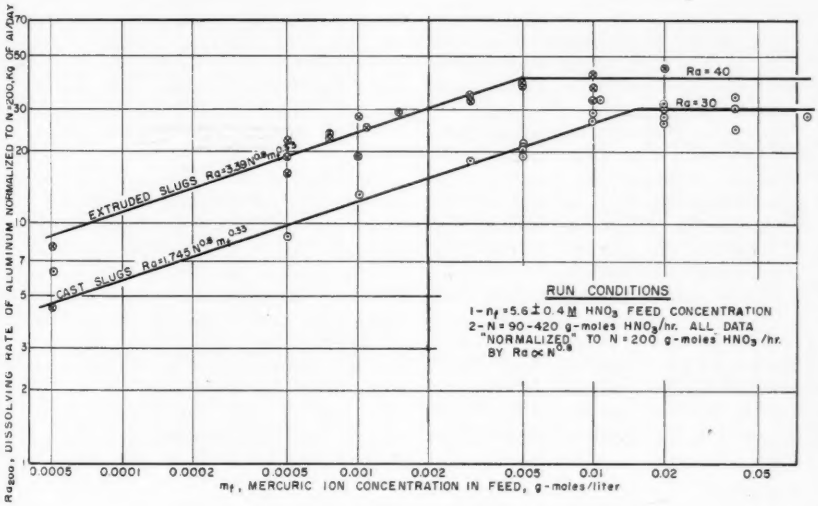

Fig. 6. Effect of mercuric ion concentration.

Effect of Feed Acid Concentration

Several runs were made with varying feed acid concentrations, all other parameters being held constant, in order to show the effect of acid concentration upon the dissolving rate. The results of such tests are shown in Figures 4 and 5, wherein the dissolving rates R_a have been "normalized" to an acid feed rate N of 200 g.-moles/hr. by the relationship $R_a \alpha (N)^{0.8}$. It will be noted that the maximum dissolution per mole of acid fed for cast slugs is obtained with about $3M$ acid feed; this maximum is seen to remain the same even when the feed catalyst concentration is changed by a factor of 5. The dissolving rate curve for extruded slugs was determined at only one catalyst concentration; in this case the maximum rate occurs with about $5M$ acid.

Effect of Catalyst Concentration

Series of runs were made with both cast and extruded uranium-aluminum alloy at varying acid feed rates with $5.6M$ acid feed and a range of feed mercuric nitrate concentration between 0.00005 and $0.08M$. The results of these runs are shown in Figure 6, wherein the acid feed rate is normalized to a standard value of 200 g.-moles/hr. by means of the 0.8 power relationship of Figure 3. It is apparent from Figure 6 that an increase in mercuric nitrate concentration in the feed results in a definite and significant increase in dissolving rate for both cast and extruded alloy up to a limiting mercuric ion concentration. Further increases in mercuric ion concentration above approximately $0.015M$ for cast slugs and $0.005M$ for extruded slugs yield no corresponding increase in dissolving rate. Below these limiting catalyst concentrations the linear relationships on the logarithmic plot of Figure 6 can be represented by the following empirical equations:

cast alloy:

$$R_a = 1.745 N^{0.8} m_f^{0.33} \qquad (2)$$

extruded alloy:

$$R_a = 3.39\ N^{0.8} m_f^{0.33} \qquad (3)$$

General Correlation

Equation (1) can be combined with the foregoing empirical equations to include the product composition and eliminate the acid feed rate, giving the following relationships:

cast alloy:

$$R_a = 20{,}200 (m_f)^{1.65} \left(\frac{n_f}{n_f - n_p} \right)^4 \qquad (4)$$

extruded alloy:

$$R_a = 557{,}000 (m_f)^{1.65} \left(\frac{n_f}{n_f - n_p} \right)^4 \qquad (5)$$

These equations show the relationship between the feed and product compositions and the dissolving rate for the dissolver used in the experimental work.

Strictly speaking, Equations (4) and (5) are applicable only for $5.6M$ acid feed as Equations (2) and (3), which are used in the derivation, were determined at this concentration. However, the plots of dissolution rate as a function of acid concentration (Figures 4 and 5) show little variation in rate for acid concentrations between 3 and $6M$ for either cast or extruded slugs. Consequently, Equations (4) and (5) are approximately correct for feed acid concentrations between 3 and $6M$ and are most accurate for $5.6M$ acid.

These equations are also significant in that they can be used to show the effect of the important process variables on

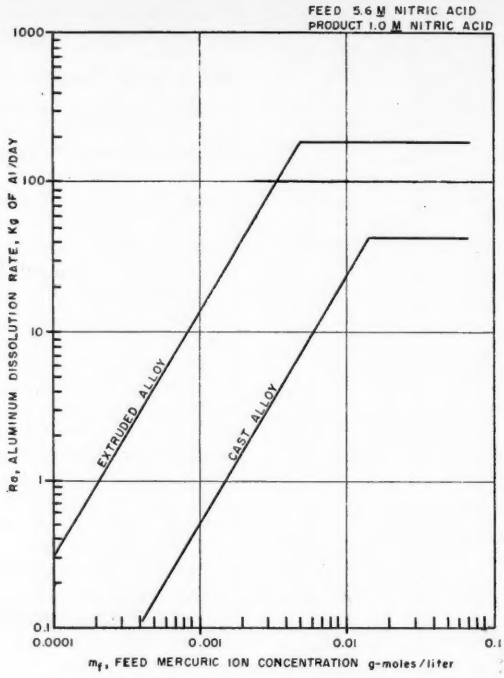

Fig. 7. General dissolver relationship.

dissolution rate at a constant product composition. The correlations developed in previous sections were obtained by keeping the feed conditions constant, except for the variable being studied, and allowing the product composition to vary at will. However, normal continuous dissolver operation would be directed toward keeping a constant product composition (within specifications for feed to a subsequent process step) and varying other conditions as necessary.

Equations (4) and (5) show that the dissolution rate varies with the 1.65 power of the catalyst concentration at constant product composition; whereas Equations (2) and (3) indicate a variation with the cube root of the mercuric ion concentration at constant acid feed rates. Beyond the limiting catalyst concentrations, an increase in mercuric ion molarity will give no corresponding increase in dissolution rate at either constant feed acid rate or a constant product concentration.

Insertion of these limiting catalyst concentrations in Equations (2), (3), (4), and (5) demonstrates that the maximum dissolution rate attainable at a constant product composition is about three times greater for extruded alloy than for cast material; whereas this ratio is only about 1.5 at a constant acid feed rate. At a given catalyst concentration below the limiting value, extruded alloy dissolves about thirty times faster than cast material for a constant product composition and only about twice as fast at a constant feed acid rate.

The effect of catalyst concentration on the dissolution rates of cast and extruded alloy for a constant product composition may be illustrated by inserting specific values for the feed and product acidity in Equations (4) and (5) and plotting the resultant relationships. For the sake of illustration, it may be assumed that a $1M$ acid product is optimum for subsequent processing. Since a $5.6M$ acid feed was used in most of the experimental work and the resultant correlations, this value is chosen for insertion in Equations (4) and (5). The resultant relationships are

cast alloy:

$$R_a = 4.42 \times 10^4 (m_f)^{1.65} \qquad (6)$$

extruded alloy:

$$R_a = 1.22 \times 10^6 (m_f)^{1.65} \qquad (7)$$

Equations (6) and (7) are plotted on Figure 7.

The significantly greater dissolution rate of extruded alloy as compared with cast material should be of special interest to those concerned with designing the fuel elements for a reactor. If there is little difference in the reactor performance of extruded and cast uranium-aluminum fuel alloys, extruded material should be specified as its considerably greater dissolution rate could result in significant savings in fuel-processing costs.

DISSOLVER OPERATION AND CONTROL

Normally a plant-scale continuous dissolver would probably be operated with all input streams (feed acid, catalyst, and metal) controlled at selected constant rates. These rates should be chosen so that they are stoichiometrically equivalent to the desired dissolution rate and product composition. With such operation, the metal would seek an equilibrium level in the dissolver and the process would be inherently stable, as small changes in some parameter would alter the slug level (and hence the available surface area) so as to compensate for the change.

Although this inherent stability would normally give a uniform product composition, unusual conditions could occasionally yield product which did not meet specifications. Such occurrences could be detected by continuous measurement of the specific gravity of cold dissolver product; this was successfully demonstrated during the pilot plant tests.

An adjustment in operating conditions must be made whenever it is apparent that the dissolver effluent will not meet specifications for subsequent processing. Various possible methods of adjusting the product composition were tested in the pilot plant including changes in feed acid concentration, in the acid feed rate, in the dissolver temperature, in the metal feed rate, and in catalyst concentration. The last method proved most satisfactory.

This method of adjustment has the advantage of not changing the metal or volumetric throughputs, and hence nearly the entire plant would function normally regardless of the rate of catalyst addition. With such a method the catalyst should logically be injected into the feed stream separately from the dilute acid to facilitate adjustments in catalyst feed rate. Several successful pilot plant runs were made to show the effect of such changes in catalyst concentration on the product analysis and on the specific gravity as recorded on an instrument chart.

CONCLUSIONS

Data and correlations have been given for the process relationships of concern in the continuous dissolution of certain uranium-aluminum alloys. These correlations can be used to aid in the design of a workable dissolver for processing uranium-aluminum–alloy reactor fuels at any given capacity to meet a wide range of product composition specifications.

Presented at Nuclear Science and Engineering Congress, Cleveland.

Diffusion of Uranium Through Graphite

L. D. LOCH, J. R. GAMBINO, and W. H. DUCKWORTH

Battelle Memorial Institute, Columbus, Ohio

Diffusion rates of uranium through graphite were determined in the temperature range of 3,000° to 4,350°F. The diffusion couples consisted of sintered UC_2 disks in contact with graphite rods. The observations indicated two distinct types of uranium transport which could be associated with volume diffusion and with migration along pores respectively.

Volume diffusion was characterized by steep concentration gradients and shallow penetration. The diffusion coefficient D_v, in sq. cm./sec. between 3,300° and 4,250°F., is given by an equation. Above 4,250°F. incipient melting of the UC_2 was evident and the diffusion coefficients were much higher than those given by the equation.

As an example of the penetration resulting from volume diffusion, calculations show that, after 1,000 hr. at 4,200°F. the uranium concentration at 0.1 cm. from the interface will be 1,000 mg./cc., compared with 10,000 mg./cc. for pure UC_2.

Pore migration resulted in uranium penetration far beyond that arising from volume diffusion at equivalent temperatures and diffusion times. However, uranium concentrations were very small compared with those corresponding to volume diffusion. Pore migration is strongly temperature dependent.

To estimate the practical importance of pore migration, the uranium flow through a graphite wall at 3,000°F. was measured. With a wall thickness of 0.32 cm., the average flow per unit area was 0.015 mg./(sq. cm.)/(hr.) for a 40-hr. test.

Graphite was used in the first nuclear reactor because it is a good moderator and because large amounts of pure graphite were obtainable. The early reactors were designed to operate at relatively low temperatures. However, graphite also is very well suited as a moderator and structural material for power-producing reactors. Except for its poor oxidation resistance, it has generally attractive properties for high-temperature service—high thermal conductivity, good strength, and excellent resistance to thermal shock and to creep.

There are several important areas in which more data are needed to extend the use of graphite in power reactors. Among these is the need for information on its compatability with nuclear fuels at high temperatures.

Uranium dioxide and uranium dicarbide are two high-melting fuel compounds which have been considered for use in contact with graphite. As the oxide reacts with graphite at high temperatures to form the carbide, uranium dicarbide appears to be the more suitable compound to use with graphite.

Uranium dicarbide, UC_2, is known to be relatively unreactive with graphite up to its melting point, but few data on the diffusion of uranium from UC_2 into graphite have been reported. In fact, prior to this investigation, the only systematic study of the problem appears to be that made by Loftness (*1*).

Loftness measured the diffusion of uranium from UC_2-impregnated graphite into pure graphite at temperatures between 3,900° and 4,700°F. The impregnated graphite had a uranium concentration of approximately 250 mg./cc. Loftness concluded that volume diffusion was the only important diffusion mechanism contributing to his results.

The present study deals with diffusion from massive UC_2 into graphite. The results should be applicable to a variety of reactor-design problems.

MATERIALS

Synthetic graphite, designated type AGOT by The National Carbon Company, was used in the experiments. This material, made and purified for use in reactor applications, is otherwise a typical high-grade commercial graphite, prepared by heating a mixture of petroleum coke and coal-tar pitch to graphitizing temperatures.

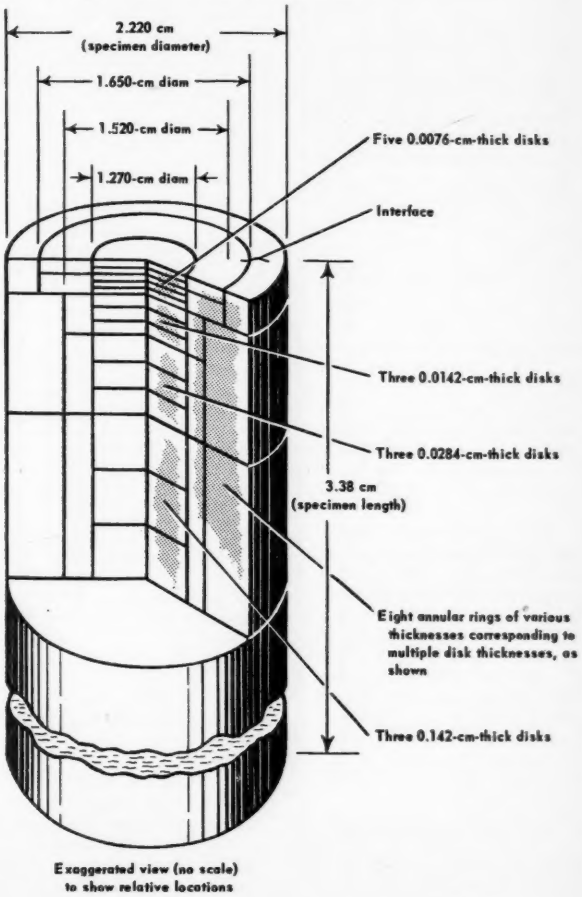

Fig. 2. Cutting scheme for diffusion couples.

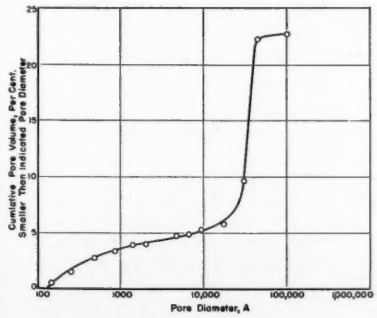

Fig. 1. Pore-size distribution in AUF graphite.

J. R. Gambino is now at General Electric Company, Schenectady, New York.

Despite multiple impregnations by pitch to increase the density, the void content ranges from 23 to 27% of the total volume. The pores are largely interconnected and permeable to gases. Figure 1 gives the mercury pore spectrum of AUF graphite, which is structurally similar to AGOT. The grains of AUF and AGOT graphites range from 1 to 20 μ and contain crystallites 2,000 Å. long in the direction of the basal plane; the majority of the pores, 80%, are in the same size range as are the grains.

Massive uranium dicarbide was crushed in a steel mortar to pass a 200-mesh sieve. All handling of the UC_2 was performed under carbon tetrachloride to prevent oxidation. Chemical analysis of the UC_2 showed 8.44% carbon, compared with the theoretical carbon content of 9.16%.

To prepare specimens, the graphite was machined into cylinders 3.8 cm. long and 2.2 cm. in diameter. The axes of the cylinders were parallel to the direction of extrusion. End surfaces were polished with 600-grit silicon carbide abrasive paper.

The UC_2 powder and 0.75 wt. % paraffin, added as a carbon tetrachloride solution, were thoroughly mixed, and then the carbon tetrachloride was evaporated in air. The resultant powder was pressed at 22,600 lb./sq. in. into disks which were sintered in vacuum at 4,200°F. for 1½ hr. One side of each disk was polished under carbon tetrachloride with 600-grit SiC paper. The finished disks were 0.3 cm. thick and 1.8 cm. in diameter. They were stored under carbon tetrachloride until used.

EXPERIMENTAL PROCEDURES

Each diffusion couple consisted of a sintered uranium carbide disk resting on one end of a graphite cylinder. The UC_2 was held in place temporarily by an organic adhesive which carbonized during heating. The diffusion couple was placed in a carbon-tube resistor furnace with the axis of the cylinder vertical and heated to maximum temperature in about 2 hr. Furnace temperatures were read to ±20°F. with a Leeds-Northrup optical pyrometer. Corrections were made in the temperature readings for losses in the glass lens and mirror used in sighting. The furnace was cooled overnight to room temperature before the couple was removed.

Argon entering the furnace was passed over heated titanium granules to remove nitrogen and was dried with anhydrous magnesium perchlorate. Traces of carbon monoxide were present in the furnace atmosphere.

After each diffusion couple was removed from the furnace, the UC_2 disk was detached and the graphite was sectioned on a lathe in accordance with the diagram in Figure 2. In every case when the couple was separated, part of the graphite stuck to the UC_2, leaving an irregular graphite surface. Therefore the distance of each cut from the original interface was measured with reference to the periphery of the graphite face, which was undamaged. As the UC_2 disks were smaller in diameter than the graphite rods, the peripheral area was not in contact with UC_2 during heating.

The cutting operation permitted an accuracy of ±0.0005 cm. in measuring the thickness and penetration distance after each cut. Penetration distance was recorded as the distance between the original interface and the midpoint of the cut.

Material shaved off by the lathe was collected carefully and its uranium content analyzed by a fluorophotometer (*2*). The accuracy of the analyses was ±10% of the uranium content. The center cuts shown in Figure 2 were used to obtain concentration-penetration curves. The outer cuts were analyzed only to determine whether radial diffusion had an effect on the uranium concentrations resulting from linear diffusion.

Table 1. Uranium Concentration-penetration Data

Cut	Specimen 23, 3,800°F., 16 hr. Uranium concentration, mg./cc.	Depth of cut, cm.	Specimen 32, 3,600°F., 8 hr. Uranium concentration, mg./cc.	Depth of cut, cm.
1	1,200	0.004	73.0	0.004
2	110	0.011	2.0	0.011
3	6.1	0.019	0.83	0.019
4	3.6	0.027	0.46	0.027
5	2.2	0.034	0.31	0.034
6	1.8	0.045	0.41	0.045
7	0.84	0.061	0.36	0.061
8	0.64	0.076	0.41	0.076
9	0.46	0.099	0.57	0.099
10	0.40	0.130	0.54	0.130
11	0.36	0.160	0.39	0.160
12	0.24	0.252	0.16	0.252
13	0.11	0.405	0.01	0.405
14	0.03	0.558	0.006	0.558
—	—	—	0.006	0.611

Cut	Specimen 19, 4,350°F., 2 hr. Uranium concentration, mg./cc.	Depth of cut, cm.	Specimen 15, 4,250°F., 12 hr. Uranium concentration, mg./cc.	Depth of cut, cm.
1	N.D.*	0.004	N.D.	0.004
2	920†	0.011	850	0.011
3	973	0.019	115	0.019
4	600	0.027	3.3	0.027
5	254	0.034	2.8	0.034
6	50	0.042	2.1	0.042
7	5.3	0.050	2.5	0.050
8	2.9	0.058	2.6	0.058
9	2.6	0.069	2.3	0.069
10	2.0	0.079	1.8	0.079
11	1.5	0.092	1.7	0.092
12	0.97	0.117	1.7	0.117
13	1.1	0.140	1.2	0.140
14	0.88	0.170	1.3	0.170
15	1.08	0.261	1.1	0.261
16	0.61	0.413	0.73	0.413
17	0.55	0.505	0.67	0.505

*N.D. = no determination.
†This point was not shown in Figure 3 as it was in obvious error and is less reliable than deeper points.
Complete tabular data are filed as document 4830 with the American Documentation Institute, Photoduplication Service, Library of Congress, Washington 25, D. C., and may be obtained for $1.25 for photoprints or 35-mm. microfilm.

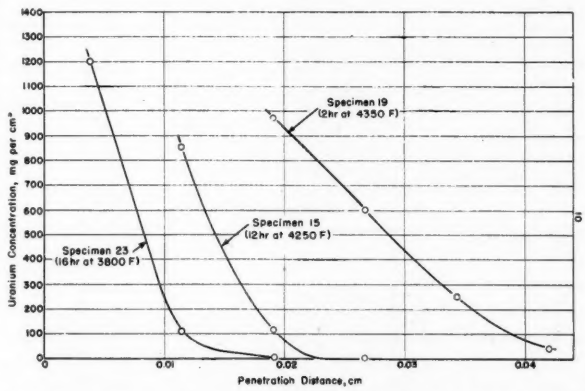

Fig. 3. Representative concentration-penetration curves for shallow penetration.

RESULTS AND DISCUSSION

The heating conditions and concentration-penetration data for the experiments are shown in Table 1. Representative penetration curves for the first few cuts are shown in Figure 3. The curves for specimens 15 and 23 in Figure 3 are typical of those obtained at and below 4,250°F. Experiments at 4,300° and 4,350°F. produced curves similar to the one shown in Figure 3 for specimen 19.

Figure 3 shows a strong dependence of penetration distance on temperature. At 4,350°F., which is near the melting point of uranium dicarbide (*3*), the penetration was 0.04 cm. after only 2 hr., and heating for 16 hr. at 3,800°F. produced a penetration of less than 0.02 cm.

An unusual feature of the results was the appearance of two types of concentration gradients: (1) large gradients near the interface, as shown in Figure 3, and (2) small gradients at deeper penetrations. The two types of gradients are illustrated in Figure 4 for specimen 15. Even though the concentrations at the deeper penetrations were small, they were significant. The data are plotted in Figure 4 as log concentration vs. distance only for convenience; the straight lines should not be taken as an indication that linear relationships were obtained with this type of plot.

The dependence of concentrations near the interface on depth and time was found to be consistent with diffusion equations and sufficiently well defined to permit the determination of diffusion coefficients. However, the data were not sufficient to answer secondary questions, such as whether the diffusion coefficient in the carbide was the same as in the graphite where the uranium concentration was much lower. Accordingly, analysis of the data was based on the equation

$$C(x, t) = \frac{C_0}{2}\left[1 - \text{erf}\left(\frac{x}{2\sqrt{Dt}}\right)\right]$$

where $C_0 = 10{,}000$ mg./cc.

This equation is applicable to the results of the present investigation provided that (1) there is no very large dependence of the diffusion coefficient on concentration, (2) no appreciable change in concentration occurs at the extremities of the couple, and (3) the effect of radial diffusion is negligible. Auxiliary experiments showed that the diffusion times used in this work were sufficiently short to prevent depletion of uranium at the outer extremities of the UC_2 disks. Also the center cuts which were taken for analysis were shown to be close enough to the center line so that radial diffusion might be ignored.

In accordance with the foregoing equation, the concentration-penetration data were plotted as 100 C/C_0 on the probability scale vs. $x/(t)^{1/2}$ on a linear scale. Straight lines were drawn through the data for the shallow penetrations so as to intersect the point 100 $C/C_0 = 50$ and $x/(t)^{1/2} = 0$. In most cases it was not necessary to force this intersection, showing that the assumption of constant D on both sides of the interface was not unreasonable. The plots obtained for the experiments at 4,200° and 4,300°F. are shown in Figure 5. All the plots showed a definite tail marking the transition from shallow penetration to deep penetration noted in Figure 4.

For the experiments at 4,200°F. and above, there were enough points available and the straight-line fit was sufficiently good to calculate a diffusion coefficient with some certainty. For specimens 13 and 19, however, very little weight was given to the first cut because of the uncertainties in the concentration and in the penetration distance.

For the experiments at 3,300°, 3,600°, 3,800°, and 4,000°F. the first cut again was doubtful, leaving only one or two reliable points in each case. Straight lines were drawn to fit the points as well as possible. Under the circumstances, the values of D obtained from these experiments are not so reliable as those at the higher temperatures.

The values of D obtained for shallow penetration are shown in Table 2. A plot of log D vs. $1/T$ is shown in Figure 6 along with values obtained by Loftness (*1*) for comparison.

Table 2. Diffusion Coefficients for Shallow Penetration

Temperature, °F.	Diffusion coefficient D, sq. cm./sec.
4,350	1.9×10^{-8}
4,300	3.6×10^{-9}
4,250	1.0×10^{-9}
4,200	7.4×10^{-10}
4,000	6.8×10^{-11}
3,800	1.6×10^{-10}
3,600	4.1×10^{-11}
3,300	2.4×10^{-11}

A least-squares treatment of these data was not made because the substantial uncertainties at the four lowest temperatures could not be estimated at all well. The line shown in Figure 6 was drawn by inspection. Using this line, one finds that the diffusion coefficient D in sq. cm./sec. between 3,300° and 4,250°F. is given by the equation

$$D = 7.6 \times 10^{-3} \exp(-82{,}000/RT)$$

On the basis of close inspection of the data, it is estimated that the activation energy of 82,000 cal./g.-atom may be in

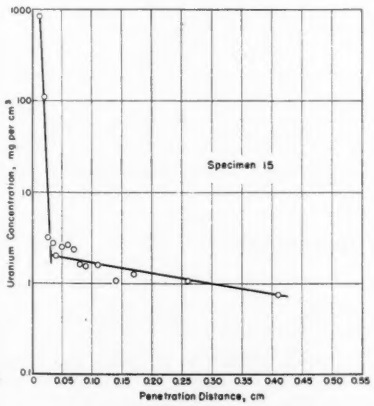

Fig. 4. Comparison of the two types of concentration gradients.

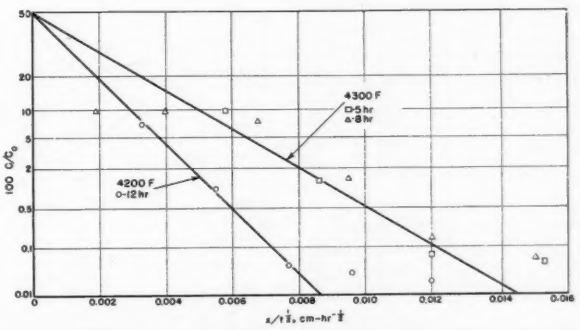

Fig. 5. Plots showing agreement of shallow-penetration data with Fick's Law.

error by as much as 20,000 cal./g.-atom, which is not unduly high for diffusion experiments of this type. The rather high value of the activation energy suggests that volume diffusion is the major contributor to shallow penetration of uranium.

The results obtained in this investigation are in general agreement with those reported by Loftness. His activation energy of 53,000 cal./g.-atom is not significantly different. The only important difference is seen in the results at temperatures above 4,250°F., where Loftness did not observe the sharp increases in diffusion rates noted in the present investigation. A possible reason for this may be that in Loftness's experiments the uranium dicarbide initially was distributed in thin layers on the pore walls in the graphite. Thus it easily could take up excess carbon, which prevented melting of the carbide (*3*). In the present experiments the amount of carbon available to the UC_2 was limited, and so some melting occurred at 4,300°F. and above.

Calculation of uranium penetrations by volume diffusion for long times indicates that this type of diffusion may be of less practical importance than the type referred to as *deep penetration*; for example, after 1,000 hr. at 3,200°F. the uranium concentration would be expected to decrease from 10,000 mg./cc. in the UC_2 to 1,000 mg./cc. at 0.01 cm. inside the graphite. After 1,000 hr. at 4,200°F. the concentration should be 1,200 mg./cc. at 0.1 cm. from the interface. Deep penetration, on the other hand, reaches a depth of a centimeter or more in a few hours at these temperatures.

Deep penetration must occur by way of the pores and may logically be called *pore migration*. Although it is presumably a type of diffusion, the available data give no evidence for this and do not justify the estimation of diffusion coefficients. To obtain some conception of the temperature dependence of the process, the data were plotted as log Q/t vs. $1/T$, where Q is the amount of uranium absorbed by the graphite as a result of pore migration and t is the time. In the present experiments volume diffusion was negligible at depths greater than 0.05 cm.; only the uranium which penetrated deeper than 0.05 cm. was used in calculating Q. The resultant plot is shown in Figure 7.

Pore migration shows a temperature dependence which is qualitatively similar to that observed for volume diffusion. A sharp increase in rate again was noted above 4,250°F.

One experiment was made to estimate the uranium loss through a graphite wall due to this form of transport. The uranium flow was measured through a thin-walled tube ½ in. in diameter and 4 in. long, closed at one end. Uranium dicarbide powder of 325 mesh was tightly packed in the ¼-in. bore of the tube to a depth of ½ in. and the bore closed with a graphite plug. The tube was placed in a carbon-black absorption bed contained by a tube 1 in. in diameter. The assembly was placed vertically in a vacuum furnace similar to that described by Smith (*4*), so that only that portion of the inner tube which contained the UC_2 was in the hot zone of the furnace. In this manner uranium leakage around the plug was minimized.

The uranium lost per unit area was 0.6 mg./sq. cm. after 40 hr. at 3,000°F. Under these conditions the penetration depth by volume diffusion would be about 0.004 cm. compared with the wall thickness of 0.32 cm. Therefore the uranium picked up in the carbon black must have reached the outer wall of the graphite tube by pore migration.

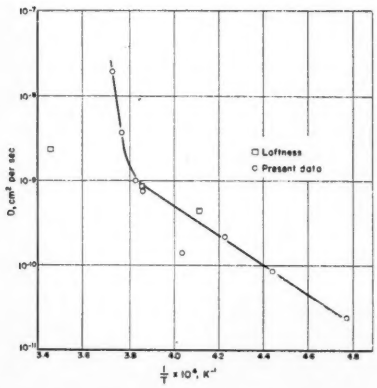

Fig. 6. Dependence of diffusion coefficient on temperature for shallow penetration.

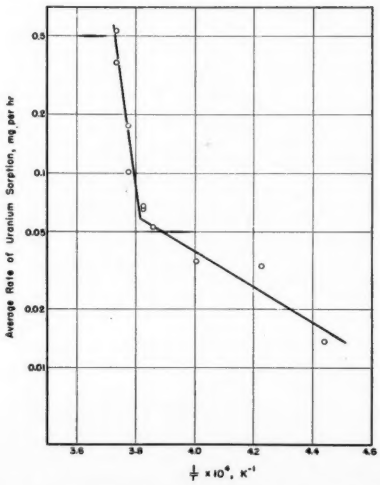

Fig. 7. Dependence of pore migration on temperature.

SUMMARY AND CONCLUSIONS

Uranium transport through polycrystalline graphite was measured in the temperature range of 3,000° to 4,350°F. Two forms of transport were observed: volume diffusion and pore migration. The volume-diffusion coefficients obtained in this investigation are in good agreement with those reported by Loftness (*1*). The activation energy of 82,000 ± 20,000 cal./g.-atom is not significantly different from Loftness's value of 53,000 cal./g.-atom. Within the time and temperature ranges studied, depths of penetration by pore migration were about 100 times as great as those by volume diffusion. Therefore, for practical purposes, pore migration may be the more important type of uranium transport.

A better understanding of pore migration is needed. More experiments, with graphites of widely different pore structures, will be helpful. It is of particular interest to determine whether pore migration occurs to the same extent in very dense graphites as it does in ordinary graphites.

NOTATION

C = uranium concentration, mg./cc.
C_0 = initial uranium concentration, mg./cc.
D = diffusion coefficient, mechanism unassigned, sq. cm./sec.
D_v = diffusion coefficient for volume diffusion, sq. cm./sec.
R = gas constant = 1.987 cal./(g.-atom)(°K.)
t = time, hr.
T = temperature, °K.
x = penetration distance, cm.
exp = base of the natural logarithms = 2.71828

$$y = \frac{x}{2\sqrt{Dt}}$$

$$\text{erf } y = \frac{2}{\sqrt{\pi}} \int_0^y \exp(-z^2)\, dz,$$

where z is a variable of integration

LITERATURE CITED

1. Loftness, R. L., *NAA SR*-64 (Aug. 2, 1950).
2. Center, E. J., *AECD*-3006 (June 30, 1948).
3. Mallet, M. W., A. F. Gerds, and H. R. Nelson, *J. Electrochem. Soc.*, **99**, 197 (1952).
4. Smith, C. A., *NAA SR*-109 (April 10, 1951).

Presented at the Nuclear Science and Engineering Congress, Cleveland.

Flow Distribution Among Parallel Heated Channels

ALAN R. GRUBER and SEYMOUR C. HYMAN

Nuclear Development Corporation of America, White Plains, New York

The coolant flow distribution among parallel tubes in a nuclear reactor (or boiler or heat exchanger) can be very sensitive to variations in heat input, dimensions, etc. Analytical expressions are given for partial derivatives which measure flow variations for several situations. The utility of orifices and valves in reducing flow sensitivity is discussed. Numerical results are reported for a system using water at supercritical pressures with an eightfold expansion from inlet to outlet.

Important flow-sensitivity problems can arise in the design of a nuclear power reactor in which the coolant undergoes an appreciable decrease in density while passing through the reactor. In such a case the distribution of the coolant flow among parallel cooling tubes can become very sensitive to variations in heat input and dimensions from tube to tube, as well as to pressure variations in the headers. The term *flow sensitivity* has been coined in connection with some studies of this type on water at pressures above the critical.

Flow sensitivity is measured by the ratio of the fractional change in mass flow rate to the fractional change in average heat flux to a tube at constant pressure drop. In a similar way, terms have been created to refer to the variations in outlet fluid temperature and in maximum tube wall temperatures due to changes in heat flux, mass flow rate, tube shape or dimensions, etc. All these factors are of prime importance in reactor design. They are interrelated and depend on the physical properties of the coolant. Although the primary reference in this paper is to reactor design, exactly the same considerations and conclusions will apply to steam boilers or heat exchangers where coolants go through large temperature changes, or when a coolant has sharply temperature-dependent physical properties even though the temperature range may be small.

In a high-performance reactor for generation of useful power the rate of energy generation within a realistic size as well as the temperature level at which the energy is made available are both limited by permissible temperatures for the materials of construction. On the other hand, the economics of investment and of operation (thermodynamics) requires higher and higher temperatures. If problems of flow sensitivity lead to nonuniformity of performance among the flow channels, then only some portion of the channels can be operating at maximum wall temperatures. This could be a serious deterrent to successful operation. Flow sensitivity magnifies any other nonuniformities, such as heat flux pattern, that may be inherent in the design.

The problem of designing a nuclear power reactor so that the coolant flow pattern matches the heat generation pattern, with the coolant outlet temperature (or maximum tube-wall temperature) the same for all tubes, is made extremely difficult by the fact that most means of reactor control (to compensate for burnout of the fuel) tend to change the heat generation pattern. When employing expansible fluids as reactor coolants, the designer must be prepared either to (*a*) sacrifice potentially achievable coolant outlet temperatures by allowing for substantial differences between the maximum (design) and the average coolant outlet temperatures, or (*b*) incorporate such devices as orifices to counteract poor flow distribution and thus increase the average coolant outlet temperature at the expense of increased coolant pressure drop.

The increased sensitivity of flow rate to coolant-passage dimensions intensifies normal problems of fuel-element–manufacturing tolerances, warping and distortion of fuel elements during operation, and fouling of heat transfer surfaces.

Some typical cases in which flow sensitivity problems become important are gas-cooled reactors with large coolant-temperature rise, as studied by Addoms (*1*); reactors cooled by liquids with the coolant exit temperatures just below the boiling point, in which case a slight change in circumstances can bring about boiling in the downstream portion of the cooling tube; and reactors cooled by liquids at pressures above the critical, with the coolant bridging the critical temperature. In all these cases, the coolant flow rates and temperatures in various cooling tubes will depend sensitively on nonuniformities (most importantly, on nonuniformities in heat input) from tube to tube.

THEORETICAL DEVELOPMENT

In a nuclear reactor the heat-flux distribution along a coolant passage length may follow a symmetrical sine curve as shown in Figure 1. Specifying the value of the ratio of maximum local heat flux to average heat flux over the whole tube would then define the heat-flux pattern. The enthalpy rise of the fluid as it moves along a differential distance in the heated passage is

$$dh = \frac{4q\,dx}{GD} \tag{1}$$

Integration results in an expression for the bulk fluid enthalpy at any point along the heated passage.

$$h = h_{in} + \left[\left(\frac{q_{max}}{Q}\right)\Delta h\left(\frac{1+2\sigma}{\pi}\right)\right] \cdot \left[\cos\left(\frac{\pi\sigma}{1+2\sigma}\right) - \cos\left(\frac{\pi\sigma + \frac{x\pi}{L}}{1+2\sigma}\right)\right] \tag{2}$$

For the case of water at supercritical pressures with very large temperature differences between wall and bulk it was considered unwise to rely on the usual heat transfer film-coefficient correlations. A set of calculations was made based on a theoretical development by Goldmann (*2*). The results of the calculation showed the heat transfer to depend in a complicated fashion on the fluid properties. It was found convenient to correlate the calculated results by plotting the parameter $(qD^{0.2}/G^{0.8})$ vs. the temperature of the fluid at the wall and in the bulk. It can be shown that

$$\left(q\,\frac{D^{0.2}}{G^{0.8}}\right) = \left(\frac{q_{max}}{Q}\right)\left(\frac{\Delta h}{4}\right)\left(\frac{G^{0.2}D^{1.2}}{L}\right) \cdot \left(\sin\left[\left(\frac{\frac{x}{L}+\sigma}{1+2\sigma}\right)\pi\right]\right) \tag{3}$$

and so the required quantities are obtained to enable one to find the wall temperature.

It is interesting to note that the temperature profile in the fluid and at the wall at any point along the passage is determined by the parameters

$$\frac{q_{max}}{Q}\,;\, h_i\,;\, h_0\,;\, \frac{G^{0.2}D^{1.2}}{L}$$

The calculations by Goldmann (*2*) also resulted in values of the parameter $(\tau_w \rho\, D^{0.3}/G^{1.7})$ plotted against bulk and wall temperatures. Since

$$\left(\frac{\Delta p_f}{L}\right)_{z/L} = \left(\frac{\tau_w \rho D^{0.3}}{G^{1.7}}\right)\left(\frac{4G^{1.7}}{D^{1.3}\rho}\right) \tag{4}$$

the pressure drop due to flow frictional losses can be obtained by integration

S. C. Hyman is also Associate Professor of Chemical Engineering at the City College of New York.

along the heated passage. To this are added the pressure drops due to acceleration, entrance, and exit effects. After integration

$$\frac{\Delta p_f}{G^2} = \frac{1}{G^{0.1}D^{0.1}} \cdot F\left(h_i,\ h_0,\ \frac{q_{max}}{Q},\ \frac{G^{0.2}D^{1.2}}{L}\right) \quad (5)$$

is obtained.

The entrance, exit, and acceleration losses for any particular shape of passage are of the form

$$\frac{\Delta p_{a.e.e}}{G^2} = F_1(h_i,\ h_0) \quad (6)$$

Therefore it is possible to plot $(\Delta p_f + \Delta p_{a.e.e})/G^2$ vs. the four parameters listed above. This plot does not include the effect of variations in the factor $(G^{0.1}\ D^{0.1})$.

At this stage design charts could be prepared to enable determination of pressure drops for coolant flow at any heat flux, temperature level, passage shape, or length.

If values of passage length and shape are fixed and if the shape of the heat flux pattern is fixed by fixing (q_{max}/Q), then one can plot the total pressure drop against the value of the average heat flux (corresponding then to a particular outlet temperature) at fixed values of $(G^{0.2}D^{1.2}/L)$ and inlet temperature. This enables one to obtain calculated values of the flow derivatives

$$\left(\frac{\partial \Delta p/\Delta p}{\partial Q/Q}\right)_G;\ \left(\frac{\partial \Delta p/\Delta p}{\partial G/G}\right)_Q \quad (7)$$

It could be shown that these flow derivatives are functions of the same four parameters listed previously.

From the properties of partial derivatives one obtains

$$\left(\frac{\partial G/G}{\partial Q/Q}\right)_{\Delta p} = -\frac{\left(\frac{\partial \Delta p/\Delta p}{\partial Q/Q}\right)_G}{\left(\frac{\partial \Delta p/\Delta p}{\partial G/G}\right)_Q} \quad (8)$$

This factor is called *flow sensitivity*.

For the flow of a fluid of constant properties following standard friction factor correlations

$$\left(\frac{\partial \Delta p/\Delta p}{\partial Q/Q}\right)_G = 0;\ \left(\frac{\partial \Delta p/\Delta p}{\partial G/G}\right)_Q = 1.8;$$

$$\left(\frac{\partial G/G}{\partial Q/Q}\right)_{\Delta p} = 0$$

A fluid having a flow-sensitivity factor of 1.0 would maintain a fixed mixed outlet enthalpy even under conditions of varying heat input to flow passages. Such a fluid would be ideally self-regulating.

In some particular cases for real fluids, e.g., where the major effect of heat addition is a decrease in viscosity or where kinetic losses predominate, the flow-sensitivity factor may be slightly positive. Usually this factor will be negative and thus will intensify the effect of variable heat flux on outlet enthalpy.

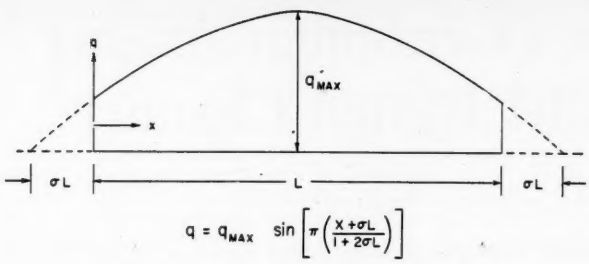

Fig. 1. Variation of heat flux along tube.

Variation of Wall Temperature with Heat Flux

The heated-passage-wall temperature at any point is a function of the average heat flux, mass velocity, and bulk fluid temperature at this point. This assumes a prior knowledge of the form of heat flux distribution along the passage.

$$T_w = f(Q,\ G,\ T_b) \quad (9)$$

In the form of a differential equation

$$\left(\frac{dT_w}{dQ/Q}\right) = \left(\frac{\partial T_w}{\partial Q/Q}\right)_{G.T_b} + \left(\frac{\partial T_w}{\partial G/G}\right)_{Q.T_b}\left(\frac{\partial G/G}{\partial Q/Q}\right) + \left(\frac{\partial T_w}{\partial T_b}\right)_{Q.G}\left[\left(\frac{\partial T_b}{\partial Q/Q}\right)_G + \left(\frac{\partial T_b}{\partial G/G}\right)_Q\left(\frac{\partial G/G}{\partial Q/Q}\right)\right] \quad (10)$$

Define

$$e \equiv \frac{\partial h/h}{\partial T/T} \quad (11)$$

and combine with forms of Equation (1) to get

$$\left(\frac{\partial T_b}{\partial Q/Q}\right)_G = \frac{(h_b - h_{in})T_b}{e_b h_b} = -\left(\frac{\partial T_b}{\partial G/G}\right)_Q \quad (12)$$

It can be shown that, if the heat transfer coefficient correlates with the mass velocity raised to the exponent n,

$$\left(\frac{\partial T_w}{\partial G/G}\right)_{Q.T_b} = -n\left(\frac{\partial T_w}{\partial Q/Q}\right)_{G.T_b} \quad (13)$$

Substituting Equations (11), (12), and (13) into (10) with n at its usual value of 0.8 gives

$$\left(\frac{dT_w}{dQ/Q}\right) = \left(\frac{\partial T_w}{\partial Q/Q}\right)_{G.T_b} \cdot\left[0.2 + 0.8\,\frac{e_0 h_0}{T_0 \Delta h_0}\left(\frac{\partial T_0}{\partial Q/Q}\right)\right] + \left(\frac{\partial T_w}{\partial T_b}\right)_{Q.G}\left(\frac{\Delta h_b}{\Delta h_0}\right)\left(\frac{h_0}{h_b}\right)\left(\frac{T_b}{T_0}\right)\left(\frac{\partial T_0}{\partial Q/Q}\right)\frac{e_0}{e_b} \quad (14)$$

Equation (14) can be evaluated by use of the flow-sensitivity factor at constant pressure drop across the heated passage to give the effect of changing heat flux on one or some of the passages in a group operating between common headers. If the bulk values of the necessary quantities are chosen at that location in the fluid associated with the maximum wall temperature, then the calculation gives the change in the maximum temperature.

Another facet would be to inquire what the flow-sensitivity factor would have to be to maintain a constant wall temperature. This can be determined by setting Equation (14) equal to zero. The result will usually be

$$\left(\frac{\partial G/G}{\partial Q/Q}\right)_{T_w} \approx 1.25$$

which could be achieved at a cost in pressure drop of

$$\left(\frac{\partial \Delta p/\Delta p}{\partial Q/Q}\right)_{T_w} = \left(\frac{\partial \Delta p/\Delta p}{\partial G/G}\right)_Q \cdot\left[\left(\frac{\partial G/G}{\partial Q/Q}\right)_{T_w} - \left(\frac{\partial G/G}{\partial Q/Q}\right)_{\Delta p}\right] \quad (15)$$

and a change in outlet enthalpy,

$$\left(\frac{\partial h_0}{\partial Q/Q}\right)_{T_w} = \Delta h\left[1 - \left(\frac{\partial G/G}{\partial Q/Q}\right)\right]_{T_w}$$

Effect of Variation of Hydraulic Diameter

The case in which (q_{max}/Q), h_i, and L are fixed and the h_0 is a function of T_0 will be considered.

$J \equiv (G^{0.2}\ D^{1.2}/L)$ is defined so that one may write $(\Delta p_t/G^2) = f(J,\ T_0)$ and by differentiation

$$\frac{d\left(\frac{\Delta p_t}{G^2}\right)}{dJ} = \left(\frac{\partial\left(\frac{\Delta p_t}{G^2}\right)}{\partial J}\right)_{T_0} + \left(\frac{\partial\left(\frac{\Delta p_t}{G^2}\right)}{\partial T_0}\right)_J \frac{dT_0}{dJ} \quad (16)$$

For the case of constant pressure drop across the heated passage $(d(\Delta p_t) = 0)$,

$$\left(\frac{\partial G/G}{\partial D/D}\right)_{\Delta p,Q} = \frac{\left(\frac{\partial\left(\frac{\Delta p}{G^2}\right)}{\partial J}\right)_{T_o} 1.2J + \left(\frac{\partial\left(\frac{\Delta p}{G^2}\right)}{\partial T_0}\right)_J \left(\frac{\partial T_0}{\partial D/D}\right)_{\Delta p,Q}}{2\left(\frac{\Delta p}{G^2}\right) + \left(\frac{\partial\left(\frac{\Delta p}{G^2}\right)}{\partial J}\right)_{T_o} 0.2J} \tag{17}$$

from Equation (1) can be obtained the relation

$$\left(\frac{\partial G/G}{\partial D/D}\right)_{\Delta p,Q} = -1 - \frac{e_0 h_0}{T_0 \Delta h}\left(\frac{\partial T_0}{\partial D/D}\right)_{\Delta p,Q} \tag{18}$$

and the simultaneous solution of Equations (17) and (18) results in

$$\left(\frac{\partial T_0}{\partial D/D}\right)_{\Delta p,Q} = \frac{1 + \left(\frac{\partial G/G}{\partial J/J}\right)_{T_o}}{-\left(\frac{\partial G/G}{\partial T_0}\right)_J - \left[1 - 0.2\left(\frac{\partial G/G}{\partial J/J}\right)_{T_o}\right]\frac{e_0 h_0}{T_0 \Delta h}} \tag{19}$$

$$\left(\frac{\partial G/G}{\partial D/D}\right)_{\Delta p,Q} = \frac{1.2\left(\frac{\partial G/G}{\partial J/J}\right)_{T_o} - \left(\frac{\partial G/G}{\partial T_0}\right)_J \frac{T_0 \Delta h}{e_0 h_0}}{\left(\frac{\partial G/G}{\partial T_0}\right)_J \frac{T_0 \Delta h}{e_0 h_0} + 1 - 0.2\left(\frac{\partial G/G}{\partial J/J}\right)_{T_o}} \tag{20}$$

To complete the picture one should discover the variation of wall temperature with hydraulic diameter.

For a case of constant heat input, there can be obtained from Equations (9) and (12) the following:

$$\left(\frac{dT_w}{dD/D}\right)_{Q,\Delta p} = \left(\frac{\partial T_w}{\partial G/G}\right)_{T_b,Q}\left(\frac{\partial G/G}{\partial D/D}\right)_{Q,\Delta p} - \left(\frac{\partial T_w}{\partial T_b}\right)_{G,Q}\left(\frac{\partial G/G}{\partial D/D}\right)_{Q,\Delta p}\frac{(h_b - h_{in})T_b}{e_b h_b} \tag{21}$$

Ideal Gases in Laminar Flow

By methods similar to the method of Addoms (*1*) for laminar flow of ideal gases, with kinetic effects neglected, where

$$\mu = \alpha T^n \tag{22}$$

the flow sensitivity is

$$\left(\frac{\partial G/G}{\partial Q/Q}\right)_{\Delta p} = \frac{(n+1)\left(\frac{T_0}{T_i}\right)^{n+2} - (n+2)\left(\frac{T_0}{T_i}\right)^{n+1} + 1}{n\left(\frac{T_0}{T_i}\right)^{n+2} - (n+2)\left(\frac{T_0}{T_i}\right)^{n+1} + 2} \tag{23}$$

For air $n = 0.65$ and the flow shows sensitivity for all values of the temperature ratio from 1.0 to 3.7. At a temperature ratio of 3.7 the flow is unstable in the sense that any increase in heat input stops the flow.

The flow sensitivity for the kinetic losses only is

$$\left(\frac{\partial G/G}{\partial Q/Q}\right)_{\Delta p} = \frac{\left(\frac{T_0}{T_i}\right) - 1}{\left(\frac{T_0}{T_i}\right) - 2\frac{p_0}{p_i} + 1} \tag{24}$$

As this latter quantity is always positive, there will be some degree of heating for which the flow is moderately self-regulating.

Ideal Gases in Turbulent Flow

The flow sensitivity is

$$\left(\frac{\partial G/G}{\partial Q/Q}\right)_{\Delta p} = \frac{-(0.2n+1)\left(\frac{T_0}{T_i}\right)^{0.2n+2} + (0.2n+2)\left(\frac{T_0}{T_i}\right)^{0.2n+1} - 1}{(0.8 - 0.2n)\left(\frac{T_0}{T_i}\right)^{0.2n+2} + (0.2n+2)\left(\frac{T_0}{T_i}\right)^{0.2n+1} - 2.8} \tag{25}$$

Although there is never flow instability, there is always flow sensitivity unless counterbalanced by kinetic effects.

CONTROL OF FLOW SENSITIVITY BY VALVES AND ORIFICES

Control of Flow Sensitivity

The previous section of this paper gave the quantitative expressions for variation in outlet fluid temperatures and in wall temperatures resulting from nonuniformity of heat flux or net hydraulic diameter among the members of a group of flow passages. The greatest effectiveness in heat transfer to the coolant would be obtained in a design in which flow rates are so controlled as to operate each heated flow passage at its maximum safe wall temperature. It would be more practical to attempt to control flows to obtain uniform outlet fluid temperatures from the heated passages.

A flow-controlling valve sensitive to temperature at the outlet of each passage will be considered. If the outlet temperature increases, then the outlet valve is to open to permit increased flow. The sum of the pressure drops in the valve and in the heated passage must always equal the constant pressure drop available between the inlet and outlet fluid headers. Under these conditions how will the outlet temperature change when the heat flux changes with any specified sensitivity of outlet-flow-valve area to outlet temperature?

The pressure drop may be written as

$$\Delta p_v = M v_0 G_v^2 = M v_0 \frac{G_c^2 A_c^2}{A_v^2} \tag{26}$$

$$b \equiv \left(\frac{\partial \Delta p_c/\Delta p_c}{\partial Q/Q}\right)_a ; c \equiv \left(\frac{\partial \Delta p_c/\Delta p_c}{\partial G/G}\right)_Q \tag{27}$$

are defined and for the differential change in pressure drop of the heated passage one writes

$$\frac{\partial \Delta p_c}{\Delta p_c} = b\frac{\partial Q}{Q} + c\frac{\partial G}{G} \tag{28}$$

From Equation (1) at fixed D, L, h_i one gets

$$\frac{\partial G}{G} + \frac{\partial h_0}{\Delta h} = \frac{\partial Q}{Q} \tag{29}$$

$$a \equiv \frac{\partial v/v}{\partial h/h} \tag{30}$$

is defined and Equations (11), (27), (29), and (30) are substituted into Equation (28) to get

$$\Delta p_v = ae\frac{\partial T_0}{T_0}\Delta p_v + 2\frac{\partial Q}{Q}\Delta p_v - \frac{2eh_0\,\partial T_0}{T_0 \Delta h}\Delta p_v - 2\frac{\partial A_v}{A_v}\Delta p_v \tag{31}$$

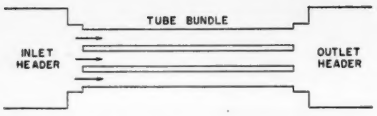

Fig. 2. Sketch of cooling tubes.

$$\partial \Delta p_c = b \frac{\partial Q}{Q} \Delta p_c + c \frac{\partial Q}{Q} \Delta p_c - \frac{ceh_0 \, \partial T_0}{\Delta h T_0} \Delta p_c \quad (32)$$

For constant total pressure drop,

$$\partial \Delta p_v + \partial \Delta p_c = 0 \quad (33)$$

$$R \equiv \frac{\Delta p_v}{\Delta p_c} \quad (34)$$

is defined, and by summing Equations (31) and (32) and setting equal to zero one obtains

$$\left(\frac{\partial T_0/T_0}{\partial Q/Q}\right)_{\Delta p} = \frac{(2R + b + c)}{2RT_0\left(\frac{\partial A/A}{\partial T_0}\right)_{\Delta p} + \frac{eh_0}{\Delta h}(2R + c) - aeR} \quad (35)$$

This equation gives the variation in outlet temperature obtained with an outlet valve of given sensitivity, certain values of the flow derivatives, and the ratio of pressure drops across the control valve and in the heated passage.

A similar derivation can be made for the case of a variable-area control valve which is placed at the inlet of the heated passage but which responds to variations in outlet temperature. This gives

$$\left(\frac{\partial T_0/T_0}{\partial Q/Q}\right)_{\Delta p} = \frac{(2R + b + c)}{2RT_0\left(\frac{\partial A/A}{\partial T_0}\right)_{\Delta p} + \frac{eh_0}{\Delta h}(2R + c)} \quad (36)$$

Comparison of Equations (31) and (32) shows that the temperature response required is less for a valve at the inlet than for one at the outlet. However, the need to transmit information from the outlet location to the inlet could well be a very difficult design problem.

It follows from Equation (36) that for a fixed-area valve (orifice) at the inlet the relationship is

$$\left(\frac{\partial T_0/T_0}{\partial Q/Q}\right)_{\Delta p} = \frac{(2R + b + c)}{\frac{e_0 h_0}{\Delta h}(2R + c)} \quad (37)$$

As the value of R defined in Equation (34) is increased, the outlet temperature sensitivity decreases. This is to be expected when the flow through the valve rather than through the heated passage provides the controlling pressure drop. It may be of interest to compare the case of a fixed outlet valve to a fixed inlet valve by using Equation (35) for an orifice of $(\partial A/A/\partial T_0)_{\Delta p} = 0$ and Equation (37). One obtains

$$\frac{R_i}{R_0} = \frac{2b - a\frac{\Delta h}{h_0}(b + c)}{2b + 2a\frac{\Delta h}{h_0}R_0} \quad (38)$$

As this indicates a ratio of less than one, it appears that an inlet orifice will always be less expensive in pressure drop than an outlet orifice of equal effectiveness. In fact it could be shown that an outlet orifice of very large pressure drop is only moderately better than no orifice at all.

Control at Less than Full Load

The value of fixed orifice control at less than design load for the reactor will be considered. With operation presumed at the same inlet and outlet temperatures at all loads, G must vary in proportion to Q (the reactor heat load). The pressure drop through the orifice will vary with G^2 while pressure drop through the heated passage will vary with $G^{1.8}$ approximately. At less than design load, then, the ratio R will be somewhat less than its design value. This change is predictable, small, and easily allowed for in the design. However, it means that the orifice must

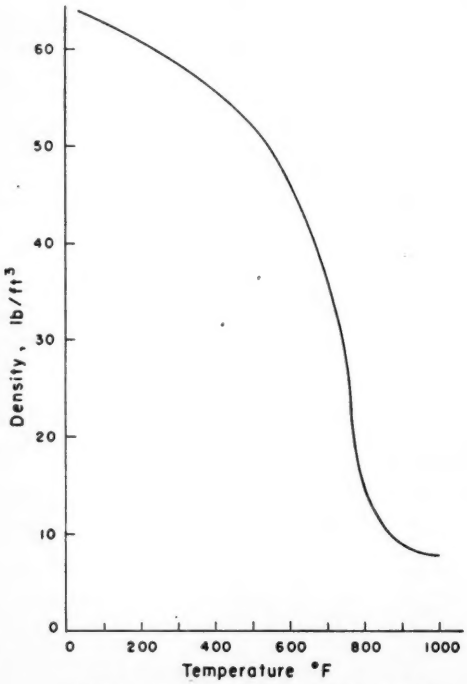

Fig. 3. Density of water at 5,000 lb./sq. in.

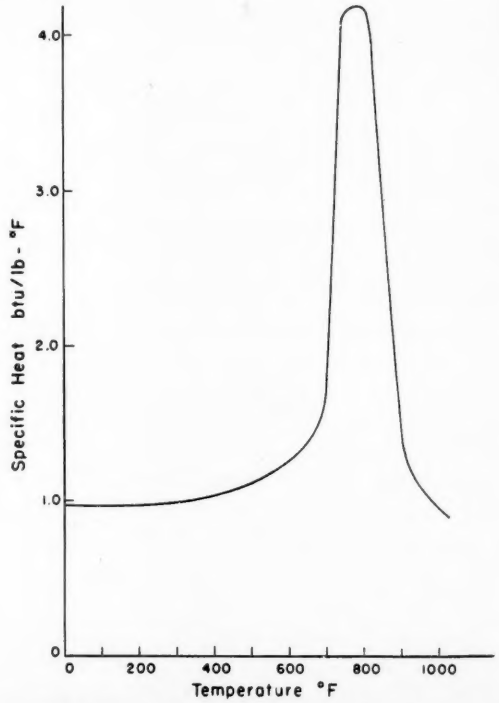

Fig. 4. Specific heat of water at 5,000 lb./sq. in.

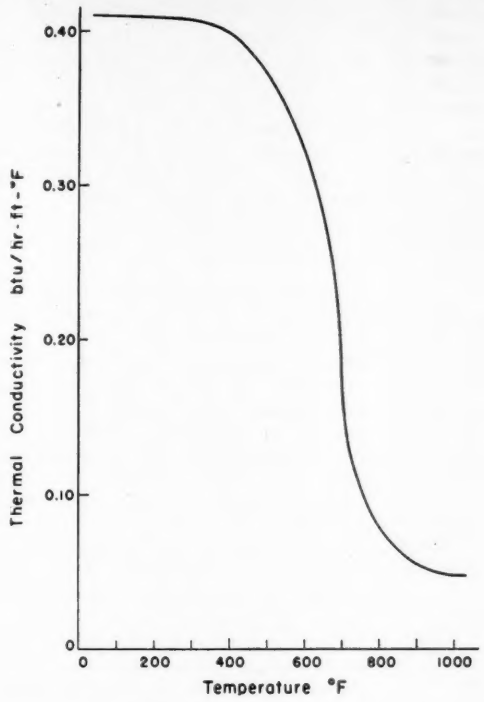

Fig. 5. Thermal conductivity of water at 5,000 lb./sq.in.

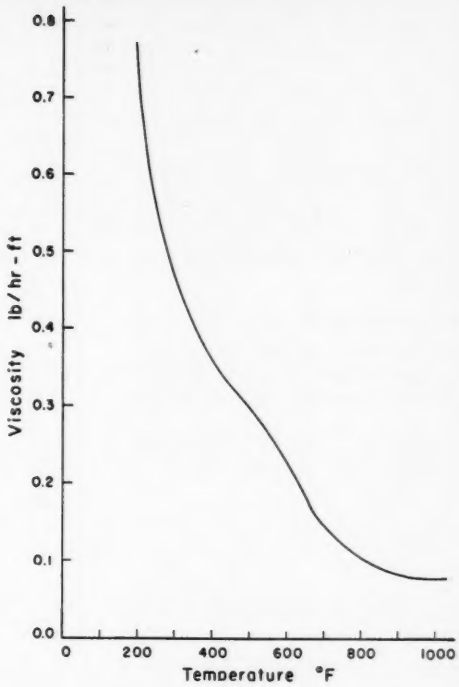

Fig. 6. Viscosity of water at 5,000 lb./sq. in.

be made to dissipate a slightly larger pressure drop at design loads in order to retain control action at reduced loads.

Manufacturing Tolerances for Orifices

If Equation (37) for a variable-area inlet valve is rewritten for the case of fixed heat input ($\partial Q = 0$), under the condition that all area variations are due to manufacturing tolerances, one gets for an outlet temperature sensitivity in this case

$$\left(\frac{\partial T_0}{\partial A/A}\right)_{\Delta p, Q} = -\frac{2RT_0\Delta h}{eh_0(2R + c)} \quad (39)$$

For a sharp-edged orifice one can write

$$\Delta p_v = \frac{G_v^2}{2k^2 g\rho} = \frac{G_c^2 A_c^2}{A_v^2 2k^2 g\rho}\frac{\Delta p_c R}{r} \quad (40)$$

For an orifice plate with N equal-size holes the area of the orifice is

$$A_v = \frac{\pi}{4} D_v^2 N \quad (41)$$

which combines with Equations (39) and (40) to give for the tolerance on orifice diameter

$$\frac{\partial D_v}{D_v} = -\frac{eh_0(2R + c)}{4T_0 R\Delta h}(\partial T_0) \quad (42)$$

where the value of the diameter is obtained from

$$D_v = 0.949\left(\frac{G_c A_c}{kN}\right)^{1/2}\left(\frac{r}{\rho g\Delta p_c R}\right)^{1/4} \quad (43)$$

The tolerance given by Equation (42) assumes that all hole diameters in a multiple-hole orifice plate deviate in the same direction.

CALCULATIONS FOR A SUPERCRITICAL WATER BOILER

The material presented in the previous sections of this paper will be used for the discussion of a particular case. This case is typical of the results obtained in a series of calculations on water at supercritical pressures, heated in parallel tubes of normally identical heat input, with the tubes between common headers. It might be noted that the temperatures and pressures of the example are similar to those of a large central-station supercritical-pressure boiler now being built for a utility company (*3*). This boiler has one-pass flow instead of recirculation as in most large boilers and would be subject to problems of flow sensitivity. Dimensions, flow rates, and heat flux are assumed arbitrarily at reasonable values and do not reflect the values for any industrial power plant or any nuclear reactor.

The Typical Case

A parallel set of cooling tubes, as sketched in Figure 2, with all the tubes nominally having identical heat input and flow conditions as given in Table 1 will be considered. The physical arrangement is pictured as several tubes clustered in a bundle with bundles arranged between large headers. The headers are assumed to be so large as to allow calculations on the basis of loss of one half a velocity head at tube entrance and one velocity head at tube outlet.

Table 1

p	5,000	lb./sq. in.
T_i	515	°F.
T_0	1,150	°F.
Q	3×10^5	B.t.u./(hr.)(sq. ft.)
G	1.8×10^6	lb./(hr.)(sq. ft.)
D	0.0416	ft.
L	62	ft.

It is assumed that the pressure drop between the headers is very small compared to 5,000 lb./sq. in. The relevant properties of water at 5,000 lb./sq. in. are shown in Figures 3 to 6. The density (Figure 3) and specific heat (Figure 4) are from Keenan and Keyes (*4*); the viscosity and thermal conductivity are extrapolated from the sparse data at lower pressures. It should be noted that the water undergoes eightfold expansion from 515° to 1,150°F.

For the example of Table 1, it is found that the maximum temperature of the tube heating surface is 1,370°F. and the pressure drop is 44.9 lb./sq. in. Heat transfer coefficients and friction factors were evaluated according to calculations of Goldmann (*2*). For present purposes, the Goldmann predictions give results substantially the same as if the method of Deissler (*5*) were used or if the usual isothermal turbulent flow formulas were used with properties based on mean film temperatures.

Flow-sensitivity Derivatives

The calculations for the example of Table 1 gave numerical values for the quantities of Equations (7) and (8) as follows:

$$\left(\frac{\partial \Delta p/\Delta p}{\partial Q/Q}\right)_G = 1.50;$$

$$\left(\frac{\partial \Delta p/\Delta p}{\partial G/G}\right)_Q = 0.40;$$

$$\left(\frac{\partial G/G}{\partial Q/Q}\right)_{\Delta p} = -3.75$$

This latter quantity is the *flow sensitivity*.

From this flow sensitivity and Equation (1) can be calculated for this case.

$$\left(\frac{\partial h_0/\Delta h}{\partial Q/Q}\right)_{\Delta p} = 4.75;$$

$$\left(\frac{\partial T_0}{\partial Q/Q}\right)_{\Delta p} = 6{,}700°\text{F}.$$

If one of the group of tubes between the common headers should receive 1% more heat input than its neighbors, then the fluid outlet of that tube would run 67°F. hotter than the others. It is of greater importance to evaluate the probable effect on wall temperature. In some designs for maximum performance any appreciable increase in wall temperature could seriously limit the life of the machine. Numerical evaluation of Equation (14) gives

$$\left(\frac{dT_w}{dQ/Q}\right)_{\Delta p} = 8{,}000°\text{F}.$$

This tube of 1% higher heat input is also running at 80°F. increased wall temperature and 3.75% reduced flow. These figures are impressive when one considers that many significant heat transfer as well as nuclear variables cannot be predicted or even measured to better than several per cent accuracy.

The designer will also be interested in the effect of nonuniformities in tube diameters. The flow sensitivities in this regard are indicated by the calculated values of the derivatives of Equations (19), (20), and (21):

$$\left(\frac{\partial T_0}{\partial D/D}\right)_{\Delta p, Q} = -10{,}300°\text{F};$$

$$\left(\frac{\partial G/G}{\partial D/D}\right)_{\Delta p, Q} = 6.3$$

$$\left(\frac{dT_w}{dD/D}\right)_{\Delta p, Q} = -11{,}500°\text{F}.$$

One can calculate the sensitivity derivatives reflecting the influence of header pressures on fluid and wall temperatures.

$$\left(\frac{\partial T_0}{\partial \Delta p/\Delta p}\right)_Q = -3{,}400°\text{F}.;$$

$$\left(\frac{\partial T_w}{\partial \Delta p/\Delta p}\right)_Q = -3{,}850°\text{F}.$$

Reduction of Flow Sensitivity

The flow and temperature changes cited above for small changes in heat input, tube diameter, and pressure drop can be reduced appreciably by modifying the design to incorporate orifices at the tube inlets.

Probably the best combination of effectiveness and practicality is to build in a fixed-area orifice at the inlet of each tube. Comparison with variable valves and orifices at the tube outlet were made earlier in this paper. It does not require very large pressure expenditure across the orifice to bring about marked reduction in sensitivity. Table 2 shows how the sensitivity to nonuniformity in heat input can be reduced by orifices.

It is seen that even the case of orifice pressure drop just equal to tube pressure drop makes the flow in the tube nearly independent of the power variation. The infinite orificing would make the flow constant, regardless of power, as for a constant-property fluid.

From Equation (42) one can calculate that a tolerance of 1% on the diameter of the controlling orifice will give a variation of 20°F. in the outlet fluid and the wall temperatures. It would be practical to hold tolerances to much smaller limits.

The sensitivity of the flow to variations in hydraulic diameter among the heated passages is also greatly reduced by the use of an inlet orifice.

Other Design Methods

Another possibility for decreasing flow sensitivity is to divide the tubes into several shorter lengths, with intermediate flow-mixing headers to permit equalization of temperatures and pressures across the tube bank. This would prevent the accumulation of effects along the entire length of an excess-powered tube. The major difficulty in actual practice is achieving good lateral temperature equalization in small headers. However, pressure equalization in intermediate headers even without appreciable mixing will substantially reduce sensitivity.

When heat-generation patterns as well as flow sensitivities are known, it is possible to calculate net mixed temperatures as well as the effects of change in operating levels of power or temperature. Both of the procedures have been investigated in studies subsequent to those reported herein.

CONCLUSION

The usual degree of sensitivity demonstrated in this example is primarily inherent in the nature of the fluid. However, engineering design can counteract most of the bad effects if the system is carefully studied. Accurate fluid friction and heat transfer data are prerequisites to successful design of power plants using sensitive fluids.

ACKNOWLEDGMENT

The work reported here draws on ideas and results of related studies by several other staff members of Nuclear Development Corporation of America, notably Kurt Goldmann, R. C. Ross, N. R. Adolph, and Leon Joseph. Elaine Scheer and Gloria Sullivan performed the computations from which these results were taken.

NOTATION

A = area, sq. ft.
a = symbol for derivative as defined in the text
b = symbol for derivative as defined in the text
c = symbol for derivative as defined in the text
D = equivalent diameter of heated passage or tube
e = symbol for derivative as defined in the text
G = mass velocity, lb. mass/(hr.)(sq. ft.)

TABLE 2

Orifice pressure drop / tube pressure drop R	Increase in water outlet temperature (°F.) for tube with 1% excess power [Equation (37)]	Increase in maximum heating-surface temperature (°F.) for tube with 1% excess power [Equations (37) and (14)]
0*	67	80
0.5	29	35
1	23	28
2	19	23
10	15	18
∞	14	16

*No orifice.

g = conversion factor, 32.2 lb. mass-ft./lb. force-sec.^{2}
h = enthalpy, B.t.u./lb. mass
Δh = difference in enthalpy between two locations, B.t.u./lb. mass
J = symbol for parameter as defined in the text
k = orifice coefficient
L = length of heated passage, ft.
M = constant of proportionality
N = number of equal-size holes in each orifice plate
n = exponent on mass velocity term or on temperature
p = pressure, lb. force/sq. ft.
Δp = difference in pressure between two locations, lb. force/sq. ft.
Q = average heat flux along heated passage, B.t.u./(hr.)(sq. ft.)
q = local heat flux, B.t.u./(hr.)(sq. ft.)
R = ratio of control valve pressure drop to fluid passage pressure drop
r = fractional permanent pressure loss across an orifice
T = temperature, °F.
v = specific volume, cu. ft./lb. mass
x = distance from passage inlet, ft.
α = coefficient in Equation (22)
ρ = density, lb. mass/cu. ft.
τ = shear stress, lb. force/sq. ft.
σ = fraction of cut-off in sine distribution
μ = viscosity, lb. mass/(ft.)(hr.)

Subscripts

a = acceleration
b = bulk
c = heated passage
e = entrance, exit
f = friction
i = inlet
max = maximum
o = outlet
t = total
v = valve or orifice
w = wall

LITERATURE CITED

1. Addoms, J. N., informal memorandum, N.E.P.A. Project, Oak Ridge, Tennessee (Aug. 15, 1949).
2. Goldmann, Kurt, *Chem. Eng. Progr. Symposium Series* No. 11, **50**, 105 (1954).
3. *Electrical World*, pp. 72 ff. (June 29, 1953).
4. Keenan, J. H., and F. G. Keyes, "Thermodynamic Properties of Steam," John Wiley and Sons, Inc., New York (1950).
5. Deissler, F. G., *Trans. Am. Soc. Mech. Engrs.*, **76**, 73 (1954).

Presented at Nuclear Science and Engineering Congress, Cleveland.

Light Transmittance as a Measure of Interfacial Area in Liquid-liquid Dispersions

VIRGIL G. TRICE, JR., and WALTON A. RODGER

Argonne National Laboratory, Lemont, Illinois

Interfacial area in liquid-liquid systems has been measured photographically. Precision and accuracy of the method have been shown to be better than 10%. To avoid tedium of counting drops, a simple light probe of easily reproducible design has been developed to measure the light transmission through the dispersions formed. A correlation of light transmittance with interfacial area is presented and its usefulness and limitations are discussed.

Frequently workers concerned with dispersions of immiscible liquids desire knowledge of the interfacial area of these systems. Unfortunately it is generally difficult or impossible to determine the interfacial area of liquid-liquid dispersions. In the few cases where interfacial areas have been determined, most investigators have relied on photographic techniques.

In recent years the phenomenon of light scattering by small particles has been the subject of a number of investigations (*14*); however, very little work has been reported in the literature concerning light scattering as a measure of particle size in liquid-liquid dispersions. Undoubtedly a major deterrent to such investigations has been the problem of measuring the interfacial area of rapidly coalescing disperse systems by other than photographic methods.

In this paper a photographic technique for measuring interfacial area is described.

Also, an empirical correlation based on theoretical considerations is presented which gives the light transmittance of liquid-liquid dispersions as a function of the interfacial area. Experimental data are presented for several nonabsorbing (water-white) liquid pairs of differing relative refractive indexes.

PREVIOUS WORK

Most of the interest in light scattering has been restricted to very dilute monodisperse* systems of small particles generally less than 1 μ in diameter. Mathematical treatments of concentrated polydisperse† systems are not available. In addition, there are few quantitative data available relative to liquid-liquid or gas-liquid dispersions.

It is interesting to note that in 1925 Stamm and Svedberg (*19*) were interested in the relationship between the right-angle scattering of light and the size distribution of soap-stabilized benzene-water emulsions. They suggested a linear relationship between light transmittance and concentration for a given particle size. Clark and Blackman (*3*) investigated light transmittance as a measure of the interfacial area of foams. On the basis of admittedly qualitative data, a linear relationship between light transmittance and volumetric area was suggested.

Recently Langlois and coworkers (*11, 12*) published a correlation of light transmission with interfacial area for liquid-liquid systems. Their results were correlated empirically by a linear equation in the following form:

$$\frac{I_0}{I} = 1 + \beta A \qquad (1)$$

where

I_0/I = the ratio of incident to emergent light intensity
A = interfacial area per unit volume of total mixed phases (volumetric area)
β = a constant characterizing a specific liquid pair

This relationship was considered to be independent of the volume-fraction dispersed phase. The constant β was given as a function of the relative refractive index of the dispersed phase.

The papers by Langlois are of particular interest because they represent the first successful attempt to establish a quantitative relationship between light transmission and volumetric area. However, no provisions were made for variation of the optical path length, and each light probe required individual calibration because the reproducibility of results with different probes of the same design was poor (*10, 15*). Duplication of this work would be difficult.

It is apparent from the literature that the theoretical equations relating particle size and concentration to light transmittance are limited and cannot be applied to concentrated polydisperse systems of large spherical particles. The available empirical relationships for polydisperse systems do not demonstrate satisfactory accuracy and precision. In addition, it is difficult to reproduce the equipment design, and each light-detector unit requires individual calibration.

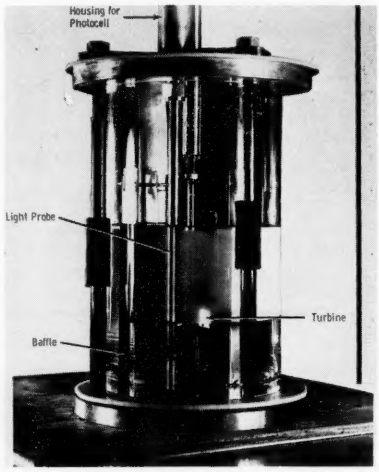

Fig. 1. Mixing vessel.

THEORY

Basic Theory

The light transmitted through a polydisperse system of transparent isotropic spherical particles provides a measure of the interfacial area if it can be demonstrated that light transmission is a function of the total projected area. This means that it must be shown that the light transmission is a function of the mean surface volume or sauter diameter d_{sv}. Conversely a correlation is not possible if the scattered light energy is sensitive to the particle-size distribution. For a polydisperse system consisting of N_i particles of diameter d_i in a given size interval

$$d_{sv} = \frac{\sum N_i d_i^{\,3}}{\sum N_i d_i^{\,2}} \qquad (2)$$

For a volume fraction of dispersed phase of ϕ the volumetric area is defined as follows:

$$A = \frac{6}{d_{sv}}\phi \qquad (3)$$

The factors which control light transmittance are embodied in the familiar extinction or Beer-Lambert relationship:

$$Sn\,dL = \frac{dI}{I} \qquad (4)$$

The scattering cross section S is the ratio of the light energy lost by scattering to the incident light energy per unit area and n is the number of particles per unit volume. Integrating over the distance between light source and detector L, as the incident light diminishes from I_0 to I, yields the conventional extinction equation

$$\ln \frac{I_0}{I} = SnL = K_s \frac{d^2\pi}{4} nL \qquad (5)$$

where

$$K_s = \frac{4S}{d^2\pi} \qquad (6)$$

d = particle diameter

Experimental data and calculations by several investigators (*2, 5* to *9, 18*) based on theory developed by Mie (*13*) show that the scattering area coefficient K_s is extremely sensitive to particle sizes near the wave length of the incident light. The effect of particle diameter, however, decreases with increasing particle size. Calculations by Boll and coworkers (*2*) show that for the limiting conditions of this investigation K_s is essentially constant for particles larger than 50 μ.

In this investigation the observed particle-size distribution has generally been between 50 and 2,000 μ and the scattering area coefficient may be considered as a constant with respect to particle diameter. Therefore, the drop diameter d may be defined in terms of the sauter diameter d_{sv}, and Equation (5) may be written in terms of the interfacial area per unit volume of total mixed phases A and a scattering factor α.

$$\ln \frac{I_0}{I} = \frac{K_s}{4}\pi d^2 nL$$

$$= \frac{K_s}{4}\pi d^2\left(\frac{6N\phi}{N\pi d^3}\right)L = \alpha AL \qquad (7)$$

For a given incident-light wave length the scattering factor α should be a unique function of the relative refractive index of the liquid pair.

Applied Theory

In the basic relationship, Equation (4), it is assumed that light once scattered from the path of the primary beam is lost. This is true only for very dilute dispersions. For the systems studied, however, light scattered from the primary beam may be returned to the original path by secondary scattering. Hence multiple scattering is an important factor which

*Monodisperse in the sense that all particles in the dispersion are the same size.
†Polydisperse in the sense that a distribution of particle size is present.

must be considered. The effect of multiple scattering is a function of both the relative refractive index and the incident-light-beam diameter.

Other factors which may be considered to have a significant effect on the transmittance relationship are functions of the light source and detector geometry. As an example the problem of measuring the emergent light intensity I may be considered. The incident light I_0 is a collimated beam. The emergent light I is defined as that portion of I_0 which passes unimpaired through L cm. of dispersion. This means that the emergent light is that portion of the incident light scattered in the forward direction parallel to the path of the primary beam. Gumprecht and Sliepcevich (*4*) point out that it is technically impossible to obtain an exact measure of the emergent light. Any detector design will measure, in addition to light scattered in the forward direction, some of the light scattered at small angles from the path of the primary beam.

The transmission relationship [Equation (7)] may be modified to conform with these practical considerations:

$$\ln \frac{I_0}{I} = f(\alpha, A, L) \qquad (8)$$

Equation (8) shows that an exponential relationship exists between light transmittance and some function of α, A, and L. The exact nature of the function must be determined experimentally.

EXPERIMENTAL

Experimental techniques and equipment were developed to measure the interfacial area per unit volume of total mixed phases (volumetric area) and the light transmittance of the dispersion at a specified optical path. The volumetric area was determined photographically, and the light transmittance by photoelectric measurements.

Mixing Equipment

Dispersions were created in 5 9/16-in.-diam. Pyrex mixing vessel shown in Figure 1. The vessel was equipped with four baffles, each one tenth of the diameter of the mixing vessel in width, and a 3-in., six-blade flat-blade turbine. The baffles and agitator were constructed to conform with the design suggestions of Rushton *et al.* (*17*). All metallic components were of 304 stainless steel; gaskets were of Teflon.

Light Source and Detector

The photoelectric equipment required for light-transmittance measurements consisted of three major components: a light source to provide a uniform, collimated beam; a sensitive light-detector unit; and an electronic circuit to measure the amplified output of the detector unit. In the design of the equipment ruggedness and reproducibility were of prime importance. Of secondary concern was the desire to mount as much of the equipment as possible external to the mixing vessel to minimize contamination of the liquid and interference of the normal flow pattern.

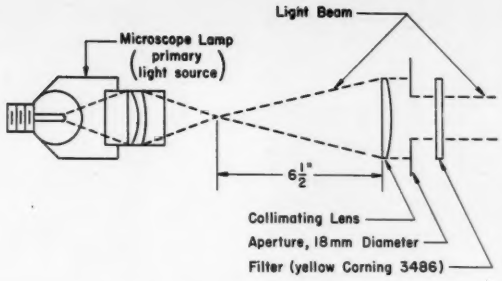

Fig. 2. Schematic diagram of light source.

Both the light source and detector were externally located. The light source was located below and the detector above the mixing vessel. A light pipe or probe extended down from the detector into the dispersion. The distance from the bottom of the vessel to the end of the light pipe determined the optical path.

The light source was a Universal Microscope Illuminator, No. 353, made by the American Optical Company and fitted with a 6-volt automobile bulb. Light from the microscope lamp converged at the focal point of a condensing lens. The collimated beam leaving the lens was restricted with an 18-mm. aperture and filtered with a Corning 3486 yellow filter. The light source is shown schematically in Figure 2.

The emergent light was transmitted to a photocell by a glass sensing probe extending into the dispersion. The probe was made adjustable to allow light paths of variable lengths through the dispersion. A 30-cm. ⅜-in.-diam. Pyrex 7740 glass rod polished on both ends served as the probe. The detector unit is shown in Figure 3.

It was found that more reproducible readings were obtained if the sides of the probe were protected from stray light by a platinum mirror finish. The mirror finish was obtained by painting the cleaned rod with a thin coat of Liquid Bright Platinum No. 05, Hanovia Chemical and Manufacturing Company, then heating to dull cherry red to produce the bright finish. The several probes made in this manner gave reproducible results. Overheating resulted in a dull finish which gave inconsistent readings.

Light was transmitted from the probe to the photocell through a seal of Dow Corning 200 silicone oil, which also lubricated the joint and prevented chipping. Black ⅜-in. rubber tubing covered the junction to prevent stray light from reaching the photocell.

An end-type photoelectric cell, RCA 1P42, was used to give a better optical seal than that obtainable from side-entry types. A vacuum tube was used in preference to a gas type, as the linearity of response was better. The tube was sensitive in the visible range, allowing liquids with interfering colors to be detected. The 1P42 tube, together with the yellow filter, responded in the light band of 560 ± 50 mμ.

The output of the photocell was amplified and measured by balancing against a constant voltage with a calibrated helipot resistance. As the photocell had a linear response, the resistance required was a measure of the light energy reaching the photocell and was used in calculations without conversion as ratios of light energy are involved.

Volumetric Area

The volumetric area which exists in a liquid-liquid system during agitation was determined from photographs of the dispersion. Photographs were taken through the base of the mixing vessel with a 35-mm. Leica camera fitted with an Ektar 5-cm. lens, reflex prism, and close-range bellows using Kodak Plus-X film. Illumination was provided by a 0.0002-sec. Comet repeating flash lamp mounted beside the vessel. Light from the droplets reached the camera by reflection. Pictures with good drop resolution were obtained by overexposing the film by one stop and double-developing the negative. Resolution was improved by photographing through a G filter. A typical photograph is shown in Figure 4.

Preliminary runs were made to establish techniques for area measurements in a rectangular-cross-section mixing vessel specially designed to facilitate photographic study. An assortment of glass beads dispersed in a mixture of carbon tetrachloride and tetrabromoethane was photographed. These beads ranged in diameter from 210 to 710 μ. Several observers working independently determined the interfacial area from photographs by tracing the droplets in the plane of focus and classifying the diameters.

The results of this test are presented in Table 1. They show both the accuracy and precision of the photographic method, based on measurements by several independent observers, to be better than ±5%.

PROCEDURE

The following procedure was used to obtain experimental data. Equal-volume portions of each phase were placed in the mixing vessel and equilibrated for from 2 to 4 hr. to saturate the liquid pair mutually. Organic liquids were pretreated by distillation. The aqueous phase was distilled-water or glycerin-water mixtures. Data were obtained at 25°C. Refractive indexes were measured at the sodium D line.

For each system at selected impeller speeds transmittance measurements were obtained at optical path lengths of 1, 1.5, and 2.0 cm. Photographs were taken to provide a measure of the volumetric area at the selected impeller speeds. The range of impeller speeds that could be employed was

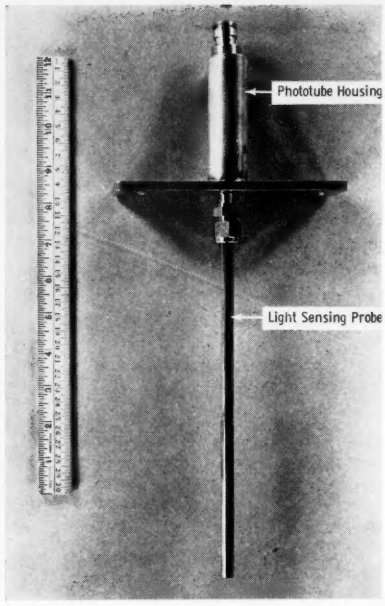

Fig. 3. Light-detector unit.

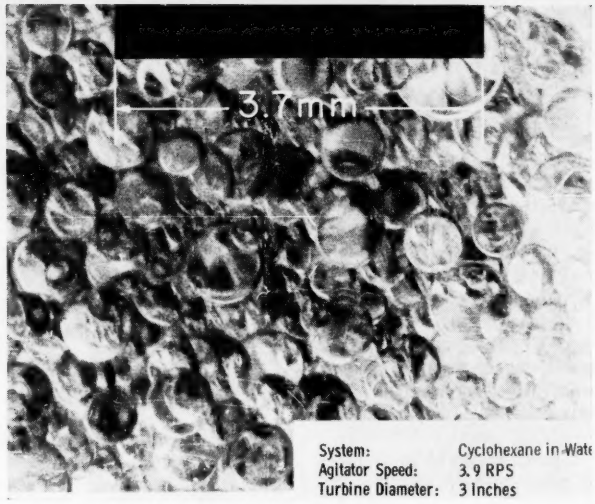

Fig. 4. Typical photograph of dispersion.

limited by the physical properties of the liquid pair. It was necessary to maintain sufficient agitation to ensure complete emulsification but not enough to beat air into the system thereby changing the optical properties. The volumetric area under a given set of conditions was found to be a reproducible function of agitator speed if surface-active contamination were absent. The presence of surface-active contamination was qualitatively indicated by the presence of surface films and by a marked change in the dispersion settling time. To minimize contamination, the equipment was thoroughly cleaned before each run.

The incident light I_0 was defined as the light energy per unit area measured through the clear-field phase before emulsification, and the emergent light I was defined as that portion of the incident light which reached the detector probe after emulsification.

The reading of the incident light was arbitrarily controlled by the voltage applied to the light source. Agitation was begun and emergent light readings were taken when steady state conditions were reached (from 2 to 45 min.), as indicated by a constant transmittance reading. Immediately after each emergent-light reading a measurement was taken to establish the reading for zero transmittance, as small changes in this quantity had considerable effect on the value obtained for the emergent light.

CORRELATION OF TRANSMITTANCE DATA

The experimental data were correlated empirically by means of a theoretically based exponential relationship:

$$\ln \frac{I_0}{I} = f(\alpha A L^{0.80}) \qquad (9)$$

The experimental data for several liquid pairs are presented in Table 2.

The experimentally determined scattering factor α is shown as a function of the relative specific refraction in Figure 5. The relative specific refraction M is defined by the following equation:

$$M = \left| \frac{m^2 - 1}{m^2 + 2} \right| \qquad (10)$$

where

m = refractive index of drop/refractive index of field phase

The scattering factor α is the optical parameter. It is primarily a measure of the effect of multiple scattering on the light transmittance as measured with the equipment employed in this investigation. For the specified light source and detector geometry, the scattering factor was found to be a complex function of the relative refractive index.

Bailey (*1*) and Rose and French (*16*), working with small solid particles less than 10 μ in diameter, obtained a satisfactory correlation by presenting their optical parameter as a function of the relative specific refraction or Lorenz-Lorentz coefficient M. In the present work the relative specific refraction proved to be a satisfactory correlating tool for polydisperse systems of large spherical particles ranging from 50 to 2,000 μ, as evidenced by the correlation.

Equally satisfactory correlations for the scattering factor may be obtained with the relative refractive index or the refractive-index difference. However, the Lorenz-Lorentz coefficient is preferable because a unique curve is obtained which should hold for values of the relative-refractive index less than 1. The relative-refractive index for water in oil dispersions is less than unity. Transmittance data for 40, 20, and 10% dispersions which included some water-in-oil data were presented in a report by Rea and Vermeulen (*15*). For purposes of comparison, these data for each volume fraction were replotted in terms of an exponential relationship. Not only were improved correlations obtained, but it was also found that the correlation of scattering factor with relative specific refraction M held for values of the relative-refractive index m both greater than and less than unity.

Unfortunately, it was not possible in this investigation to obtain data for water-in-oil systems because they proved to be unstable. Photographs of 50% dispersions of water in oil showed that

Table 1. Glass-bead Test for Accuracy and Precision of Photographic Method for Measuring Interfacial Area per Unit of Volume Dispersion

Photographically determined interfacial area

Observer	Sq. cm./cc.
A	123
B	121
C	125
D	122
E	122

Interfacial area determined by classification of glass beads

	Sq. cm./cc.
Maximum value	129
Minimum value	107
Arithmetic average value	117
Average value determined photographically	123

Size distribution of beads used in test

Diameter, μ	Wt. %
210–297	4.1
420–500	35.1
500–590	29.6
590–710	31.2

they consisted of drops of water in a field of oil with small drops of oil in the larger water drops.

The generalized correlation showing light transmittance as an exponential function of a scattering factor α, the volumetric area A, and the optical path L is presented in Figure 6. The average deviation in area based on transmittance is 4.7%. The optical path length L, it will be noted, appears as a reduced power function. An exponent less than unity is required because the attenuation of the light beam in passing through the dispersion was less than would be predicted from basic light-extinction theory, which ignores the effect of multiple light scattering. This correlation presents data for nine liquid pairs. The range of relative-refractive index was 1.004 to 1.168. The range in interfacial area was from 20 to 90 sq. cm./cc.

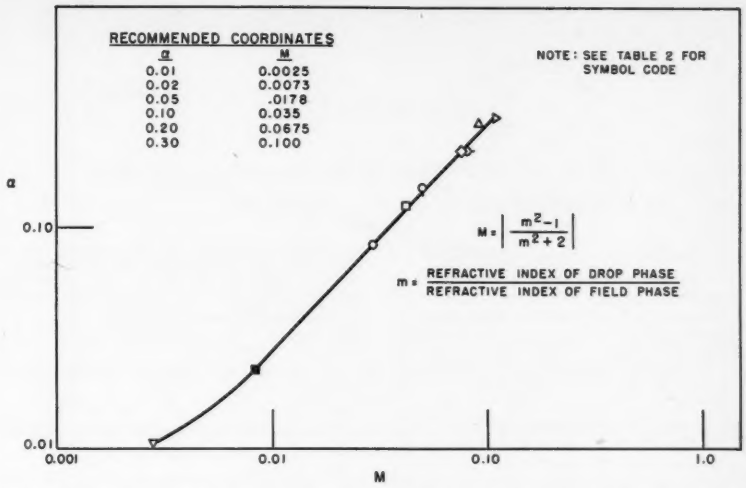

Fig. 5. Scattering factor α as a function of the relative specific refraction M for yellow-light spectrum.

DISCUSSION

General Observations

Perhaps the most surprising fact was the limited range of particle sizes present in any given dispersion. It was evident from the photographs that the particle size usually varied by not more than a factor of 5. In rare cases the particle size was found to vary by as much as a factor of 15. Usually the drops appeared to be perfect spheres except in cases where the drops were relatively large. It was interesting to note that systems characterized by large drops, about 1.5 mm., did not correlate quite so well as others, possibly because of deformation of the large drops.

Investigators have occasionally reported difficulty in deciding which phase is dispersed and which is continuous. It should be borne in mind that a phase present in a volume fraction greater than 0.50 may still be the dispersed phase. The dispersed phase may be detected by simply observing the settling pattern of the dispersion to determine the direction of travel of the droplets toward the interface.

The continuous phase is usually that phase which best wets the mixing vessel. For that reason the dispersions studied in this work were oil in water with the exception of the methyl isobutyl ketone–glycerin-water system where methyl isobutyl ketone was the continuous phase.

Reproducibility of Data

Consecutive transmittance readings were reproducible to within 3% and in most cases 1%. In the case of duplicate runs, with the same supply of the liquid pair, the introduction of additional variables such as substitution of probes and readjustment of the optical path length caused some loss in reproducibility. However, transmittance measurements for these duplicate runs were usually within 3% and rarely varied by as much as 5%.

Both area and transmittance data used in the correlation were obtained from measurements at the bottom of the mixing vessel. For that reason, there can be little doubt that the photographically determined areas represented the area at the point where the transmittance measurements were obtained. However, even considering the extreme degree of turbulence in these agitated systems, there might be some question concerning the homogeneity of the bulk of the dispersion, particularly near the agitator. To resolve this question a simple test was devised

Table 2. Summary of Experimental Data

System	Symbol	Refractive index* Drop phase	Refractive index* Field phase	Volumetric area, sq.cm./cc.	ln I_0/I at specified optical path length 1.0 cm.	1.5 cm.	2.0 cm.
Bromobenzene in water	▷	1.5575	1.3335	33.2	4.17	5.02	
Monochlorobenzene in water	△	1.5221	1.3330	22.5	3.28	3.95	
				27.7	3.62	4.34	
				22.2	2.73	3.33	3.82
Benzene in water	○	1.4975	1.3332	28.5	3.20	3.84	4.32
				35.6	3.56	4.20	4.65
				28.8	3.04	3.72	4.25
Xylene in water	◇	1.4877	1.3330	34.0	3.57	4.21	4.72
				40.2	3.98	4.59	5.19
				49.6	3.49	4.17	4.82
Kerosene in water	♀	1.4338	1.3330	56.7	3.81	4.60	5.03
				71.5	4.33	5.01	5.62
				48.3	2.95	3.71	4.27
				52.6	3.28	3.93	4.53
Cyclohexane in water	□	1.4181	1.3331	64.0	3.64	4.26	4.95
				73.3	3.88	4.52	5.35
				39.1	2.19	2.66	3.04
Methyl isobutyl ketone in water	○	1.3942	1.3349	50.6	2.53	3.02	3.45
				62.1	2.87	3.40	3.83
				87.1	1.49	1.84	2.22
60% Glycerin water in methyl isobutyl ketone	■	1.4118	1.3942	91.2	1.68	2.03	2.43
Cyclohexan in 60% glycerin water	▽	1.4182	1.4122	48.1	0.482	0.698	0.815

I_0/I = ratio of incident- to emergent-light intensities.
Experimental data were obtained at 25°C.
*Refractive indexes of mutually saturated liquids measured at sodium D line.

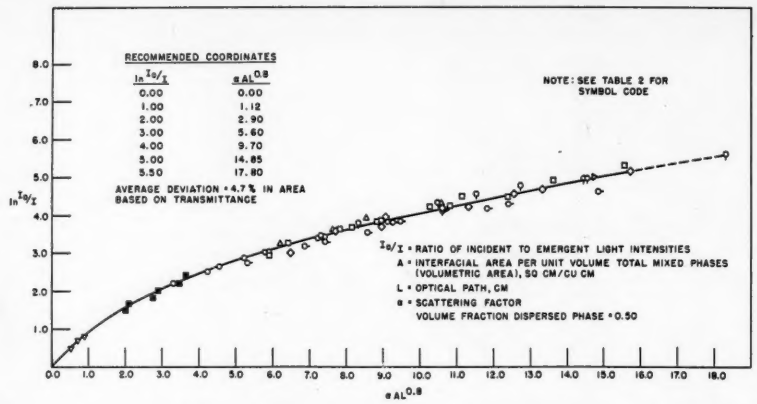

Fig. 6. General correlation of light transmittance with volumetric area for yellow-light spectrum.

which showed the dispersions to be essentially homogeneous. A portable one-piece detector-source unit consisting of phototube and flash-light bulb was placed in several different locations in the mixing vessel. Within the limits of experimental precision, no variation in light transmittance was observed, indicating essentially complete homogeneity of the dispersion.

SUMMARY

Satisfactory equipment and techniques were developed to measure the interfacial area and light transmittance of liquid-liquid dispersions. Both the accuracy and precision of the photographic technique for measuring interfacial area were shown to be better than 10%. A light detector and source were designed which featured readily available component parts and permitted variation of the optical path length.

The over-all reproducibility of transmittance measurements, with substitution of components, readjustment of optical path length, and realignment of the light source and detector taken into account, was always within 5% and in most cases 3%.

The present work was designed to cover a useful range of relative-refractive index and to provide a sufficient quantity of experimental data to test adequately various methods of interpreting these data. The experimental data were correlated by means of an exponential relationship based on a combination of theoretical and applied light-scattering considerations. Attempts to develop a linear correlation were not successful.

The general correlation is valid only for the conditions of this investigation. The physical conditions are the specified light source, light detector, and incident-light spectrum. Other conditions, as defined by the experimental data and the restrictions imposed by the underlying theoretical and practical considerations, are

1. Liquids which are transparent in the incident-light spectrum.
2. Dispersions consisting of 50% by volume dispersed phase.
3. Systems where the relative specific refraction M is between 0.01 and 0.11.
4. Dispersions in which the smallest particle size present is greater than 50 μ.
5. Dispersions through which the percentage of light transmittance ($I/I_0 \times 100$) is greater than 0.65% for optical path lengths from 1.0 to 2.0 cm.

The results of this investigation show the combined effects of multiple scattering and equipment geometry on light transmittance. First considerably more light reached the detector than may be predicted from light-extinction equations, which do not take into account multiple scattering. Second, the attenuation of the incident light passing through these dispersions was less than may be predicted, as evidenced by the fact that optical path length entered the correlation as a reduced power function.

The correlation with an average deviation of less than 5% shows that the ability of nonabsorbing liquid-liquid dispersions to transmit light is of value as a method of estimating the amount of interfacial area present. Additional work is necessary, however, before this technique can be regarded as a standard service tool. Some criteria of absorbency, other than simply nonabsorbing liquids, must be established. Work in progress with 25 and 10% dispersions and with a light spectrum in the near infrared region indicates that similar correlations may be developed for these conditions.

ACKNOWLEDGMENT

The authors wish to acknowledge with gratitude the contributions of L. F. Dorsey, who obtained most of the experimental data, and to thank D. K. Fleming and J. B. West for their valuable criticism of the contents of this paper, G. Lindholm of the Graphic Arts Section for the development of photographic techniques, and various members of the Chemical Engineering Division of Argonne National Laboratory for technical assistance in the design of the experimental apparatus.

NOTATION

A = interfacial area per unit volume of total mixed phases (volumetric area), sq. cm./cc.
d = drop diameter, cm.
d_i = drop diameter in interval i, cm.
d_{sv} = mean surface-volume or sauter drop diameter, cm.
I_0 = incident-light intensity
I = emergent-light intensity
K_s = scattering-area coefficient
L = optical path length, cm.
M = relative specific refraction of drop (Lorenz-Lorentz coefficient)
m = relative-refractive index of drop
N_i = number of drops in interval i
n = number of drops per unit volume of total mixed phases, cc.$^{-1}$
S = scattering cross section, sq. cm.
α = scattering factor (optical parameter)
β = optical parameter
ϕ = volume fraction of dispersed phase

LITERATURE CITED

1. Bailey, E. D., *Ind. Eng. Chem. (Anal.)*, **18**, 365 (1946).
2. Boll, R. H., R. O. Gumprecht, and C. M. Sliepcevich, *J. Optical Soc.*, **44**, 18 (1954).
3. Clark, N. O., and M. Blackman, *Trans. Faraday Soc.*, **44**, 1 and 7 (1948).
4. Gumprecht, R. O., and C. M. Sliepcevich, *J. Phys. Chem.*, **57**, 90 (1953).
5. ———, "Tables of Light Scattering Functions for Spherical Particles," Univ. Mich. Eng. Research Inst., Ann Arbor, Mich. (1951).
6. ———, *J. Phys. Chem.*, **57**, 95 (1953).
7. LaMer, V. K., and M. D. Barnes, *J. Colloid Sci.*, **2**, 361 (1947).
8. *Ibid.*, **1**, 71, 79 (1946).
9. LaMer, V. K., and D. Sinclair, *OSRD Repts.* 1857 and 944, Office of Publications Board, U. S. Department of Commerce, Washington, D. C.
10. Langlois, G. E., Ph.D. thesis, Univ. Calif. (1952).
11. ———, J. E. Gulberg, and Theodore Vermeulen, *Rev. Sci. Instr.*, **25**, 360 (1954).
12. Langlois, G. E., G. M. Williams, and Theodore Vermeulen, *Chem. Eng. Progr.*, **51**, 81F (1955).
13. Mie, G., *Ann Physik* (14), **25**, 377 (1908).
14. Oster, G., *Chem. Rev.*, **43**, 319 (1948).
15. Rea, H. E., Jr., and Theodore Vermeulen, *Univ. Calif. Radiation Lab. Publ.* 2123, Berkeley, Calif. (1953).
16. Rose, H. E., and C. J. French, *J. Soc. Chem. Ind.*, **67**, 283 (1948).
17. Rushton, J. H., E. W. Costich, and H. J. Everett, *Chem. Eng. Progr.*, **46**, 395 (1950).
18. Sinclair, D., and V. K. LaMer, *Chem. Rev.*, **44**, 245 (1949).
19. Stamm, A. J., and T. Svedberg, *J. Am. Chem. Soc.*, **47**, 1582 (1925).

Presented at A.I.Ch.E. Detroit Meeting

Effect of Gamma Radiation on Aqueous Ethylene-oxygen Solutions

ERNEST J. HENLEY, WESLEY P. SCHIFFRIES, and NATHANIEL F. BARR

Columbia University, New York, New York

Mixtures of ethylene and oxygen dissolved in water under pressures ranging from 200 to 700 lb./sq. in. were irradiated with Co^{60} gamma rays at a dose rate of 180,000 r./hr. G values (molecules/100 ev.) for aldehyde production as high as 200 were observed. Increasing total pressure and dose were found to decrease these G values. Alcohol, acids, hydrogen peroxide, and organic peroxide are also products of the reaction; however, the yields are much smaller.

Large-scale industrial use of ionizing radiation will certainly be limited to exothermic reactions in which the radiation serves to initiate long reaction chains (*1*). Processes in which ionizing radiation does not give large product yields per unit energy input will be excluded by the high cost of energy in this form. The reaction of hydrocarbons with oxygen is an exothermic reaction which, if controlled, yields products of commercial importance.

Recent studies with saturated hydrocarbons and oxygen (*2*) and with saturated hydrocarbon gases in aqueous solution (*3*) have clearly indicated that the oxidation initiated by gamma rays proceeds with a very poor yield of product per energy expenditure. In terms of molecules per 100 ev. (G units) yields of approximately unity have been observed for these oxidations. In the work reported here it has been found that when aqueous solutions of ethylene and oxygen under pressure are irradiated with gamma rays from cobalt-60, G values for the production of aldehyde as high as 200 are observed.

Wesley P. Schiffries is at present with Foster Wheeler Corporation, New York, and Nathaniel F. Barr with Brookhaven National Laboratory, Upton, New York.

The difference in yield values obtained from ethylene in contrast to saturated hydrocarbons would be due to the high heat content of the vinyl bond. This makes all reactions of ethylene which involve additions across the double bond potential chain reactions. The best example of this, and the only one that has captured the attention of radiation chemists, is polymerization of ethylene to form polyethylene. Yale and Michigan groups (*4, 5*), among others, have recently studied this reaction. The polymerization is reported to proceed readily under gamma-ray catalysis, chain lengths over one thousand having been observed at higher pressures and slightly elevated temperatures.

Reported in this paper are results obtained under a variety of experimental conditions, and an attempt is made to correlate these with the presently accepted picture of radiation chemical reactions in aqueous solutions.

DESCRIPTION OF APPARATUS

Figures 1 and 2 show the apparatus used. The reactor is a stainless steel cylinder of approximately 150-ml. capacity with gas entrance and exit lines extending through the nut. The entrance line, reaching almost to the bottom of the reactor, is connected externally through the piping shown to the ethylene-oxygen feed mixture. The entrance tube extends back and is connected in series to a cross, a needle valve, and a tee. To the cross are attached a blow-out disk assembly and a needle valve for filling and sampling. The exit tube extends back to the tee into which the by-pass valve enters, the other connections being used for a needle valve to control gas flow rate. For sampling, the by-pass and sampling valves are open, the other two closed. A standard gas cylinder with a pressure regulator is attached to the other connection of the tee on the entrance line.

IRRADIATION TECHNIQUE

The irradiations are carried out by lowering the reactor into the source; a hollow cobalt-60 cylinder of the type described by Henley (*6*) was used for these runs. The dose rate was determined by means of a cellophane dosimeter (*7*) and found to be 180,000 r./hr.

The high-pressure reactor is charged with 150 ml. of distilled water by opening the exit line and adding water at the sampling valve.

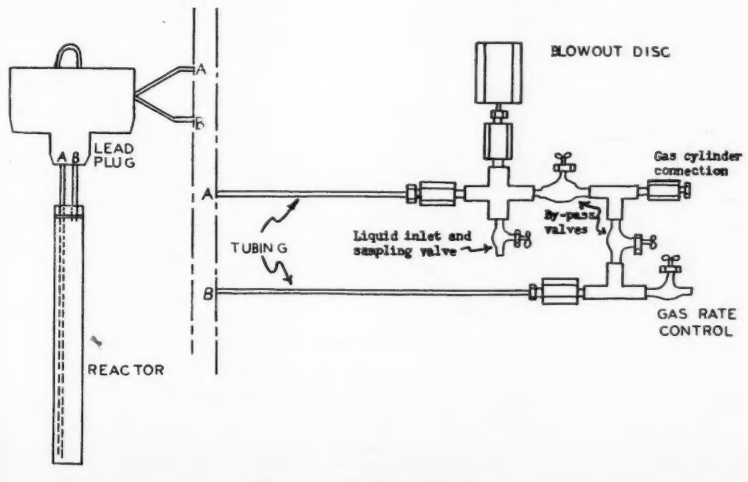

Fig. 1. Diagram of apparatus.

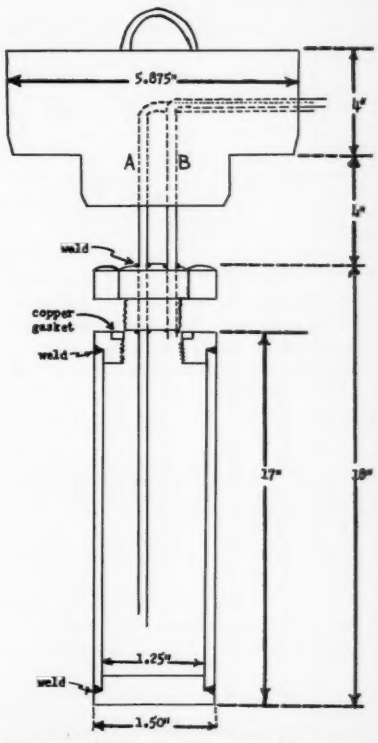

Fig. 2. Detailed diagram of reactor and plug

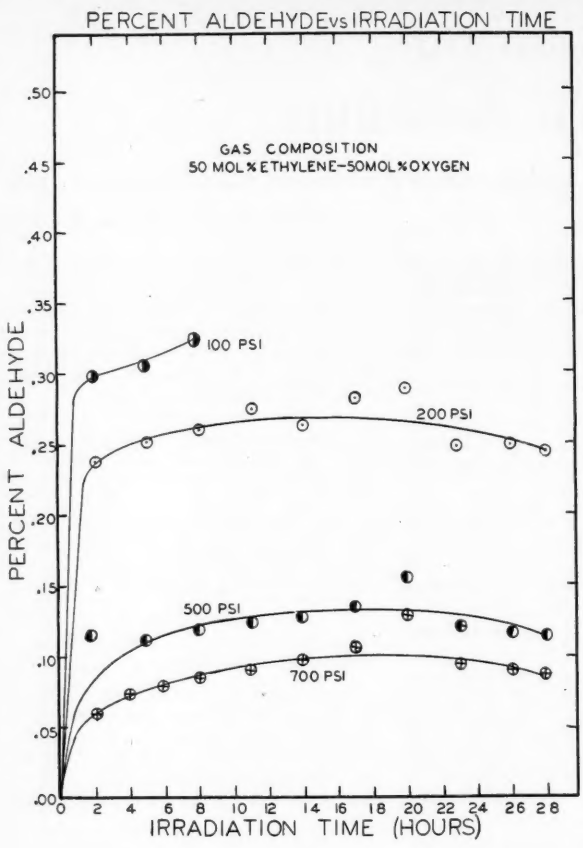

The previously filled gas cylinder is attached through the pressure regulator to the entrance line of the reactor and the pressure set at some predetermined value. In this case once the gas flow rate is set, by the exit valve, it will remain constant. The gas flow was adjusted to give a slow sparge. To take a sample it is necessary only to open the by-pass valve and close the valve in the entrance line. The sample is then collected at the sampling valve. The sampling operation can be carried out in less than 10 sec. with no loss of pressure in the reactor.

ANALYTICAL PROCEDURE

The following methods of analysis have been employed for the quantitative determination of acid, aldehyde, alcohol, hydrogen peroxide, and formaldehyde (*8, 9, 10, 11, 12*).

Acid

The sample is a very dilute solution of a weak acid and direct titration cannot be used because the end point is obliterated by dissolved carbon dioxide.

The weighed sample is added to 5 ml. of standard 0.05 *N* KOH and the excess KOH is titrated with standard 0.05 *N* HCl to a *p*H of 6.7. This value of the *p*H has been experimentally determined to give the stoichiometric end point most accurately.

Aldehyde

The sample is added to 25 ml. of approximately 7 wt. % H_2O_2 and after it stands for 10 min. 5.0 ml. of standard 0.05 *N* KOH is added. The presence of ethanol in the sample does not interfere, as more stringent oxidizing conditions are required for alcohols to go to acids. The excess KOH is titrated with standard 0.05 *N* HCl to a *p*H of 6.7.

A correction for the acid originally present (assumed to be acetic) must be applied to the percentage of aldehyde calculated from the titration.

Alcohol

To 5.0 ml. of standard 0.05 *N* $K_2Cr_2O_7$ and 5 to 6 ml. of concentrated H_2SO_4 in an iodine flask a 1- to 2-g. sample is added and the solution brought slowly to boiling. After cooling, a small piece of dry ice and approximately 3 g. of potassium iodide (iodate free) are added and the solution is allowed to stand 10 min. The dry ice sublimes and the carbon dioxide displaces air from the flask to prevent air oxidation of potassium iodide. The excess of $K_2Cr_2O_7$ is found by titrating with standard 0.05 *N* $Na_2S_2O_3$ to a starch-iodide end point. A correction for the aldehyde present must be applied to the percentage of alcohol calculated from the titration.

← **Fig. 3. Percentage of aldehyde vs. irradiation time.**

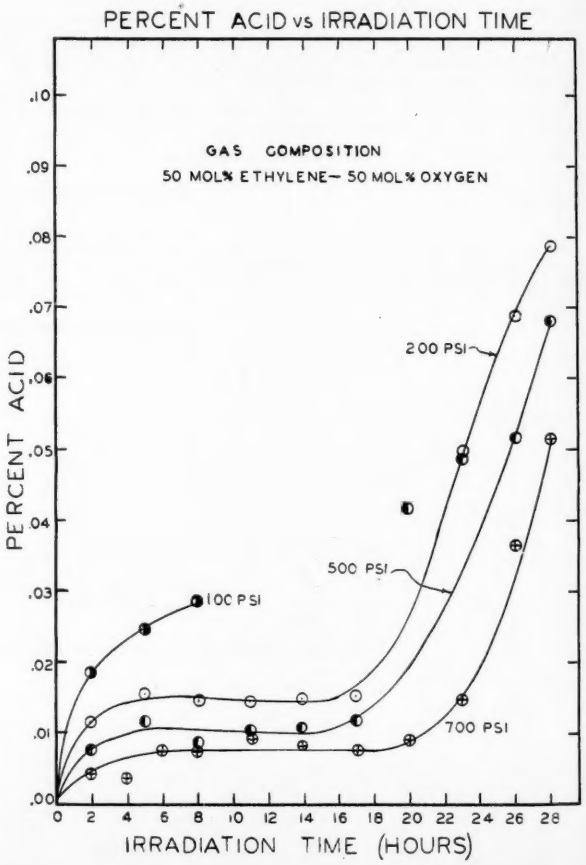

Fig. 4. Percentage of acid vs. irradiation time. →

Hydrogen Peroxide

Hydrogen peroxide is reacted with potassium iodide in the presence of a molybdate catalyst, and the triiodide ion produced is determined colorimetrically at 350 μ by use of a Beekman model DU spectrophotometer (*11, 13*). Calibration curves using standardized H_2O_2 were straight lines when optical density differences were plotted against H_2O_2. Organic peroxides were determined by the method indicated by Weiss (*3*).

Formaldehyde

The method of Denige as described by Walker (*12*) was used. Schiff's reagent is added to the acidified sample, and the resulting color is read spectrophotometrically at 580 mμ. Peroxides are destroyed as suggested by Satterfield (*8*).

RESULTS

Figure 3 indicates the production of aldehyde as a function of irradiation time under a variety of experimental conditions. The aldehyde for the purpose of this calculation was considered to be acetaldehyde. Owing to the limited gas supply the pressure dropped somewhat during these runs. The magnitude of this drop was dependent upon the rate of sparging and was usually between 5 and 20 lb. Various sparging rates had no detectable effect, and no effect of temperature was noted in the range of 25° to 61°C.

Similar data for the production of acid are summarized in Figure 4. The acid present was assumed to be acetic.

The dependence of the steady state concentration of aldehyde on total pressure is indicated in Figure 5. The maximum concentration of aldehyde is seen to be inversely proportional to the log of the total pressure.

Alcohol and peroxide production as a function of dose for total pressures of 200, 500, and 700 lb./sq. in. is summarized in Figures 6 and 7. The alcohol was calculated as ethyl alcohol, the peroxide as hydrogen peroxide.

G values for the 200 lb./sq. in. runs as a function of dose are plotted in Figure 8.

DISCUSSION

The solute concentration in these solutions varies directly with total pressure. At the highest pressure used (700 lb./sq. in.) the total solute concentration is approximately 0.05M; consequently all the energy is absorbed in the solvent water. It is commonly postulated that the result of this energy absorption is the production of reactive radical pairs, H + OH, along with smaller quantities of H_2 + H_2O_2 (*14*). Each 100 ev. of energy absorbed by the water (1 r. = $6.08 \cdot 10^{13}$ ev./g.) produces 4.5 detectable water decomposition; 7.6 radicals are produced along with 0.8 molecule of H_2 + H_2O_2 (*15*).

As more than 200 molecules of aldehyde are produced per 100 ev. absorbed, it appears that the radicals are initiating a chain reaction between ethylene and oxygen.

The initiation steps for this reaction could be

$$H\cdot + O_2 \rightarrow HO_2\cdot \quad (1)$$

$$HO_2\cdot + H_2C = CH_2 \rightarrow H_2O_2 + H\dot{C} = CH_2 \quad (2)$$

$$HO\cdot + H_2C = CH_2 \rightarrow H_2O + H\dot{C} = CH_2 \quad (3)$$

followed by

$$H\dot{C} = CH_2 + O_2 \rightarrow HC(-O-O)-CH_2 \quad (4)$$

Chain propagation must thus involve the reaction of this radical with ethylene.

$$HC(-O-O)-CH_2 + H_2C = CH_2 \rightarrow HC(-O-O)-CH_2-H + H\dot{C} = CH_2 \quad (5)$$

followed by

$$HC(-O-O)-CH_2-H \rightarrow 2HCHO \quad (6)$$

This postulated mechanism leads to the formation of formaldehyde. If one chose to use the oxidative scheme of Bell et al., one could predict that acetaldehyde would be the primary product (*16*). The initiation and propagation steps could be similar; however, instead of reaction (6) one would have

$$H_2C = CHO_2H \rightarrow H_2C = CHO\cdot + OH\cdot \quad (7)$$

followed by

$$H_2C = CHO\cdot + H_2C = CH_2 \rightarrow CH_3{-}CHO + H\dot{C} = CH_2 \quad (8)$$

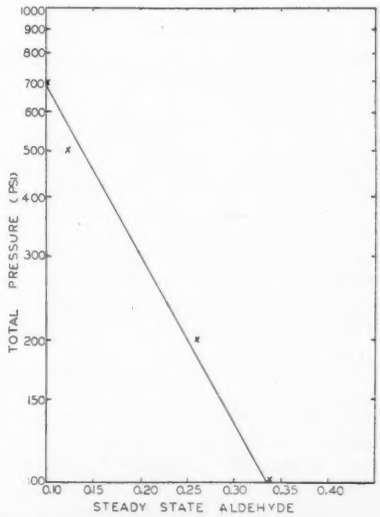

Fig. 5. Steady state aldehyde concentration vs. total pressure.

These reactions are observed in the low-temperature oxidation of paraffins.

The initial high G value for aldehyde production falls rapidly with dose (Figure 8). After an initial rapid increase the concentration of the aldehyde remains constant with dose. The molar concentration of the labile aldehyde is at this point greater than the concentration of dissolved ethylene. As no carbon dioxide was detected in the effluent gas stream, it does not appear likely that aldehyde is being destroyed at a rate equal to its rate of production by another chain process. Most probably the aldehyde and other reaction products (hydrogen peroxide, organic peroxide, and alcohols) are preventing initiation and propagation steps in the reaction of ethylene with oxygen.

The fact that increased total pressure decreases the maximum concentration of aldehyde is not easily explainable, for it indicates that O_2 is involved in a termination step to a higher power than in the initiation and propagation steps.

The other reaction products are produced with much smaller G values. The constant G value for total peroxide production may be accounted for by the molecular yield for H_2O_2 (G = 0.8) and that produced in reaction (2) (G = 1.7).

Acid is apparently produced in a nonchain oxidation by further oxidation of the aldehyde.

It is interesting to compare these results with those initially reported by Henley et al. (*17*) for the same system at lower

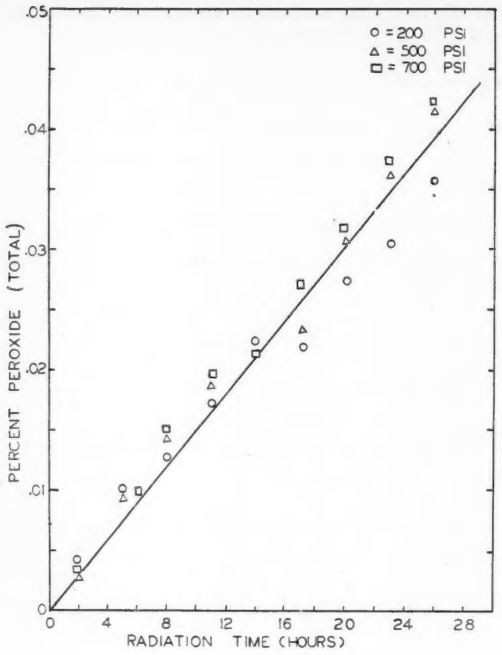

Fig. 6. Percentage of peroxide vs. irradiation time.

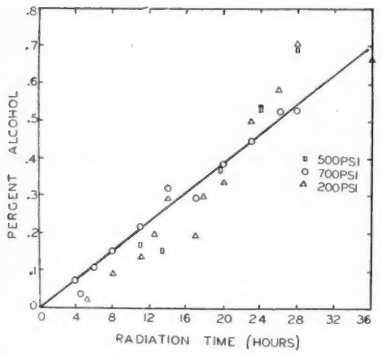

Fig. 7. Percentage of alcohol vs. irradiation time.

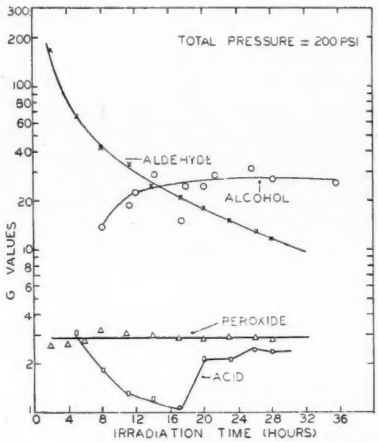

Fig. 8. *G* values for 200 lb./sq. in. run vs. irradiation time.

pressures. The results differ in some respects, the most notable being the difference in peroxide and aldehyde yields. The latter is probably due to the fact that in the low-pressure apparatus the gas storage tank was too small and so the gas pressures varied continuously during the runs, no steady state being achieved. The difference in peroxide concentrations is not easily explained except in terms of materials used and of pressures.

Differences in alcohol and acid concentrations reported here and in previous papers are not great. The acid determination is relatively unreliable at these low concentrations, as may be inferred from Figure 8. As for the alcohol determination, this also is less precise at low-alcohol and high-aldehyde concentrations. This is the reason little weight can be given to the lower part of the data in Figure 7. Also there is an error in reference *17*; the alcohol and acid curves are interchanged.

It should also be mentioned that polarographic measurements of oxygen uptake rates for the ethylene-oxygen system at atmospheric pressure showed the absence of a chain reaction. This has since been confirmed by British workers (*18*).

The origin of the alcohol, which is produced with a constant *G* value of approximately 25, is as yet not completely known. It is hoped that experiments now in progress on higher olefins will help in the achievement of an understanding both of the hydration process and the effect of pressures. Refinements in analytical techniques are also desirable.

Originally qualitative analysis and the reports of others led to the conclusion that all hydrocarbons would be of the two-carbon variety. From the gas-analysis mechanism, and an analysis for total carbon (*19*), it became apparent that a good deal of the aldehyde was formaldehyde rather than acetaldehyde. This was confirmed by a separate analysis which showed that in the case of the 20-hr. sample of the 500 lb./sq. in. run about 25% of the aldehyde was formaldehyde.

ACKNOWLEDGMENT

The authors would like to acknowledge the helpful suggestions of Elmer L. Gaden, Jr., and the assistance of Edward Goldberg. Facilities for carrying out this program have been provided through A.E.C. sponsorship of Contract AT(30-1)-1186.

LITERATURE CITED

1. Henley, E. J., and N. F. Barr, "Advances in Chemical Engineering," Vol. I, Academic Press, New York (in press).
2. Bach, N., "Proc. Intl. Conf. Peaceful Uses of Atomic Energy," **1**, 538 (1956).
3. Weiss, J., *Chemistry & Industry*, **13**, 358 (1955).
4. Bretton, R. H., J. C. Hayward, and K. A. Shair, *Progr. Rept.* IV, NYO-3311, Yale Univ., New Haven, Conn. (Oct. 1, 1952).
5. Lewis, J. G., J. J. Martin, and L. C. Anderson, *Chem. Eng. Progr.*, **50**, No. 5, 249 (1954).
6. Henley, E. J., *Nucleonics*, **11**, No. 10, 41 (1953).
7. *Ibid.*, **12**, No. 9, 62 (1954).
8. Satterfield, C. N., R. C. Wilson, R. M. Le Clair, and R. C. Reid, *Anal. Chem.*, **26**, 11, 1792 (1954).
9. Kingscott, P. C. R., and R. S. G. Knight, "Quantitative Organic Analysis," Longmans Green, Inc., New York, (1914).
10. Pierce, W. E., and E. L. Haenisch, "Quantitative Analysis," John Wiley & Sons, Inc., New York (1951).
11. Patrick, W. A., and H. B. Wagner, *Anal. Chem.*, **21**, 1279 (1949).
12. Walker, J. F., "Formaldehyde," p. 367, Reinhold Publishing Company, New York (1953).
13. Allen, A. O., T. W. Davis, G. Elmore, J. A. Ghormley, B. M. Haines, and C. J. Hochanadel, *ORNL* 130 (1949).
14. Allen, A. O., *Radiation Research*, **1**, 85 (1954).
15. Hochanadel, C. J., "Proc. Intl. Conf. Peaceful Uses of Atomic Energy," **1**, 521 (1956).
16. Bell, E. R., J. H. Raley, F. F. Rust, F. H. Seubold, and W. E. Vaughn, *Discussions Faraday Soc.*, No. 10, p. 242 (1951).
17. Henley, E. J., and J. Schwartz, *J. Am. Chem. Soc.*, **77**, 3167 (1955).
18. Johnson, G. R. A., personal communication, King's College, England.
19. Gertner, A., and C. Irekovic, *Z. anal. Chem.*, **192** (1), 36 (1954).

Presented at Nuclear Science and Engineering Congress, Cleveland.

Apparatus for Visual Study of Corrosion by Hot Water

DANIEL R. GRIESER and EUGENE M. SIMONS

Battelle Memorial Institute, Columbus, Ohio

The design and operation of a windowed autoclave suitable for studying corrosion of materials by pressurized hot water are described. The technique for taking time-lapse motion pictures of a specimen from the instant of contact with the high-temperature water until the corrosion is complete is explained, and a set of typical pictures is presented showing the progress of the attack. Pressure and temperature measurements provide a means for rough computation of corrosion rates, as is shown by the results of two tests of uranium specimens subjected to pressurized hot water.

A windowed autoclave was designed and constructed to permit visual study of the reaction of a corrosion specimen with high-temperature water. Although similar research is being done elsewhere, several features of the Battelle device are unique. One advantage is that the upper temperature is limited only by stresses in the pressure vessel, rather than by corrosive attack on the glass windows. Another is that the hot water can be made to contact the specimen suddenly, and thus a more interpretable test is provided than in the case where the specimen is subject to attack during the time the system is being heated and pressurized.

APPARATUS

The Viewing Autoclave

Figure 1 shows a cross section of the autoclave. There are two windows, one for illumination and one for viewing. These are mounted in the bottoms of water-cooled legs in order to permit cooling without introducing convection currents, which would distort the image.

The body of the pressure vessel is surrounded by eight Cromalox strip heaters, so arranged as to provide a slightly higher temperature at the top than at the bottom. These help to ensure that the image will not be distorted by convection currents or by rising steam bubbles. The heaters are surrounded by about 1 in. of thermal insulation. The temperature at the test specimen is maintained at the desired value by a controller which responds to a thermocouple located in the heating jacket. This method of control minimizes temperature cycling and accompanying pressure cycling. The temperature of the water in the vicinity of the specimen is measured by a second thermocouple located in the thermocouple well.

All parts of the autoclave were machined from type-304 stainless steel, with the exception of the copper window gaskets and cooling coils, the serrated nickel main gasket, the main thrust ring of oil-die steel, and the alloy-steel set screws. Heliarc welding was used for all welded joints.

The Herculite glass windows were cemented to the window heads, by means of a thin coating of water-resistant adhesive. The neoprene 0 rings were added to a standard Bridgman window seal, as shown, to permit the vessel to be evacuated without danger of dislodging the windows. These 0 rings are not intended to seal, but merely to act as spacers. The seal is formed between the glass and the window head, as well as at the copper gasket.

The upper seal is a standard pressure closure, utilizing a serrated nickel gasket compressed between a closure head and the body of the pressure vessel. The thermocouple well, welded to the closure head, serves also to hold the specimen mount, thereby providing a convenient arrangement for inserting and removing specimens.

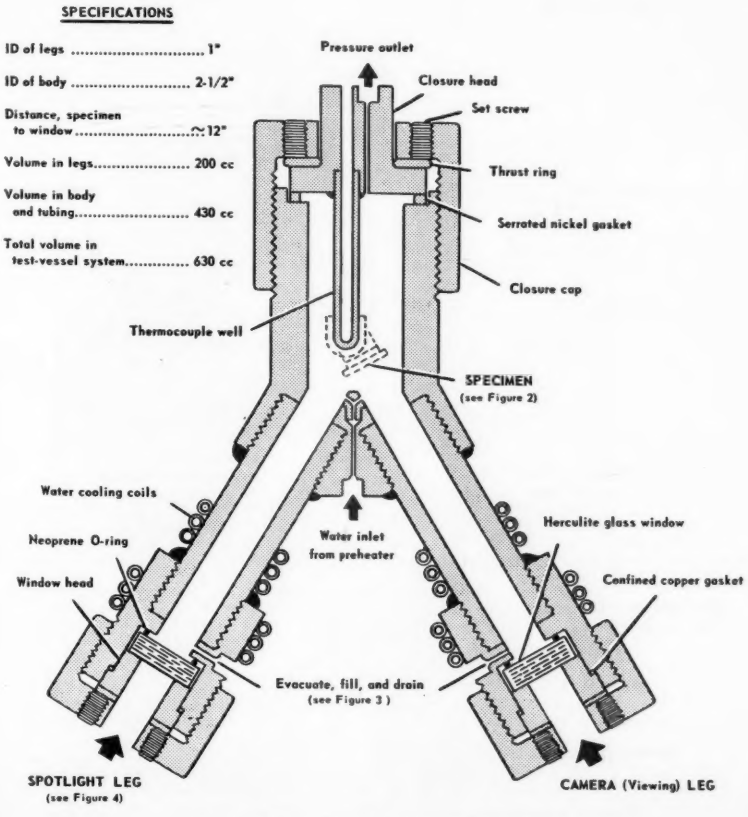

Fig. 1. Cross section of windowed autoclave.

Specimen Mount

The closure head with a test specimen mounted on the end of the thermocouple well is shown in Figure 2. The mounting permits sufficient rotating and sliding adjustments to position the specimen for maximum lighting and to center it along the axis of sight. Early trials with polished specimens gave images which showed only a narrow band of specularly reflected light. This difficulty was remedied by using a frost-gold background, as shown in Figure 2, and putting a satin finish on the specimen with emery paper. The

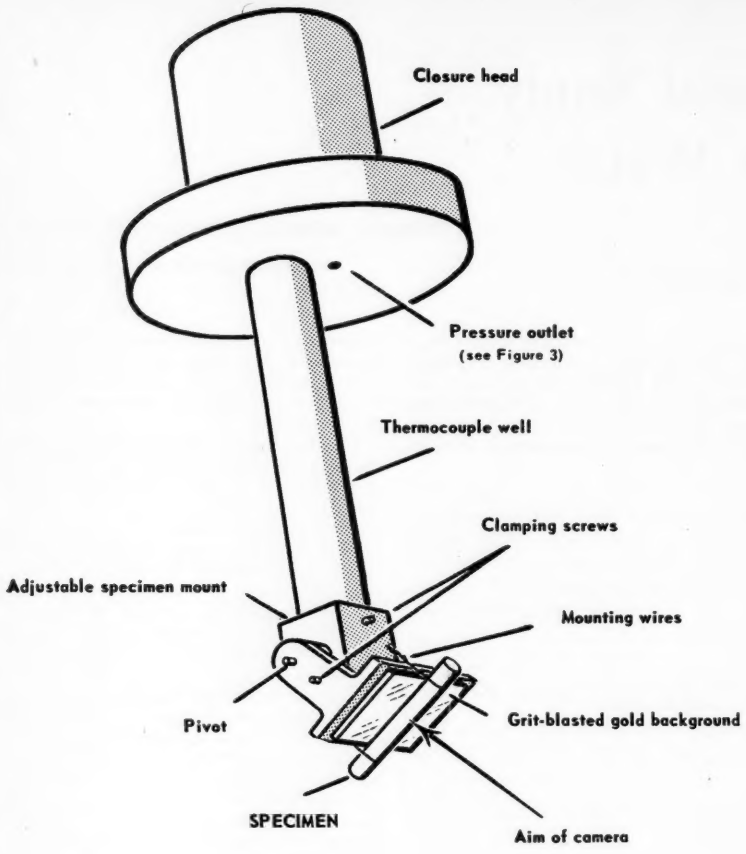

Fig. 2. Closure head for windowed autoclave, with specimen mounted.

Camera Setup

Figure 4 is a sketch of the arrangement used to obtain time-lapse pictures of the specimen during the corrosion process. The light source illuminates a 1-in.-diam. circular area of specimen and background. The mirror at the end of the viewing leg is positioned so that the camera sees the specimen and the digital clock simultaneously. A beam-splitter is positioned in front of the camera lens so that a small fraction of the light is reflected at right angles to the photographic axis. This arrangement allows the operator to follow the progress of the corrosion visually without disturbing the picture taking. The camera used is a 16-mm. Paillard-Bolex, fitted with an external electric motor and spring drive and a 63-mm. Ektanon Kodak lens. The time-lapse control and actuating solenoid is a Samenco movie control, capable of 1-, 2-, 4-, and 6- to 1,200-sec. intervals between frames.

TEST PROCEDURE

The specimen is prepared and mounted in the desired position, and then the test vessel is closed and sealed. Next 100 cc. of deionized water is introduced into the water-cooled legs to protect the glass

resulting image is much clearer, and the edges of the specimen are more sharply defined.

In cases where the specimen has a corrosion-resistant shell, it is fastened to the mount with Nichrome wires as shown. Bare specimens must be placed in a wire basket or in a stainless steel boat wired to the mount, in order to keep the specimen from falling into the cooled legs before the corrosion is complete. With bare specimens, viewing is consideraby more difficult and often impossible, because either the specimen container or the corrosion débris obscures the view.

Preheat Autoclave and Pressure System

Figure 3 is a diagram of the pressure system. The independently controlled 1,000-cc. water-preheating autoclave is fitted with two outlets, one of which extends to the bottom of the vessel. It is thus possible to transfer the water to the previously heated test vessel as a liquid. The valving allows the legs of the test vessel and the preheat autoclave to be charged independently with predetermined amounts of water and then evacuated to outgas the water and to remove air.

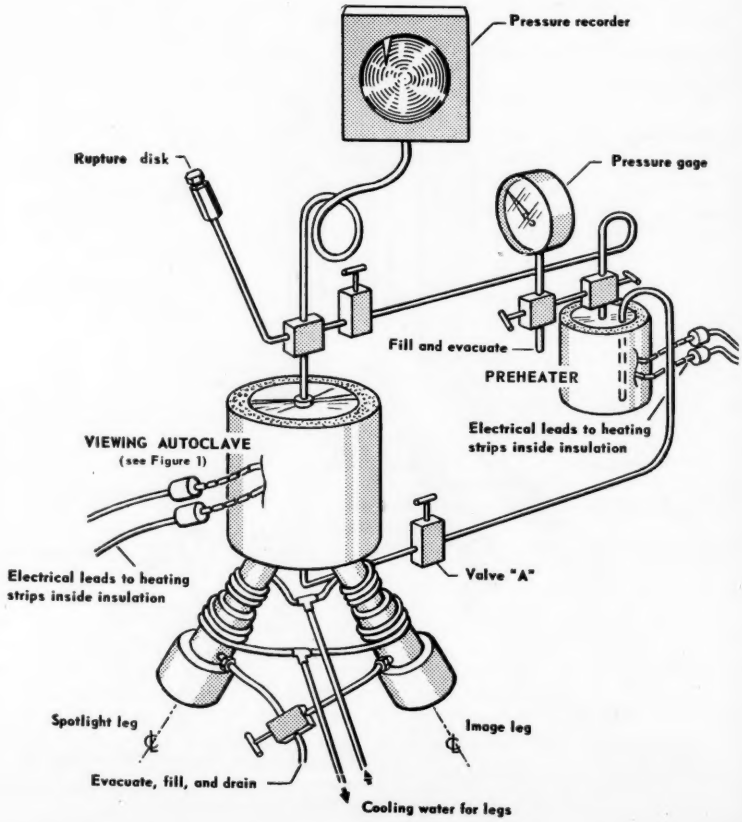

Fig. 3. Windowed-autoclave system.

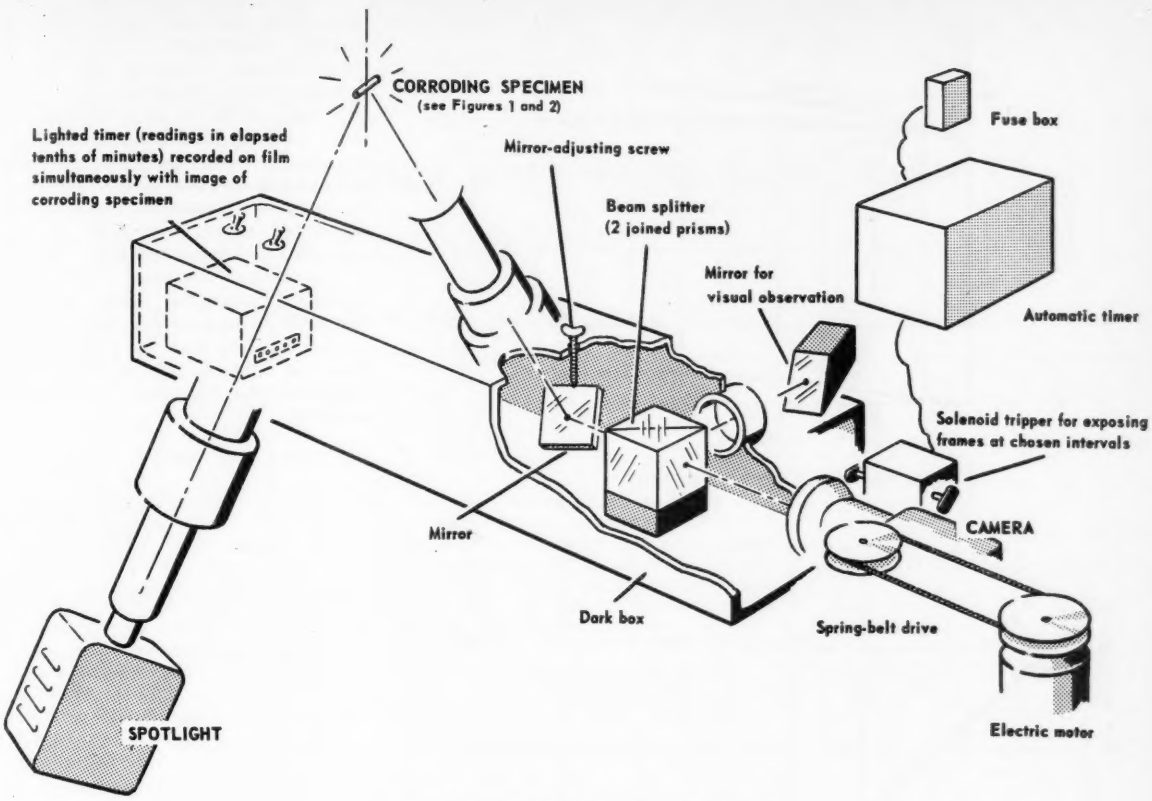

Fig. 4. Photographing and observation system.

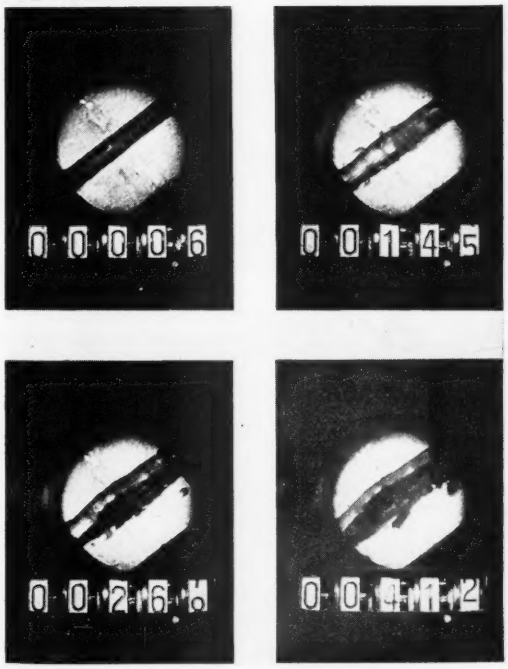

Fig. 5. Representative reproductions from films of test.

during the preheat period. The preheat autoclave is loaded with 550 cc. of water and the entire system evacuated to outgas the water. With all valves in the system closed, the preheat and viewing autoclaves are heated independently to the test temperature. The test is initiated by turning on the pressure recorder and then opening valve *A* (*see* Figure 3) to allow approximately 300 cc. of preheated water to enter the viewing autoclave and engulf the test specimen. At 600°F. this transfer is accomplished in less than 30 sec. The preheat vessel is then allowed to cool, as it has no further function in the experiment. Simultaneously with opening the valve, the time-lapse control and the specimen and timer lights are turned on. From this time until the corrosion is complete, the operation is entirely automatic. When the test is over, the heaters and camera controls are turned off and the system is allowed to cool. The pressure record is continued until the system has cooled to room temperature. Then the quantity of water emptied from the window autoclave is measured.

TYPICAL RESULTS

A selection of four frames from an actual test has been reproduced in Figure 5. This particular specimen contained a

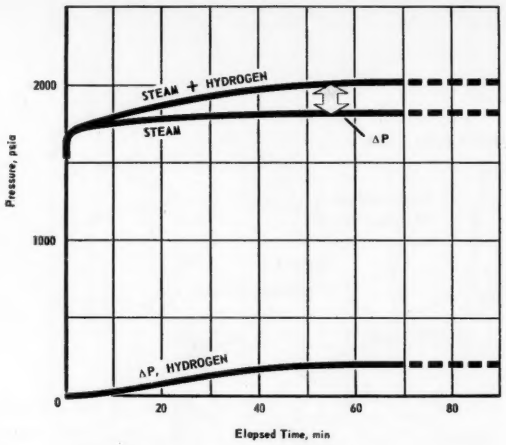

Fig. 6. Typical plot, pressures vs. time.

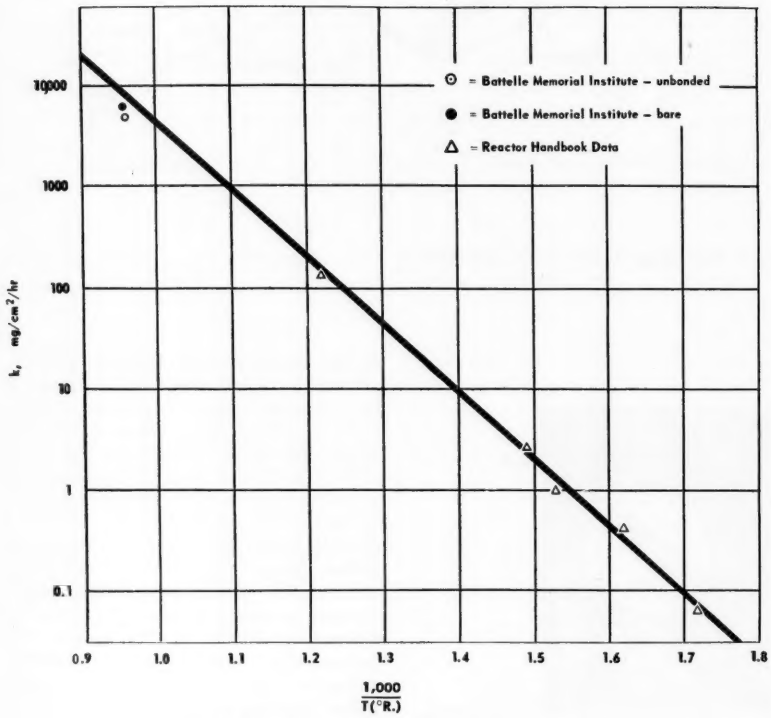

Fig. 7. Corrosion rate of uranium vs. temperature.

uranium rod welded to zirconium plugs and slipped into a shell which was bonded to the rod and plugs. The 0.010-in. hole drilled in the shell is visible in Figure 5. The numbers at the bottom of each frame represent the respective times, in tenths of minutes, that the specimen had been in contact with 600°F. water. The progress of the corrosion is easily followed from the swelling and subsequent cracking and bursting open of the shell. Bubbles of hydrogen are visible in some of the pictures, although the progress of any one bubble can rarely be traced on the film because of the time interval between frames.

Figure 6 is a graph plotted to show the manner in which the amount of hydrogen evolved may be obtained. The calibration curve shows the pressure history inside the test vessel when it is filled with 600°F. water with no specimen in place. This is necessary as it takes a finite length of time for pressure equilibrium to be reached (in this case, about 40 min.). The difference in pressure between a test with a specimen in place and a test without is, therefore, attributable to evolved gas. Of course, allowance must be made for the hydrogen which dissolves in the water and that which is lost by diffusion through the walls of the test vessel. By the use of suitable geometric equations which relate the area open to attack to the volume of material corroded, the hydrogen-evolution rate may then be translated to a corrosion rate.

This method has been employed to obtain the corrosion rates listed in Table 1. A comparison has been made in Figure 7 of the data in Table 1 with literature data reported at lower temperatures. The line shown (*1*) has the equation

$$\log_{10} k(\text{mg. cm.}^{-2}\,\text{hr.}^{-1}) = -\frac{6{,}710}{T(^\circ R.)} + 10.34$$

Table 1. Summary of Corrosion Data

Bonding condition	Temperature, °F.	Corrosion rate (k), mg./(sq. cm.)(hr.)
Bare	587	6,260
Unbonded	582	4,910

DISCUSSION

Clarity of detail in the pictures is limited primarily by the grain size in the film and the intensity of the illumination. In the tests made thus far, type Kodachrome *A* film has been used, and, even though the grain size is not as small as is obtainable with Super XX, it was felt that the identification of color would compensate for the lack of definition and at the same time show up any characteristic color of the reaction products.

Thus far the accuracy of the calculated corrosion rates, based on hydrogen-evolution data, is no better than 20%, owing largely to the extreme sensitivity of steam pressure to small changes in temperature. This could be improved by substantially more precise control of steam temperature. In any event, the windowed autoclave affords a relative evaluation of the influence of such variables as geometry, alloying, type of bonding, water temperature, and water impurities on corrosion rate. The most important advantage of this instrument is, however, that it provides a pictorial representation of the corrosion phenomenon while it is occurring.

LITERATURE CITED

1. "Reactor Handbook," vol. 3, U. S. Atomic Energy Commission, U. S. Gov't Printing Office, Washington, D. C. (1955).

Presented at Nuclear Science and Engineering Congress, Cleveland.

Neutron Lifetimes and Void Coefficients for Research Reactors

THOMAS H. PIGFORD, MARIUS TROOST, JAMES R. POWELL, and MANSON BENEDICT

Massachusetts Institute of Technology, Cambridge, Massachusetts

Prompt neutron lifetimes and void coefficients were calculated for research reactors using M.T.R.-type fuel elements, moderators of light and heavy water, and reflectors of light water, heavy water, graphite, and beryllium. Heavy-water–reflected and –moderated research reactors may have neutron lifetimes of the order of 0.001 sec. as compared with about 0.00006 sec. for a light-water–reflected and –moderated research reactor. Lifetime of the light-water core can be improved considerably by use of better reflectors, but at a substantial reduction and even reversal in sign of the void coefficient.

A desirable and important safety feature of a nuclear reactor is the automatic shutdown of the reactor by temperature rise and/or boiling in case of a sudden excursion in power level. To allow for fuel depletion, fission-product buildup, and possible consumption of neutrons by experiments, an operating reactor must have excess reactivity available from an amount of fuel greater than that required to make the reactor just critical in the cold, clean condition. The reactor is inherently safe if this available excess reactivity can be suddenly imposed on the reactor without melting of fuel elements or creation of destructive pressure surges before the imposed reactivity is canceled by effects of heat liberation.

A dramatic demonstration of the results of sudden addition of excess reactivity to a light-water research reactor of the swimming-pool type was given by the borax tests at Arco, Idaho (*1*). With sudden addition of a small amount of excess reactivity to the reactor operating at 80°F. the reactor shut itself off safely by boiling the water moderator and coolant. For those experiments which resulted in safe shutdown of the reactor operating initially at 80°F. the shortest initial period studied was "about 0.013 sec.," corresponding to the sudden introduction of 1.24% excess reactivity. Sudden addition of 3.3% excess reactivity resulted in a violent pressure surge which destroyed the reactor.

If the imposed excess reactivity is considerably greater than the delayed neutron fraction β, the period T of the power transient can be approximated by

$$T = \frac{l}{k_{eff}(1 - \beta) - 1} \qquad (1)$$

If the power surge boils the coolant and/or moderator, k_{eff} will change as boiling occurs:

$$k_{eff} = k^0_{eff} + \alpha V_v \qquad (2)$$

k^0_{eff} = effective reproduction factor at the beginning of the power surge

α = steam void coefficient, or the increase in k_{eff} per unit increase in steam volume. This is assumed to be constant for a given reactor.

V_v = volume of steam within the reactor core at time t

To minimize danger to a water-cooled and -moderated reactor in a power transient, it is desirable that the reactor period be large to allow time for heat to transfer from fuel elements into the water and to allow time for water to vaporize and flow out of the reactor core. A long prompt neutron lifetime is of obvious advantage.

For self-regulation it is necessary that the void coefficient α be negative. For given values of k^0_{eff} and l, the greater the magnitude of the negative α, the lower the total heat release required to shut down the reactor.

In this study the prompt neutron lifetime and void coefficient have been calculated for research reactors using M.T.R. (Materials Testing Reactor)-type fuel elements with various combinations of light- and heavy-water coolant moderator and reflectors of light water, heavy water, beryllium, and graphite.

CALCULATION OF NEUTRON LIFETIME AND VOID COEFFICIENT

An equation for calculating mean thermal lifetime of prompt neutrons is derived in the Appendix:

$$l = \frac{\int_V \frac{\phi_s^* \phi_s}{v_s}\, dV}{\int_V \frac{k_\infty}{p} \Sigma_s \phi_f^* \phi_s\, dV} \qquad (3)$$

where the volume integrals are taken over the entire reactor volume. The subscripts s and f refer to properties of neutrons in the thermal and fast groups respectively. The asterisk refers to adjoint properties. Other terms are defined under notation. The numerator of Equation (3) gives the statistically weighted population of thermal neutrons in the reactor, which, for a thermal reactor, is essentially equal to the total neutron population. The denominator gives the statistically weighted neutron production rate for the reactor. The ratio of the two is the time to replace one neutron population by another generation of neutrons.

The equation for the fractional void coefficient $[\partial k_{eff}/k_{eff}]/[\partial V_v/V_{mod}]$, or the differential change in effective reproduction factor k_{eff} per differential fraction of moderator converted to steam, is derived in the Appendix.

If one considers the effect of a differential volume ∂V_v of steam formation on the effective reproduction factor, the steam void coefficient α is given by

$$\alpha = \frac{1}{V_{mod}} \frac{\partial k_{eff}/k_{eff}}{\partial V_v/V_{mod}} \qquad (4)$$

CALCULATION OF CRITICAL MASS AND FLUX DISTRIBUTION

For simplicity the calculations were made for spherical reactor cores completely surrounded by reflector. The radius of the light-water cores was determined as that radius required for

criticality when the core contains approximately the same concentration of water, uranium, and aluminum as the borax reactor and is surrounded by an infinitely thick reflector of light water. When other reflectors were considered, the core radius and aluminum and water concentration were held constant, but the amount of uranium 235 alloyed in the aluminum fuel elements was varied to obtain criticality. In every case it was assumed that the reactor core contained 5% excess absorption in the form of removable control elements, to allow for operational requirements of reactivity.

In a heavy-water core M.T.R.-type fuel elements are spaced several inches apart and there is considerable latitude in the core size; so various core radii as well as reflector combinations were considered in this study.

Also, heavy-water cores require lower critical masses and fewer fuel elements than do light-water cores and the aluminum content was therefore reduced to 57.8 kg. for the heavy-water cores. Five per cent excess absorption was assumed.

Nuclear data used in these calculations are shown in Table 1. All calculations were made by means of two-group diffusion theory, and the core was treated as a homogeneous medium.

RESULTS AND DISCUSSION

Light-water Cores

Results for the light-water cores are shown in Table 2. Figure 1 shows flux distributions for the seven light-water cases, normalized to unit thermal flux at the reactor center. Because of the short slowing-down length and diffusion length of light water, the results of case 1 apply as well for an infinitely thick-water reflector. For the borax experiment (*1*) the reactor lifetime was 0.000065 sec. and the fractional void coefficient was −0.24. These are near the values calculated for the water-reflected, water-moderated reactor (case 1).

The savings in critical mass as graphite, beryllium, or heavy water replace the light-water reflector are apparent. As would be expected, beryllium is the most effective reflector for fuel savings. The prompt neutron lifetime can be increased considerably over case 1 by use of a better reflector. The lifetime gain with beryllium is due largely to the lower critical mass and hence to the lower value of $k_\infty\Sigma_a$ in the core. With heavy-water reflector the almost fivefold increase in lifetime results mainly from the buildup of a large neutron population in the reflector. This is also evidenced by comparing the flux plots for cases 1 and 7 in Figure 1.

For a given reflector material, increasing the reflector thickness increases the neutron lifetime because of the lower critical mass and the greater neutron population. Reactors reflected by graphite and heavy water benefit the most from the additional 30.5 cm. of reflector because of the large slowing-down length in graphite and the large thermal diffusion length in heavy water. Large values of these properties result in appreciable neutron concentration at considerable distances from the core, and additional reflector thickness is effective in allowing neutron population buildup and in reflecting neutrons back to the core.

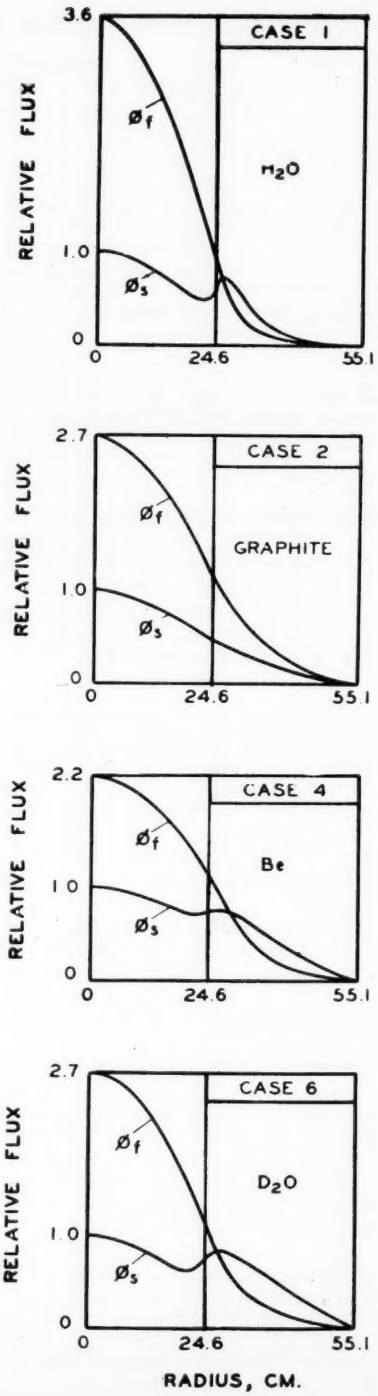

The gains in lifetime with better reflectors are counterbalanced by the less favorable void coefficients. In fact, the positive void coefficients in cases 4 and 5 mean that these reactors are definitely unstable to density changes. The negative void coefficients in cases 3 and 7 are so near zero as to be of little value in providing a means of self-shutdown of the reactor.

The less favorable and positive void coefficients result from the fact that a good reflector reduces the neutron leakage. Any loss in core moderation and increased core leakage from void formation is of lesser importance in affecting the neutron balance than is a poorly reflected or bare reactor. The main result of voiding light-water moderator, which has high neutron absorption, is to decrease parasitic capture, and this tends to make the reactor supercritical. The well-reflected reactor is particularly sensitive to changes in parasitic capture of neutrons by light-water moderator because the reactor has a relatively low critical mass and a much larger fraction of thermal neutrons are being absorbed by water than with a poorly reflected reactor of the same core size.

These results must be qualified, however, as practical research reactors using M.T.R.-type fuel elements have parallelopiped rather than spherical cores, and it is

Fig. 1. Flux distributions for light-water cores.

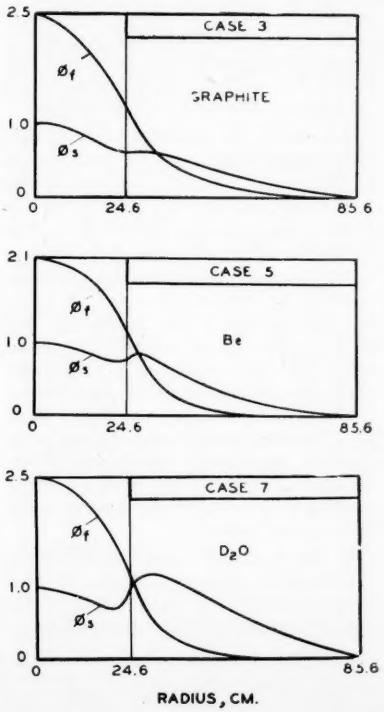

usually necessary to use the water coolant as the reflector on the two core faces through which the water flows. If the other four core faces are surrounded by a better reflector than light water, the trends will be toward more favorable lifetimes and less favorable void coefficients than in the borax case, but the differences in these properties from the borax case will not be so great as those listed in Table 2. For example, the Materials Testing Reactor at Arco, Idaho, is a light-water core reflected on two opposing faces by light-water coolant and on the remaining faces by approximately 30 cm. of beryllium and 120 cm. of graphite. It is reported that the void coefficient for this reactor is negative.

Table 1. Nuclear Data Used in Reactor Calculations

Nuclide	Density, g./cc.	Microscopic cross sections, barns: Thermal absorption*	Thermal transport	Fermi age, sq. cm.
U^{235}	....	597		
H_2O	1.0	0.585	62.9 (3)	31.4
D_2O(0.25%H_2O)	1.1	0.00229	12.0	126.0
Be	1.85	0.00865	5.65 (3)	98.0
C	1.60	0.00412	4.24 (3)	364
Al	2.7	0.204	1.32 (2)	

$$\alpha \text{ for } U^{235} = \frac{\text{capture cross section}}{\text{fission cross section}} = 0.184$$

For the light-water core:

Aluminum-to-water volume ratio = 0.626
Fermi age = 59.1 sq. cm. (4)
Fast-diffusion coefficient = 1.242 cm.

For Al–D_2O mixtures at 20°C. where $X = \frac{\text{aluminum volume}}{\text{water volume}}$

$$\tau = 126.0 + 190.0X \text{ sq. cm.}$$

$$D_f = 1.28 + 0.602X - 0.125X^2 \text{ cm.}$$

*Thermal absorption cross sections from BNL-325 (2), averaged for a Maxwell-Boltzmann distribution of neutrons at 20°C.

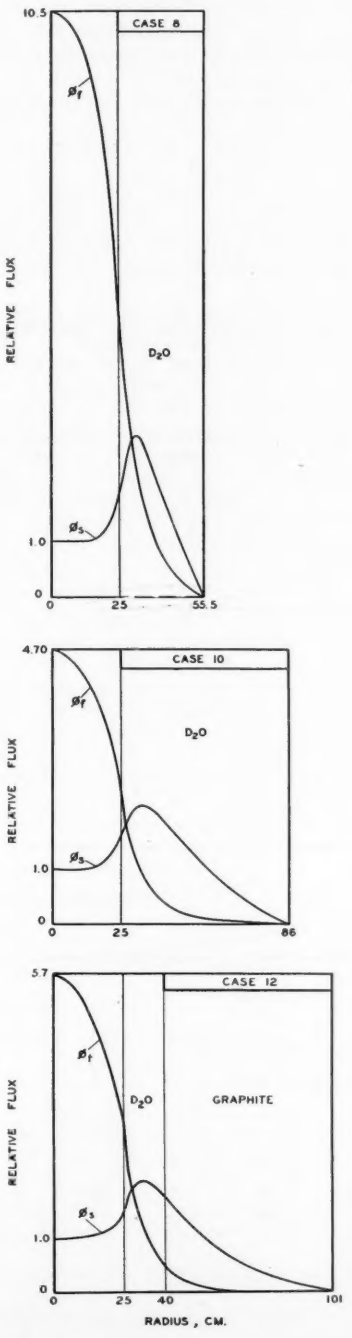

Fig. 2. Flux distributions for heavy-water cores.

Heavy-water Cores

Calculated values of critical mass, neutron lifetime, and void coefficients for the heavy-water cores with various reflectors are presented in Table 3, and flux plots are shown in Figures 2 and 3. The most striking comparison between these results and those of Table 2 lies in the much larger values of neutron lifetimes for heavy-water cores. The lifetimes of all heavy-water cores other than case 9 are much greater even than the heavy-water–reflected light-water cores (cases 6 and 7) of Table 2 because the lower macroscopic thermal absorption cross section in a heavy-water core allows a core neutron to live considerably longer before dying by absorption.

The steam void coefficients in Table 3 are in some cases less favorable and in some cases more favorable than the coefficient of the borax-type reactor (case 1), but they are all more negative than for the other light-water cores of Table 2. As heavy water is such a weak absorber of neutrons, loss of parasitic absorption through steam formation in heavy water in the core contributes little to reactivity changes. Decreased moderation and increased fast leakage as voids are formed account for the negative void coefficients for the heavy-water cores.

Increasing the core radius at constant reflector thickness results in a more negative fractional void coefficient for heavy-water cores. This results from the greater dependence of the smaller core (25-cm. radius) upon the reflector as a source of thermal neutrons. This can be seen from the flux plots, Figures 2 and 3,

Table 2. Nuclear Properties of Cores Cooled and Moderated by Light Water

Core radius: 24.6 cm.
Fuel elements: M.T.R. plate type containing 64.7 kg. of aluminum and amounts of U^{235} indicated below.

Case	1	2	3	4	5	6	7
Reflector	H_2O	C	C	Be	Be	D_2O	D_2O
Reflector thickness, cm.	30.5	30.5	61	30.5	61	30.5	61
k_∞	1.594	1.438	1.386	1.305	1.290	1.457	1.391
Critical mass of U^{235}, kg.	2.257	1.538	1.371	1.157	1.121	1.608	1.387
Prompt neutron lifetime, 10^{-3} sec.	0.0629	0.109	0.202	0.161	0.207	0.144	0.329
Fractional void coefficient $(\partial k_{eff}/k_{eff})/(\partial V_v/V_{H_2O})$	−0.277	−0.110	−0.0391	+0.0536	+0.0735	−0.102	−0.0130
Steam void coefficient $(\partial k_{eff}/k_{eff})/\partial V_v$, 10^{-6} cm.$^{-3}$	−7.21	−2.86	−1.02	+1.40	+1.91	−2.66	−0.338

which show a significant peak of thermal flux in the reflector for the 25-cm. cores and a positive gradient in thermal flux over a large portion of the core volume. As the smaller core is voided, a significant fraction of the increased fast leakage is moderated in the reflector and returned to the core. Since most of the thermal neutrons diffuse toward the center of the small core, loss of heavy water allows them to penetrate nearer the center of the core, where their statistical weight is greatest.*

The 35-cm. heavy-water cores depend much less upon the reflector for moderation, as evidenced by the lower reflector flux peaks in Figure 2. Likewise, thermal neutrons diffuse outward over most of the 35-cm. cores, and with loss of heavy water thermal neutrons tend to penetrate farther away from the regions of high statistical weight in the center of the core. The over-all effect is greater negative fractional void coefficients for the larger heavy-water core because of effectively greater loss of neutrons by leakage when voids are formed in the core moderator.

*The adjoint fluxes, which determine statistical weights, are greatest in the center and decrease monotonically with increasing core radius.

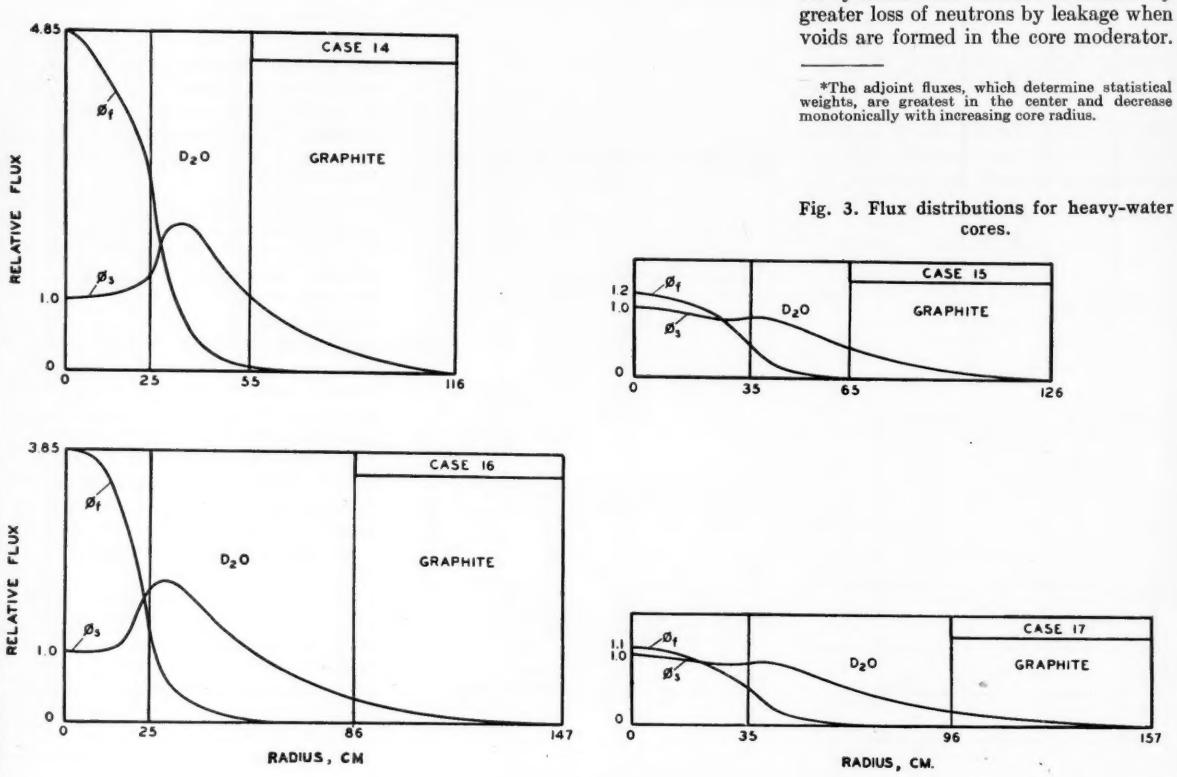

Fig. 3. Flux distributions for heavy-water cores.

Table 3. Nuclear Properties of Cores Cooled and Moderated by Heavy Water

Fuel elements: 57.8 kg. of aluminum containing amount of U^{235} indicated below

Case	8	9	10	11	12	13	14	15	16	17
Core radius, cm.	25	35	25	35	25	35	25	35	25	35
Thickness of D_2O reflector, cm.	30.5	30.5	61	61	15	15	30.5	30.5	61	61
Thickness of graphite reflector, cm.	0	0	0	0	61	61	61	61	61	61
k_∞	1.854	1.734	1.732	1.645	1.746	1.658	1.721	1.637	1.686	1.608
Critical mass of U^{235}, kg.	2.612	1.281	1.227	0.890	1.315	0.933	1.166	0.862	1.008	0.782
Prompt neutron mean lifetime, 10^{-3} sec.	0.239	0.444	0.708	0.955	0.633	0.872	0.835	1.087	1.223	1.490
Fractional void coefficient $(\partial k_{eff}/k_{eff})/(\partial V_v/V_{D_2O})$	−0.272	−0.330	−0.191	−0.232	−0.200	−0.242	−0.184	−0.223	−0.166	−0.200
Steam void coefficient $(\partial k_{eff}/k_{eff})/\partial V_v$, 10^{-6} cm.$^{-3}$	−6.19	−2.08	−4.34	−1.466	−4.55	−1.53	−4.18	−1.41	−3.78	−1.26

Obviously this effect must eventually be reversed as core size is increased further. For an infinitely large reactor there is no leakage, and, if no resonance absorbers are present, loss of moderator by voiding can only increase reactivity due to loss of poisons.

The reactivity change per unit volume of steam formed is greater for the smaller cores, because a unit volume of steam is a much greater fraction of the total moderator volume for the smaller cores. The reactivity change per unit volume of steam is probably more significant than the fractional void coefficient in assessing the inherent safety of a reactor, as it is a measure of the reactivity change per unit amount of heat liberated.

The results of Table 3 for spherically reflected cores should be good approximations for a practical parallelopiped reactor core, because the core, cooled, moderated, and reflected by heavy water, will be surrounded on all sides by heavy water. The graphite outer reflector may be missing beyond two of the core faces, but corrections for this are of less importance.

CONCLUSIONS

It is clear that the greatest safety gain over the borax reactor is due to the use of heavy water for both moderator and reflector. This is shown by the large increase in prompt neutron lifetime with only slight decrease in reactivity change per unit volume of steam.

It is difficult to give a precise measure of the gain in safety since it is not possible to determine quantitatively the amounts of reactivity which, if suddenly imposed on a given reactor, would produce the same result as the borax experiments. Analytical approaches to this have not been completely successful because of lack of information concerning transient heat transfer to boiling water at high heat fluxes and in narrow channels and insufficient knowledge of characteristics of two-phase fluid flow under rapidly varying conditions of pressure and steam quality.

ACKNOWLEDGMENT

This research is in part supported by the Office of Naval Research.

NOTATION

A, C, F, G = coefficients of real fluxes in core and reflector
A^*, C^*, F^*, G^* = coefficients of adjoint fluxes in core and reflector
D = diffusion coefficient, cm.
k_∞ = infinite reproduction factor
k_{eff} = effective reproduction factor
k^0_{eff} = effective reproduction factor immediately after excess reactivity is introduced
l = mean lifetime of prompt neutrons, sec.
L = diffusion length, cm.
p = resonance escape probability
r = radius, cm.
R_1 = radius of reactor core, cm.
R_2 = outside radius of reflector, cm.
S_1, S_2, S_3 = coupling coefficients between fast and thermal fluxes
S_1^*, S_2^*, S_4^* = coupling coefficients between fast and thermal adjoint fluxes
t = time, sec.
T = reactor period after transients from higher flux harmonics have died out, sec.
v = neutron speed, cm./sec.
V = volume, cc.
W, X, Y, Z = space-dependent functions in the expressions for neutron flux
α = steam void coefficient, change in reactivity per unit volume of steam formed, cm.$^{-3}$
η = fission neutrons per neutron absorbed in fuel
κ = reciprocal diffusion length, cm.$^{-1}$
λ = reciprocal period, sec.$^{-1}$
μ = positive component of reciprocal buckling, cm.$^{-1}$
ν = negative component of reciprocal buckling, cm.$^{-1}$
ϕ = neutron flux, neutrons/(sq. cm.)(sec.)
ϕ' = spatial component of neutron flux after a perturbation, neutrons/(sq. cm.)(sec.)
ϕ'' = spatial component of neutron flux after a uniformly occurring perturbation in k_∞, neutrons/(sq. cm.)(sec.)
ϕ^* = adjoint neutron flux, neutrons/(sq. cm.)(sec.)
Σ = macroscopic cross section, cm.$^{-1}$
τ = Fermi age, sq. cm.

Subscripts

c = reactor core
f = properties of fast-neutron group
mod = moderator in reactor core
n = eigenvalue of space-dependent solution of neutron flux
o = first eigenvalue of space-dependent solution of neutron flux
s = properties of thermal neutrons
tr = transport properties
v = steam voids

LITERATURE CITED

1. Dietrich, J. R., 8/P/481, International Conference on the Peaceful Uses of Atomic Energy (1955).
2. Hughes, D. J., and J. A. Harvey, BNL-325, Office of Technical Services, U. S. Department of Commerce (1955).
3. Hughes, D. J., "Pile Neutron Research," Addison-Wesley, Cambridge (1953).
4. Roberts, L. D., and T. E. Fitch, ORNL-294 (1949).

APPENDIX

Derivation of Equations for Void Coefficients and Neutron Lifetimes

The time-dependent neutron-balance equations for a two-group model of a thermal reactor are

$$(\nabla \cdot D_s \nabla - \Sigma_s)\phi_s + p\Sigma_f\phi_f = \frac{1}{v_s}\frac{\partial \phi_s}{\partial t} \quad \text{(A-1)}$$

$$\frac{k_\infty \Sigma_s}{p}\phi_s + (\nabla \cdot D_f \nabla - \Sigma_f)\phi_f = \frac{1}{v_f}\frac{\partial \phi_f}{\partial t} \quad \text{(A-2)}$$

where Σ_f refers to the slowing-down cross section for the fast group. Resonance absorption is assumed to occur in a narrow energy band between the thermal and fast group. Effects of delayed neutrons have been ignored.

The solutions of Equations (A-1) and (A-2) are of the form

$$\phi_s(r, t) = \sum A_n \phi_{sn}(\mathbf{r}) e^{\lambda_n t} \quad \text{(A-3)}$$

$$\phi_f(r, t) = \sum A_n \phi_{fn}(\mathbf{r}) e^{\lambda_n t} \quad \text{(A-4)}$$

where the functions ϕ_{sn} and ϕ_{fn} satisfy the time-independent equations

$$(\nabla \cdot D_s \nabla - \Sigma_s - \lambda_n/v_s)\phi_{sn} + p\Sigma_f\phi_{fn} = 0 \quad \text{(A-5)}$$

$$\frac{k_\infty}{p}\Sigma_s\phi_{sn} + (\nabla \cdot D_f \nabla - \Sigma_f - \lambda_n/v_f)\phi_{fn} = 0 \quad \text{(A-6)}$$

The adjoint fluxes ϕ_{sn}^* and ϕ_{fn}^* are those which are the solutions of the differential equations resulting from transposing the matrix of coefficients of Equations (A-5) and (A-6).

$$(\nabla \cdot D_s \nabla - \Sigma_s - \lambda_n/v_s)\phi_{sn}^* + \frac{k_\infty}{p}\Sigma_s\phi_{fn}^* = 0 \quad \text{(A-7)}$$

$$p\Sigma_f\phi_{sn}^* + (\nabla \cdot D_f \nabla - \Sigma_f - \lambda_n/v_f)\phi_{fn}^* = 0 \quad \text{(A-8)}$$

A just critical reactor ($\lambda = 0$) will be considered in which the following small changes are made:

$$D_s \to D_s + \delta D_s \qquad D_f \to D_f + \delta D_f$$

$$\Sigma_s \to \Sigma_s + \delta\Sigma_s \qquad \Sigma_f \to \Sigma_f + \delta\Sigma_f$$

$$\frac{k_\infty \Sigma_s}{p} \to \frac{k_\infty \Sigma_s}{p} + \delta\left(\frac{k_\infty \Sigma_s}{p}\right) \qquad p\Sigma_f \to p\Sigma_f + \delta(p\Sigma_f) \quad \text{(A-9)}$$

After the changes summarized by Equation (A-9), the reactor flux will fall or rise with an ultimate steady period $1/\lambda$. The space-dependent part of the perturbed fluxes ϕ_{so}' and ϕ_{fo}' obey the equations

$$[\nabla\cdot(D_s + \delta D_s)\nabla - (\Sigma_s + \delta\Sigma_s) - \lambda/v_s]\phi_{so}' + [p\Sigma_f + \delta(p\Sigma_f)]\phi_{fo}' = 0 \quad \text{(A-10)}$$

$$\left[\frac{k_\infty\Sigma_s}{p} + \delta\left(\frac{k_\infty\Sigma_s}{p}\right)\right]\phi_{so}' + \left[\nabla\cdot(D_f + \delta D_f)\nabla - (\Sigma_f + \delta\Sigma_f) - \frac{\lambda}{v_f}\right]\phi_{fo}' = 0 \quad \text{(A-11)}$$

where the subscript o refers to the fundamental mode of the space-dependent solutions.

To compute λ, one multiplies (A-10) by ϕ_{so}^* and (A-11) by ϕ_{fo}^* and adds. λ is set equal to zero in Equations (A-7) and (A-8), (A-7) is multiplied by ϕ_{so}', (A-8) by ϕ_{fo}', and both are added. The second sum is subtracted from the first and the resulting equation is integrated over the reactor volume. The result, arrived at from Green's theorem and the fact that the flux vanishes at the outer surface of the reactor, is

$$\lambda = \frac{\int_V \left[\delta(p\Sigma_f)\phi_{so}^*\phi_{fo}' + \delta\left(\frac{k\Sigma_s}{p}\right)\phi_{fo}^*\phi_{so}' - \delta\Sigma_s\phi_{so}^*\phi_{so}' - \delta\Sigma_f\phi_{fo}^*\phi_{fo}' - \nabla\phi_{so}^*\cdot\delta D_s\nabla\phi_{so}' - \nabla\phi_{fo}^*\cdot\delta D_f\nabla\phi_{fo}'\right] dV}{\int_V \left[\frac{\phi_{so}^*\phi_{so}'}{v_s} + \frac{\phi_{fo}^*\phi_{fo}'}{v_f}\right] dV} \quad \text{(A-12)}$$

A reactivity change is described by that equivalent to a uniform change in k_∞, $\overline{\delta k}_\infty$, which if imposed on the just critical reactor would lead to the same period, $1/\lambda$, as do all the actual changes. The neutron flux ϕ_o'' in this equivalent reactor will satisfy

$$(\nabla\cdot D_s\nabla - \Sigma_s - \lambda/v_s)\phi_{so}'' + p\Sigma_f\phi_{fo}'' = 0 \quad \text{(A-13)}$$

$$\frac{\Sigma_s}{p}(k_\infty + \overline{\delta k}_\infty)\phi_{so}'' + (\nabla\cdot D_f\nabla - \Sigma_f - \lambda/v_f)\phi_{fo}'' = 0 \quad \text{(A-14)}$$

By the same technique that led to (A-12), the relation between λ and $\overline{\delta k}_\infty$ is found to be

$$\lambda = \frac{\overline{\delta k}_\infty \int_V \frac{\Sigma_s}{p}\phi_{fo}^*\phi_{so}''\, dV}{\int_V \left(\frac{\phi_{so}^*\phi_{so}''}{v_s} + \frac{\phi_{fo}^*\phi_{fo}''}{v_f}\right) dV} \quad \text{(A-15)}$$

For a single multiplying region the fractional change $\overline{\delta k}_\infty/k_\infty$ is identical with the fractional change in the effective reproduction factor $\delta k_{eff}/k_{eff}$. One may solve explicitly for $\overline{\delta k}_\infty/k_\infty$ by eliminating λ from (A-12) and (A-15) and making the approximation of first-order perturbation theory that

$$\phi_0'' = \phi_0' = \phi$$

where ϕ is the solution of Equations (A-5) and (A-6) with λ equal to zero.

There results

$$\frac{\overline{\delta k}_\infty}{k_\infty} = \frac{\int_V \left[\delta(p\Sigma_f)\phi_s^*\phi_f + \delta\left(\frac{k_\infty\Sigma_s}{p}\right)\phi_f^*\phi_s - \delta\Sigma_s\phi_s^*\phi_s - \delta\Sigma_f\phi_f^*\phi_f - \nabla\phi_s^*\cdot\delta D_s\nabla\phi_s - \nabla\phi_f^*\cdot\delta D_f\nabla\phi_f\right] dV}{\int_V \frac{k_\infty\Sigma_s}{p}\phi_f^*\phi_s\, dV} \quad \text{(A-16)}$$

As delayed neutrons in the original equations have been neglected, the reciprocal asymptotic period λ, when all harmonics have died out, is related to the effective reproduction factor k_{eff} and mean lifetime of prompt neutrons l by

$$\lambda = \frac{k_{eff} - 1}{l} \quad \text{(A-17)}$$

For perturbations to an initially critical reactor, k_{eff} initially equals unity, and so for a reactor with a single multiplying region

$$k_{eff} - 1 = \frac{\delta k_{eff}}{k_{eff}} = \frac{\overline{\delta k}_\infty}{k_\infty} \quad \text{(A-18)}$$

and

$$\lambda = \frac{\overline{\delta k}_\infty}{k_\infty l} \quad \text{(A-19)}$$

Solving for l from Equations (A-15) and (A-19) one obtains

$$l = \frac{\int_V \left[\frac{\phi_s^*\phi_s}{v_s} + \frac{\phi_f^*\phi_f}{v_f}\right] dV}{\int_V \frac{k_\infty\Sigma_s}{p}\phi_f^*\phi_s\, dV} \quad \text{(A-20)}$$

For thermal reactors the second term in the numerator of the equation is much smaller than the first term and may be neglected, so that

$$l \cong \frac{\int_V \frac{\phi_s^*\phi_s}{v_s} dV}{\int_V \frac{k_\infty\Sigma_s}{p}\phi_f^*\phi_s\, dV} \quad \text{(A-21)}$$

This is equivalent to saying that the slowing-down time is small compared with the thermal lifetime.

A spherical reactor core of radius R_1 surrounded by a spherical reflector shell of outside radius R_2 will be considered. The reactor is assumed to be just critical before perturbations occur. The solutions of the real and adjoint fluxes in the core and reflector are as follows:

Core

$$\phi_{fc} = AW + CX \quad \text{(A-22)}$$

$$\phi_{sc} = AS_1W + CS_2X \quad \text{(A-23)}$$

where

$$W = \frac{\sin \mu r}{r} \quad \text{(A-24)}$$

$$X = \frac{\sinh \nu r}{r} \quad \text{(A-25)}$$

$$S_1 = \frac{D_{fc}}{D_{sc}\tau_c}\left[\frac{p}{\kappa_{sc}^2 + \mu^2}\right] \quad \text{(A-26)}$$

$$S_2 = \frac{D_{fc}}{D_{sc}\tau_c}\left[\frac{p}{\kappa_{sc}^2 - \nu^2}\right] \quad \text{(A-27)}$$

$$\mu^2 = \frac{1}{2}\left[-\left(\frac{1}{\tau_c} + \frac{1}{L_{sc}^2}\right) + \sqrt{\left(\frac{1}{\tau_c} + \frac{1}{L_{sc}^2}\right)^2 + \frac{4(k_\infty - 1)}{\tau_c L_{sc}^2}}\right] \quad \text{(A-28)}$$

$$\nu^2 = -\frac{1}{2}\left[-\left(\frac{1}{\tau_c} + \frac{1}{L_{sc}^2}\right) - \sqrt{\left(\frac{1}{\tau_c} + \frac{1}{L_{sc}^2}\right)^2 + \frac{4(k_\infty - 1)}{\tau_c L_{sc}^2}}\right] \quad \text{(A-29)}$$

$$\kappa_{sc}^2 = \frac{1}{L_{sc}^2} \quad \text{(A-30)}$$

$$\phi_{fc}^* = A^*W + C^*X \quad \text{(A-31)}$$

$$\phi_{sc}^* = A^*S_1^*W + C^*S_2^*X \quad \text{(A-32)}$$

$$S_1^* = \frac{\mu^2\tau + 1}{p} \quad \text{(A-33}a\text{)}$$

$$S_2^* = \frac{1 - \nu^2\tau}{p} \quad \text{(A-33}b\text{)}$$

Reflector

$$\phi_{fr} = FY \quad \text{(A-34)}$$

$$\phi_{sr} = FS_3Y + GZ \quad \text{(A-35)}$$

where

$$Y = \frac{\sinh \kappa_{fr}(R_2 - r)}{r} \quad \text{(A-36)}$$

$$Z = \frac{\sinh \kappa_{sr}(R_2 - r)}{r} \quad \text{(A-37)}$$

$$\kappa_{fr}^2 = \frac{1}{\tau_r} \quad \text{(A-38)}$$

$$S_3 = \frac{D_{fr}}{D_{sr}}\left(\frac{1}{\kappa_{sr}^2\tau_r - 1}\right) \quad \text{(A-39)}$$

$$\phi_{fr}^* = F^*Y + G^*Z \quad \text{(A-40)}$$

$$\phi_{sr}^* = G^*S_4^*Z \quad \text{(A-41)}$$

where

$$S_4^* = 1 - \kappa_{sr}^2\tau_r \quad \text{(A-42)}$$

The fast and thermal fluxes, real and adjoint, must satisfy the boundary conditions of continuity of flux and neutron current at the core-reflector interface (at R_1):

$$\left.\begin{array}{llll} WA + XC - YF = 0 \\ D_{fc}\nabla WA + D_{fc}\nabla XC - D_{fr}\nabla YF = 0 \\ S_1WA + S_2XC - S_3YF - ZG = 0 \\ D_{sc}S_1\nabla WA + D_{sc}S_2\nabla XC - D_{sr}S_3\nabla YF - D_{sr}\nabla ZG = 0 \end{array}\right\} \quad \text{(A-43)}$$

$$\left.\begin{array}{llll} WA^* + XC^* - YF^* - ZG^* = 0 \\ D_{fc}\nabla WA^* + D_{fc}\nabla XC^* - D_{fr}\nabla YF^* - D_{fr}\nabla ZG^* = 0 \\ S_1^*WA + S_2^*XC^* - S_4^*ZG^* = 0 \\ D_{sc}S_1^*\nabla WA^* + D_{sc}S_2^*\nabla XC^* - D_{sr}S_4^*\nabla ZG^* = 0 \end{array}\right\} \quad \text{(A-44)}$$

For given R_1 and R_2, the critical fuel concentration (or k_∞) can be calculated from (A-43). Relative values of the coefficients A, C, F, and G can then be calculated for (A-43), and relative values of A^*, C^*, F^*, and G^* from (A-44).

If there are two reflector regions, as with the D_2O-core reactors, the flux expressions for the inner reflector must contain both sinh and cosh terms, and an additional set of boundary conditions must be written for the interface between the two reflectors. The treatment is otherwise the same as for the single reflector.

Flux expressions obtained as above can be substituted in (A-21) to determine the prompt neutron lifetime.

Void Coefficient

When a differential volume ∂V_s of steam is formed, the total moderator volume increases by the same amount ($\partial V_{mod} = \partial V_s$), and a volume ∂V_{mod} is displaced from the reactor core. The fractional change in k_{eff} per fractional increase in core moderator volume is obtained from (A-16):

$$\frac{\partial k_{eff}/k_{eff}}{\partial V_s/V_{mod}} = \frac{\partial \overline{k}_\infty/k_\infty}{\partial V_{mod}/V_{mod}}$$

$$= \frac{1}{\int_V \frac{k_\infty \Sigma_s}{p}\phi_f^*\phi_s\, dV}$$

$$\cdot \left[\frac{\partial(p\Sigma_f)_c}{\partial V_{mod}/V_{mod}}\int_{V_c}\phi_s^*\phi_f\, dV + \frac{\partial\left(\frac{k_\infty\Sigma_s}{p}\right)}{\partial V_{mod}/V_{mod}}\int_{V_c}\phi_f^*\phi_s\, dV - \frac{\partial\Sigma_{fc}}{\partial V_{mod}/V_{mod}}\int_{V_c}\phi_f^*\phi_f\, dV - \frac{\partial\Sigma_{sc}}{\partial V_{mod}/V_{mod}}\int_{V_c}\phi_s^*\phi_s\, dV - \frac{\partial D_{sc}}{\partial V_{mod}/V_{mod}}\int_{V_c}\nabla\phi_s^*\cdot\nabla\phi_s\, dV - \frac{\partial D_{fc}}{\partial V_{mod}/V_{mod}}\int_{V_c}\nabla\phi_f^*\cdot\nabla\phi_f\, dV\right] \quad \text{(A-45)}$$

For reactors fueled with fully enriched U^{235}, p is unity and the second term in the brackets of (A-45) drops out.

The differential perturbations are evaluated as follows for a core consisting of U^{235}, aluminum, and moderator:

$$\Sigma_s = \Sigma_s(\mathrm{U}) + \Sigma_s(\mathrm{Al}) + \Sigma_s(\mathrm{mod})$$

As voids are formed, the total volume occupied by moderator atoms increases, and the macroscopic cross section for moderator absorption is given by

$$\Sigma_s'(\mathrm{mod}) = \Sigma_s(\mathrm{mod})\frac{V_{mod}}{V_{mod}'}$$

where the primed quantities are the values after a change in moderator density. For a differential increase in moderator volume,

$$\frac{\partial\Sigma_s}{\partial V_{mod}/V_{mod}} = -\Sigma_s(\mathrm{mod}) \quad \text{(A-46)}$$

$$D_s' = \frac{1}{3\left[\Sigma_{tr}(\mathrm{Al}) + \Sigma_{tr}(\mathrm{mod})\frac{V_{mod}}{V_{mod}'}\right]}$$

so that

$$\frac{\partial D_s}{\partial V_{mod}/V_{mod}} = \frac{D_{sc}^2}{D_s(\mathrm{mod})} \quad \text{(A-47)}$$

The change in slowing-down cross section resulting from an increase in volume occupied by moderator is written by analogy to Equation (A-46):

$$\frac{\partial\Sigma_f}{\partial V_{mod}/V_{mod}} = -\Sigma_f(\mathrm{mod}) \quad \text{(A-48)}$$

The total slowing-down cross section Σ_f will be essentially that of the moderator $\Sigma_f(\mathrm{mod})$, because of the low logarithmic energy decrement of aluminum relative to that of the moderator.

Since the total slowing-down cross section in two-group theory is

$$\Sigma_f = \frac{D_f}{\tau}$$

Equation (A-48) becomes

$$\frac{\partial\Sigma_f}{\partial V_{mod}/V_{mod}} = -\frac{D_f}{\tau} \quad \text{(A-49)}$$

The perturbation in fast diffusion coefficient is written by analogy to Equation (A-47):

$$\frac{\partial D_f}{\partial V_{mod}/V_{mod}} = \frac{D_f^2}{D_f(\mathrm{mod})} \quad \text{(A-50)}$$

In the calculation of a differential void coefficient for a reactor with no resonance capture, Equations (A-46), (A-47), (A-49), and (A-50) are substituted in (A-45). The flux integrals are easily evaluated from the flux expressions obtained as described above. The volume integrals involving products of flux gradients are easily evaluated from Green's theorem.

Presented at Nuclear Sciences and Engineering Congress, Cleveland

Heat Transfer to Water Flowing Parallel to a Rod Bundle

PHILIP MILLER, JAMES J. BYRNES, and DAVID M. BENFORADO

Walter Kidde Nuclear Laboratories, Inc., Garden City, New York

Heat transfer was measured for water flowing parallel to 5/8-in. rods in a triangular lattice (0.914-in. spacing). Velocity was varied from 5 to 20 ft./sec., temperature from 150° to 325°F., and heat flux from 50,000 to 200,000 B.t.u./(hr.)(sq. ft.). Reynolds numbers ranged from 70,000 to 700,000. Coefficients were 40% higher than predicted from the Colburn equation for flow in pipes by use of the equivalent diameter. The effect of heated length was studied. No variation in local coefficient around the rod periphery was found. Pressure drops were 65% higher than predicted by the Fanning equation (by use of D_e).

No published data have been found for the case of heat transfer to a fluid in turbulent flow outside rods or tubes in a bundle, with flow parallel to the rod axes. In the most recent general texts on heat transfer the following information is offered. McAdams (*8*) and Jakob (*7*) do not mention this case. Eckert (*5*) recommends using the equation for turbulent flow inside tubes, with an equivalent diameter $D_e = 4 \times$ flow area $\div$ wetted perimeter. His recommendation is apparently made on theoretical grounds, as no data are cited. In the section on heat transfer in "The Chemical Engineers' Handbook" (*10*) McAdams states that test data for gases are in rough agreement with equations for gases inside pipes when the equivalent diameter is used. Experimental results have been published on shell-side heat transfer in unbaffled shell-and-tube heat exchangers, and these were correlated by Donohue (*4*). However, in these studies the local velocity within the tube bundle was not known, and the average velocity was used in the correlation. Because of the considerable space between the tube bundle and the shell, the leakage was undoubtedly sufficient to make the local velocity within the tube bundle much less than the average velocity. Presumably on this account Donohue's correlation predicts values of shell-side coefficients that are one-half to one-third the values obtained by Eckert's procedure. Consequently, it is not safe to apply Donohue's equation to cases other than shell-and-tube heat exchangers of the type for which the original data were obtained.

The lack of information on parallel-flow heat transfer in rod bundles no doubt reflects the absence of examples of its occurrence in industrial equipment. In baffled shell-and-tube heat exchangers true parallel flow probably does not occur; and in unbaffled heat exchangers it has evidently proved expedient to use empirical correlations involving average velocities and various correction factors rather than to measure the leakage and make more basic correlations. However, a need for reliable data on parallel-flow heat transfer has developed with the advent of nuclear reactors. Among the large variety of reactor designs under serious consideration for various applications, a number involve parallel-flow heat transfer from cylindrical rods at high heat fluxes and large Reynolds numbers. In particular, some of these contemplate the use of pressurized water at high temperature as the coolant for power-producing reactors. Both technical and economic reasons make it important to know the heat transfer coefficients for reactor design with considerable accuracy. For this reason an experimental investigation was undertaken of parallel-flow heat transfer to water flowing through a lattice of cylindrical rods.

The experimental equipment was of a rather large scale, as evident from the photograph in Figure 1; the maximum water-circulation rate was 1,100 gal./min., provided by a 25-hp. pump. Several factors contributed to this large size. The first was the decision to study a section of a full-scale lattice of ⅝-in. rods, rather than a small-scale model. Then, in the absence of advance knowledge of the wall effect, a lattice of reasonably large cross section was needed; the one used contained thirty-seven rods enclosed in a 6¼-in. cylinder (plus eighteen partial rods attached to the boundary wall). Finally, the interest in relatively high velocities, up to 20 ft./sec. maximum, contributed to the high circulation rate.

The lattice was made up of unheated dummy aluminum rods except for one test rod, which had a 4- or 8-in.-long middle section internally heated by an electrical resistance coil. Measurements were made at relatively high heat fluxes [50,000 to 200,000 B.t.u./(sq. ft.)(hr.)], corresponding to a maximum power density as high as 0.8 kw./in. of heated length. Development of a satisfactory heated test rod, and of a method of measuring the temperature of the heated surface, proved to be the major problems of this investigation. All the rods had tapered ends and were supported vertically between perforated plates, so that no change of flow direction was required in the entrance and exit sections. Frictional pressure drops were measured along the rod length.

This work was concerned primarily with obtaining heat transfer data for parallel flow of water in a triangular lattice of cylindrical rods at high temperature, high flow rate, and high heat flux. The maximum water temperature used was 325°F. at an imposed pressure of 140 lb./sq. in. gauge to ensure the absence of boiling at the heated surface, which reached a maximum temperature of 360°F. This temperature limit, which is several hundred degrees below the temperatures that would be encountered in water-cooled power reactors, is a compromise with the rapidly increasing cost and complexity accompanying the higher temperatures. In addition to the normal lattice studies, measurements were made in four different lattice positions to study the wall effect, the effect of a neighboring control-rod thimble (⅞-in. diam.), and the effect of severe lattice distortion. Information was also obtained on the variation of the local heat transfer coefficient around the rod periphery and on the effect of heated length.

DESCRIPTION OF EQUIPMENT

Circulation System

A flow diagram of the water loop is shown in Figure 2. The loop was constructed mainly of welded standard carbon steel pipe with bolted flange connections. Starting at the lower left-hand corner of the diagram and proceeding clockwise, water flowed upward through the test lattice, which was enclosed in a flanged section of 10-in. pipe. The water then flowed through an 11-ft. horizontal run (22 pipe diameters) of 6-in. pipe before passing through an orifice for flow measurement. After a 2½-ft. horizontal run (5 pipe diameters) it entered a vertical downcomer (8-in. pipe) leading to the suction side of the circulating pump. A surge tank consisting of an 18-in. section of 12-in. pipe with a total volume of 9 gal. was mounted above this downcomer. The tank was separated from the circulating system by a bottom plate with a 1-in. opening. System pressure was adjusted by introducing compressed nitrogen into the gas space in the upper part of the surge tank, which was equipped with a liquid-level gauge glass. The pump was a Weinman bronze-fitted, horizontal split-case, cast-iron centrifugal with outboard bearings, direct-driven by a 25-hp. motor. Flow rate was controlled by means of both a gate valve in a 4-in. by-pass line around the pump and a gate valve in the main 6-in. discharge line from the pump. The entire loop was insulated with 2 in. of 85% magnesia.

The loop was operated at water temperatures of 150°, 200°, 250°, 300°, and 325°F.

For complete tabular data, order document 4831 from A.D.I. Auxiliary Publications Photoduplication Service, Library of Congress, Washington 25, D. C., remitting $1.75 for microfilm or $2.50 for photoprints readable without optical aid.

For the lower temperatures the water was heated by introducing live low-pressure steam. To reach higher temperatures five electrical Calrod heaters with a combined capacity of 14 kw. were used. One 3-kw. unit, on automatic control, was used mainly in keeping the system hot overnight between tests (two-shift operation was used for most of the data taking). To maintain steady conditions at the lower temperatures, it was necessary to remove heat because the pump added more heat than was lost from the insulated system. The heat was removed by circulating a small by-pass stream through a Heliflow water-to-water heat exchanger. The heat exchanger had 2.76 sq. ft. of heat transfer area in the form of a helical coil of ½-in. tubing and used a maximum flow of 10 gal./min. of cooling water. Both the temperature and pressure in the loop were controlled manually, with satisfactory results.

Water was injected into the system intermittently to make up for losses through the pump packing glands. Leakage rates became quite high at the higher temperatures and pressures; the 7-gal. effective liquid capacity of the surge tank permitted operation without make-up for 2 hr. at the highest pressure used (140 lb./sq. in. gauge). Make-up water, partially preheated, was added by means of a pressurized storage tank made of a 4-ft. section of 10-in. pipe.

Instrumentation

The general instrumentation of the circulation system is indicated in Figure 2. Water flow was measured with an orifice meter equipped with standard horizontal flange taps, a 4.175-in. orifice in a 6-in. line (6.065 in. I.D.) being used. In order to cover the entire flow range with a single orifice, a mercury-filled manometer was used to measure the pressure differentials for the higher flow rates, and an inverted gas-filled manometer (using the water in the system as the manometer fluid) measured the lower rates. In this way the smallest differential measured was 8 in.

Static pressures in the system were measured with Bourdon gauges with a range of 0 to 160 lb./sq. in. gauge, graduated to 4 lb./sq. in. gauge, at the locations shown in Figure 2. The surge tank and make-up water tank were equipped with safety valves set at 150 lb./sq. in. gauge. The top of the surge tank was also equipped with a ball-float water-drain valve.

The following instrumentation was provided for the test lattice. Pressure drops were measured across the entire lattice (over a 4½-ft. length of the test section) and over the 3-ft. straight length of the dummy rods. For the lattice measurements pressure connections were made just below the bottom support plate and above the top one. In each case four taps in the 10-in. pipe spaced at 90° were connected to a piezometer ring. The internal measurements were made by means of suitably modified dummy rods, in which the pressure was likewise averaged around the circumference by means of four openings 90° apart. In addition to one of the standard ⅝-in. rods (*A* in Figure 3), the ⅞-in. rod used to simulate a control-rod thimble (*B* in Figure 3) was used for pressure-drop measurements).

The bulk water temperature was measured upstream of the lattice with both a thermometer and a thermocouple. The thermometer, which was used as an operating control and a check on the thermocouple, was located in an oil-filled steel well in the horizontal line approaching the lattice. It was a Fisher total-immersion thermometer with a scale covering 0° to 200°C. over a length of 18 in. and graduated to 0.2°C. The thermocouple was chromel-alumel and was inserted in an oil-filled copper well below the bottom support plate. The reference junction was placed in an ice bath. Both the thermometer and the thermocouple were calibrated in an oil bath against a set of four Anshutz precision thermometers covering the range from room temperature to 200°C. and in addition were calibrated at 0°C. in an ice bath and at 100°C. with condensing steam. When a standard immersion correction was applied to the thermometer reading, it generally checked the thermocouple reading within 0.5°F.

The temperature difference between the heater surface and the water was measured directly by placing a reference junction for each surface thermocouple in the same well that contained the chromel-alumel thermocouple for measuring water temperature. Since the test heater raised the temperature of the adjacent water by a small but appreciable amount, a correction was calculated on the basis that all the heat released upstream of the given thermocouple location was used to raise the average temperature of one rod's "share" of the total water flow. The correction reduced the measured temperature difference by 1 to 2%. The thermocouple voltages were read with a Leeds and Northrup type K-2 potentiometer and a Leeds and Northrup D.C. (No. 2430) galvanometer. A 12-point rotary switch was used to permit rapid readings. The surface thermocouples were calibrated in the water loop by comparison with the calibrated chromel-alumel thermocouple used to measure the bulk water temperature. By means of an ice-bath reference junction for all thermocouples, comparative steady state readings were made of the temperature of the circulating water, with no heat input to the test heater.

The test element was heated with d.c. current from a Westinghouse type R.A. arc welder, rated to supply 200 amp. at 40

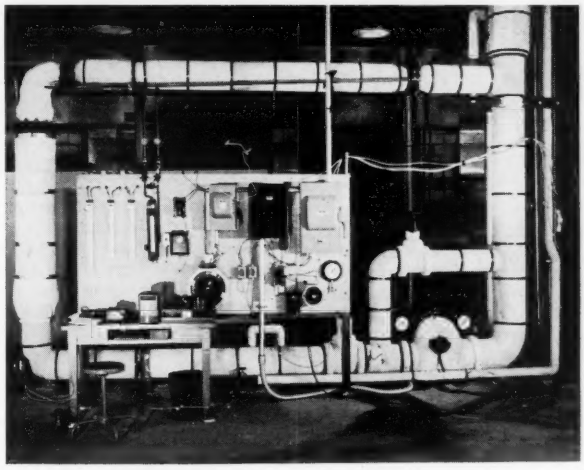

Fig. 1. Water-circulation loop for heat transfer measurements.

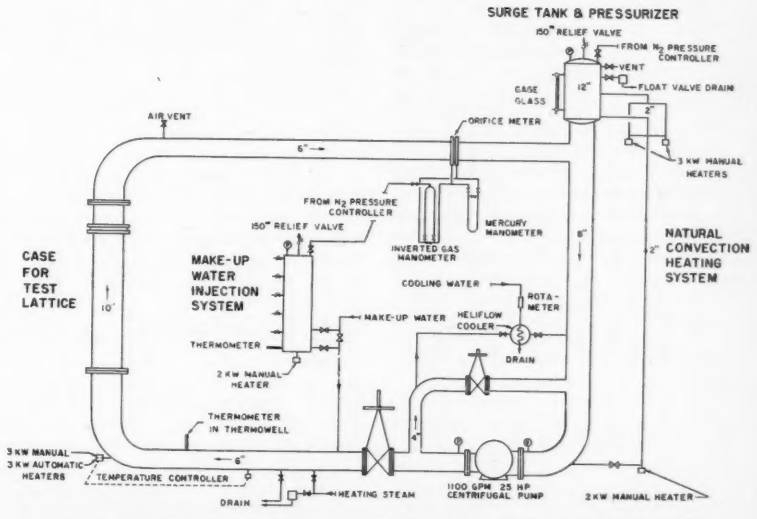

Fig. 2. Flow diagram including general instrumentation for circulation system.

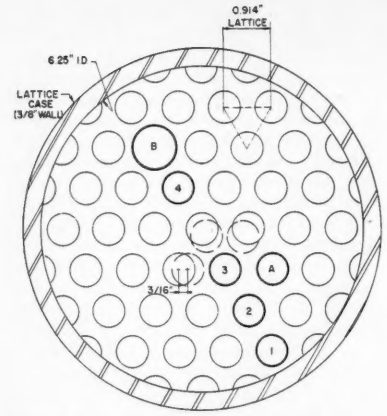

Fig. 3. Cross section through lattice showing arrangement of rods.

volts. The maximum power input obtainable with the heaters used (close to 1 ohm of resistance) was approximately 3.2 kw. corresponding to a current of 56.5 amp. and a voltage drop of 56.5 volts across the heater. The power input was measured with a Weston model 310 wattmeter, which had scales of 1,000, 2,000, and 4,000 watts. Independent calibrations of this meter by the vendor and by another laboratory showed the maximum error on any scale to be less than ¼ of 1% of full-scale value.

Test Lattice

The test lattice consisted of a vertical bundle of solid 61ST-6 aluminum rods supported between two perforated plates. The lattice was enclosed in a cylindrical steel case of 6¼-in. I.D., which was contained in a 10-in. pipe. The case was supported at the top by a flange which was sandwiched between two flanges connecting two sections of the 10-in. pipe. The annular space between the pipe and inner case was filled with water at the system pressure, but the top supporting flange prevented any flow through this space, forcing all the water through the lattice.

The rods were 4.0 ft. long (clear distance between support plates). They had an O.D. of 0.625 in. and were arranged in a triangular lattice with 0.914 in. between centers. Figure 3 shows a cross section through the lattice; it is seen that the 6¼-in. circular boundary encloses thirty-seven full-sized rods and intersects eighteen additional rods. Partial rods of the indicated cross section were attached to the cylinder wall in these eighteen positions. A single rod of 0.875-in.-diam., designated *B*, was installed to simulate a control-rod thimble. The rod positions numbered from 1 to 4 indicate the locations where heater rods were installed in various tests. The three displaced circles (dashed line) adjacent to position 3 indicate the locations to which these three dummy rods were moved in a special test of lattice distortion.

The dummy rods were tapered for 6 in. at each end to avoid blocking the openings in the support plates. The rods were fastened rigidly to the top plate by means of an extension pin, threaded for a standard nut. A lower extension pin made a slip fit in an opening in the lower plate, to allow for longitudinal thermal expansion or contraction. [It was found that a coating of liquid moly (molybdenum disulfide) prevented freezing of this pin.] The support plates were made of 61ST-6 aluminum; the top one was ¼ in. thick and the bottom one ⅛ in. The openings for water flow had a diameter of 0.485 in.; they were arranged in a hexagonal pattern which resulted in an average of two openings for each rod and a free-flow area of 44.3%, or 13.6 sq. in.

Table 1. Dimensional Tolerances for Test-lattice Components

Component	Dimension	Magnitude, in.	Specified tolerance, in.	Actual tolerance, in.
Support plates	Rod support spacing	0.914	±0.015	±0.003
	Diameter	7.998	+0.000	+0.000
			−0.003	−0.003
	Concentricity of center rod with 7.998 O.D.		0.005	0.005
Dummy rods	Diameter of support	0.202	+0.000	+0.000
			−0.005	−0.002
	Concentricity of support pins and rod		0.010	0.005
	Rod straightness		0.010	0.005
	Rod diameter	0.625	±0.005	±0.002
Steel cylinder	Inside diameter	6¼	±1/64	±0.005

Dimensional tolerances for the test lattice were established on the basis that they should contribute to the probable error of the measurements equally with other sources, such as flow measurement, temperature measurement, etc. (See discussion on accuracy of results, page 231.) Table 1 lists the resulting specified tolerances. It is of interest that the error analysis resulted in a considerable relaxation from more rigid tolerances originally felt to be necessary, which led to a considerable reduction in time and cost of machining. The tolerances actually achieved are also listed in Table 1; they were considerably better than the specified values.

Description of Heater Rod

Three heated test rods, all basically similar in construction, were used in obtaining the data reported in this paper. The construction of rod 15, an aluminum-jacketed unit that was used in most of the work, was described completely in a recent paper (9). Figure 4 shows some of the construction details of this heater rod, which had a 4-in. heated section located midway in its length.

Heater rod 18, which was used in some cases when rod 15 was under repair and in some cases in the same tests as rod 15, differed from it only in the following respects. The heater jacket was nickel instead of aluminum. The thermocouples were chromel-alumel instead of copper-nickel; the thermocouple wires were 5 mils in diameter and were insulated with resin-impregnated Fiberglas. Because of the larger O.D. of this insulation, the grooves for the two external thermocouples with which the heater was provided had to be enlarged to 12 mils wide by 12 mils deep. The junctions for these thermocouples were soldered, and the two wires for each thermocouple were only 10 degrees apart on the circumference. In addition, rod 18 was provided with two "internal" thermocouples, which were used to test a method of thermocouple installation that involved minimum disturbance of the heater surface. A 6-in. groove 25 mils wide by 20 mils deep was made along the inside of the nickel jacket. Two holes, each 31 mils in diameter, were drilled out to the surface, each being ½ in. from the center of the groove on either side. Two chromel-alumel thermocouples were brought in along this groove, one from either end, and the junctions were bent into the holes and brought out to within about 5 mils of the surface. The hole was then filled in with hot solder and smoothed over. The leads for these two thermocouples were brought out through the hollow end pieces of the rod, along with the power and voltage leads.

The two internal thermocouples were located respectively ½ in. upstream (No. 1) and ½ in. downstream of the middle. (See Figure 5.) One external thermocouple (No. 3) was located ½ in. downstream, 180 degrees away from No. 2, and the other (No. 4) was located ½ in. upstream, 90 degrees from No. 1.

Heater rod 20, which was constructed late in the investigation, had an 8-in. heated length and a copper jacket. It was provided with eight thermocouples spaced axially along the rod from ⅝ to 7½ in. past the upstream end and 45 degrees apart circumferentially. Each thermocouple required only a single groove, for a nickel wire, as the copper jacket completed the thermocouple circuit. (It was found by test that the thermoelectric effect between the copper tube and copper wire was negligible.)

Surface Temperature Measurement

Measurement of the surface temperature presented serious difficulties. The thermocouple had to be mounted in a manner that would avoid local flow disturbance and at the same time would place the junction at the surface. The use of a plated thermocouple, as described by Bonilla (*6*), was considered but had to be discarded because it would require either an insulating layer between the thermocouple and the rod jacket or the use of a nonmetallic rod, and neither was practical. Both calculation and experiment showed that a thermocouple plated directly on the metal jacket would read the temperature only at the point where the insulated lead wire made a junction with the plate, and so the plate served no purpose.

The method used, that of embedding the thermocouple wires in shallow downstream grooves which were then filled and smoothed, avoided interference with

water flow. However, it presented several possibilities for error that had to be investigated. First, because the thermocouple junction was below the surface and there was a temperature gradient in the jacket, the thermocouple might read high. Second, because the thermal conductivities of the thermocouple itself, or the cold solder used to wedge it in, and of the intermetallic boundaries were different from those of the jacket material, a disturbance might result in the thermal flux pattern which could make the thermocouple read either high or low. Both of these effects would vary with the thermal conductivity of the jacket material, and for this reason heated elements were initially constructed with both aluminum and nickel jackets [k = 119 and 34 B.t.u./(hr.)(ft.)(°F.), respectively], and later with a copper jacket (k = 218).

rods were incorporated in an annulus heat transfer experiment.

Heat Transfer Measurements in a Tube

The tubular tests were made in a vertical copper tube 0.548 in. I.D. Water flowed upward. An 8-in. length was heated by an external winding of asbestos-insulated chromel-A wire, covered with 1 in. of 85% magnesia. The inner wall temperature was measured by two thermocouples located 90 degrees apart, each consisting of a 3-mil nickel wire inserted in a groove 8 mils wide by 8 mils deep, with the copper tube completing the circuit. The soldered junctions were located 6 in. from the upstream end of the heater. Two external thermocouples were similarly installed in grooves on the outside of the tube, 90 degrees apart from each other and each 90 degrees apart from one of the interval thermo-

adequate for full development of the thermal boundary layer. The total straight upstream length was 29 in. (53 diameters), sufficient for a fully developed hydraulic boundary layer.

The two external thermocouples differed by 8% (based on ΔT), and their mean was consistently higher than the mean of the internal thermocouples. The difference varied from 0.1° to 1.9°F. with a mean of 0.7°F. This compares with a calculated temperature drop of 0.8°F. across the copper tube wall.

The reliability of the measurements was confirmed by a heat balance, which indicated that the water picked up 95 ± 5% of the total electrical heat input. This was corroborated by an external loss of 3 to 5% from the heating coil, as indicated by both measurement and calculation. A value of 95% of the measured power input was used in calcu-

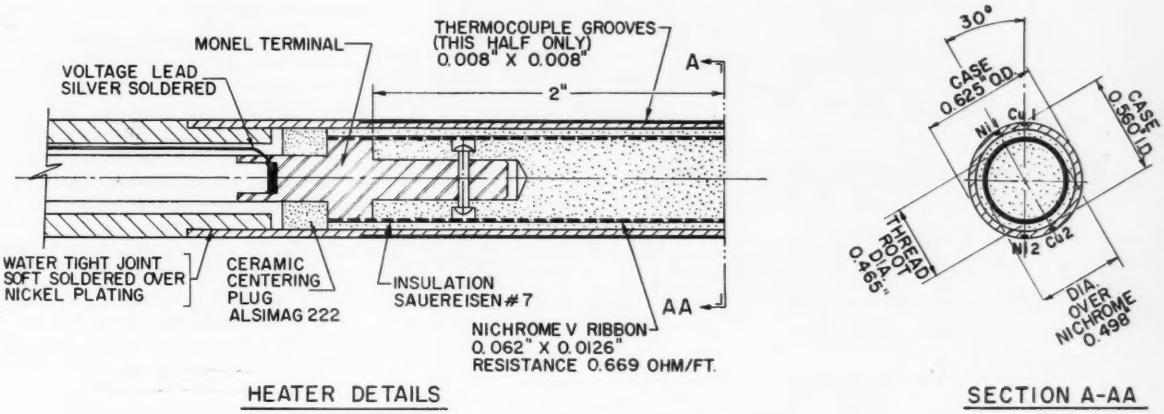

Fig. 4. Details of construction of heater in rod 15.

Calculations were made for nickel and aluminum to evaluate these two sources of error. Rather drastic assumptions had to be made with regard to thermal resistances at boundaries, etc., and these limit the applicability of the calculated results. They supported the conclusion, however, that higher temperatures (lower values of h) should be measured for the nickel rod than for the aluminum rod under comparable conditions. This agrees with the experimental results.

In view of the difficulty of establishing directly the accuracy of the surface-temperature measurement, it was desirable to check the over-all accuracy of the heat transfer measurements by comparison with previous work. There are no pertinent data available for an open lattice. Two other methods of checking the measurements were resorted to. In one, heat transfer coefficients were determined for water flowing inside a tube, the same technique of thermocouple installation being used here as for the heater rods. In the second, the actual couples. A layer of aluminum foil was wrapped around the tube, covering the external thermocouples, before the heating coil was applied, to minimize the possibility that these thermocouples could reach a temperature higher than that of the outer copper surface.

Measurements were made at water temperatures of 73° and 140°F., velocities of 3½ and 7 ft./sec., and a single flux of 34,000 B.t.u./(hr.)(sq. ft.). The water-film temperature drops measured by the two internal thermocouples differed consistently by about 7%. Values of the heat transfer coefficient based on an average of the two were about 20% higher than values predicted by the Colburn equation (*10*):

$$\frac{hD}{k} = 0.023\left(\frac{DG}{\mu_f}\right)^{0.8}\left(\frac{C_p\mu_f}{k}\right)^{1/3} \quad (1)$$

When the heated upstream length was decreased from 6 to 2 in., the values of h increased by 4%; this small change indicated that a 6-in. heated length was

lating experimental heat transfer coefficients.

The agreement of the external and internal thermocouples was direct evidence that the method of installation did not introduce any systematic error. It demonstrated even more strongly that the internal thermocouples were not reading erroneously low (leading to high values of h), as it is difficult to conceive of factors that would make the external thermocouples read too low. The accuracy of the temperature measurements was corroborated by the agreement of the measured heat transfer coefficients, to 20%, with the Colburn equation.

Annulus Heat Transfer Measurements

The annulus measurements have been reported separately (*9*). The results indicated that coefficients measured with rod 15 (aluminum jacketed) and rod 20 (copper jacketed) were about 20% higher than predicted by the Colburn equation, by use of the equivalent diameter $D_e = D_2 - D_1$. Coefficients measured with

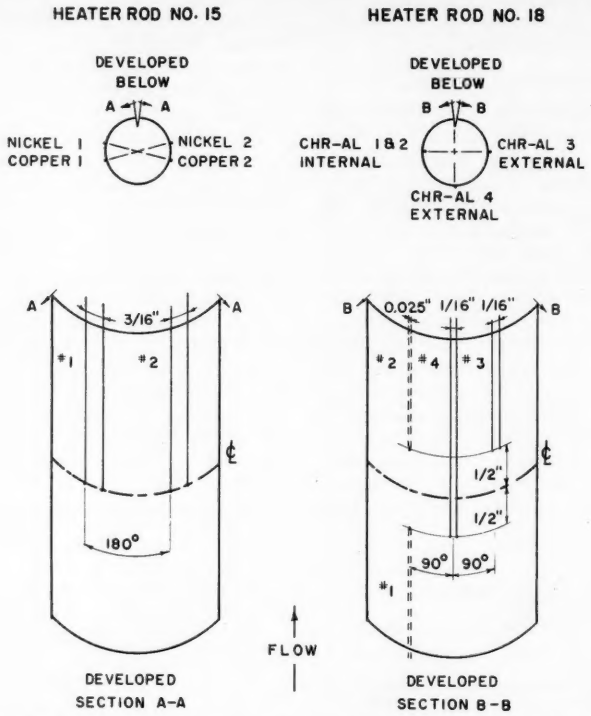

Fig. 5. Developed views of heater surfaces showing thermocouple locations.

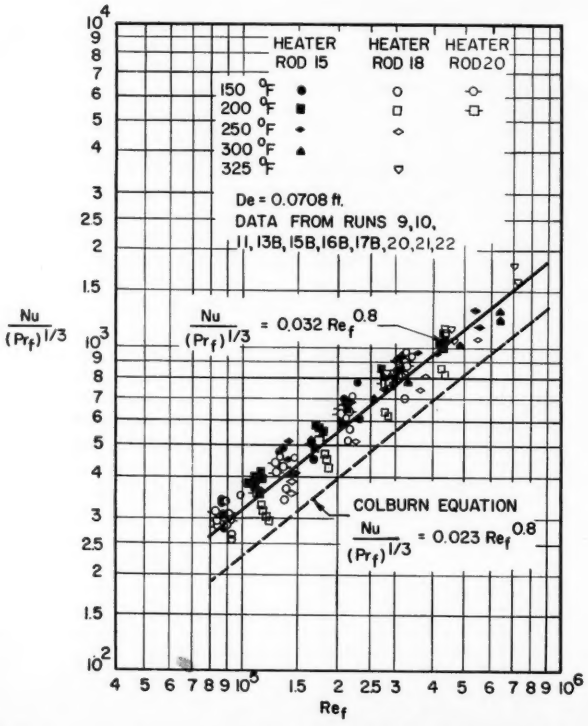

Fig. 6. Heat transfer data for water flowing parallel to cylindrical rods.

nickel-jacketed rod 18 (not reported elsewhere), based on thermocouples 3 and 4, were about 10% higher than the Colburn values, which is in accord with the prediction that thermocouples embedded in nickel should indicate values higher than the true surface temperature. From these results, and the considerations mentioned above, it is concluded that a true measure of the surface temperature was obtained with rod 15, and that the temperatures measured with rod 18 indicated water-to-jacket temperature differences that were 10% too high.

However, rather than to make the indicated adjustment of 10% in the rod 18 measurements, it has been deemed preferable to report the uncorrected results. While this increases the scatter of the data taken as a whole, the scatter is still not excessive for measurements of this type. (*See* Figure 6.)

Behavior in Lattice Tests

Heating element 15 (aluminum) was equipped with two copper-nickel thermocouples designated No. 1 and No. 2, located 180 degrees apart at the midlength of the heater. (*See* Figures 4 and 5.) The film temperature drop measured with thermocouple 1 was consistently higher than that measured with No. 2 by about 10 to 20%. The difference was virtually unaffected by rotating the heating element 30 or 180 degrees (runs 9, 10, and 11), which indicated that it was not caused by local differences in flow conditions in a triangular lattice. It was likewise unchanged by at least three successive repairs to the thermocouples, in which the wire tips were removed from their grooves, the grooves cleaned, and the junctions reconstituted. This behavior indicated that the thermocouple readings were not sensitive to minute differences in the method of installation.

After considering and eliminating bowing of the heated element as the cause of the difference in reading between No. 1 and No. 2, the authors concluded that it was probably due to nonsymmetrical heat flux around the periphery. The layer of Sauereisen insulation separating the heating coil from the aluminum jacket was 31 mils thick, and because of its relatively poor conductivity there was an estimated temperature drop of as much as 1,500°F. across it. For this reason, even small differences in the thickness of the layer or in its thermal conductivity around the circumference could result in a nonuniform flux distribution. Measurement of the thermal conductivity of several samples of Sauereisen in a Cenco-Fitch apparatus (*2*) gave values varying from 0.27 to 0.48 B.t.u./(hr.)(ft.)(°F.); although the absolute accuracy of these measurements is questionable (owing to boundary effects), this degree of variation would readily account for the observed differences in thermocouple readings.

The procedure was followed of averaging the readings to No. 1 and No. 2 whenever an average coefficient was being measured with rod 15. In some cases rod 15 was used in locations where the coefficient was expected to vary around the circumference, i.e., next to the wall (run 12) or next to a simulated control rod (run 13*A*). In such cases the values measured with the individual thermocouples were compared directly with the readings of the same thermocouple when the rod was tested in a central, or "normal," location (run 10, lattice position 3).

For rod 18 (nickel jacketed), thermocouples 3 and 4 agreed quite closely (within 3%), and their average value was 10 to 15% above the values given by No. 2. Number 1 failed at an early stage and was not repaired. Number 2 failed after it had been used in several runs; however, it was the only thermocouple functioning on rod 18 in run 16*B*, because of failure of the external leads of No. 3 and No. 4.

ACCURACY OF RESULTS

From the degree of scatter in Figure 6, the reproducibility of measurements in different runs, and the tubular- and annular-flow heat transfer measurements, it is estimated that the over-all accuracy of the results was ±8%. This uncertainty was greater than the maximum probable error, which was estimated as ±4.1% from procedures described by Sherwood and Reed (*11*). Q was measured to ±0.5% or better, and A was known with at least this accuracy; calculations confirmed that axial heat flow was negligible in the vicinity of the thermocouples. The orifice measurement was accurate to ±2%, and this combined with the uncertainty in the free-flow area gave V a probable error of ±2.8%. However, a further uncertainty is introduced by the possible difference between the average velocity, V, and the local velocity at the heated rod. The added surface (or reduced equivalent diameter) at the wall tends to give a lower velocity near the wall, making the velocity in the inner zone higher than the average. A calculation of this effect, based on the Fanning equation and the assumption of two zones of constant velocity, indicated that the velocity in the inner zone might be 4.5% higher than the average velocity.

HEAT TRANSFER MEASUREMENTS IN NORMAL LATTICE

Table 2 lists the variables studied and their range of variation; the rod diameter and normal lattice spacing were not varied.

Table 2. Range of Test Variables

Water temperature, °F.	150–325
Water velocity, ft./sec.	5–20
Lattice positions	4
Reynolds number	70,000–700,000
Power density, kw./ft.	2.5–10
Heat flux, B.t.u./(sq. ft.)(hr.)	52,000–208,000

A total of twenty-two runs was made, of which runs 1 through 8 were preliminary, being devoted to testing and improving the heated test elements and the method of surface-temperature measurement. Heater rod 15 was tested in positions 1, 3, and 4 (*see* Figure 3), heater rod 18 was tested in positions 2 and 3, and heater rod 20 was tested in position 3. Table 3 gives detailed results for a typical run.

Figure 6 presents a plot of all the heat transfer data that were obtained for normal lattice conditions.* These comprise the measurements for lattice positions 2 and 3, with rods 15, 18, and 20. For rod 15 the results for thermocouples 1 and 2 were averaged, and for rod 18 the values are either an average for "external" thermocouples 3 and 4 or the measurement with "internal" thermocouple 2, whichever was functioning. For rod 20, thermocouples 2 to 7 were averaged.

The slope of the best straight line through the data is very close to 0.8, in agreement with heat transfer behavior in pipes. With the slope fixed at 0.8, least squares analysis (using vertical deviations) gave the following equation:

$$\frac{hD_e}{k} \Big/ \left(\frac{C_p\mu_f}{k}\right)^{1/3} = 0.032\left(\frac{D_eG}{\mu_f}\right)^{0.8} \quad (2)$$

The data for copper rod 20 (tagged open symbols) fall slightly higher than those for aluminum rod 15 (solid symbols), which are higher than those for nickel rod 18 (open symbols). The equations for the three sets of data taken separately would have constants of 0.034, 0.033, and 0.031, respectively (with the slopes kept arbitrarily at 0.8).

Table 3. Typical Heat Transfer Data

Run 9††, Purpose-normal lattice; Test element 15, Lattice position 3

Bulk water temp.*, °F.	Average water velocity, ft./sec.	Heat flux, B.t.u./(hr.)(sq. ft.)	Re_f × 10^{-3}	Corrected film temp. drop, °F. T.C.1	T.C.2	h,† B.t.u./(hr.)(sq. ft.)(°F.)
200.3	4.95	104,300	118.0	46.6	43.3	2,320
200.2	9.94	105,200	211.8	27.8	25.0	3,990
200.4	14.91	105,200	299.8	20.7	18.8	5,340
199.4	19.90	104,500	434.3	16.8	15.0	6,600
199.2	4.97	104,600	117.2	44.5	40.7	2,460
199.5	4.97	52,100	110.7	21.3	19.4	2,570
199.4	9.97	52,100	215.3	12.8	11.3	4,350
199.9	14.93	52,000	319.2	9.5	8.5	5,790
201.0	19.91	52,000	426.6	7.9	7.0	7,020
202.2	4.80	52,000	107.8	21.2	19.3	2,570

*Upstream of heater, uncorrected for heat input.
†Based on calculation using average corrected film temperature drop.
††Data for 150°, 250°, and 295°F. are omitted to conserve space.

Effect of Heat Flux

Most of the measurements were made at a power density of 5 kw./ft. [heat flux of 104,000 B.t.u./(hr.)(sq. ft.)], but comparative measurements were made also at power densities of 2.5 and 10 kw./ft. The available results are compared in Table 4. Heat transfer coefficients at 5 kw./ft. were 6 or 7% lower, on the average, than values measured either at the higher or lower power density. No explanation of this behavior has been suggested. Allowance for increased film temperature would indicate a small increase in coefficient with power density, less than that observed.

Table 4. Effect of Heat Flux

Run	Heater rod	Bulk water temp., °F.	Ratio of power densities	Ratio of heat transfer coefficients (avg.)	Values No.	Range
9	15	200	1650/825	0.939	5	0.910–.980
10	15	200	1650/825	0.964	5	0.930–.981
17B	18	325	1650/825	0.929	3	0.918–.937
16B	18	150	3200/1650	1.085	5	0.937–1.170
16A	15	150	3200/1650	1.063	3	1.035–1.078

Heater Entrance Effects

The effect of heated length on apparent heat transfer coefficient was studied in some detail with rod 20, which had an 8-in. heated section. Representative results are shown in Figure 7. To facilitate comparison a relative value of the coefficient h_r has been plotted; h_r is the ratio

*The physical property data were taken from Eckert (*5*).

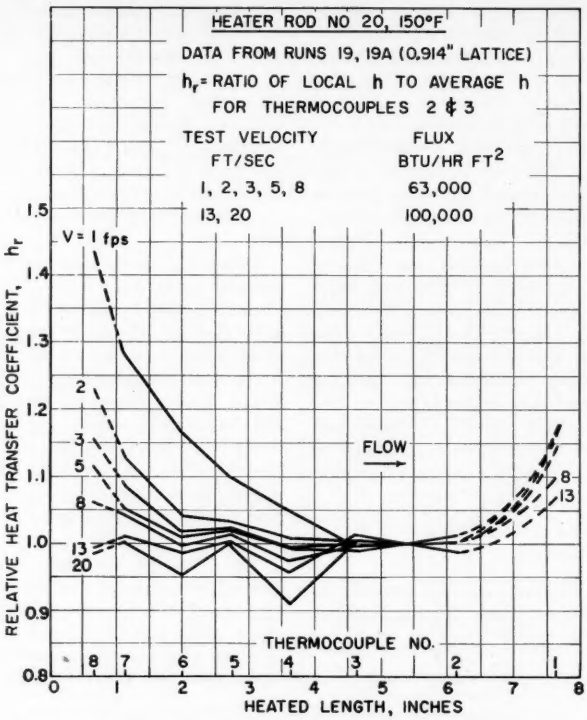

Fig. 7. Effect of heated length on heat transfer coefficient.

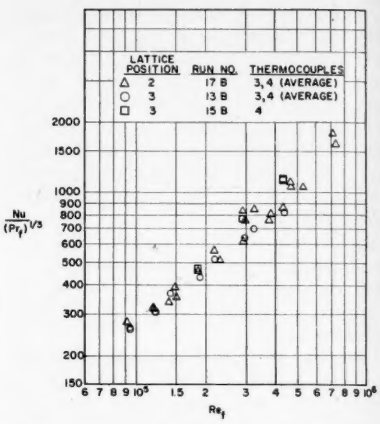

Fig. 8. Effect of lattice position on heat transfer (rod 18).

of h as measured by a particular thermocouple to the h calculated from the average readings of thermocouples 2 and 3 at the given velocity. Thermocouples 2 and 3 were chosen as the reference because they were the furthest downstream and agreed with each other at all velocities. (Number 1 was actually the furthest downstream but was evidently close enough, ⅜ in., to the end to have its reading lowered by axial conduction.) For these tests the velocity range was extended down to 1 ft./sec.

An effect of heated length is clearly evident at the lower velocities, which increases with decreasing velocity. However, for thermocouple 7 (1½-in. station) it was less than 5% maximum for the velocities of 5 ft./sec. and higher at which the general heat transfer study was made. At the 2-in. station, corresponding to the thermocouple location in the 4-in. heater rods, no significant effect of heated length was evident at velocities above 3 ft./sec. It will be observed that the readings of thermocouple 8 (⅝-in. station) may or may not have been influenced by axial cooling; calculations placed it on the border line of such effects.

Measurements at two different heat fluxes, 63,000 and 100,000 B.t.u./(sq. ft.)(hr.) showed close agreement.

The results indicate that a 2-in. heated length ($L/D_e = 2.4$) was sufficient for full development of the thermal boundary layer at velocities of 5 to 20 ft./sec. The systematic indication of an increasing effect of heated length with decreasing velocity below 5 ft./sec. is evidence of the adequacy of the method to detect any effects that do exist.

The results also confirm that the hydraulic boundary layer ($L/D_e = 21$) was fully established.

Additional evidence on the question of heated length was obtained with heater rod 18, on which thermocouple 3 was located 1 in. further downstream than thermocouple 4. (*See* Figure 5.) Data for a comparison are available from runs 13*B* and 17*B*. In run 13*B* the average value of h_4/h_3 was 1.045 ± 0.039 (based on twelve values), and in run 17*B* it was 1.028 ± 0.031 (based on twenty-one values). The difference between h_3 and h_4 is within the experimental accuracy.

Simultaneous Heating of Two Rods

In run 17 advantage was taken of the opportunity to test two heated rods simultaneously, with rod 15 in lattice position 3 and with its No. 2 thermocouple directly adjacent to rod 18 in lattice position 2. A comparison of heat transfer coefficients measured with this thermocouple, with and without simultaneous heating of the adjacent rod, showed no effect.

EFFECT OF LATTICE VARIABLES ON HEAT TRANSFER

Tests were made to obtain information on the effect upon the heat transfer coefficient of lattice position, lattice distortion, and thermocouple orientation in the unit lattice cell. Rod 15 was used in all these tests. As any of these variables might result in a peripheral variation in heat transfer coefficient, the average value for thermocouples 1 and 2 was not of much use in evaluating the results. Instead, the value measured with each thermocouple was compared directly with the readings of the sample thermocouple under the same conditions in run 10 (lattice position 3). The deviations of the bulk water temperatures, power densities, and flow rates for the various runs from the nominal values were small enough to make such a comparison valid. As the values of h obtained in run 10 were somewhat higher than the average results, this basis of comparison exaggerates slightly the effect of lattice variables.

Effect of ⅞-in. Rod

Run 13*A* was made with rod 15 in lattice position 4, adjacent to the ⅞-in.-diam. dummy rod which simulated a typical control thimble. Heat transfer was measured at 150° and 200°F. at a heat flux of 104,000 B.t.u./(hr.)(sq. ft.). Thermocouple 2 was located directly adjacent to the ⅞-in. rod.* The average value of the ratio of h_2 (run 13*A*) to h_2 (run 10) was 0.916 ± 0.028†, and for h_1 the average ratio was 0.956 ± 0.030. The comparison indicates a reduction of about 8% in the coefficient directly adjacent to the ⅞-in. rod and a reduction of about 4% on the opposite side.

Wall Effect

Run 12 was made with rod 15 in lattice position 1, next to the wall, with thermo-

*Actually the nickel wire of thermocouple 2 had this location, but the Ni–Al junction contributes about 80% of the total Ni–Cu voltage.

†The value ±0.028 is the probable error = 0.6745 × standard deviation.

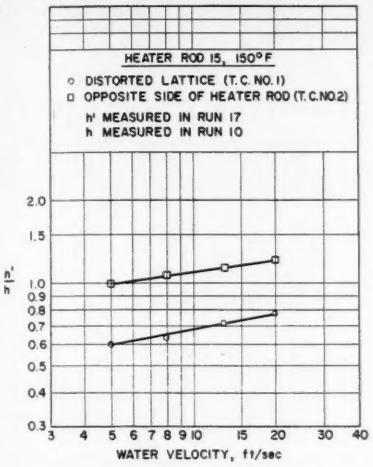

Fig. 9. Effect of lattice distortion on heat transfer.

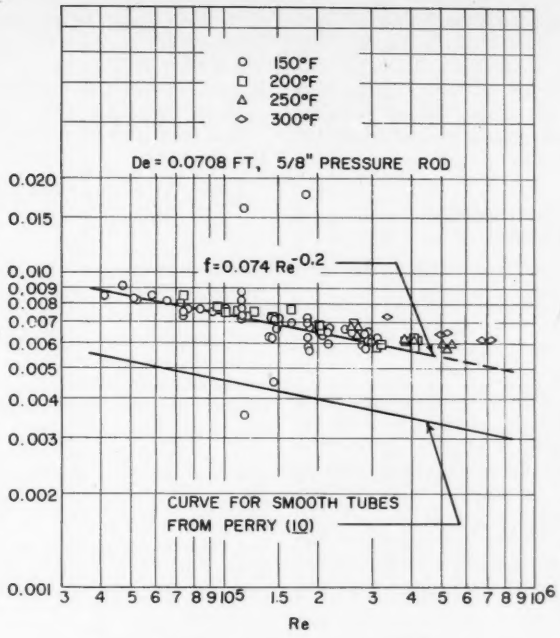

Fig. 10. Friction-factor data for open lattices.

couple 1 adjacent to the wall. Measurements were made at 150°, 200°, and 250°F. and a heat flux of 104,000 B.t.u./(hr.)(sq. ft.). The average value of the ratio of h_1 (run 12) to h_1 (run 10) was 0.616 ± 0.022, and for h_2 the average value of the ratio was 0.876 ± 0.020. Thus the coefficient was reduced about 40% on the side nearest the wall and about 12% on the opposite side.

These figures indicate that the wall effect does not extend very far into the lattice. This conclusion is confirmed by a comparison of the results obtained in lattice positions 2 and 3 (obtained with rod 18; rod 15 was not tested in position 2). Tests were made in position 3 in runs 13*B* and 15*B* (with thermocouple 3 facing the wall) and in position 2 in run 17*B* (with thermocouple 2 facing the wall). As a point-to-point comparison of these tests would leave a majority of the data out of consideration, it is more convenient to make the comparison in a plot, and this is done in Figure 8. The data showed considerable scatter, with the points for lattice position 2 bracketed by values obtained for position 3 in runs 13*B* and 15*B* respectively. The evidence, within its limits of accuracy, indicates that the wall effect did not extend to lattice position 2 (and on this basis the data for position 2 were included in Figure 6).

Lattice Distortion

The effect of severe fuel-rod distortion was simulated by reducing the minimum clearance between heated rod 15 and three of its six neighbors by 3/16 in., from 0.289 to 0.101 in. (*See* Figure 3.) Three sets of measurements were made at 150°F. and a heat flux of 104,000 B.t.u./(hr.)(sq. ft.), with thermocouple 1 facing the crowded lattice (run 17*A*). The results are compared with those of run 10 in Figure 9. The ratio of the heat transfer coefficient in the crowded lattice to that in the normal lattice varied from 0.596 to 0.773. When this ratio is plotted against the velocity on log-log paper, the points are fitted quite well by a straight line.

Also plotted in Figure 9 are values of the ratio of heat transfer coefficients measured with thermocouple 2 (180 degrees from No. 1) in runs 17*A* and 10 respectively. The values ranged from 0.992 to 1.213 and also fell on a straight line.

Local Coefficient

Between runs 10 and 11 heater rod 15 was rotated 30 degrees, with no other change in the lattice. This change moved thermocouple 1 from a position on a line of centers to a point of maximum removal from the neighboring rods and did the reverse for thermocouple 2, thus providing a test of the maximum potential variation in local coefficient around the periphery. The ratio of heat transfer coefficients measured with the two thermocouples h_2/h_1 was compared for the conditions common to both runs: 150°, 200°, and 250°F. at a flux of 104,000 B.t.u./(hr.)(sq. ft.).

The average value of the ratio was 1.113 ± 0.018 in run 10 and 1.141 ± 0.045 in run 11. The difference is less than the experimental uncertainty and is considered to indicate the absence of peripheral variation.

Average values of h were 97% as high in run 11 as in run 10.

PRESSURE-DROP MEASUREMENTS

The frictional pressure drops within the lattice were measured over a 3-ft. length of the 5/8-in.-diam. pressure rod. Pressure drops were not measured in all runs, but values were obtained covering the entire range of operating conditions. Measurements made with the 7/8-in. pressure rod agreed with those made with the 5/8-in. rod, apart from some random variation.

The observed pressure drops were used to calculate values of the friction factor f from the relation

$$f = \frac{FgD_e}{2LV^2} \qquad (3)$$

obtained from the Fanning equation. The results are plotted against the Reynolds number in Figure 10. On the whole, the data are fitted quite well on a log-log plot by a straight line with a slope of -0.2, having the equation

$$f = 0.074\, Re^{-0.2} \qquad (4)$$

This slope agrees with predicted behavior for turbulent flow in pipes.

The experimental values of f fall considerably above the curve for turbulent flow in smooth tubes, taken from Perry (*10*). On the average, the measured values are about 65% higher than the curve. It is believed that the rods were initially comparable to smooth tubes in surface finish and remained so as evidenced by physical appearance and lack of a trend in heat transfer and pressure-drop data with time.

The measured frictional pressure drops varied from about 0.076 lb./(sq. in.)/(ft.) at 5 ft./sec. to about 0.91 lb./(sq. in.)(ft.) at 20 ft./sec. at 150°F. The pressure drop over the entire lattice, including both support plates, ranged from 0.55 to 8.04 lb./sq. in.

RELATION OF HEAT TRANSFER TO PRESSURE DROP

Colburn (*3*) showed that the heat transfer factor

$$j = \frac{h}{C_p G}\left(\frac{C_p \mu_f}{k}\right)^{2/3}$$

was equal to $f/2$ for turbulent flow in pipes and parallel to plane surfaces but was less than $f/2$ for flow across tube banks. A recent report (*1*) shows that for heating and cooling of water in rectangular ducts, the ratio of j to $f/2$ varied from about 0.8 for square ducts to 0.64 for a duct with an aspect ratio of 7.9. For the present case, by combining Equation (2)

$$Nu = 0.032\, Re_f^{0.8}\, Pr_f^{1/3} \qquad (2)$$

and Equation (4)

$$f = 0.074\, Re^{-0.2} \qquad (4)$$

one obtains

$$\frac{j}{f/2} = 0.86$$

This procedure is not strictly correct, as the pressure-drop measurements were made for unheated rods; however, it is estimated that the correction for this discrepancy would be less than 2% for most of the range studied. It would be less than 6% for a heat flux of 208,000 B.t.u./(hr.)(sq. ft.), a temperature of 150°F., and a velocity of 5 ft./sec., which represents the worst case.

The fact that the ratio is less than 1.0 indicates that the pressure-drop data support the correctness of the relatively high values found for the heat transfer coefficients.

SUMMARY

Heat transfer coefficients were determined for parallel flow of water through a bundle of cylindrical rods at water temperatures of 150° to 325°F., velocities of 5 to 20 ft./sec., and heat fluxes of 50,000 to 200,000 B.t.u./(hr.)(sq. ft.). No previous data for this case were found in the literature. For this range of conditions the apparent coefficient remained unchanged for heated lengths greater than 1½ in. ($L/D_e = 1.6$). The experimental values were 40% higher than would be predicted by use of Colburn's equation for flow inside tubes, with the equivalent diameter D_e replacing the tube diameter, as proposed by Eckert. The frictional pressure losses were likewise higher, by 65%, than would be predicted by substituting D_e in the Fanning equation. These two results are mutually consistent in the light of the modified Reynolds analogy.

The heat transfer data are fitted by the equation

$$\frac{hD_e}{k} = 0.032\left(\frac{D_e G}{\mu_f}\right)^{0.8}\left(\frac{C_p \mu_f}{k}\right)^{1/3} \qquad (2)$$

which is analogous to the Colburn equation. However, there is no assurance that this relation will prove correct for lattices of dimensions different from those of the single lattice studied in the present work. Heat transfer measurements are needed in various lattices before a general relation can be established.

No variation in local coefficient around the rod periphery was found. The coefficient was reduced by 40% directly adjacent to the wall of the lattice case, but there was practically no reduction at the second rod from the wall. The effect of local distortion of the lattice was measured.

ACKNOWLEDGMENT

Most of the results reported in this paper were obtained during work performed by the Walter Kidde Nuclear Laboratories, Inc., under Contract AT(30-1)-1374 for the United States Atomic Energy Commission. The permission of the A.E.C. to publish this paper is hereby gratefully acknowledged.

The authors are indebted to K. P. Cohen and W. I. Thompson for advice and encouragement; to J. J. Barker, R. F. Benenati, A. Weiss, and H. Yanowitz for assistance in the design and operation of the equipment; and to G. G. Bartolomei for construction of the heated test rods.

NOTATION

A = heat transfer area, sq. ft.
C_p = Specific heat of water at bulk temperature, B.t.u./(lb.)(°F.)
D or D_1 = outside diameter of rod, ft.
D_2 = for annulus, jacket diameter, ft.
D_e = Equivalent diameter, ft. =

$$\frac{4 \times \text{flow area}}{\text{wetted perimeter}}$$

f = friction factor, defined by Equation (4)
F = pressure loss, ft. of fluid flowing
g = gravitational constant, ft./(sec.)²
G = mass velocity of water, avg., lb./(hr.)(sq. ft.)
h = heat transfer coefficient, B.t.u./(hr.)(sq. ft.) (h is used with various subscripts through report, as defined in text in each case)
j = heat transfer factor =

$$\frac{h}{C_p G}(Pr_f)^{2/3}$$

k = thermal conductivity of water at bulk temperature, B.t.u./(hr.)(ft.)(°F.)
L = length of flow passage, ft.
Nu = Nusselt number,

$$\frac{hD}{k} \text{ or } \frac{hD_e}{k}$$

P = frictional pressure drop, lb./(sq. in.) (ft.)
Pr = Prandtl number,

$$\frac{C_p \mu}{k}$$

Pr_f = Prandtl number,

$$\frac{C_p \mu_f}{k}$$

Q = heat-flow rate, B.t.u./hr.
Re = Reynolds number,

$$\frac{DV\rho}{\mu} \text{ or } \frac{D_e V \rho}{\mu}$$

Re_f = Reynolds number,

$$\frac{DV\rho}{\mu_f} \text{ or } \frac{D_e V \rho}{\mu_f}$$

T = temperature, °F.
ΔT = temperature difference from rod surface to bulk water, °F.
V = water velocity, avg., ft./sec. or ft./hr.
μ = viscosity of water at bulk temperature, lb./(ft.)(hr.)
μ_f = viscosity of water at average film temperature, lb./(ft.)(hr.)
ρ = density of water at bulk temperature, lb./cu. ft.

LITERATURE CITED

1. Armour Research Foundation, *Rept. NEPA-1559*, unclassified (Aug. 3, 1950).
2. Central Scientific Co., "Selective Experiments in Physics: Thermal Conductivity," No. 71990-H52b (1940).
3. Colburn, A. P., *Trans. Am. Inst. Chem. Engrs.*, **29**, 174 (1933).
4. Donohue, D. A., *Ind. Eng. Chem.*, **41**, 2499 (1949).
5. Eckert, E. R. G., "Introduction to the Transfer of Heat and Mass," McGraw-Hill Book Company, Inc., New York (1950).
6. Hyman, S. C., and C. F. Bonilla, *A.E.C. Rept. NYO-560*, unclassified (June 30, 1950).
7. Jakob, M., "Heat Transfer," VI, John Wiley and Sons, Inc., New York (1949).
8. McAdams, W. H., "Heat Transmission," 3d ed., McGraw-Hill Book Company, Inc., New York (1954).
9. Miller, P., J. J. Byrnes, and D. M. Benforado, *A.I.Ch.E. Journal*, **1**, 501 (1955).
10. Perry, J. H., ed., "Chemical Engineers' Handbook," 3d ed., McGraw-Hill Book Company, Inc., New York (1950).
11. Sherwood, T. K., and C. E. Reed, "Applied Mathematics in Chemical Engineering," McGraw-Hill Book Company, Inc., New York (1939).

Presented at the Nuclear Science and Engineering Congress, Cleveland.

Factorial Experiments in Sequence: the Attainment of Optimum Conditions for a Decontamination Process

M. K. BARNETT, P. M. HAMILTON, and F. C. MEAD, JR.

Mound Laboratory, Monsanto Chemical Company, Miamisburg, Ohio

The advantages of factorial design are first illustrated by a simple experiment devoted to the effect of two *p*H factors and an iron-concentration factor on the efficiency of a decontamination process employing iron sulfide as a scavenging agent. The broadening of the base of an investigation by the expansion of a factorial is illustrated by addition of the sulfide concentration as a factor. Finally the principle of expanded factorials is further utilized in the later phases of the study, in which additional levels are assigned to the *p*H factors in order to arrive at a closer estimate of the optimum conditions for the process.

Factorial experiments, that is, those embracing all possible combinations of the process variables, are peculiarly suited to the prosecution of a systematic approach in laboratory investigations. If such experiments have yet to attain wide usage among chemical workers, one reason must be the excessive advance commitment of time and manpower and resultant loss of flexibility in scientific planning which the execution of an elaborate factorial scheme often requires. This difficulty may be circumvented by employing factorial designs in sequence. Thus initially simple factorial experiments may, as experience accumulates, be successively expanded and perhaps redirected to form more elaborate factorial plans whose relevance to the objectives of the investigation is more assured than if the entire program had been planned in advance.

The utility of such sequential factorials is illustrated by a study devoted to the improvement of a process for removal of radioactivity from liquid wastes. The process employed iron sulfide as a scavenging agent, and the problem was to adjust operating conditions in such a manner that the major portion of the activity became associated with the solid phase. The latter, after separation by settling, could be disposed of by burial.

DESCRIPTION OF WASTE AND PROCESS

To make the results of the study applicable to general laboratory wastes encountered in practice, a complex waste sample was deliberately chosen. Although its exact composition was not established, it was known to contain a wide variety of radioactive species, including both alpha and beta emitters; nonradioactive inorganic salts; and organic material, some of which was visible as suspended matter in the liquid. The initial activity of the waste, measured as alpha plus beta on a 0.5-ml. sample, was 26,453 counts/min. Of this total, 1,850 counts/min. was recorded as alpha only. Also, 17,050 counts/min., or about two thirds of the total, was associated with suspended matter.

The process was studied on a laboratory scale, separation of the solid being effected by filtration. In the first step sulfuric acid was added to 250 ml. of the waste solution until the *p*H attained a previously prescribed value called the *initial* *p*H. Ferrous chloride solution (100 mg. of ferrous iron/ml.) was then added until the iron concentration attained a prescribed value. After addition and solution of a prescribed quantity of finely divided solid sodium sulfide, acid or base was added until the *p*H attained a certain value, called the *final* *p*H. After 30 min., allowed for settling, the solid was filtered off and the filtrate was sampled and mounted in duplicate. Each mount was counted in duplicate for alpha plus beta.

CHOICE OF FACTORS AND LEVELS FOR INITIAL EXPERIMENTS

Although prior knowledge was inadequate for precise prediction, it was freely utilized as a guide in the choice of independent variables, or "factors," and values, or "levels," of these factors for the initial experiment. Previous application (*1*) of the process to a different type of waste had established the initial *p*H, *I*; the iron concentration, *F*; and the final *p*H, *A*, as important factors affecting the extent of decontamination. It was decided to devote the initial work to these factors with two levels to be assigned to each factor. The amount of sulfide reagent was held constant at 0.5 g. The earlier work (*1*) had suggested an iron concentration of 1 mg./ml., an initial *p*H of 1, and a final *p*H of 4 as desirable conditions, and these levels were adopted as one set of factor values for the present study. As the aforementioned level for iron concentration was near the upper economic limit, a lower value, 0.5 mg./ml., was adopted for the second level of this factor. Because of the need for reducing corrosion in the metal equipment in which the large-scale process would be carried out, reduced acidity was desirable. The second levels for the initial *p*H and final *p*H were therefore set at 2 and 6, respectively.

CHOICE OF EXPERIMENTAL DESIGN

There was no reason to suppose that the efficiency of decontamination was a simple additive function of the three factors under study. For example, the effect of changing the iron content on the decontamination might well depend on the levels or values assigned to the other two factors or independent variables included in the study. The complete exploration of the causal relations would require the observation of the effect of each factor under all combinations of values of the others, thus consuming a large number of tests.

The use of the larger number of tests needed for more complete coverage of interrelations among the factors would seem to incur a corresponding reduction in the number of replicate tests, thus decreasing the reliability of the conclusions drawn from the data. This seemed particularly serious in the present case, because previous experience had indicated the presence of considerable uncontrolled variability in the process. The horns of a dilemma thus presented themselves: on the one horn, generality at the expense of precision; on the other, precision at the expense of generality.

A solution of this dilemma was supplied by R. A. Fisher (*2*) some twenty-five years ago when he proposed the factorial design, a plan for simultaneously attaining both maximum reliability and maximum generality, or coverage. This design was adopted for the study of the three factors under consideration. Such a design, by definition, must include all possible combinations of the factors at their different levels, each combination or "treatment" being repeated an equal number of times. In the present case,

---

P. M. Hamilton is at present with Central Research Laboratories, Monsanto Chemical Company, Dayton, Ohio.

because each of the three factors was studied at two levels, there were $2 \times 2 \times 2 = 8$ possible treatments. The treatments were run in triplicate, and the results of the experiment are represented in Table 1.

The treatment symbols appearing in the first column of the table utilize the factor symbols with appropriate subscripts. Subscripts 1 and 2 indicate that the lower or higher levels, respectively, of the factors were employed in the treatments. The number representing the activity remaining was computed by averaging the four results obtained from the pair of mounts prepared from each filtrate. The activity is reported as alpha plus beta in tens of counts per minute per 0.5 ml. of filtrate.

Table 1. Results of the 2^3 Factorial Experiment*

Treatment symbol	F, Iron concentration, mg./ml.	A, Final pH	I, Initial pH	Activity remaining, $\alpha + \beta$ (tens of counts/min./0.5 ml. of filtrate) Block I	Block II	Block III	Average
$F_1A_1I_1$	0.5	4	1	1,065	946	999	1,003
$F_1A_1I_2$			2	689	784	875	783
$F_1A_2I_1$		6	1	244	281	275	267
$F_1A_2I_2$			2	474	387	357	406
$F_2A_1I_1$	1.0	4	1	1,036	1,028	977	1,014
$F_2A_1I_2$			2	869	907	893	889
$F_2A_2I_1$		6	1	167	236	230	211
$F_2A_2I_2$			2	157	165	173	165
Average				587	592	597	592

*The eight treatments were carried out in random order in each block.

Table 2. Main Effects of the 2^3 Factorial Experiment

Conditions	Effect of iron concentration		
$A = A_1, I = I_1$	$F_2A_1I_1 - F_1A_1I_1$	= 1,014–1,003 =	11
$A = A_1, I = I_2$	$F_2A_1I_2 - F_1A_1I_2$	= 889–782 =	106
$A = A_2, I = I_1$	$F_2A_2I_1 - F_1A_2I_1$	= 211–267 =	− 56
$A = A_2, I = I_2$	$F_2A_2I_2 - F_1A_2I_2$	= 165–406 =	−241
Average or main effect		=	− 45
	Effect of final pH		
$F = F_1, I = I_1$	$F_1A_2I_1 - F_1A_1I_1$	= 267–1,003 =	−736
$F = F_1, I = I_2$	$F_1A_2I_2 - F_1A_1I_2$	= 406–783 =	−377
$F = F_2, I = I_1$	$F_2A_2I_1 - F_2A_1I_1$	= 211–1,014 =	−803
$F = F_2, I = I_2$	$F_2A_2I_2 - F_2A_1I_2$	= 165–889 =	−724
Average or main effect		=	−660
	Effect of initial pH		
$F = F_1, A = A_1$	$F_1A_1I_2 - F_1A_1I_1$	= 783–1,003 =	−220
$F = F_1, A = A_2$	$F_1A_2I_2 - F_1A_2I_1$	= 406–267 =	139
$F = F_2, A = A_1$	$F_2A_1I_2 - F_2A_1I_1$	= 889–1,014 =	−125
$F = F_2, A = A_2$	$F_2A_2I_2 - F_2A_2I_1$	= 165–211 =	− 46
Average or main effect		=	− 63

Note: Results in tens of counts per minute per 0.5 ml. of filtrate.

PROBLEM OF ERROR CONTROL

To most physical scientists the refinement or stabilization of experimental technique is the most obvious method of error control. A number of unusual refinements were adopted in the present experiment. Thus the pH adjustments and the addition of all reagents were carried out by the same operator throughout the study. Such factors as the rate and manner of addition were thus held as constant as possible. A second operator was responsible for all the filtrations, and a third did all the sampling and mounting. The total time consumed in pH adjustments and addition of reagents was held constant at 7 min., and all solutions were allowed exactly 30 min. for settling. Filtrates were sampled and mounted immediately after filtration, and mounts were counted on the same day that they were prepared.

Error control may also be achieved by suitable arrangement of the experimental tests and conditions in a manner consistent with the over-all experimental design. The present experiment provides an elementary illustration of this type of error control. As indicated in Table 1, the twenty-four tests were segregated into three blocks, each block of eight comprising a complete replication of the factorial experiment. These three blocks were assigned to the 3 days required to complete the experiment. The advantage of this arrangement is that any day-to-day differences in operating conditions will have no influence on the comparisons to be drawn from the experiment. Thus the effect of the iron factor may be formulated by subtracting the average of the four low-iron tests in the first block from the average of the four high-iron tests in the same block. This contrast may also be formulated for each of the other two blocks. The over-all or average iron effect is obtained by pooling the three contrasts from the three blocks, and this pooled contrast, obtained by averaging, is obviously independent of any differences between blocks, i.e., days.

The eight runs within each block were not carried out in the systematic order shown in Table 1 but in random order, a different random order being used for each block. Randomization accomplished two results. First, it greatly reduced the likelihood that bias would be present in comparisons drawn to reveal the effect of a particular factor. If, for instance, some unknown factor increased gradually during each day, the decontamination would be progressively greater or less than it would otherwise have been. If the eight treatments had been carried out in a systematic order, say all the low-iron treatments first followed by the high-iron treatments, then the influence of the accidental factor would be indistinguishable from the effect of the iron factor. The apparent effect of the latter might have been either smaller or larger than its real effect. The second result of randomization is a more valid estimate of the experimental error. This estimate must be based on the observed discrepancies between replicate tests. However, if the same order is used for all three blocks, then replicate tests are likely to be run under more uniform conditions than if different random orders are used. The result will be to make the measured error smaller than the true error present in the experiment. Since the significance of observed effects will be ascertained by comparing them with the measured error, the use of this smaller error would cause experimental effects to appear more significant than they really are.

MAIN EFFECTS OF THE EXPERIMENT

The eight treatment averages shown in the last column of Table 1 provide four unbiased comparisons for the formulation of the effect of each of the three factors. These are shown in Table 2. It is evident that the effect of each of the three factors has been measured under each of the four possible sets of conditions defined by the levels assigned to the other two factors. These four simple effects may be averaged to produce a "main effect" of the factor. The main effect of a given factor, so defined, is obviously equivalent to the excess of the average activity remaining for the four treatments having the higher level of the factor over the average for the four with the lower level of the factor.

The efficiency of the factorial design begins to make itself evident. Not only has each factor been studied under the widest range of conditions, but also, by virtue of the symmetry of the design, all the data have been utilized in formulating the effect of each factor.

It should be noted that a negative effect, if large enough to be significant, indicates that there was less activity remaining at the higher level of the factor and that raising the level was beneficial.

CALCULATION OF INTERACTIONS

The extent to which the effect of a factor depends on the value assigned to a second factor attains simple quantitative formulation in the concept of *interaction*. From Table 2, the average effect of increasing the final pH when the iron concentration was at its higher level was $\frac{1}{2}[(-803) + (-724)] = -763$, and the average effect when the iron concentration was at its lower level was $\frac{1}{2}[(-736) + (-377)] = -556$. The influence of raising the iron concentration on the effect of the final pH would be given by the difference: $(-763) - (-556) = -207$. Actually, it is preferable to take one half of this difference as the interaction, denoted by FA, as this will identify the interaction with the difference between the average of four treatments and the average of the remaining four and will therefore impart to the interaction the same precision as the main effects. Therefore $FA = -207/2 = -103$.

In a three-factor experiment there are two additional "first-order" interactions. One, denoted by IA, may be formulated as the dependence of the final pH effect on the initial pH; and the other, denoted by FI, as the dependence of the initial pH effect on the iron concentration. This enumeration exhausts the possible first-order interactions, as only one interaction exists between any two factors; thus the effect of the iron concentration on the effect of the final pH is identical with the effect of the final pH on the effect of the iron concentration.

However, there remains a single "second-order" interaction symbolized by FAI, which represents the dependence of the interaction between any two factors on the level assigned to the third factor. Thus the interaction between the iron concentration factor and the final pH factor when the initial pH is held at I_2 is, from Table 1, $(-241) + (-106) = -347$, and, when $I = I_1$, is $(-56) + (-11) = -67$. The effect of changing the initial pH on the first-order interaction might be taken as $(-347) - (-67) = -280$. Again, to maintain uniformity of precision among the main effects and interactions, the interaction is taken as one fourth of this difference: $FAI = -280/4 = -70$.

The symmetry of the design has permitted utilization of all the data in the formulation of each interaction; and so the four interactions, like the three main effects, have been measured with maximum precision.

EVALUATION OF RESULTS

The seven effects of the experiment are tabulated in the second column of Table 3. Again, because of the symmetry of the experimental structure and the care taken in randomization, a clear-cut straightforward statistical procedure is available for objectively evaluating the results. This procedure, called *analysis of variance*, is discussed in standard texts (*3*). By means of it, the discrepancies among triplicate determinations may be made to furnish certain critical values for judging the significance of an effect. Thus there are but 5 chances in 100 that the experimental error could produce an observed effect as large as 46, and 1 chance in 100 that it could produce one as large as 63.

Examination of Table 3 shows that the outstanding feature of the experiment was the marked beneficial effect of increasing the final pH. This effect far exceeded the 1% level of significance. An over-all beneficial effect of increasing the initial pH is also present, though the 1% level was not quite achieved. The effect of the iron factor was less pronounced, the main effect falling just short of the 5% significance level. However, the beneficial effect of increasing the iron content makes a firm appearance in the strongly negative FA interaction, indicating that the beneficial effect of increasing the final pH was accentuated by operating at the higher iron content. The significantly negative FAI interaction again suggests the beneficial effect of simultaneously raising all three factors to their higher levels. The statistically significant, positive AI interaction presents the only puzzling aspect of the experiment and will be discussed later.

The three block averages, tabulated at the bottom of Table 1, differed but little from one another, and, in fact, a simple extension of the statistical analysis showed that the variation among the three was readily attributable to the same experimental error which operated within the blocks. Thus nothing was gained, so far as the consistency of the seven factorial effects was concerned, by carrying out the experiment in three randomized blocks instead of a single completely randomized block of twenty-four tests. However, the auxiliary information that laboratory technique and operating conditions had been sufficiently uniform to eliminate day-to-day variability was extremely useful and, in fact, was immediately utilized in laying out the succeeding experiment.

Table 3. Comparison of the Results of the Original 2^3 Factorial with Those of the Expanded 2^4 Factorial

Effect	2^3 Factorial	2^4 Factorial
F	− 45	− 17
A	−660†	−677†
I	− 62*	− 56*
FA	−103†	− 77†
FI	− 22	− 11
AI	110†	40
FAI	− 70†	− 24
S		17
FS		− 28
AS		17
IS		− 7
FAS		− 26
FIS		− 12
AIS		+ 70†
$FAIS$		− 46*

*Attains 5% significance level, 46.
†Attains 1% significance level, 63.
Note: Results in tens of counts per minute per 0.5 ml. of filtrate.

Table 4. Expansion of 2^3 Factorial into a 2^4 Factorial by Inclusion of the Sulfide Factor ($S_1 = 0.25$ g., $S_2 = 0.50$ g.)

Treatment	Count	Treatment	Count
$F_1A_1I_1S_1$	891	$F_1A_1I_1S_2$	1,003
$F_1A_1I_2S_1$	892	$F_1A_1I_2S_2$	783
$F_1A_2I_1S_1$	298	$F_1A_2I_1S_2$	267
$F_1A_2I_2S_1$	197	$F_1A_2I_2S_2$	406
$F_2A_1I_1S_1$	973	$F_2A_1I_1S_2$	1,014
$F_2A_1I_2S_1$	933	$F_2A_1I_2S_2$	889
$F_2A_2I_1S_1$	236	$F_2A_2I_1S_2$	211
$F_2A_2I_2S_1$	180	$F_2A_2I_2S_2$	165

Note: Activity remaining, $\alpha + \beta$, in tens of counts per minute per 0.5 ml. of filtrate.

EXPANSION OF THE 2^3 FACTORIAL BY ADDITION OF THE SULFIDE FACTOR

The initial 2^3 factorial experiment, just described, pointed rather firmly to the desirability of further increases in both initial and final pH, while the iron content is maintained at the higher concentration. Before the investigation was extended in this direction, however, it was deemed desirable to check the influence of variations in the sulfide factor, which had been held constant at 0.5 g. of reagent in the initial experiment. Previous experience with this factor had indicated that quantities of sulfide in excess of 0.5 g. tended

to give colloidal solutions which passed through the filter and hence retained considerable activity. In fact, some difficulty was experienced in the 2^3 factorial with colloid formation. Therefore the new level of the sulfide factor was set at a lower value, 0.25 g.

The device adopted for incorporating the sulfide factor into the investigation might be called the principle of *expanded factorials*. If, in adding the new factor, one wishes to reap the full advantages of factorial design, he will need to include in the over-all plan all $2 \times 2 \times 2 \times 2 = 16$ treatments. However, eight of these, for which the sulfide was at its higher level, have already been included in the original factorial. To complete the new 2^4 factorial, it will suffice to carry out eight new treatments. These will be identical with the original eight treatments in respect to combinations of levels for iron concentration, initial *p*H, and final *p*H but will utilize 0.25 g. of sulfide in place of 0.5 g.

Although the eight additional treatments were carried out in random order, complete randomization of the sixteen was impossible. However, this does not mean that the comparison between the average of the original eight treatments, all having the higher quantity of sulfide, and the average of the new block of eight, all having the lower quantity of sulfide, is a biased comparison unsuitable for measuring the main effect of the sulfide factor. For, except for amount of sulfide used, the new block of eight treatments was carried out under the same conditions as prevailed during the earlier experiment, and, as significant day-to-day variations were absent from the earlier experiments, they were presumably likewise missing from the later experiments. Therefore, the raising or lowering of the apparent main effect of the sulfide factor by interblock differences is highly unlikely.

The results of the additional eight treatments, along with the average results for the original eight, are listed in systematic order in Table 4. The symbolism has been expanded to take care of the new factor, the symbol S denoting the sulfide factor, and S_1 and S_2 its lower and higher levels, respectively.

The widened base of the 2^4 factorial affords answers to a greater variety of questions than was provided by the original experiment. These new effects are the main effect of the sulfide factor; the interactions of this factor with each of the other three, *FS*, *AS*, *IS*; the interactions of the sulfide factor with the others, taken two at a time, *FAS*, *FIS*, *AIS*; and the single third-order interaction, *FAIS*. In addition, the seven effects of the original 2^3 factorial may also be reformulated to provide confirmatory information on their magnitude and significance.

The mechanics of computation is strictly analogous to that used in the 2^3 factorial. Thus, to formulate the main effect of any factor, the average activity remaining for the eight treatments with the low level of the factor is subtracted from the average value for the eight with the high level of the factor. The interactions are likewise formulated in a manner similar to that employed in the simpler case. As was the case in the original factorial, each effect will be based on all the data and will be formed by subtracting from the average of eight of the treatment results the average of the remaining eight. The table of signs (*3*), presented as Table 5, shows how the data must be grouped in order to compute the fifteen different effects.

As previously noted, any over-all difference between the conditions prevailing for the first eight treatments and those for the last eight treatments, though unlikely to exist, would vitiate the evaluation of the main effect of the sulfide factor. However, from Table 5 it is evident that such interblock differences could have no influence on the remaining fourteen effects of the 2^4 factorial. For in each of the fourteen cases the expression for the effect may be written as the sum of two groups of contrasts, one group involving only high-sulfide treatments, the other involving only low-sulfide treatments. In formal language the main effect of the sulfide factor has been "confounded" with blocks, leaving all other effects free from interblock differences.

The fifteen effects of the 2^4 factorial are listed in the last column of Table 3. The values obtained from the expanded experiment are based on twice as many comparisons as was the case with the 2^3 factorial, although this advantage is partly balanced by the circumstance that the eight treatments required for the expansion were not replicated. Since the error prevailing among the last eight treatments was not measured, no rigorous calculation of significance levels for the expanded factorial experiment is possible. As a first approximation, they are assumed to have the same values as in the first experiment.

Consider the question of agreement between the original 2^3 factorial and the expanded 2^4 factorial, as measured by the values obtained for the seven effects not involving the sulfide factor. As far as the first five effects listed in Table 3 are concerned, agreement was good. The effects attaining statistical significance were the same in both experiments, and, furthermore, the level of significance attained was the same. Discrepancies appeared, however, in the *AI* and *FAI* interactions. The *AI* interaction, which was significantly positive in the first experiment, now falls short of significance, and the *FAI* interaction, though still negative, is no longer large enough to claim reality.

Turning to the main object of the expanded experiment, the evaluation of effects involving the sulfide factor, it appears that neither the main effect of sulfide nor its simple interactions with the other three factors are significant. In the absence of any simple effects

Table 5. Table of Signs for Calculation of Effects of 2^4 Factorial

	Effect														
Treatment	*F*	*A*	*I*	*S*	*FA*	*FI*	*AI*	*FS*	*AS*	*IS*	*FAI*	*FAS*	*FIS*	*AIS*	*FAIS*
$F_1A_1I_1S_1$	−	−	−	−	+	+	+	+	+	+	−	−	−	−	+
$F_2A_1I_1S_1$	+	−	−	−	−	−	+	−	+	+	+	+	+	−	−
$F_1A_2I_1S_1$	−	+	−	−	−	+	−	+	−	+	+	+	−	+	−
$F_2A_2I_1S_1$	+	+	−	−	+	−	−	−	−	+	−	−	+	+	+
$F_1A_1I_2S_1$	−	−	+	−	+	−	−	+	+	−	+	−	+	+	−
$F_2A_1I_2S_1$	+	−	+	−	−	+	−	−	+	−	−	+	−	+	+
$F_1A_2I_2S_1$	−	+	+	−	−	−	+	+	−	−	−	+	+	−	+
$F_2A_2I_2S_1$	+	+	+	−	+	+	+	−	−	−	+	−	−	−	−
$F_1A_1I_1S_2$	−	−	−	+	+	+	+	−	−	−	−	+	+	+	−
$F_2A_1I_1S_2$	+	−	−	+	−	−	+	+	−	−	+	−	−	+	+
$F_1A_2I_1S_2$	−	+	−	+	−	+	−	−	+	−	+	−	+	−	+
$F_2A_2I_1S_2$	+	+	−	+	+	−	−	+	+	−	−	+	−	−	−
$F_1A_1I_2S_2$	−	−	+	+	+	−	−	−	−	+	+	+	−	−	+
$F_2A_2I_1S_2$	+	−	+	+	−	+	−	+	−	+	−	−	+	−	−
$F_1A_2I_2S_2$	−	+	+	+	−	−	+	−	+	+	−	−	−	+	−
$F_2A_2I_2S_2$	+	+	+	+	+	+	+	+	+	+	+	+	+	+	+

Table 6. Results of the $2 \times 3 \times 3$ Factorial

	$F = F_1$			$F = F_2$		
	$A = A_1$	$A = A_2$	$A = A_3$	$A = A_1$	$A = A_2$	$A = A_3$
$I = I_1$	1,003*	267*	340	1,014*	211*	187
$I = I_2$	783*	406*	557	889*	165*	141
$I = I_3$	499	726	1,115	555	153	113

*Taken from the original 2^3 experiment.
Note: Activity remaining in tens of counts per minute per 0.5 ml. of filtrate.
Iron concentration: $F_1 = 0.5$, $F_2 = 1.0$
Final *p*H: $A_1 = 4$, $A_2 = 6$, $A_3 = 8$
Initial *p*H: $I_1 = 1$, $I_2 = 2$, $I_3 = 4$

involving this factor, little weight can be assigned to the formally significant *AIS* and *FAIS* interactions.

The failure of the change in sulfide concentration to affect the results constitutes useful information. From the standpoint of economics it means that the quantity of sulfide may be halved without deleterious effect. From the standpoint of operational control, it means that the amount of sulfide might be allowed to vary within wide limits without decreasing the efficiency of the process.

The advantages of exploring the sulfide factor by expansion of the original factorial, rather than by an independent study, are now apparent; first, the sulfide factor, as well as its interactions with the first three factors, has been evaluated with maximum precision; second, the main effects and interactions of the original experiment have been further checked by utilization of the larger number of comparisons afforded by the expanded design.

EXPANSION OF THE 2^3 FACTORIAL BY ADDITION OF NEW LEVELS

Any factorial experiment may be expanded in two ways: by addition of new factors or by increase in the number of levels of the original factors. The first device having been utilized to explore the sulfide factor, the second was adopted to check the influence of further increases in the initial and final *p*H. The new *p*H levels were chosen as $A_3 = 8$ for the final *p*H and $I_3 = 4$ for the initial *p*H. The iron factor was retained at its original levels. The sulfide factor, which had given only negative results, was eliminated by being held constant at the original level of 0.5 g. The expanded factorial was thus a three-factor experiment, with the iron factor at two levels and each *p*H factor at three levels. There were $2 \times 3 \times 3 = 18$ treatment combinations required, of which eight were included in the original 2^3 factorial. The ten additional treatments were carried out in random order.

The outstanding conclusions of the experiment are revealed in a general way in Table 6, in which the results of the eighteen treatment combinations are tabulated in a systematic fashion. The table draws attention to a marked improvement in decontamination attributable to elevating the iron content and also to consistently better results with increasing initial and final *p*H provided the iron is held at the higher level.

The results may be examined more rigorously by computing the effect of each factor for each combination of levels of the remaining two factors. This has been done in Table 7 (*a*), (*b*), and (*c*) for the iron concentration factor, the final *p*H, and the initial *p*H, respectively. As the new treatments were not replicated, no error term is available for rigorous significance tests. However, because of the additional levels included, the consistency of trends is available as a criterion of significance. The maximum efficiency characteristic of the factorial plan again is evident: each of the three tables utilizes all the data. Because of the presence of pronounced interactions and the increasing concentration on specific results as optimum conditions are approached, the main or over-all effects are of only limited interest.

The effect of raising the iron concentration is given in Table 7 (*a*) for each of the nine different combinations of initial and final *p*H included in the expanded experiment. The table affords ample evidence of the *FA* interaction: for every *I* value, the iron effect becomes progressively more beneficial with increasing final *p*H. Also an *FI* interaction exists at the two higher levels of final *p*H, the effect of the iron factor becoming more beneficial with increasing initial *p*H.

The effect of a three-level factor requires two comparisons for its expression. Thus the effect of the final *p*H may be expressed as the differences $A_2 - A_1$, and $A_3 - A_2$. In Table 7 (*b*) each of these differences is tabulated for the six iron-concentration–initial-*p*H combinations included in the experiment. The *FA* interaction is again apparent: the beneficial effect of increasing the final *p*H is invariably greater at the higher iron level.

The effect of the initial *p*H, again expressed as two comparisons, is tabulated for each of the six iron-concentration–final-*p*H combinations in Table 7 (*c*). The *FI* interaction is exemplified by the circumstance that increasing the initial *p*H is consistently beneficial only at the higher iron level.

The positive *AI* interaction, suggested by the earlier experiments, is again present. Thus from Table 7 (*b*) the beneficial effect of increasing the final *p*H becomes less pronounced with increasing initial *p*H. Conversely, from Table 7 (*c*), the beneficial effect of increasing the initial *p*H drops off with increasing final *p*H. The positive interaction seems to be associated with the circumstance that with increasing final (initial) *p*H the limiting performance of the process is approached and therefore progressively smaller initial (final) *p*H effects are encountered. It is nonetheless clear from Table 6 that it is desirable to increase both *p*H factors together to attain the best decontamination.

THE 4 × 4 FACTORIAL

The results of the $2 \times 3 \times 3$ experiment indicated that still further increases in

Table 7. Simple and Main Effects of the $2 \times 3 \times 3$ Factorial Experiment

(*a*) Effect of Iron Concentration ($F_2 - F_1$)

	$A = A_1$	$A = A_2$	$A = A_3$	Avg.
$I = I_1$	11	− 56	− 153	− 66
$I = I_2$	107	−241	− 417	−184
$I = I_3$	56	−573	−1002	−506
Average	58	−290	− 524	−252

(*b*) Effect of Final *p*H

	$F = F_1$		$F = F_2$		Avg., F_1 and F_2	
	$A_2 - A_1$	$A_3 - A_2$	$A_2 - A_1$	$A_3 - A_2$	$A_2 - A_1$	$A_3 - A_2$
$I = I_1$	−737	73	−803	−24	−770	25
$I = I_2$	−377	151	−725	−24	−551	63
$I = I_3$	228	389	−402	−40	− 87	174
Average	−295	204	−643	−29	−469	87

(*c*) Effect of Initial *p*H

	$F = F_1$		$F = F_2$		Avg., F_1 and F_2	
	$I_2 - I_1$	$I_3 - I_2$	$I_2 - I_1$	$I_3 - I_2$	$I_2 - I_1$	$I_3 - I_2$
$A = A_1$	−220	−284	−124	−335	−172	−309
$A = A_2$	139	320	− 46	− 12	47	154
$A = A_3$	218	558	− 46	− 28	86	265
Average	46	198	− 72	−125	− 13	37

Note: Results in tens of counts per minute per 0.5-ml. of filtrate.

Table 8. Results of the 4×4 Factorial Experiment

	$A_1 = 4$	$A_2 = 6$	$A_3 = 8$	$A_4 = 10$
$I_1 = 1$	1,014	211	187	163
$I_2 = 2$	889	165	141	114
$I_3 = 4$	555	153	113	62
$I_4 = 6$	567	155	113	44

Note: Activity remaining in tens of counts per minute per 0.5 ml. of filtrate.

nitial and final pH might give greater decontamination. Accordingly, one additional level was assigned to each of the pH factors, namely, $A_4 = 10$ and $I_4 = 6$. The iron concentration factor was eliminated by holding it constant at the higher level.

A factorial experiment, devoted to the two pH factors, each at four levels, required $4 \times 4 = 16$ treatments, seven of which are new. All sixteen results are tabulated in Table 8. The expected improvement, from increasing the final pH to 10, is confirmed for all three initial pH levels. The advantage of increasing the initial pH to 6 is slight and appears only at the highest final pH.

CONCLUSIONS

The decontamination obtained with an initial pH of 6 and a final pH of 10, when an iron concentration of 1 mg./ml. and 0.5 g. of sulfide were used, was the best result observed in the study. Judging from results at the lower pH levels, halving of the amount of sulfide used has no influence on the results. The possibility of further improving the process with still higher values of the pH did not appear attractive because of the smallness of any anticipated effect and the increasing cost entailed by additional chemical treatment.

The value of using a sequence of progressively expanding and contracting factorial designs in a study devoted to the establishment of optimum operating conditions has been clearly demonstrated. Such a procedure generates a series of coherent conclusions characterized by maximum reliability and generality. While the goal of optimum conditions is attained in a highly efficient manner, the functional dependence of the dependent variable on those conditions is thoroughly explored.

ACKNOWLEDGMENT

The services of the following chemists are gratefully acknowledged: T. C. Tesdahl, T. G. Linxweiler, and D. R. Spangler.

Mound Laboratory is operated by Monsanto Chemical Company for the U. S. Atomic Energy Commission under contract AT-33-1-GEN-53.

LITERATURE CITED

1. Lowe, C. S., L. L. Bentz, E. L. Murphy, E. Orban, F. Reichel, C. E. Shoemaker, and T. C. Tesdahl, *MLM*-662 (*Rev.*) (Dec. 28, 1953).
2. Fisher, R. A., "The Design of Experiments," 4 ed., Hafner Publishing Company, New York (1949).
3. Cochran, W. G., and G. Cox, "Experimental Designs," John Wiley and Sons, Inc., New York (1950).

Presented at Nuclear Science and Engineering Congress, Cleveland.

A System for Counting Variables in Separation Processes

MOOSON KWAUK

Hydrocarbon Research, Inc., New York, New York

In the proposed system for counting variables in separation processes the processes are resolved into their simpler component classes, e.g., theoretical plates, heat exchangers, reboilers, distillation columns, etc., and a distinction is made between those variables which are inherent in the systems and those which may be specified for design. Results are presented for the most commonly occurring component classes, and all possible process relations existing among these classes are expressed by a set of generalized equations [(16) to (19)]. The procedure of counting variables is therefore reduced to composition from variables for the component classes by use of the generalized equations.

In the design of processes for physical separation of components by mechanisms involving mass and heat transfer, the first step usually consists of specification of process conditions or independent variables. When the sufficient and necessary independent variables are fixed, the system is determined and other variables may be found by design computations. Normally the variables of a system are interrelated in such a way that only a few of them could be expressed as explicit functions of the others; the remaining ones have to be determined by lengthy calculations.

An example is the design of a distillation column separating a binary mixture of benzene and toluene. The column is to be designed to have one intermediate feed, a partial reboiler with a liquid-bottoms-product stream, and a total condenser with a liquid-distillate-product stream, and it will operate at atmospheric pressure. It is possible to specify for this column the concentration of either benzene or toluene in either the distillate or the bottoms stream, the recovery of either component in either stream, and the reflux ratio, viz., three independent variables. Then the number of theoretical plates both above and below the feed could be found by the familiar McCabe-Thiele diagram, thus determining two implicit dependent variables. A formal analysis shows, however, that for the column there exist four independent variables that could be specified. The fourth variable, not stated above, is implicit in the McCabe-Thiele method, that is, optimum location of the feed plate; the stepwise procedure is to be transferred from one operating line to the other in the vicinity of the intersection of the lines in order to secure a minimum total number of plates.

Another example is a so-called "double-distillation column" separating the ternary mixture, air—N_2, A, and O_2—with vapor air feed to the high-pressure column and a nitrogen-rich vapor distillate stream and an oxygen-rich vapor bottoms stream from the low-pressure column. In this case the number of independent variables that could be specified is not at all apparent. However, without a knowledge of the exact number of independent variables it is difficult, if not impossible, to proceed with a design problem in a systematic way. Often experience helps in setting trial values of certain variables very close to the correct answer, without the need of actually differentiating the implicit from the independent variables. With recent increase in use of electronic computers for design studies, however, it is desirable to know at the outset of a problem the correct number of independent variables as process conditions and to feed into the machine neither more nor less than those variables that can be specified, thus letting the machine perform the trial-and-error loops in finding the correct values of the dependent variables. In such a situation experience could hardly substitute for correct logic.

PRINCIPLES OF THE METHOD OF ANALYSIS

The difficulty of finding the correct number of independent variables was recognized by Gilliland and Reed (*2*), who proposed a method of attack by use of the phase rule and the first law of thermodynamics. Other discussions on the subject can be found in the literature

Tabular material has been deposited as document 4807 with the American Documentation Institute, Photoduplication Service, Library of Congress, Washington 25, D. C., and may be obtained for $5.00 for photoprints or $2.25 for 35-mm. microfilm.

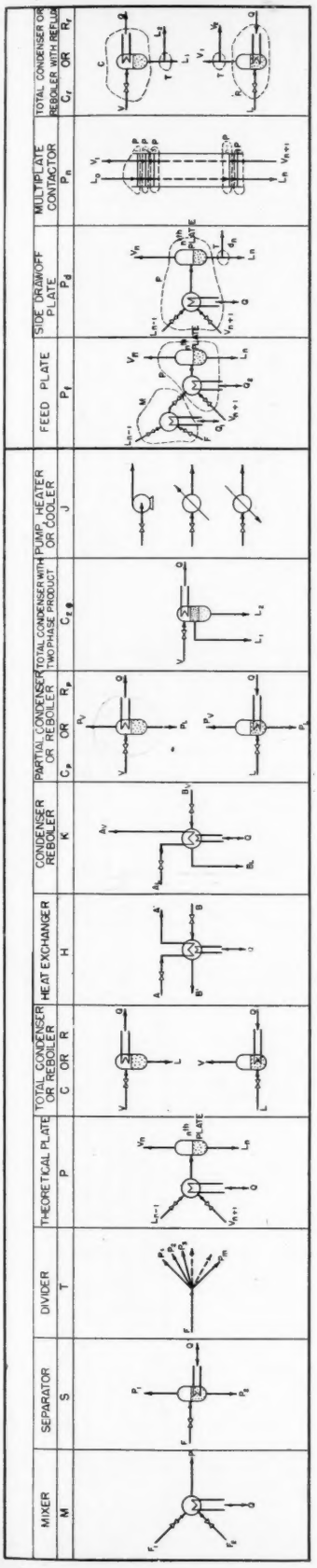

Fig. 1. Elements.

Fig. 2. Complex elements.

(*1, 3*). As will be shown below, the phase rule contributes toward accounting for all variables, N_v, in a system, and the first law toward accounting for all possible conditions, N_c, inherent and necessary in the system. The difference between the possible variables and the possible conditions represents the independent variables, N_i. Thus

$$N_i = N_v - N_c \qquad (1)$$

The possible variables of a system, N_v, could be enumerated as follows:

1. The phase rule gives the degree of freedom of any single-stage system in which there exists either one phase or two or more phases in equilibrium:

$$N = C + 2 - \phi \qquad (2)$$

These degrees of freedom represent the so-called "intensive" variables such as concentration, temperature, pressure, entropy, and other thermodynamic properties determined by the state and independent of the quantities of the components present. For a flow system, however, there is associated with any stream an additional extensive variable —its rate of flow—which is not determined by the state and is therefore not dealt with by the phase rule itself. Therefore, for a one-phase system there are $C + 1$ intensive variables, 1 extensive variable, or $C + 2$ total variables. For a two-phase system, where the flow rates of both phases could be set independently, there are C intensive variables, 2 extensive variables, and $C + 2$ total variables.

2. For any system, considered as a whole, or any part thereof, there remains, in addition to the foregoing variables, the degree of freedom of choosing the amount, or rate, of energy exchanged between the system and its surroundings.

In a strict sense the method is applicable to systems in equilibrium, inasmuch as the basis of the phase rule is equilibrium. Therefore the analysis will be rigorously correct for separation processes reducible to a stagewise nature. Differential types of operation should be viewed as consisting of an infinite number of stages each of which approaches some presupposed percentage of equilibrium.

The conditions inherent and necessary in a system, N_c, are enumerated as follows:

1. A system has to be in material and energy balance. The first law of thermodynamics states that the total amount of energy entering any system must be exactly equal to that leaving plus any accumulation of energy within the system. For flow processes in which changes in kinetic energy, potential energy, and work done are negligible, the first law is simplified to straightforward enthalpy, or heat, balance. Normally heat balance determines one condition in any system, and as many conditions are fixed by material balances as there are components in the system.

2. Additional conditions inherent in a system are found in equality of variables of certain streams, such as those joining different parts of a composite system.

For ordinary operations certain of the variables are often set by design, such as the composition and flow rate of the feeds, the pressure on each plate of a distillation column, and the heat leak to or from each plate. Thus for any system the number of these normally fixed variables is

$$N_x = N_F + N_r + N_Q \qquad (3)$$

The difference between the independent variables, N_i, and those normally fixed, N_x, stands for the independent variables available, N_a, for process specifications:

$$N_a = N_i - N_x \qquad (4)$$

$$= N_v - N_c - N_x \qquad (5)$$

The available independent variables, N_a, are the principal ones of interest in the solution of design problems, and the present method is devoted mainly to their enumeration.

A SYSTEMATIC APPROACH

The basic principles set forth above are relatively simple, and in theory the desired number of variables could always be obtained by starting from these fundamentals. In practice, it will be found that such a procedure is not only tedious but also sometimes confusing. One frequent difficulty in applying the foregoing principles lies in the recognition of variables and conditions so that none is overlooked or counted twice. As an example, from the use of the McCabe-Thiele method of designing distillation columns one is likely to reach the erroneous conclusion that only three independent variables exist in a distillation column with an intermediate feed. As indicated, the correct number is four. As a further example the heat input to and heat leak from a reboiler may be considered. The question arises of whether they are two independent variables or just one. Sometimes it is not easy to see whether certain conditions should be classed as inherent in a system or as normally fixed in design. For instance, when a stream is divided the operation is adiabatic. The fact of no heat exchange between the system and its surrounding would appear either as an inherent condition of the system or as a normally fixed variable representing zero heat leak.

The present paper presents a self-consistent system of classifying and accounting variables and conditions, designed to avoid the errors and dilemmas described above. The results of this study are tabulated and summarized so that any complex system may be analyzed with a minimum of time without resorting to first principles.

PROPOSED METHOD

In the present method the component parts of a separation process or a system of operations are classified as elements, complex elements, units, and complex units, in the order of increasing complex-

TABLE 1. ELEMENTS

Element Symbol	Variables: Description	Variables: Number	Mixer M	Separator S	Divider T	Theoretical plate P	Total condenser or reboiler C or R	Heat exchanger H	Condenser reboiler K	Partial condenser or reboiler[7] C_p or R_p	Total condenser with two-phase product $C_{2\phi}$	Pump, heater or cooler J
No. of streams	$1-\phi$	—	3	1	$m+1$	2	2	4	4	1	1	2
	$2-\phi$	—	0	1	0	1	0	0	0	1	1	0
N_v^e	$1-\phi$	$C+2$	$3(C+2)$	$C+2$	$(m+1)(C+2)$	$2(C+2)$	$2(C+2)$	$4(C+2)$	$4(C+2)$	$C+2$	$C+2$	$2(C+2)$
	$2-\phi$	$C+2$	0	$C+2$	0	$C+2$	0	0	0	$C+2$	$C+2$	0
	Q	1	1	1	1	1	1	1	1	1	1	1
	Total		$3C+7$	$2C+5$	$mC+C+2m+3$	$3C+7$	$2C+5$	$4C+9$	$4C+9$	$2C+5$	$2C+5$	$2C+5$
N_c^e	Material balance	C	C	C	C	C	C	$2C$[4]	$2C$[5]	C	C	C
	Heat balance	1	1	1	1	1	1	1	1	1	1	1
	Q	1	—	—	$1(Q=0)$	—	$1(Q=$ latent heat)[3]	—	—	—	$1(Q=$ latent heat)[3]	—
	Equality	—	—	—	[1]$(m-1)(C+1)+1$[2]	—	—	—	2[6]	—	—	—
	Total		$C+1$	$C+1$	$mC+m+2$	$C+1$	$C+2$	$2C+1$	$2C+3$	$C+1$	$C+2$	$C+1$
$N_i^e = N_v^e - N_c^e$		—	$2C+6$	$C+4$	$C+m+1$	$2C+6$	$C+3$	$2C+8$	$2C+6$	$C+4$	$C+3$	$C+4$
N_x^e	Feed	$C+2$	$2(C+2)$	$C+2$	$C+2$	$2(C+2)$	$C+2$	$2(C+2)$	$2(C+2)$	$C+2$	$C+2$	$C+2$
	π	1	1	1	—	1	1	2	2	1	1	} 1[8]
	Q	1	1	1	—	1	—	1	1	—	—	
	Total		$2C+6$	$C+4$	$C+2$	$2C+6$	$C+3$	$2C+7$	$2C+7$	$C+3$	$C+3$	$C+2$
$N_a^e = N_i^e - N_x^e$			0	0	$m-1$	0	0	1	-1	1	0	1
Example of N_a^e								Temp. of A' or B'	For assigned heat leak and pressures of streams A and B both flow rates of A and B cannot be fixed at same time.	Q or P_L/P_v ratio		Discharge pressure or temperature

NOTES: (1) Equality of intensive variables of all product streams.
(2) Pressure of system equals pressure of feed.
(3) Net heat exchange with surrounding including latent heat and heat leak.
(4) Since there is no material exchange between streams AA' and BB', there are C material balances for each stream, or altogether $2C$ material balances.
(5) Since there is no material exchange between streams A_LA_v and B_vB_L, there are C material balances for each stream, or altogether $2C$ material balances.
(6) Heat exchanged equal to latent heat of vaporization of both streams.
(7) An evaporator is a special case of R_p.
(8) Constant heat leak for pump, or constant pressure for heater and cooler.

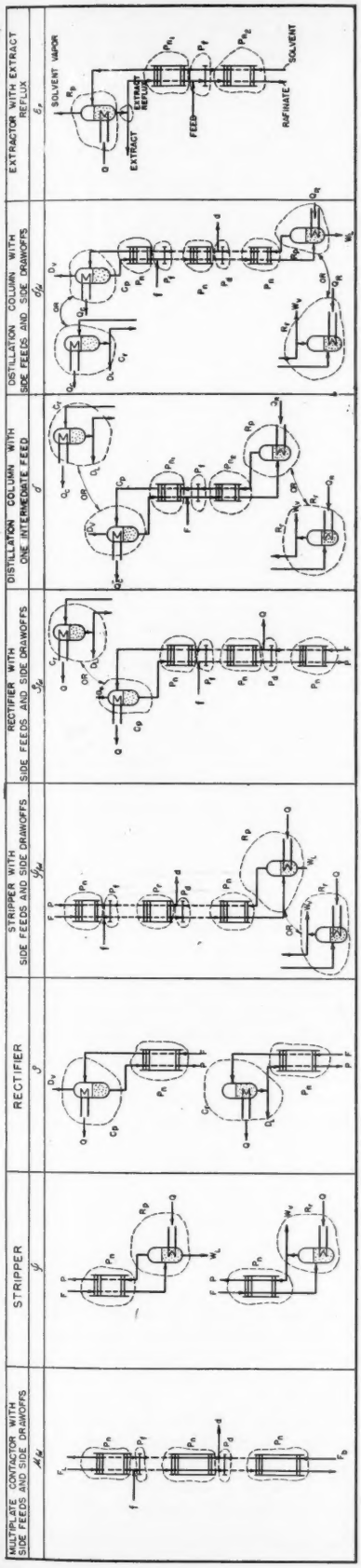

Fig. 3. Units.

ity. The classification is somewhat arbitrary and is made for convenience' sake. An element is a single-stage equipment, such as a flash drum, a total condenser, a theoretical plate, etc. A complex element is an element with certain minor additional features, such as a total condenser with reflux—that is, a total condenser from which the condensate is divided into a distillate stream and a reflux stream. Another example of a complex element is a repetition of theoretical plates in series so as to form a multiplate contactor, a particular case of which is found in an absorber. A combination of elements or complex elements gives rise to a unit, such as a stripping column, which is a multiplate contactor combined with a reboiler. When units, complex elements, or elements are connected, they form complex units, such as a petroleum fractionator with strippers attached to side drawoff streams. It can be seen that a more complex, or major, class (such as a stripping column) is composed of less complex, or minor, classes (theoretical plates and reboiler of the stripping column).

The problem of enumerating variables and conditions is therefore reduced to the following two stages:

1. Enumeration of variables and conditions of the simplest class, the element, by direct application of the principles adopted.
2. Establishment of relations among the various classes so that the major classes might be analyzed by applying the results obtained for the minor classes without resort to the first principles.

Throughout this study the normally fixed variables for any system will be limited to the composition and flow rate of the feed,* the pressure of the system, and heat exchanged between the system and its surroundings. This selection of fixed variables is arbitrary, but the logic of the method is hardly affected by any other selection.

Elements

For the first stage of the problem, a start will be made with the element. The number, N, representing variables or conditions, will be assigned a superscript to designate one of the four classes listed above and a subscript denoting the nature of the variable or condition. For example, N_i^e denotes the number of *independent* variables for an *element*. Equations (1), (4), and (5) could be written for any element as follows:

$$N_i^e = N_v^e - N_c^e \qquad (6)$$

$$N_a^e = N_i^e - N_x^e \qquad (7)$$

$$= N_v^e - N_c^e - N_x^e \qquad (8)$$

*Exceptions will be found in which the flow rate of a feed is not normally fixed. For instance, the flow rate of the strippant in a stripper is usually considered a variable available for process specification. In this case one more variable will therefore have to be added to the number resulting from the present analysis.

An example of an element is the case of a theoretical plate, P. Two single-phase streams containing C components each are fed to the plate in the form of liquid from the plate above and vapor from the plate below. The total number of variables of these two streams is $2(C + 2)$. Leaving the plate are two streams in equilibrium, vapor to the plate above and liquid to the plate below. These two streams in equilibrium are counted as a two-phase system representing $C + 2$ variables. Another variable is found in any heat exchange with the surroundings. Therefore the total number of variables is

$$N_v^e = 2(C + 2) + (C + 2) + 1$$

$$= 3C + 7$$

The inherent conditions are material balances for the C components and one heat balance of all the streams entering and leaving the plate:

$$N_c^e = C + 1$$

Therefore according to Equation (6)

$$N_i^e = (3C + 7) - (C + 1)$$

$$= 2C + 6$$

The usually fixed variables are the compositions and flow rates of the two feeds, $2(C + 2)$, and the pressure on plate, 1, and the heat exchange (heat leak) with the surrounding, 1, or

$$N_x^e = 2(C + 2) + 1 + 1$$

$$= 2C + 6$$

Therefore

$$N_a^e = (2C + 6) - (2C + 6)$$

$$= 0$$

A little reflection will show that a constant-pressure theoretical plate with fixed vapor and liquid feeds and fixed heat leak is a nonvariant system.

Table 1† repeats the foregoing analysis for a number of representative elements, viz., mixer, separator, divider, condenser or reboiler, total condenser with two-phase product, and pump, heater, or cooler, all of which are illustrated schematically in Figure 1. Each element is assigned a symbol, such as P for the theoretical plate, and is described in a sketch in Figure 1. In what follows it will be seen that the results set forth in Table 1 may be used directly in deriving variables of more complex classes without need to refer to first principles.

Complex Elements

A complex element is essentially a modified element, the modification usually being the addition or division of a

†See footnote on page 240.

(8) Constant heat leak for pump, or constant pressure for heater and cooler.

TABLE 2. COMPLEX ELEMENTS

Complex element Symbol	Variables: Description	Variables: Number	Feed plate P_f	Side drawoff plate P_d	Multiplate contactor P_n	Total condenser or reboiler with reflux C_r or R_r
No. of streams	Feed		3	2	2	1
	inter-		1	1	$2(n-1)$	1
No. of elements	M		1	0	0	0
	T		0	1	0	1
	P		1	1	n	0
	C or R		0	0	0	1
No. of plates			1	1	n	—
N_v^E	M	$2C+6$	$2C+6$	—	—	—
	T	$C+m+1$	—	$C+3$	—	$C+3$
	P	$2C+6$	$2C+6$	$2C+6$	$n(2C+6)$	—
	C or R	$C+3$	—	—	—	$C+3$
	α	1	0	0	1	—
	Total		$4C+12$	$3C+9$	$2nC+6n+1$	$2C+6$
N_c^E = Interstreams		$C+2$	$C+2$	$C+2$	$2(n-1)(C+2)$	$C+2$
$N_i^E = N_v^E - N_c^E$			$3C+10$	$2C+7$	$2n+2C+5$	$C+4$
N_x^E	N_F^E	$C+2$	$3(C+2)$	$2(C+2)$	$2(C+2)$	$C+2$
	$N_x^e - N_F^e$: M	2	2	—	—	—
	$N_x^e - N_F^e$: T	0	—	0	—	0
	$N_x^e - N_F^e$: P	2	2	2	$2n$	—
	$N_x^e - N_F^e$: C or R	1	—	—	—	1
	Total		$3C+10$	$2C+6$	$2n+2C+4$	$C+3$
$N_a^E = N_i^E - N_x^E$			0	1	1	1
Example of N_a^E				Flow rate of side drawoff	Number of plates or concentration of any component in either of two product streams.	Reflux ratio or Q

stream. For a complex element, Equations (1), (4), and (5) can be written as follows:

$$N_i^E = N_v^E - N_c^E \quad (9)$$

$$N_a^E = N_i^E - N_x^E \quad (10)$$

$$= N_v^E - N_c^E - N_x^E \quad (11)$$

Since a complex element is made up of a combination of elements, the following relation between the complex element and its component elements holds:

$$N_v^E = \sum N_i^e + N_\alpha \quad (12)$$

This equation states that the *total* number of variables of a complex element is equal to the sum of the *independent* variables of the component elements, plus N_α, which stands for the freedom of choice of the number of times which any component element could be repeated. The variable, N_α, is not equal to the number of such repetitions but represents the single degree of freedom with which the number of such repetitions could be chosen. By means of Equation (12), the inherent conditions in the component elements which are already covered in $\sum N_i^e$ will not be counted again as conditions specific to the complex element. This illustrates a rule of counting variables devised to avoid redundancy. It will be referred to as the rule of coverage, which will be used repeatedly in this study.

The conditions inherent and necessary in the complex element are limited to those streams interconnecting the component elements. These streams will be referred to as *interstreams*. When two elements are connected by an interstream, the stream leaving one element and the stream entering the other, which are considered as two independent streams when the elements are treated separately, necessarily possess the same intensive and extensive variables. Such equality in the intensive and extensive variables constitutes the inherent and necessary conditions of an interstream. If an interstream is single phase, these conditions stand for $C + 2$ variables.

In counting the normally fixed variables for a complex element, the following relation is adopted:

$$N_x^E = N_F^E + \sum (N_x^e - N_F^e) \quad (13)$$

This equation divides the normally fixed variables into two groups, those pertaining to the feed, N_F, and those belonging to pressure and heat leak, $N_x - N_F$. Since a complex element and its component element will often have common feeds, the foregoing division is designed to avoid redundancy in enumeration. This measure is arbitrary, but as long as it is followed consistently the present system of counting variables will maintain its validity.

Substitution of Equations (12) and (13) in Equations (9) and (11) yields

$$N_i^E = \sum N_i^e + N_\alpha - N_c^E \quad (14)$$

$$N_a^E = \sum N_i^e + N_\alpha - N_c^E - N_F^E - \sum (N_x^e - N_F^e) \quad (15)$$

As an example of a complex element one may consider a multiplate contactor, of which a gas absorber is a particular case. (*See* Table 2*.) With the number of plates equal to n, from Table 1, for a theoretical plate, $N_i^e = 2C + 6$. For n theoretical plates the number of variables is $n(2C + 6)$. Since the number of plates, n, could be specified by design, the specification of n represents one additional independent variable, or $N_\alpha = 1$.

*See footnote on page 240.

Table 3. Summary

Class	System	Symbol	N_i	N_x-N_F	N_x	N_a
Elements	Mixer	M	$2C+6$	2	$2C+6$	0
	Separator	S	$C+4$	2	$C+4$	0
	Divider	T	$C+m+1$	0	$C+2$	$m-1$
	Theoretical plate	P	$2C+6$	2	$2C+6$	0
	Total condenser or reboiler	C or R	$C+3$	1	$C+3$	0
	Heat exchanger	H	$2C+8$	3	$2C+7$	1
	Condenser reboiler	K	$2C+6$	3	$2C+7$	-1
	Partial condenser or reboiler	C_p or R_p	$C+4$	1	$C+3$	1
	Total condenser with two-phase product	$C_{2\phi}$	$C+3$	1	$C+3$	0
	Pump, heater, or cooler	J	$C+4$	1	$C+3$	1
Complex elements	Feed plate	P_f	$3C+10$	4	$3C+10$	0
	Side drawoff plate	P_d	$2C+7$	2	$2C+6$	1
	Multiplate contactor	P_n	$2n+2C+5$	$2n$	$2n+2C+4$	1
	Total condenser or reboiler with reflux	C_r or R_r	$C+4$	1	$C+3$	1
	Multiplate contactor with side feeds and side drawoffs	μ_{fd}	$2\sum_{1}^{f+d+1} n_i+f(C+7)+4d+2C+5$	$2\sum_{1}^{f+d+1} n_i+4f+2d$	$2\sum_{1}^{f+d+1} n_i+f(C+6)+2d+2C+4$	$f+2d+1$
	Stripper	ψ	$2n+C+5$	$2n+1$	$2n+C+3$	2
	Rectifier	ρ	$2n+C+5$	$2n+1$	$2n+C+3$	2
	Stripper with side feeds and side drawoffs	ψ_{fd}	$2\sum_{1}^{f+d+1} n_i+f(C+7)+4d+C+5$	$2\sum_{1}^{f+d+1} n_i+4f+2d+1$	$2\sum_{1}^{f+d+1} n_i+f(C+6)+2d+C+3$	$f+2d+2$

Units	Rectifier with side feeds and side drawoffs	ρ_{fd}	$2\sum_{1}^{f+d+1} n_i+f(C+7)+4d+C+5$	$2\sum_{1}^{f+d+1} n_i+4f+2d+1$	$2\sum_{1}^{f+d+1} n_i+f(C+6)+2d+C+3$	$f+2d+2$
	Distillation column with one intermediate feed	δ	$2(n_1+n_2)+C+12$	$2(n_1+n_2)+6$	$2(n_1+n_2)+C+8$	4
	Distillation column with side feeds and side drawoffs	δ_{fd}	$2\sum_{1}^{f+d+1} n_i+f(C+7)+4d+5$	$2\sum_{1}^{f+d+1} n_i+4f+2d+2$	$2\sum_{1}^{f+d+1} n_i+f(C+6)+2d+2$	$f+2d+3$
	Extractor with extract reflux	ϵ_r	$2(n_1+n_2)+2C+13$	$2(n_1+n_2)+5$	$2(n_1+n_2)+2C+9$	4
Complex units	Distillation columns in series	$\delta+\delta$	$2\sum_{1}^{4} n_i+C+22$	$2\sum_{1}^{4} n_i+12$	$2\sum_{1}^{4} n_i+C+14$	8
	Distillation column with auxiliary stripper or rectifier	$\delta+(\psi)_{aux.}$ or $\delta+(\rho)_{aux.}$	$2\sum_{1}^{5} n_i+C+24$	$2\sum_{1}^{5} n_i+13$	$2\sum_{1}^{5} n_i+C+15$	9
	Distillation column with auxiliary complete column	$\delta+(\delta)_{aux.}$	$2\sum_{1}^{6} n_i+C+31$	$2\sum_{1}^{6} n_i+18$	$2\sum_{1}^{6} n_i+C+20$	11
	Simple double column	$(\delta)^2$	$2(n_1+n_2+n_3)+C+13$	$2(n_1+n_2+n_3)+7$	$2(n_1+n_2+n_3)+C+9$	4
	Double column with side feeds and side drawoffs	$(\delta_{fd})^2$	$2\sum_{1}^{\sigma+2} n_i+(f_l+f_h+1)(C+7)+4(d_l+d_h)+6$	$2\sum_{1}^{\sigma+2} n_i+4(f_l+f_h+1)+2(d_l+d_h)+3$	$2\sum_{1}^{\sigma+2} n_i+(f_l+f_h+1)(C+6)+2(d_l+d_h)+3$	$f_l+f_h+2(d_l+d_h)+4$
	Binary azeotropic distillation column	$(\delta)_{2\phi}$	$2(n_1+n_2)+C+11$	$2(n_1+n_2)+6$	$2(n_1+n_2)+C+8$	3
	Twin azeotropic distillation columns	$(\delta+\psi)_{2\phi}$	$2(n_1+n_2+n_3)+C+16$	$2(n_1+n_2+n_3)+9$	$2(n_1+n_2+n_3)+C+11$	5
	Absorption–desorption cycle (2 pressures; 1 temp.)	–	$2(n_1+n_2)+2C+8$	$2(n_1+n_2+1)$	$2(n_1+n_2)+2C+5$	3*
	Absorption–desorption cycle (2 pressures; 2 temp.)	–	$2(n_1+n_2)+2C+16$	$2(n_1+n_2)+6$	$2(n_1+n_2)+2C+10$	6*

*See footnote * on page 243.

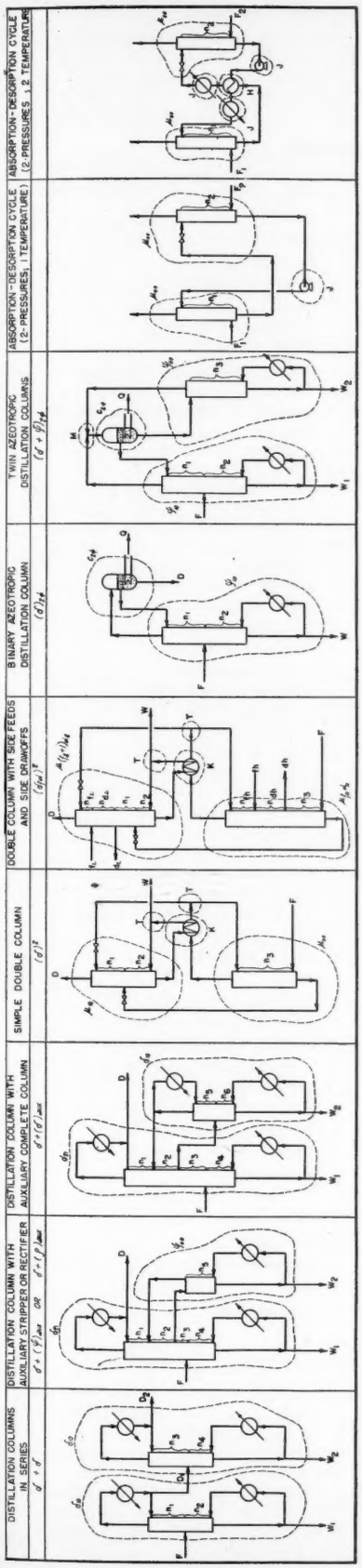

Fig. 4. Complex units.

Therefore

$$N_v^E = n(2C + 6) + 1$$

Every two adjacent plates are connected by two interstreams, each representing $C + 2$ conditions, or $N_c^E = C + 2$ per interstream. As there are $2(n - 1)$ interstreams for the n theoretical plates, there are $2(n - 1)(C + 2)$ inherent conditions associated with these interstreams, or

$$N_c^E = 2(n - 1)(C + 2)$$

$$N_i^E = n(2C + 6) + 1 - 2(n - 1)(C + 2)$$

$$= 2C + 2n + 5$$

The conditions normally fixed for each theoretical plate are its pressure, 1, and heat leak, 1 (*see* Table 1 and Figure 2) or 2 per plate. Therefore for n plates

$$\sum (N_x^e - N_F^e) = 2n$$

The variables set by specifying the two feed streams to the multiplate contactor are

$$N_F^E = 2(C + 2)$$

Therefore

$$N_x^E = 2(C + 2) + 2n$$

and

$$N_a^E = [2C + 2n + 5] - [2(C + 2) + 2n] = 1$$

One way of interpreting this single available independent variable, $N_a^E = 1$, is that for two given feeds the two product streams are entirely determined if the number of plates of an absorber is specified.

Table 2 repeats the foregoing analysis for representative complex elements, viz., feed plate, side-drawoff plate, multiplate contactor, and total condenser or reboiler with reflux. These complex elements are shown in Figure 2.

Units and Complex Units

In a similar manner, it can be shown that the following relations hold between major and minor classes:

$$N_v^y = \sum_{minor} N_i + N_a \qquad (16)$$

$$N_i^y = \sum_{minor} N_i + N_a - N_c^y \qquad (17)$$

$$N_x^y = N_F^y + \sum_{minor} (N_x - N_F) \qquad (18)$$

$$N_a^y = \sum_{minor} N_i + N_a - N_c^y - N_F^y - \sum_{minor} (N_x - N_F) \qquad (19)$$

where the superscript y, stands for any major class and $\sum_{minor}$ for the appropriate summation of all classes minor to y.

Figures 3 and 4 illustrate representative units and complex units respectively. The results of analysis of Figures 1 to 4 are summarized in Table 3* in a form convenient for carrying out the variable-counting procedure. Table 3 includes the more important components of separation processes frequently encountered in chemical plant design.

Examples

The application of the preceding general relations will be illustrated with two examples, one for a unit and one for a complex unit.

An example of a unit is a conventional distillation column, δ, consisting of an intermediate feed, a total condenser with reflux and liquid distillate product (or a partial condenser with vapor distillate product), and a total reboiler with vapor bottoms product (or a partial reboiler with liquid bottoms product). Such a column is shown as the sixth case, δ, in Figure 3.

Before the appropriate equations are applied to an analysis of the preceding case, it is desirable to define precisely the minor classes of which the system consists, the interstreams among these minor classes, and the streams entering and leaving the system as a whole. The present system could be broken into the following minor classes:

one feed plate, P_f
two multiplate contactors, P_n
one partial condenser, C_p, or one total condenser with reflux, C_r
one partial reboiler, R_p, or one total reboiler with reflux, R_r

Reference to the sketch of this system shown in Figure 3 indicates one feed and eight interstreams.

Therefore according to Equation (16) the total number of variables is as follows: (*See* results given in Table 1.)

one feed plate, P_f: $3C + 10$
two multiplate contactors, P_n: $2(n_1 + n_2) + 2(2C + 5)$
one condenser, C_p or C_r: $C + 4$
one reboiler, R_p or R_r: $C + 4$
N_a: 0 (since no component class is repeated)
Therefore $N_v^u = 2(n_1 + n_2) + 9C + 28$

The only conditions inherent in combining the foregoing minor classes are those offered by the eight interstreams, or

$$N_c^u = 8(C + 2)$$

Therefore the total number of independent variables is, according to Equation (17),

*See footnote on page 240.

$$N_i^u = [2(n_1 + n_2) + 9C + 28] - 8(C + 2) = 2(n_1 + n_2) + C + 12$$

The normally fixed variables of the minor classes, except feed, are as follows: (*See* Table 2.)

one feed plate, P_f: 4
two multiplate contactors, P_n: $2(n_1 + n_2)$
one condenser, C_p or C_r: 1
one reboiler, R_p or R_r: 1

$$\sum_{minor} (N_x - N_F) = 2(n_1 + n_2) + 6$$

The normally fixed variables for the unit are, according to Equation (18), greater than the preceding by those variables represented by the feed into the unit, or $C + 2$. Therefore

$$N_x^u = (C + 2) + [2(n_1 + n_2) + 6] = 2(n_1 + n_2) + C + 8$$

And, according to Equation (19),

$$N_a^u = [2(n_1 + n_2) + C + 12] - [2(n_1 + n_2) + C + 8] = 4$$

This number of 4 was discussed in the introduction, and the independent variables often chosen to give this number will not be repeated here. One fact which is of interest is that the number of normally available independent variables, $N_a^u = 4$, is not affected by the number of components, C, which the unit involves. This fact would be found true for the even more complex combinations of the various classes, as may be seen in Table 3.

As a second example illustrating the application of the general relations given by Equations (16), (17), (18), and (19), one may consider a case of the complex unit—an absorption-desorption cycle operating at two pressures and two temperatures. Such an operation is exemplified in the purification of gases by removal of its carbon dioxide content with an ethanolamine solution. The carbon dioxide is absorbed by the ethanolamine solution in an absorber at a lower temperature and higher pressure. The dissolved carbon dioxide in the ethanolamine solution is removed in a stripper by steam at a higher temperature and lower pressure. Interconnecting the absorber and stripper are heat exchangers for cooling and warming the liquid streams and a circulating pump. This cycle is given as the last case of the complex units in Figure 4. The cycle could be broken into the following minor classes:

one cooler, one heater, and one pump: J
one heat exchanger: H
two multiplate contactors with no side feeds and side drawoffs: μ_{00}

The sketch in Figure 4 shows two feeds and seven interstreams. According to Equation (16) the total number of variables is

one cooler, one heater, and one pump: $3(C + 4)$
one heat exchanger: $2C + 8$
two simple multiplate contactors: $2(n_1 + n_2) + 4C + 10$
N_α: 0

$$N_v^U = 2(n_1 + n_2) + 9C + 30$$

The inherent conditions are represented by the seven interstreams:

$$N_c^U = 7(C + 2)$$

Therefore the total number of independent variables is, according to Equation (17),

$$N_i^U = 2(n_1 + n_2) + 9C + 30 - 7(C + 2) = 2(n_1 + n_2) + 2C + 16$$

The normally fixed variables, except feed, of the minor classes are

one cooler, one heater, and one pump: 3
one heat exchanger: 3
two simple multiplate contactors: $2(n_1 + n_2)$

$$\sum_{minor} (N_x - N_F) = 2(n_1 + n_2) + 6$$

The variables fixed by fixing the two feed streams entering the absorption-desorption cycle are $2(C + 2)$.

Therefore

$$N_x^U = 2(C + 2) + 2(n_1 + n_2) + 6 = 2(n_1 + n_2) + 2C + 10$$

According to Equation (19)

$$N_a^U = [2(n_1 + n_2) + 2C + 16] - [2(n_1 + n_2) + 2C + 10] = 6$$

The following represents a possible combination of the six variables available for process specification:

1. Concentration of a key component in the stream leaving the absorber.
2. Concentration of this key component in the lean liquor entering the absorber.
3. Circulation rates of the absorbing liquor.
4. Rate of heat exchange in heat exchanger.
5. Temperature approach to cooling water in cooler.
6. Temperature approach to heating medium in heater.

As noted earlier*, an exception to normally fixing the flow rate of a feed is found in the flow rate of a strippant in a stripper. Therefore, there is a seventh variable available for process specification, viz., the strippant flow rate.

*See footnote on page 243.

ACKNOWLEDGMENT

The author gratefully acknowledges the criticism and changes made by A. M. Squires and Manson Benedict on the original manuscript.

NOTATION

C = condenser; also component
d = side drawoff
D = distillate stream
f = side feed
F = feed, terminal
H = heat exchanger
J = pump, heater or cooler
K = condenser reboiler
L = liquid stream
m = number of divided stream
M = mixer
n = number of theoretical plates
N = number of variables or conditions
p = product
P = theoretical plate
Q = heat exchanged between system and surroundings
R = reboiler
S = separator
T = divider
V = vapor stream
w = bottoms stream
δ = distillation column
ϵ = extraction column
μ = multiplate contactor
π = pressure
ρ = rectifier
σ = $f + d + 1$
ϕ = phase
ψ = stripper

Subscripts

a = available variables for process specification
c = conditions inherent in system
d = with side drawoffs
f = with side feeds
F = feeds
h = high-pressure column of δ^2
i = total independent variables
l = low-pressure column of δ^2
Q = heat exchanged between system and surroundings
v = total variables of system
x = normally fixed variables
α = repetitions of elements
π = pressure

Superscripts

e = element
E = complex element
u = unit
U = complex unit

LITERATURE CITED

1. Dunstan, A. E., et al., "The Science of Petroleum," p. 1563, Oxford University Press, Oxford (1938).
2. Gilliland, E. R., and C. E. Reed, *Ind. Eng. Chem.*, **34**, 551 (1942).
3. Robinson, C. S., and E. R. Gilliland, "Elements of Fractional Distillation," p. 215, McGraw-Hill Book Company, Inc., New York (1950).

A Common Basis for the Correlation of Forced and Natural Convection to Horizontal Cylinders

ROBERT LEMLICH and RONALD HOKE

University of Cincinnati, Cincinnati, Ohio

Natural and forced convection have always been correlated on different bases although the two phenomena have much in common. Accordingly, a method for correlating both types of convection on the same basis, at least for heat transfer outside horizontal cylinders, would be of interest.

A tentative method of accomplishing this for transverse convection is presented, involving certain simplifying assumptions relating to drag and buoyancy, from which an "effective velocity" for natural convection is calculated (by means of the well-known drag correlation) and incorporated in a Reynolds number. The Nusselt number for natural convection is then correlated in terms of the Prandtl number and this Reynolds number in much the same manner as that for McAdams's well-known correlation for forced convection. For 150 different combinations of independent variables covering seven different fluids and wide ranges of diameter, surface temperature, and bulk fluid temperature, the transformed natural-convection data agree with Douglas and Churchill's recent refinement of McAdams's relationship for forced convection with an average deviation of about ±10%.

The methods for correlating forced and natural convective heat transfer differ. For forced convection the Nusselt number Nu is generally presented as a function of the Prandtl number Pr and the Reynolds number Re, and for natural convection Nu is generally correlated as a function of Pr and the Grashof number Gr. Qualitatively speaking, however, the two types of convective heat transfer have much in common. It is therefore of interest to investigate the possibility of devising a method whereby both forced and natural convection can be correlated on the same basis.

One possible scheme is to apply the method of correlating forced convection, namely expressing Nu as a function of Pr and Re, to natural convection as well. This can be accomplished if a suitable effective velocity for natural convection can be obtained for substitution in the Reynolds number. For transverse convection outside horizontal cylinders Brown and Marco (*1*) assumed that the moving fluid film in natural convection uniformly accelerates over a distance of one cylinder diameter D. This assumption, of course, completely neglects the drag of the moving fluid against the stationary fluid. No experimental check is presented although Jakob (*4*) indicates that the analogous assumption for vertical surfaces yields results that agree in their order of magnitude with experimental data.

THEORY

Accordingly, in an effort to include the effect of drag, the following set of simplifying assumptions is tentatively proposed for horizontal cylinders.

1. The boundary layer surrounding the body is the fictive film of Langmuir (*5*), defined as a uniform layer of fluid with a thickness B sufficient to account by conduction alone for all the nonradiative heat transferred. Thus the fictive film has an outside diameter of $D + 2B$, as shown in Figure 1.
2. This hot fictive fluid cylinder rises under a buoyant force equal to that exerted on a cylinder of diameter $D + 2B$ filled with fluid which is at the arithmetic mean film temperature t_f, defined as half the sum of the bulk fluid temperature t_b and the temperature at the surface of the solid t_s.
3. The fluid film rises at a constant velocity u.
4. The drag resistance is that for a cylinder of diameter $D + 2B$ moving at this velocity through the bulk fluid.

These assumptions are admittedly only simplifying approximations to the real situation. Nevertheless, by means of them, a wide range of natural-convection data for horizontal cylinders was converted (*3*) into the same form as forced-convection data and correlated in the same way. The source of the natural-convection data was McAdams's generalized dimensionless correlation (*7*), which represents the smoothed experimental results of many investigations covering a wide variety of conditions. Various combinations of fluid, D, t_b, and t_s, were hypothesized, and Nu was computed for each combination using this generalized correlation for natural convection. The fluids considered included the gases air, carbon dioxide, and ethane and the liquids water, aniline, n-octane, and m-xylene. D ranged from 0.01 to 10 in,.

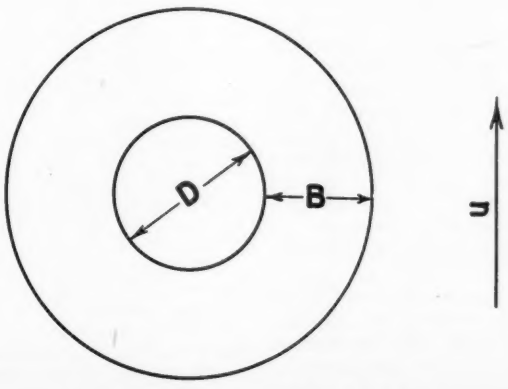

Fig. 1. Cylinder surrounded by fictive film.

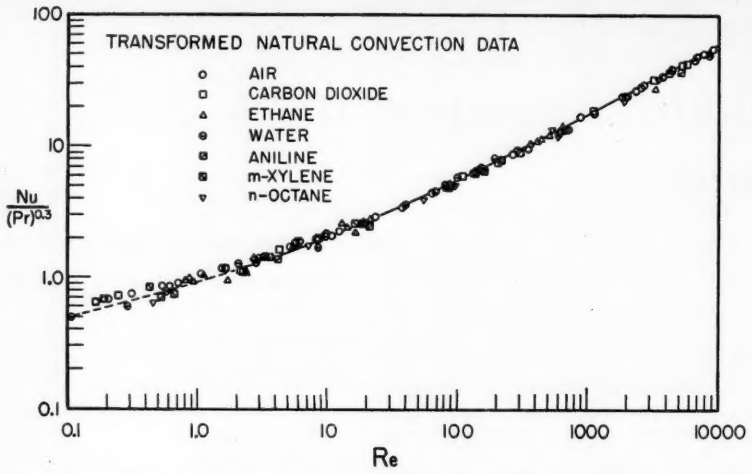

Fig. 2. Comparison of transformed natural-convection data with a generalization (to include *Pr*) of the forced-convection correlation of Douglas and Churchill.

t_0 ranged from 0° to 1,000°F., and $\Delta t = t_s - t_0$ ranged from 1° to 1,000°F. Pr ranged from 0.71 to 0.78 for the gases, and from 1.9 to 11.4 for the liquids. The fictive film thickness was then computed from the expression

$$B = \frac{D}{2}\left(e^{2/Nu} - 1\right) \qquad (1)$$

which follows (*6*) from the definition of B.

The forces acting on a body moving at constant velocity must balance; in other words, the net upward buoyant force F_b acting on the rising film must balance the downward drag force F_d. Per unit length of cylinder, this upward force is given by

$$F_b = \frac{\pi}{4}(D + 2B)^2(\rho_0 - \rho_f)g \qquad (2)$$

where g is the acceleration due to gravity and ρ_0 and ρ_f are the densities of the fluid evaluated at t_0 and t_f respectively. The downward force per unit length can be expressed in terms of the drag coefficient by

$$F_d = \tfrac{1}{2}C\rho_0 u^2(D + 2B) \qquad (3)$$

Perry (*10*) gives C as a function of the Reynolds number $Re' = (D + 2B)u\rho_0/\mu_0$, where μ_0 is the viscosity at t_0. Combining Equations (2) and (3) and incorporating Re' into the result yields

$$C(Re')^2 = \frac{\pi(D + 2B)^3(\rho_0 - \rho_f)g\rho_0}{2\mu_0^2} \qquad (4)$$

Accordingly, by substitution of D, B, and the appropriate fluid properties into Equation (4) the quantity $C\ (Re')^2$ was calculated. From this, Re' itself was determined from the aforementioned drag correlation replotted in the form $C\ (Re')^2$ vs. Re'. From Re' the effective velocity u was computed. The procedure of using a replot was applied merely to eliminate trial-and-error solutions for u. Next the Reynolds number for heat transfer $Re = Du\rho_f/\mu_f$, where μ_f is the viscosity at t_f, was computed. Finally Nu was plotted as a function of Pr and Re in accordance with a generalization (*9*) (merely to include Pr) of Douglas and Churchill's recent refinement (*2*) of McAdams's generalized correlation for forced convection (*8*) and compared with the correlation curve itself.

DISCUSSION

Figure 2 shows this comparison. The generalization of Douglas and Churchill's curve for forced convection fits the transformed natural-convection data with an average deviation of about ±10%. This is almost as good as the fit between the curve itself and the experimental forced-convection data (not shown here) on which it is based. In view of the very wide range of variables involved, this is considered very satisfactory agreement. Thus these simplifying assumptions make possible the correlation of natural convection on the same basis as forced convection, at least for horizontal cylinders.

If application of Figure 2 to an actual calculation in natural convection is desired, say to find Nu, a simple trial procedure is employed, as follows.

Nu is assumed, B calculated from Equation (1), $C\ (Re')^2$ computed from Equation (4), Re' determined from the replot of the drag correlation mentioned above, Re itself calculated, and Nu obtained from Figure 2, the entire procedure being repeated as necessary.

By incorporating the appropriate modifications in the derivation to account for the difference in geometry, the authors have attempted to extend the principle to spheres but so far with less success, perhaps owing to greater deformation. A modification in assumption 2, namely consideration of the fluid cylinder as being hollow with an internal diameter of D, has been studied as well. For cylinders this has proved somewhat less satisfactory than the original assumption although so far it appears fairly satisfactory for spheres. Further work on the entire subject is planned.

CONCLUSION

By means of suitable assumptions involving buoyancy and drag, data for natural convection can be transformed and correlated on the same basis as forced convection, at least for heat transfer outside horizontal cylinders.

ACKNOWLEDGMENT

The authors wish to express their appreciation to Dr. William Licht for reviewing the manuscript.

NOTATION

B = thickness of fictive film, ft.
C = drag coefficient, dimensionless
D = diameter of solid cylinder, ft.
e = base of natural logarithms, dimensionless
F = force per unit length, poundals/ft.
Gr = Grashof number, dimensionless
g = gravitational acceleration, ft./sec.²
Nu = Nusselt number, dimensionless
Pr = Prandtl number, dimensionless
Re, Re' = Reynolds number for the solid cylinder and the fluid cylinder respectively, dimensionless
t = temperature, °F.
Δt = difference in temperature between the surface of the solid and the bulk fluid, °F.
u = effective velocity, ft./sec.
μ = viscosity, lb./(ft.)(sec.)
ρ = density, lb./cu. ft.

Subscripts

b = buoyant
d = drag
f = average for film
0 = bulk
s = solid surface

LITERATURE CITED

1. Brown, A. I., and S. M. Marco, "Introduction to Heat Transfer," p. 111, McGraw-Hill Book Company, Inc., New York (1942).
2. Douglas, W. J. M., and S. W. Churchill, *Chem. Eng. Progr. Symposium Series* No. 18, **52**, to be published.
3. Hoke, R., M.S. thesis, Univ. Cincinnati (June, 1954).
4. Jakob, M., "Heat Transfer," p. 493, McGraw-Hill Book Company, Inc., New York (1949).
5. Langmuir, I., *Phys. Rev.*, **34**, 401 (1912).
6. McAdams, W. H., "Heat Transmission," 2 ed., p. 244, McGraw-Hill Book Company, Inc., New York (1942).
7. *Ibid.*, 3 ed., p. 176 (1954).
8. *Ibid.*, p. 259.
9. *Ibid.*, p. 267.
10. Perry, J. H., "Chemical Engineers' Handbook," 3 ed., p. 1018, McGraw-Hill Book Company, Inc., New York (1950).

Role of Eddy Conductivity in Thermal Transport

W. H. CORCORAN and B. H. SAGE

California Institute of Technology, Pasadena, California

Interest in the course of chemical reactions in turbulent flow has made desirable detailed knowledge of the temperature distribution in flowing streams. One method of predicting the temperature distribution under a variety of conditions is reviewed here, the approach being limited to conditions of local uniform transport of momentum. A discussion of some of the aspects of eddy conductivity is included along with a brief review of the velocity distribution in uniform flow.

The results serve to illustrate the relation of microscopic conditions of flow to the temperature distribution in a turbulently flowing stream. The importance of the molecular Prandtl number upon the transfer process is stressed.

Turbulence exerts a marked influence upon the transport of energy through a fluid as a result of a temperature gradient. The early concepts of a boundary layer in which all the resistance to flow was localized at the edge of the stream appear to be a useful tool in many situations but do not afford a detailed knowledge of the effect of time and position on temperature in various flow processes. The statistical theory of turbulence has made much progress in recent years. The basic contributions of Von Kármán and Howarth (*14*) and the recent review by Batchelor (*2*) laid a reasonable theoretical basis for the statistical theory of turbulence. The work of Corrsin (*4, 5, 6*) at Johns Hopkins is an illustration of the results obtained from the combined action of analysis and experiment. Until the statistical theory of turbulence has reached a somewhat more advanced state than at present, it appears desirable to employ time averages to describe the characteristics of the turbulent-exchange process.

Little experimental information is available concerning the decay of turbulence except in the wake of grids (*7*). For this reason the present discussion will be limited to steady, uniform flow. Progress is being made by Taylor (*25*), Uberoi (*26*), and others in predicting the deviations from isotropy which result from contraction or expansion of flow. The period required for the attainment of steady state in regard to the turbulent-exchange process is also under limited study. For the time being it appears reasonable to limit quantitative considerations to the isotropic characteristics of turbulence, although it must be realized that near boundaries (*16*) and in streams which have not yet reached steady state in the Lagrangian sense, marked deviations from isotropy result.

VELOCITY DISTRIBUTIONS

As noted, the transport of energy in a fluid stream is markedly affected by turbulence. To understand the transport problem it is first necessary to assess the nature of the momentum transport problem, by examining the velocity distributions in turbulent streams.

It is convenient to employ distance and velocity parameters to describe the velocity distribution near the boundary of a stream (*1*). These are defined by

$$y^+ = \frac{y_d}{\nu}\sqrt{\frac{\tau_0 g}{\sigma}} = \frac{y_d u_*}{\nu} \qquad (1)$$

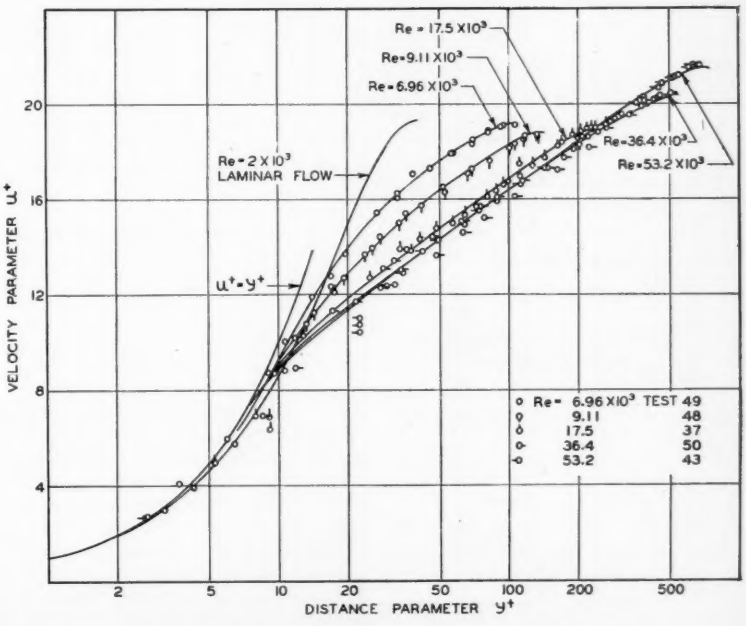

Fig. 1. Experimentally measured velocity distribution.

$$u^+ = \frac{u}{\sqrt{\frac{\tau_0 g}{\sigma}}} = \frac{u}{u_*} \qquad (2)$$

These quantities are known as the distance parameter and the velocity parameter, y^+ and u^+ respectively. Experimental measurements (*23*) of the velocity distribution in an air stream flowing between parallel plates are shown in Figure 1. The experimental results for Reynolds numbers below 20,000 do not agree with the simple theory that u^+ is a single-valued function of y^+ (*1*). The marked effect of shear upon the behavior in the laminar region is shown for a Reynolds number of 2,000 (*23*). A comparison of these experimental data with earlier measurements by Laufer (*15*), Skinner (*24*), Nikuradse (*18*), and Deissler (*8*) is shown in Figure 2. The smoothed data (*23*) for flow between parallel plates are compared in Figure 3 with Deissler's experimental measurements (*8*) for flow in a circular conduit. Good agreement is obtained at the higher Reynolds numbers but significant deviation from a single-valued relationship for the flow between parallel plates was found at the lower Reynolds numbers (*21*). Similar behavior was found in regard to the velocity deficiency (*1, 12*), as is shown in Figure 4. The velocity deficiency is defined by

$$u_d = \frac{u_m - u}{u_*} = \frac{u_m - u}{\sqrt{\frac{\tau_0 g}{\sigma}}} \qquad (3)$$

These data serve to illustrate the complexity of the microscopic velocity distribution in turbulent flow. At the present state of knowledge it appears that for Reynolds numbers below 20,000 the simple generalization of u^+ as a single-valued function of y^+ should not be employed.

For the higher Reynolds numbers this generalization appears to be satisfactory. Utilizing the data of Skinner and Laufer for flow between parallel plates and of Nikuradse and Deissler for flow in a circular conduit gives the relationship of u^+ to y^+ as approximately

$$u^+ = \frac{1}{\sqrt{K_1}} \tanh \sqrt{K_1}\, y^+$$

$$= \frac{1}{0.0695} \tanh 0.0695 \frac{y_d \sqrt{\frac{\tau_0 g}{\sigma}}}{\nu}$$

$$y^+ < 26.7 \qquad (4)$$

$$u^+ = A + \frac{1}{B} \ln y^+$$

$$= 5.5 + \frac{1}{0.4} \ln \frac{y_d \sqrt{\frac{\tau_0 g}{\sigma}}}{\nu}$$

$$y^+ > 26.7 \qquad (5)$$

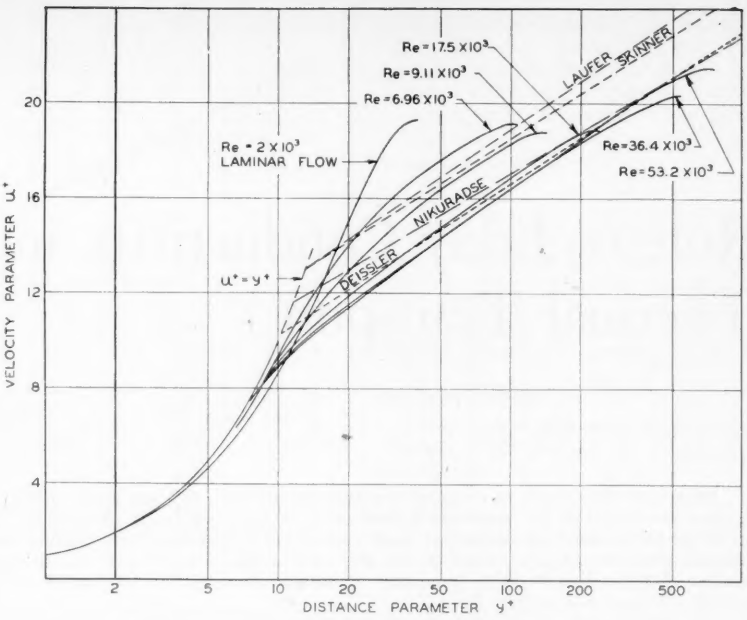

Fig. 2. Comparison of results from different investigators.

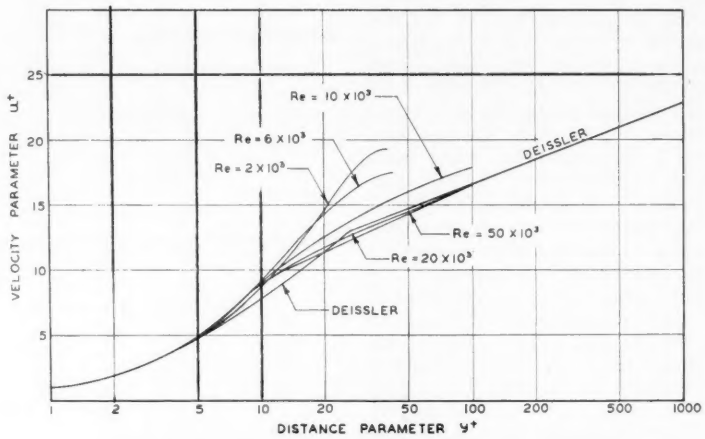

Fig. 3. Comparison of results with flow in circular conduits.

where the fluid properties are constant throughout the stream. These expressions for the flow near the wall (*10*) and in the main body of the stream (*8*) yield a continuous first derivative of the velocity with respect to position. However, Equations (4) and (5) assume that u^+ is a single-valued function of y^+, and, as indicated in the preceding figure, such behavior is encountered only for Reynolds numbers above 20,000 (*23*). A similar situation was found in the relation of the velocity deficiency to position.

Deissler (*8*) prepared an analysis of the relationship of the distance and velocity parameters based upon the similarity hypothesis and certain dimensional considerations as to the factors influencing eddy viscosity. If the shear is assumed constant along with the properties of the fluid, there results for the region near the wall the following expression:

$$y^+ = \frac{1}{n} \frac{\frac{1}{\sqrt{2\pi}} \int_0^{nu^+} e^{-(nu^+)^2/2}\, d(nu^+)}{\frac{1}{\sqrt{2\pi}} e^{-(nu^+)^2/2}} \quad (6)$$

Fig. 4. Smoothed values of velocity deficiency.

In Equation (6) the quantity $1/\sqrt{2\pi}\ e^{-(nu^+)^2/2}$ is the normal error function of nu^+. Likewise Deissler, following the methods proposed by Von Kármán, obtained an expression of the following form for the variation in u^+ with y^+ in the main body of the stream:

$$u^+ = \frac{1}{K_2} \ln y^+ + C = \frac{1}{0.36} \ln y^+ + 3.8 \quad (7)$$

Fig. 5. Comparison of several predictions of velocity distribution.

Equation (7) assumes constant shear and fluid properties in the main body of the stream. Figure 5 includes the relations of u^+ and y^+ as described by Equations (4) to (7) inclusive. It is apparent that there is little to choose between the two approaches. In the present discussion most of the comparisons of velocity distribution and of the evaluations of the eddy viscosity have been made on the basis of Equations (4) and (5).

More recently Deissler (*9*) considered a somewhat different approach and for constant fluid properties suggested the following integral form for the behavior in the boundary layer:

$$u^+ = \int_0^{y^+} \frac{dy^+}{1 + n^2 u^+ y^+ (1 - e^{-n^2 u^+ y^+})} \quad (8)$$

Fig. 6. Relative viscosity as a function of position in flow channel.

In a similar fashion an extension of his more recent approach (*9*) yielded an expression similar to Equation (5) for the turbulent core. In addition, he extended his treatment of velocity distributions to include the behavior when there is a variation in viscosity with temperature. If all the other properties are considered to be invariant, he suggests the following expressions for the velocity parameter and a temperature parameter:

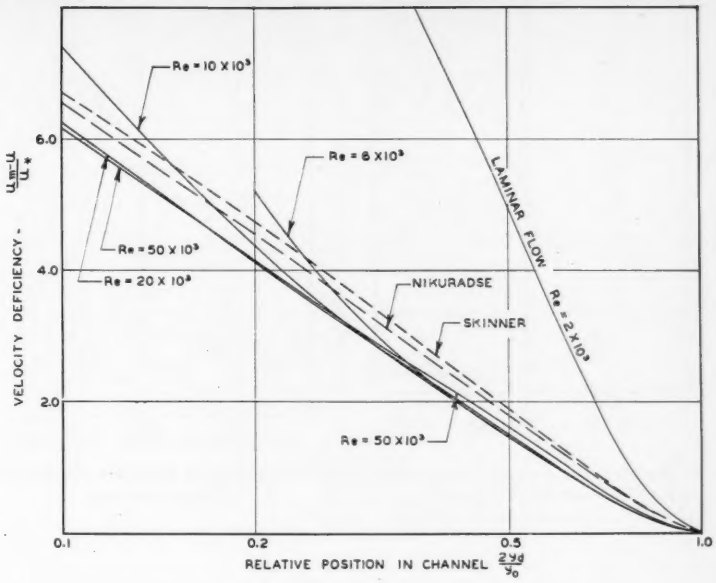

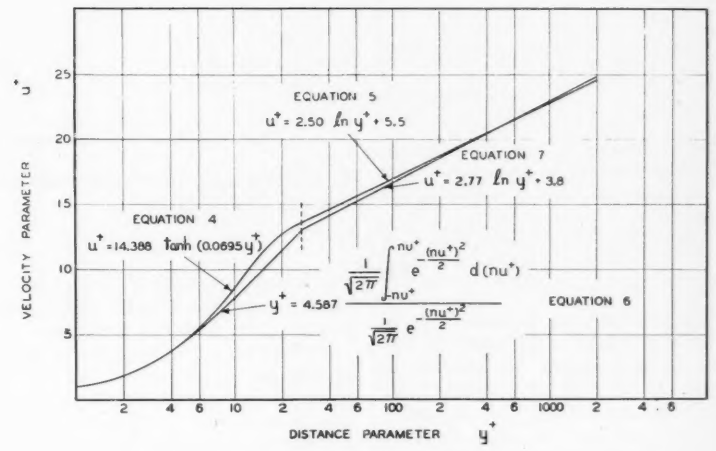

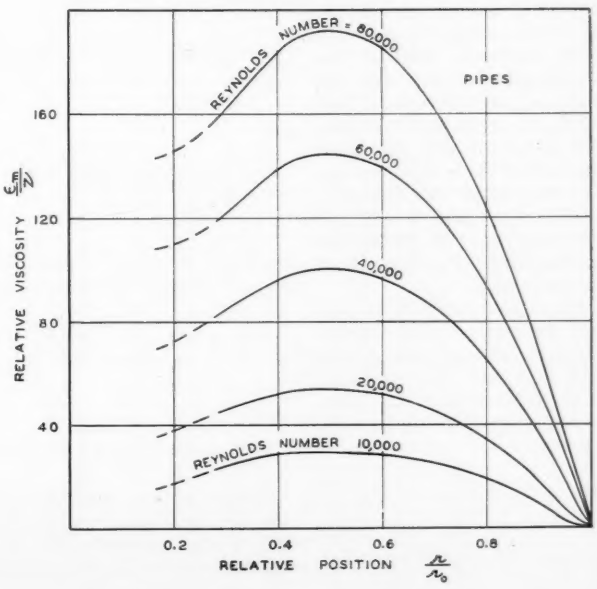

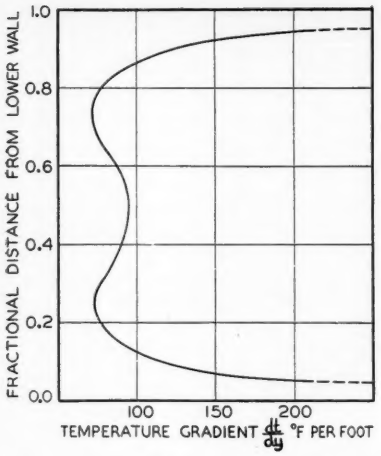

Fig. 7. Temperature gradients for steady uniform flow between parallel plates (upper wall at 105°F. and lower wall at 95°F.).

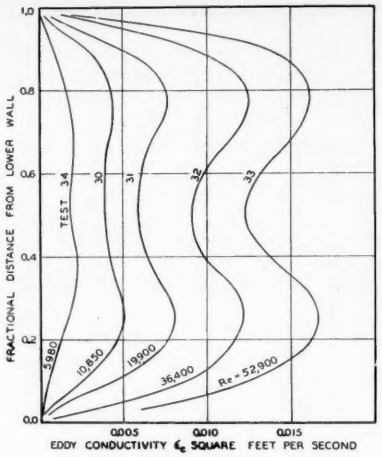

Fig. 8. Influence of Reynolds number upon eddy conductivity.

$$u^+ = \int_0^{y^+} \frac{dy^+}{(1 - \beta t^+)^d + n^2 u^+ y^+ (1 - e^{-(n^2 u^+ y^+)/(1-\beta t^+)^d})} \quad (9)$$

$$t^+ = \int_0^{y^+} \frac{dy^+}{\frac{1}{Pr_0} + n^2 u^+ y^+ (1 - e^{-(n^2 u^+ y^+)/(1-\beta t^+)^d})} \quad (10)$$

In the application of Equations (9) and (10) it was assumed by Deissler (*9*) that the variation in viscosity could be described by

$$\frac{\mu}{\mu_0} = (1 - \beta t^+)^d \quad (11)$$

The simplification of Equation (9) to the form of Equation (8) when the viscosity is independent of position is evident. Deissler (*8, 9*) discussed the underlying assumptions and boundary conditions involved in the foregoing equations. In the interest of brevity these matters have not been discussed in detail.

It should be realized that the preceding equations are applicable only for the higher Reynolds numbers and that significant errors may be introduced if they are employed for Reynolds numbers below about 20,000. In the following discussion it will be assumed that the relationships of u^+ and y^+ established experimentally as shown in Figures 1 and 2 apply at Reynolds numbers below 20,000 and as indicated in Equations (4) and (5) at higher Reynolds numbers.

The velocity-position data may be used in computing the eddy viscosity which has application in relating momentum transfer with heat and mass transfer. Von Kármán (*13*) defined an eddy viscosity for steady, uniform flow between parallel plates as

$$\epsilon_m = \frac{g\tau}{\sigma \frac{du}{dy}} - \nu = \frac{g \frac{\partial P}{\partial x}}{2\sigma \frac{\partial u}{\partial (y^2)}} - \nu \quad (12)$$

It is convenient to consider the total viscosity as defined by

$$\epsilon_m = \epsilon_m + \nu \quad (13)$$

The relative viscosity ϵ_m/ν may be calculated from the velocity distribution, pressure drop, and fluid properties.

At Reynolds numbers above 20,000 expressions which are based on the generalization shown in Equation (4) may be developed (*22*) for evaluation of the relative viscosity. At values of y^+ less than 26.7 there results

$$\frac{\epsilon_m}{\nu} = \frac{l}{l_0} \cosh^2 \left[0.0695 \left(\frac{l_0 - l}{\nu} \right) \sqrt{\frac{\tau_0 g}{\sigma}} \right] \quad (14)$$

or

$$\frac{\epsilon_m}{\nu} = \frac{l}{l_0} \cosh^2 \left[0.0695 \left(\frac{l_0 - l}{\nu} \right) U \sqrt{\frac{f}{2}} \right] \quad (15)$$

For larger values of y^+ the relative viscosity is obtained by use of Equation (5):

$$\frac{\epsilon_m}{\nu} = \frac{0.4}{\nu} \sqrt{\frac{\tau_0 g}{\sigma}} \left(\frac{l}{l_0} \right) (l_0 - l) \quad (16)$$

or

$$\frac{\epsilon_m}{\nu} = 0.4 \frac{U}{\nu} \sqrt{\frac{f}{2}} \left(\frac{l}{l_0} \right) (l_0 - l) \quad (17)$$

Deissler (*9*) also developed an expression for the relative viscosity near the wall of the conduit when considering constant physical properties of the fluid

$$\frac{\epsilon_m}{\nu} = \frac{\epsilon_m}{\frac{\mu_0}{\rho_0}} = n^2 u^+ y^+ (1 - e^{-n^2 u^+ y^+}) \quad (18)$$

If variation only in molecular viscosity is considered, the last term of Equation (18) becomes $e^{-n^2 u^+ y^+/(\mu/\mu_0)}$ where μ/μ_0 may be obtained by development of Equation (11).

The relative viscosity (*23*) in a circular conduit which is large in comparison with the thickness of the boundary layer is presented in Figure 6 for constant physical properties. It is apparent that both the Reynolds number and the position in the steady, uniform stream exert a pronounced influence upon the relative eddy viscosity. Again it is emphasized that for a Reynolds number below 20,000 the relative viscosity is subject to uncertainty as a result of the difficulty in predicting the velocity distribution with accuracy.

EDDY CONDUCTIVITY

After estimating values of the eddy viscosity, it is possible by making reasonable assumptions to use these data in establishing values of the analogous term for thermal transport, the eddy conductivity (*13*). Before such relations are considered, however, it is desirable first to consider the nature of the eddy conductivity. It has been defined in the following way:

$$\epsilon_c = -\frac{\mathring{Q}}{C_p \sigma} \frac{dy}{dt} - \mathrm{K}$$

$$= -\frac{\mathring{Q}}{C_p \sigma} \frac{dy}{dt} - \frac{k}{C_p \sigma} \quad (19)$$

Likewise, the total conductivity may be described as

$$\epsilon_c = \epsilon_c + \mathrm{K} = -\frac{\mathring{Q}}{C_p \sigma} \frac{dy}{dt} \quad (20)$$

Under steady, uniform conditions all the variables in Equations (19) and (20) may be measured directly. For example, the temperature gradient normal to the flow of air between parallel plates at a mean temperature of 100°F. is shown in Figure 7 for a gross velocity of 28.1 ft./sec. and a Reynolds number of 17,100. The average temperature gradient was 164.5°F./ft. Thermal flux may be readily measured under steady conditions by conventional calorimetric techniques. From such information it is possible to establish the eddy conductivity as a function of position in the stream and the Reynolds number by use of Equation (19). The results of these measurements (*19, 20*) for the flow of air between parallel plates are shown in Figure 8.

In the treatment of the relation between momentum transfer and heat transfer, the Prandtl number is often used as a means of correlating data. It is convenient to define three Prandtl numbers, one

relating to molecular transport, one to eddy transport, and one to the total transport. These are shown, respectively, in the following expressions:

$$Pr_m = \frac{\nu}{K} \tag{21}$$

$$Pr_e = \frac{\epsilon_m}{\epsilon_e} \tag{22}$$

$$\mathbf{Pr} = \frac{\xi_m}{\xi_c} = \frac{\epsilon_m + \nu}{\epsilon_c + K} \tag{23}$$

The effect of Reynolds number and position in the stream upon the total and

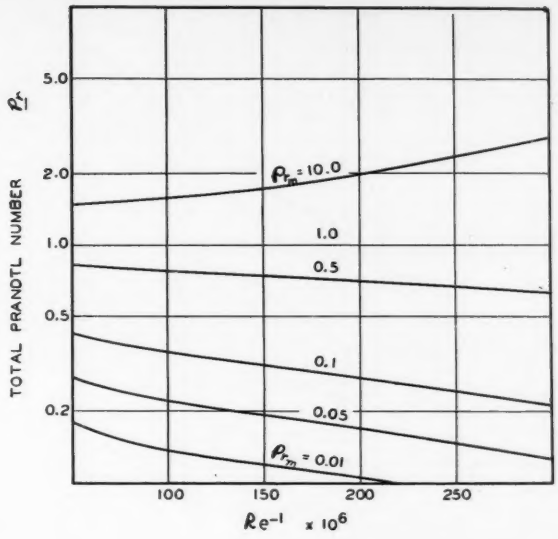

Fig. 9. Estimated effect of Reynolds number and molecular Prandtl number on total Prandtl number in turbulent core.

eddy Prandtl numbers was investigated for a stream of air (*20*). It was found in this case that the Prandtl numbers did not vary rapidly with position near the center of the stream and that for an increase in the Reynolds number the eddy Prandtl number gradually increased. More recent unpublished data for air under a slightly different level of turbulence, however, indicate the reverse trend at Reynolds numbers above 20,000. Rather complicated trends in the turbulent Schmidt number are also encountered with variations in conditions of flow. On the basis of the experimental evidence accumulated, it appears that the eddy

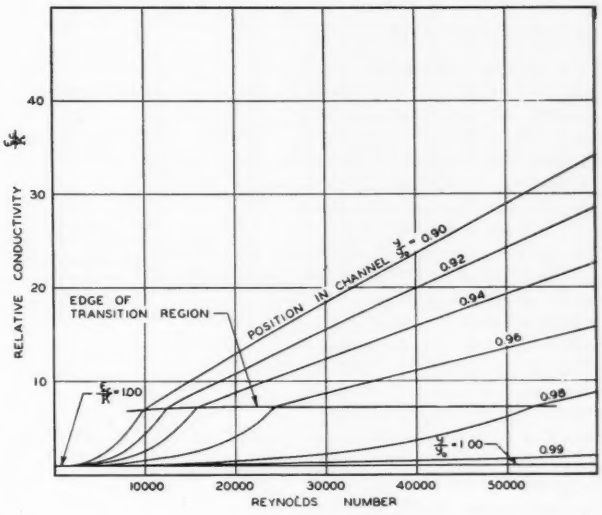

Fig. 10. Ratio of total to molecular conductivity on basis of Reynolds analogy.

Prandtl number for air is sensitive to the conditions of flow beyond those described by the gross Reynolds number. The primary uncertainty may well lie in the eddy viscosity, which is most sensitive to momentum transport.

The total Prandtl number is estimated to be a marked function of the Reynolds number (*20*) and the molecular Prandtl number, as shown in Figure 9. The trends as to the effect of the molecular Prandtl number shown here are based in a large measure upon theoretical considerations (*11*) and are subject to uncertainties.

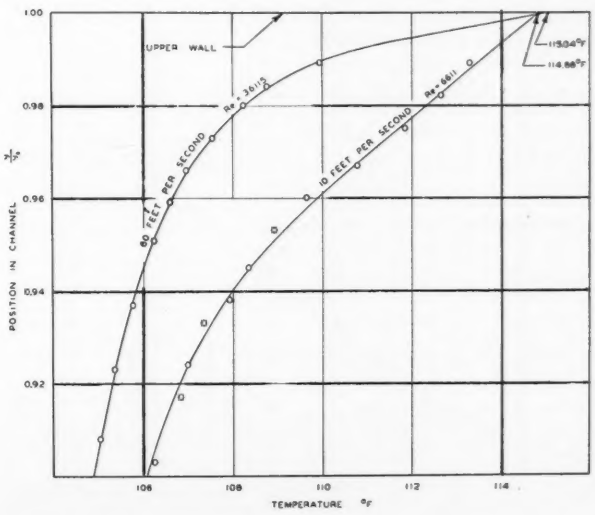

Fig. 11. Temperature distribution near wall.

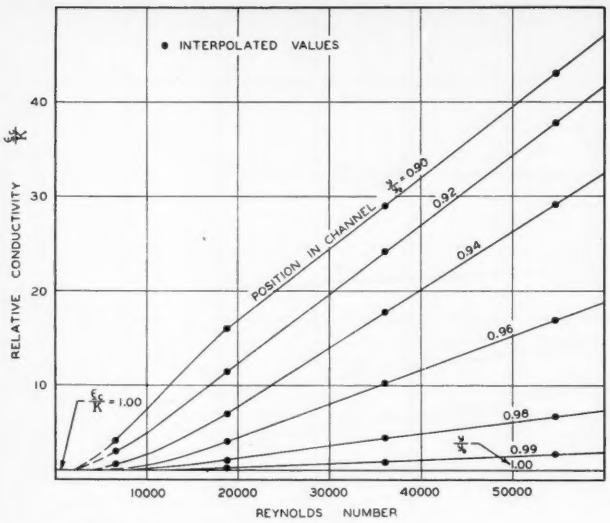

Fig. 12. Effect of Reynolds number upon relative conductivity.

BEHAVIOR IN THE BOUNDARY LAYER

It is obvious from the variations of the eddy conductivity with position that the greater part of the resistance to thermal transport is located near the boundary of the stream. From the characteristic transport of momentum in the boundary layer, which is presented in the first part of this discussion, the relative conductivity may be evaluated as a function of position and Reynolds number for that region, as shown in Figure 10. This figure assumes that the eddy conductivity and eddy viscosity are equal, which has been found not to be strictly true (*20*). However, the complex nature of turbulence near the boundary layer and the indication of marked deviations from isotropic behavior in this region introduce added uncertainties. For this reason it does not appear worth while to refine the information presented in Figure 10 by taking into account the deviations from Reynolds analogy (*20*). There is a marked effect of position in the channel on the relation between Reynolds number and the relative conductivity ϵ_c/K in steady, uniform flow.

The temperature variation (*3*) near the wall associated with the flow of air between parallel plates is shown in Figure 11. A marked effect of Reynolds number upon temperature distribution is evident. The relative conductivity based upon these experimental data (*3*) is shown in Figure 12 as a function of Reynolds number.

The total conductivity obtained experimentally is compared with the experimental and calculated total viscosities in Figure 13. It can be seen that there is a marked similarity between the curves for eddy conductivity and eddy viscosity. Because of the thicker boundary layer the curve for the calculated total viscosity at the lower Reynolds number does not show the discontinuity in slope as evidenced in the curve at the higher Reynolds number.

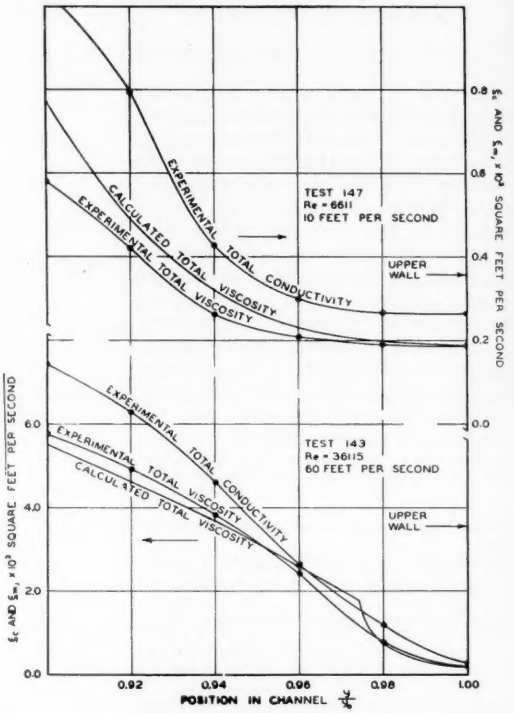

Fig. 13. Comparison of total conductivity and total viscosity.

It is of interest to compare the variation of the relative conductivity as a function of the distance parameter y^+. Such behavior is shown in Figure 14, where a relative conductivity term is plotted as a function of the distance parameter y^+.

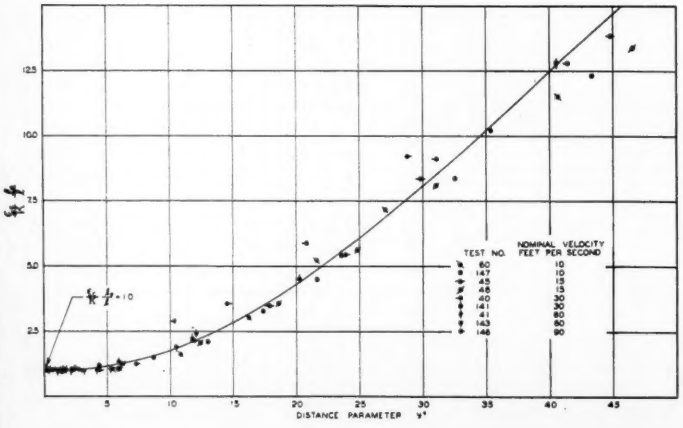

Fig. 14. Effect of distance parameter upon average relative conductivity.

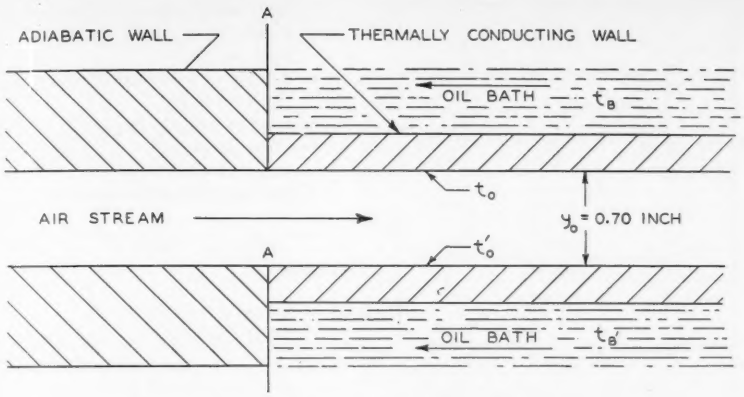

Fig. 15. Schematic diagram of two-dimensional air stream.

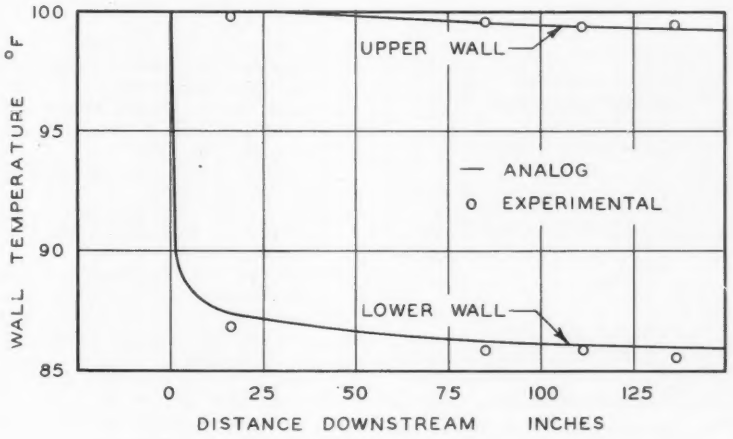

Fig. 16. Variation in wall temperatures with downstream position.

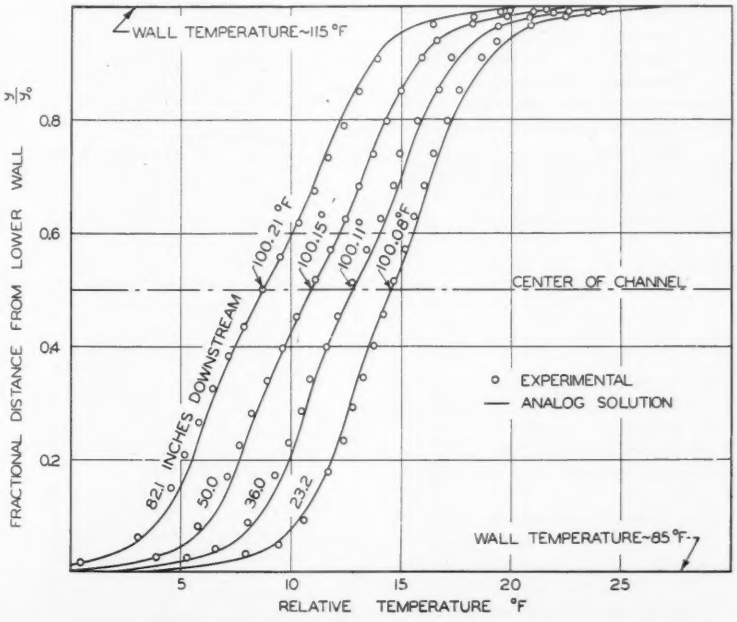

Fig. 17. Temperature distribution in flow channel with upper oil bath temperature at 115° F.

ESTIMATION OF TEMPERATURE DISTRIBUTION

It is often of interest to predict the temperature distribution in flow which is substantially uniform with regard to the transfer of momentum and nonuniform with respect to thermal transport. Such a situation is portrayed in Figure 15 for two-dimensional, steady, uniform flow between parallel plates. Under the circumstances the over-all energy balance may be expressed as

$$\frac{\partial \epsilon_c \dfrac{\partial T}{\partial y}}{\partial y} = u_x \frac{\partial T}{\partial x} \qquad (24$$

Equation (24) neglects the effect of changes in elevation, kinetic energy, and pressure upon the characteristics of the stream for both the gross and turbulent motion. This nonlinear equation may be solved by field methods or by an electrical analogue. It does not appear worth while to consider the details of the solution of this partial differential equation except to indicate that the resistance of the thermally conducting wall must be taken into account to establish the boundary conditions for the fluid. By use of the specific characteristics of a copper wall for a two-dimensional channel, the wall-temperature distribution was both calculated and measured as a function of downstream position as shown in Figure 16. It is apparent that the predicted and experimental wall temperatures were in satisfactory agreement. Comparisons of the predicted and calculated temperatures in the stream at several positions downstream for the same channel are shown in Figure 17, where good agreement between the experimental and predicted temperature distributions was obtained. In this instance the air was introduced at 100°F. and the upper and lower walls were at the indicated temperatures. The agreement of the experimentally determined and predicted temperatures with other boundary conditions is shown in Figure 18. In this case the air was introduced at 100°F., which corresponded to the upper wall temperature; whereas the lower wall was at 85°F., as before. Agreement was also obtained for this set of conditions. It is possible to predict the thermal flux at the wall by integration of Equation (24) for specific boundary conditions. Under these circumstances the gross heat-transfer coefficient based upon the bulk temperatures of the stream has been calculated for comparison and is shown in Figure 19. At the transition from the adiabatic to the conducting wall a rapid change in conditions takes place and the actual thermal transfer coefficient is large. However, the coefficient approaches a uniform value at a downstream distance approximately equal to forty times the channel height and is in good agreement with predictions made by methods described by McAdams (*17*).

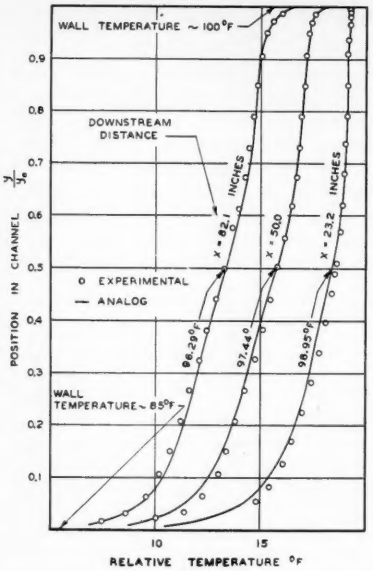

Fig. 18. Temperature distribution in flow channel with upper oil bath temperature at 100° F.

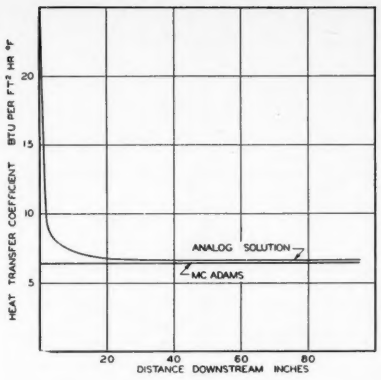

Fig. 19. Thermal transfer coefficient near entrance to flow channel.

ACKNOWLEDGMENT

Figures 1 to 4, 6, 7, and 10 to 18 are reprinted by permission of the copyright owner, *Industrial and Engineering Chemistry*. Figure 19 is reprinted by permission of the copyright owner, Institution of Mechanical Engineers, London, England. B. Lawson Miller assisted in the assembly of the manuscript and L. Fay Prescott reviewed the finished copy.

NOTATION

A, B = constants
C = constant of integration
C_p = isobaric heat capacity, ft./°F.
d = differential operator
e = base of natural logarithms
f = friction factor
g = acceleration due to gravity, ft./sec.²
K_1, K_2 = constants of proportionality
k = thermal conductivity, ft./(sec.)(ft.)(°F.)
l = distance from center of channel, ft.
l_0 = distance from center of channel to wall, ft.
ln = natural logarithm
n = constant of proportionality taken as 0.109
P = pressure, lb./sq. ft.
Pr = total Prandtl number
Pr_e = eddy Prandtl number
Pr_m = molecular Prandtl number
Pr_0 = Prandtl number with properties evaluated at t_0
$\mathring{Q}$ = thermal flux, lb./(ft.)(sec.)
r = radius, ft.
r_0 = radius of conduit, ft.
Re = Reynolds number
T = absolute temperature, °R.
t = temperature, °F.
t^+ = temperature parameter,

$$\frac{(t_0 - t)C_p g \tau_0}{\mathring{Q}\sqrt{\frac{\tau_0}{\rho_0}}} = \frac{1 - \frac{t}{t_0}}{\beta}$$

t_B = temperature of bath, °F.
t_0 = temperature of wall, °F.
U = gross velocity, ft./sec.
u = point velocity, ft./sec.
u_* = friction velocity, $\sqrt{\tau_0 g/\sigma}$, ft./sec.
u^+ = velocity parameter defined by Equation (2)
u_d = velocity deficiency defined by Equation (3)
u_m = maximum velocity, ft./sec.
u_x = velocity in x direction, ft./sec.
x = downstream distance, ft.
y = distance from wall, ft.
y^+ = distance parameter, defined by Equation (1)
y_d = distance from nearest wall, ft.
y_0 = separation of plates, ft.
β = heat transfer parameter,

$$\frac{\mathring{Q}\sqrt{\frac{\tau_0}{\rho_0}}}{C_p g \tau_0 t_0}$$

ϵ_c = eddy conductivity, sq. ft./sec.
$\underline{\epsilon}_c$ = total conductivity, $(\epsilon_c + \mathrm{K})$, sq. ft./sec.
ϵ_m = eddy viscosity, sq. ft./sec.
$\underline{\epsilon}_m$ = total viscosity, $(\epsilon_m + \nu)$, sq. ft./sec.
K = thermometric conductivity, sq. ft./sec.
μ = absolute viscosity of fluid, (lb.)(sec.)/sq. ft.
μ_0 = absolute viscosity of fluid evaluated at t_0, (lb.)(sec.)/sq. ft.
ν = kinematic viscosity, sq. ft./sec.
ν_0 = kinematic viscosity evaluated at wall, sq. ft./sec.
ρ_0 = density of fluid evaluated at wall, (lb.)(sec.²)/ft.⁴
σ = specific weight, lb./cu. ft.
τ = shear, lb./sq. ft.
τ_0 = shear at wall, lb./sq. ft.
∂ = partial differential operator

Superscripts

d = viscosity exponent
$'$ = lower oil bath

LITERATURE CITED

1. Bakhmeteff, B. A., "The Mechanics of Turbulent Flow," Princeton University Press, Princeton (1941).
2. Batchelor, G. K., "The Theory of Homogeneous Turbulence," University Press, Cambridge (1953).
3. Cavers, S. D., N. T. Hsu, W. G. Schlinger, and B. H. Sage, *Ind. Eng. Chem.*, **45**, 2139 (1953).
4. Corssin, S., *J. Aero. Sci.*, **18**, 417 (1951).
5. *Ibid.*, **22**, 469 (1951).
6. ———, *Proc. Third Midwestern Conference on Fluid Mechanics*, p. 435, Univ. Minnesota (1953).
7. Davis, L., *Jet Propulsion Lab. Rept.* 3-22, Pasadena, Calif. (1950).
8. Deissler, R. G., *Natl. Advisory Comm. Aeronaut., Tech. Note* 2138 (1950).
9. *Ibid.*, 3145 (1954).
10. Dunn, L. G., W. B. Powell, and H. S. Seifert, paper at Roy. Aeronaut. Soc., Third Anglo-American Aeronaut. Conf. (1951).
11. Jenkins, R., Ph.D. thesis, Calif. Inst. Technol., Pasadena, Calif. (1950).
12. Kármán, von, Th., *J. Aero. Sci.*, **1**, 1 (1934).
13. ———, *Trans. Am. Soc. Mech. Engrs.*, **61**, 705 (1939).
14. ———, and L. Howarth, *Proc. Roy. Soc. (London)*, **A164**, 192 (1938).
15. Laufer, J., *Natl. Advisory Comm. Aeronaut., Tech. Note* 2123 (1950).
16. *Ibid.*, 2954 (1953).
17. McAdams, W. H., "Heat Transmission," McGraw-Hill Book Company, Inc., New York (1942).
18. Nikuradse, J., *Forsch. Gebiete Ingenieurw., Forschungsheft 356* (1932).
19. Page, F., Jr., W. H. Corcoran, W. G. Schlinger, and B. H. Sage, *Am. Doc. Inst.*, Washington, D. C., Doc. 3293 (1950).
20. ———, *Ind. Eng. Chem.*, **44**, 419 (1952).
21. Page, F., Jr., W. G. Schlinger, D. K. Breaux, and B. H. Sage, *Am. Doc. Inst.*, Washington, D. C., Doc. 3294 (1951).
22. Schlinger, W. G., V. J. Berry, J. L. Mason, and B. H. Sage, *Ind. Eng. Chem.*, **45**, 662 (1953).
23. Schlinger, W. G., and B. H. Sage, *Ind. Eng. Chem.*, **45**, 2636 (1953).
24. Skinner, G., thesis, California Inst. Technol., Pasadena, Calif. (1950).
25. Taylor, G. I., *Advisory Comm. Aeronaut. (London), Tech. Rept.* 2, 423 (1916–17).
26. Uberoi, M. S., *Natl. Advisory Comm. Aeronaut., Tech. Note* 1865 (1949).

Fluid Flow in Simulated Fractures

J. L. HUITT

Magnolia Petroleum Company, Dallas, Texas

Fractures in some petroleum reservoirs often play an important role in the production of fluid from the pay formation. In fact, in some cases the oil or gas could not be produced economically in the absence of fractures functioning as principal conduits for transporting the fluids from the reservoir to the well bore. On occasions, special well treatments designed to induce fractures, to widen fractures, and/or to extend existing fractures are employed in oil wells.

The flow of a fluid in fractures in the vicinity of the well bore may be of either a viscous or a turbulent type, depending upon the fluid properties and the conditions prevailing in the fractures. It is the purpose of this paper to present correlations of the fluid properties and conditions prevailing in simulated fractures so that engineering flow calculations for the single-phase flow of Newtonian fluids in actual fractures may be made more expediently than at present.

For present purposes a fracture is defined as a three-dimensional conduit; that is, it has length, width, and depth. The flow within the fracture is considered unidirectional and steady state and is treated similarly to the flow between two parallel plates. Any surface irregularity extending from the surface of a plate is designated as surface roughness. For the case of packed fractures, such as those filled with sand or similar granular material, the flow problem is considered analogous to that encountered in packed columns.

RELATED STUDIES

A survey of the literature reveals many studies that are related to, but not directly concerned with, fluid flow in fractures. An equation for viscous flow between parallel plates which may be used to simulate the geometry of a fracture may be written as

$$Q = \frac{\Delta P g_c b W_f^3}{12 \mu l_f} \qquad (1)$$

Lamb (*13*) states that Equation (1) is approximately valid even if the interval W_f between the two surfaces is variable, provided that the gradient dW_f/dl_f is small and, even if both surfaces are curved, provided that W_f is small compared with the radii of curvature.

Another means of describing fluid flow behavior in fractures is in terms of a Fanning-type friction-factor plot, in which the Reynolds number

$$Re = \frac{2 W_f U \rho}{\mu} \qquad (2)$$

is correlated with the friction factor

$$f = \frac{\Delta P g_c W_f}{l_f \rho U^2} \qquad (3)$$

Under conditions of viscous flow in fractures, it may be shown that the friction factor and Reynolds number have the relation

$$f = \frac{24}{Re} \qquad (4)$$

Davies and White (*7*) in experimenting with variable-width rectangular pipes as water conduits found that Equation (4) did not hold for Reynolds numbers above 1,800. The reported data covered a Reynolds number range of 60 to 4,500. Page et al. (*16*) in a study of temperature gradients in turbulent gas streams flowing between parallel glass plates reported flow data in the Reynolds number range of 7,000 to 60,000. The data and correlations of these two studies cover a sufficiently wide range of flow conditions to be adequate to describe the flow in most smooth-surface fracture systems.

The flow of a fluid in rough-surface conduits has been under study for a considerable period of time. However, very little of this work has dealt with conduits resembling fractures. Darcy (*6*) was one of the first to recognize that the nature of the wall of a pipe affected the flow. Bazin (*1*) continued the experiments of Darcy and developed empirical equations relating the flow to surface conditions of specific materials. Stanton (*18*) worked with two pipes of different size, the inner surfaces of which were threaded so that the surface-roughness-to-diameter ratio was the same, and from these experiments concluded that the Reynolds number concept held for flow in such rough-surface pipe. Although the friction factor and Reynolds number for flow in these two particular pipes agreed, the friction factor for a corresponding Reynolds number in a smooth-surface pipe was lower at large Reynolds number values. Schiller (*17*), in working with brass tubes threaded similarly to those used by Stanton, studied the flow behavior in the critical region of flow and concluded that the critical Reynolds number was independent of the surface roughness of the pipe. This conclusion, however, was based on a limited degree of surface roughness. Mises (*14*) in an attempt to correlate the existing published data introduced the term *relative roughness*, which is the ratio of the arithmetic mean elevation of surface roughness to the radius of the pipe. The resulting empirical correlations gave the resistance to flow as a function of both the Reynolds number and the relative roughness. Hopf (*10*) used rectangular conduits made from sheets of various smooth- and rough-surface materials to study the effect of surface roughness on flow behavior. For flow at sufficiently large Reynolds numbers, the following expression for the Fanning-type friction factor was offered:

$$f = 0.04 \left(\frac{z}{r}\right)^{0.314} \qquad (5)$$

The most recent and exhaustive study is that of Nikuradse (*15*), who investigated the relative roughness effect of artificially roughened pipe surfaces. A coating of lacquer to which sand grains adhered served as the surface. For viscous flow in the rough-surface pipe, the equation for flow in smooth surface pipe was adequate, which expressed in terms of the Fanning-type friction factor is

$$f = \frac{16}{Re} \qquad (6)$$

[It should be noted that Equation (6) for circular conduits has the constant 16 and that Equation (4) for fractures has the constant 24.] For complete turbulence and sufficiently large Reynolds numbers, the friction factor proposed by Nikuradse for flow in rough-surface pipe is

$$f = \frac{1}{4\left(1.74 + 2 \log \frac{r}{z}\right)^2} \qquad (7)$$

The above-reported studies of rough surfaces, although adequate for flow

Present address is Gulf Research and Development Company, Pittsburgh, Pennsylvania.

calculations involving large-diameter pipes, are not conclusive for use in calculations involving fractures with widths of the order of a millimeter or less.

Another condition that may affect fluid flow in some fracture systems, particularly in oil-production practice, is the presence of granular material such as sand, which may be placed there as a propping agent to maintain a fracture in an "open" condition under the existing high overburden pressures. In many respects a fracture packed with sand resembles a packed column; thus, the studies of flow through beds of solids have offered some information useful in a study of packed fractures. One of the first to treat the flow in a packed column as similar to the flow in a pipe was Blake (*2*), who proposed a modified Reynolds number in which D_p/ϵ replaced the diameter in pipe-flow calculations. Using this parameter, he found that the pressure loss through the packing was inversely proportional to ϵ^3. In similar studies Burke and Plummer (*3*) reported that at high rates of flow the resistance to flow was proportional to $(1 - \epsilon)/\epsilon^3$, and Kozeny (*12*) reported that at low rates of flow the resistance to flow was proportional to $(1 - \epsilon)^2/\epsilon^3$.

Carman (*4*) showed that at low rates of flow the Blake method of correlation led to the equation offered by Kozeny, namely,

$$\frac{\Delta P g_c}{l} = C_1 \frac{(1 - \epsilon)^2}{\epsilon^3} \frac{\mu U}{D_p^2} \qquad (8)$$

Also, at high rates of flow the Blake method of correlation led to the equation reported by Burke and Plummer, which is

$$\frac{\Delta P g_c}{l} = C_2 \frac{(1 - \epsilon)}{\epsilon^3} \frac{\rho U^2}{D_p} \qquad (9)$$

Later Ergun (*8*) showed that for all rates of flow, Equations (8) and (9) were additive. He proposed the equation

$$\frac{\Delta P g_c}{l} = 150 \frac{(1 - \epsilon)^2}{\epsilon^3} \frac{\mu U}{D_p^2} + 1.75 \frac{(1 - \epsilon)}{\epsilon^3} \frac{\rho U^2}{D_p} \qquad (10)$$

from which the Blake-type friction factor is

$$f = 1.75 + 150 \frac{(1 - \epsilon)}{Re} \qquad (11)$$

Equations (10) and (11) are valid for flow in columns packed with solids; however, for flow in a packed fracture where the particle diameter is of the same order of magnitude as the fracture, the validity of the equations has not been established.

Studies reported in the literature adequately cover the flow in conduits usually encountered; however, the use of the reported data to anticipate the flow behavior in a conduit resembling a fracture was considered questionable. Therefore, the study reported in this paper was undertaken to provide the necessary data so that the flow in fractures might be treated similarly to the flow in pipes or in packed columns, as the specific condition in the fracture required.

Fig. 1. Flow cell for rough-surface fracture only.

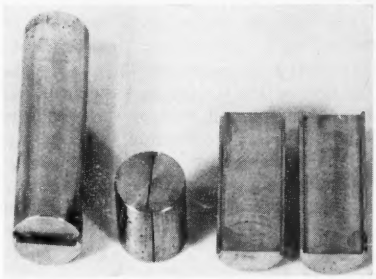

Fig. 2. Steel plugs for simulated fractures.

EXPERIMENTAL METHODS*

Fractures in oil reservoirs may vary widely in the characteristics that define the flow within the fractures. Inasmuch as it was necessary in this study to control the characteristics of the fracture as well as the other variables in the flow system, the fractures were formed in such a manner that all the pertinent variables might be controlled. The flow cell shown in Figure 1 was used for the study of flow in planar fractures. The surfaces which formed the boundaries of the flow cell were coated with a layer of shellac (1 part shellac, 1 part methyl alcohol) by submerging the surfaces in the liquid and then allowing the excess shellac to drain from the surface. Close-cut fractionized sand was sprinkled on the shellacked surface through a sieve screen. The sand grain size was predetermined experimentally by a three-dimensional measurement method (*11*) for each particular sand fraction. The shellac was allowed to dry for about 12 hr. before the surfaces were observed under a microscope for uniformity. For a surface to be used in the flow study, the sand grains covered 40 to 60% of the shellacked surface with no sand particle resting on top of another. Repeated micrometer measurements of the shellacked portion of the surface showed that the shellac film thickness was about 0.01 mm. Upon examination of the surfaces, it appeared that the sand grains were partially immersed in the shellac; for calculation purposes it was assumed that the grains rested on the steel surfaces.

Flow experiments for rough-surface fractures were for the most part performed with air as the fluid at room temperature and atmospheric pressure. Several "calibration runs" were made at the lower flow rates by

*Experimental data are available as document 4832 from the American Documentation Institute, Photoduplication Service, Library of Congress, Washington 25, D. C., for $1.25 for photoprints or 35-mm. microfilm.

use of water, mineral oil, and Soltrol-C (a narrow-boiling-range petroleum fraction resembling kerosene). Flow rates were observed at various differential pressures over a 5.08-cm. test section of the fracture, which was 13.3 cm. in over-all length. The test section was 7.0 cm. from the fluid entrance to the fracture and 1.22 cm. from the exit. Flow data were obtained for fracture widths of 1.58 to 3.74 mm. and surface roughnesses of 0.167 to 0.247 mm. The resulting relative surface roughnesses (z/W_f) were 0.0446 to 0.156. The depth of the fracture in each case was 3.75 cm.

For the study of flow in packed fractures, flat-faced half sections of steel plugs from 2.56 to 7.63 cm. in length were spaced with thin steel plates of sheet metal (shim stock material) and the open section thus formed was packed with fractionized sand samples of predetermined particle diameter. The steel plugs are shown in Figure 2. The average particle diameter of the sand fraction was determined in the following manner. Sand particles of a particular fraction were counted (200 to 2,000) with the aid of a microscope and weighed to determine the number of particles per gram of sand. The particle volume per gram of sand was obtained by measuring the volume of water displaced by a given bulk volume (and weight) of sand in an ordinary burette. The particles were considered as spheres and the average particle diameter was calculated. The bulk volume of the sand was measured in the burette at the time the particle volume was measured. The porosity of the bulk sand was calculated from the particle volume and the bulk volume of the sand.

The fracture of known width was packed with the sand, and the steel plug was tapped to settle the sand in the fracture. The sand was wetted with the fluid to be used in the flow study with further tapping of the plug to ensure close packing of the sand within the fracture. During the packing of the fracture, and during the subsequent flow study, the downstream end of the fraction was "blocked" by a wire screen to retain the sand in the fracture.

The plug was placed in a Hassler-type flow cell for the flow study. After the completion of the flow experiments, the sand pack was removed and dried, and the sand particle volume determined. With the volume of the fracture known, the porosity of the sand pack was calculated.

Flow data were obtained for air, water, a mineral oil, and Soltrol-C in fractures of 0.356- to 1.47-mm. widths. The average particle diameter of the various sand packs varied from 0.111 to 0.803 mm. The resulting particle-diameter–to–fracture-width ratios were 0.084 to 0.78. In each case the fracture depth was 1.85 cm.

A limited amount of flow data on water and Soltrol-C were obtained in a radial flow system using sand packs between circular glass plates 27 cm. in diameter. The plates were oriented in a horizontal plane and fluid entry was through a 7-mm.-diameter hole in the center of one of the plates. The fracture was packed during the flowing of the fluid from the center to the circumference of the fracture. Sand packs having average particle diameters of 0.708 and 0.409 mm. were used in fractures of widths 0.80 and 1.4 mm., respectively The method of obtaining the porosities was the same as previously described.

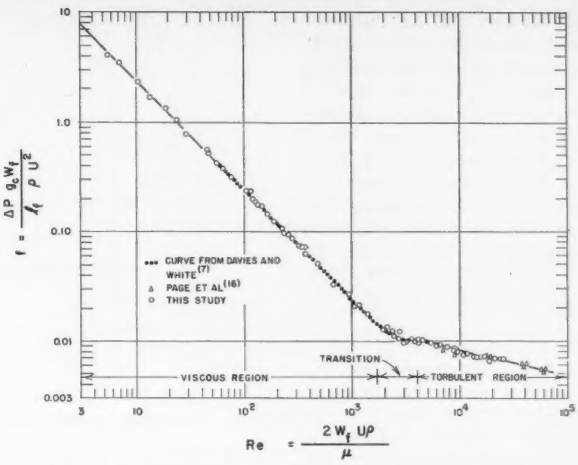

Fig. 3. Friction-factor–Reynolds-number relation for flow in smooth-surface fractures

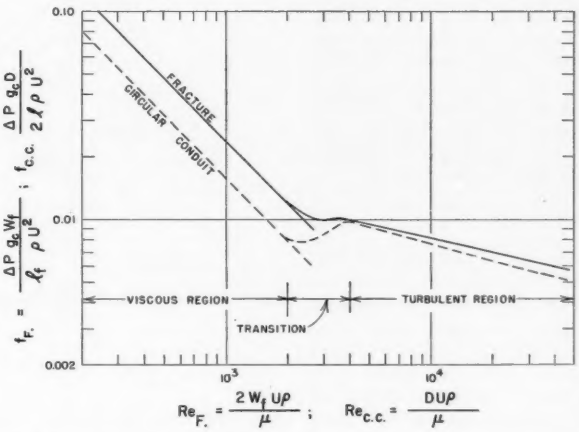

Fig. 4. Friction-factor–Reynolds-number relation for flow in smooth fractures and circular conduits.

DISCUSSION

Previously reported data (*7, 16*) are considered adequate for flow calculations involving fractures possessing smooth surfaces. These reported data are compared in Figure 3 with data obtained from this study. The agreement substantiates the conclusion of Davies and White (*7*) that there is departure from viscous flow at a Reynolds number of about 1,800 and that full turbulence is manifested at about 4,000 and above.

A comparison of flow in a fracture and a circular conduit is made in Figure 4. It is assumed here that the equivalent diameter of a fracture (for use in calculating the Reynolds number) approaches twice the width of the fracture if the depth is large in comparison with the width. For corresponding Reynolds numbers, the friction factors for flow in fractures are higher than for flow in circular conduits; however, at the lowest point where full turbulence is manifested in both systems (*Re* of about 4,000) the friction factors are approximately the same.

Figure 5 shows the friction factors calculated from experimental flow data obtained with rough surface fractures of various relative roughnesses. As was mentioned previously, 40 to 60% of each plate area forming the fracture was "covered" with the sand particles, which provided roughness to the fracture surface. This range of roughness was chosen because it is believed that when a rock is ruptured the roughness of each of the two surfaces forming the resulting fracture would be about the same.

In the viscous flow region the line calculated by Equation (4), which describes the friction factor f at different Reynolds numbers *Re* shows good agreement with

the experimental flow data. In the Reynolds number range of 1,800 to 4,000 the flow is erratic and in some cases the calculated f values lie on the smooth-surface curve up to Reynolds numbers of about 3,000; in other cases the f values show an increase above a Reynolds number of 1,800. With the particular apparatus used in the flow studies, this behavior was probably due to the eddy currents caused by the fluid entrance to the fracture still existing as the fluid flowed through the test section of the fracture.

For relative surface roughnesses (z/W_f) above 0.10, once turbulence is established, the friction factors f are relatively insensitive to higher rates of flow. At z/W_f values below 0.10 investigated in this study, f values in the turbulent range increase slightly above the values established at the beginning of turbulence. It appears that at Reynolds numbers above 20,000, the curves describing the friction factors effective for the various relative roughnesses studied would be parallel.

Friction factors for flow in rough-surface fractures are compared with those of Nikuradse (*15*) for circular conduits in Figure 6. At sufficiently large Reynolds numbers where f is dependent only on z/W_f, an empirical relation obtained from the flow data on fractures is

$$f = 0.055(z/W_f)^{0.472} \qquad (12)$$

In comparison of f values obtained with Equations (5), (7), and (12) the agreement is within 15%; however, none of these equations are valid when f is dependent on both the Reynolds number and the relative surface roughness. This condition is usually obtained with small relative surface roughness at low Reynolds numbers in the turbulent region of flow. An extrapolation of the curves for the various z/W_f values of the fractures to the lower range of Reynolds numbers is not attempted. However, from Schiller's (*17*) work, which reported that large increases in the friction factor for high relative roughnesses are produced immediately after complete turbulence is developed, it would be expected that the extrapolations would probably join the smooth-surface, friction-factor curve at a Reynolds number of about 3,500.

In Figure 7 a comparison of the friction factors calculated from experimental flow data on packed fractures is made with those predicted by Equation (11). The correlation parameters used in the calculations are essentially the same as those first proposed by Blake (*2*), namely, the friction factor

$$f = \frac{\Delta P g_c D_p \epsilon^3}{l_f \rho U^2 (1 - \epsilon)} \qquad (13)$$

and the modified Reynolds number

$$Re = \frac{D_p U \rho}{\mu_{(1-\epsilon)}} \qquad (14)$$

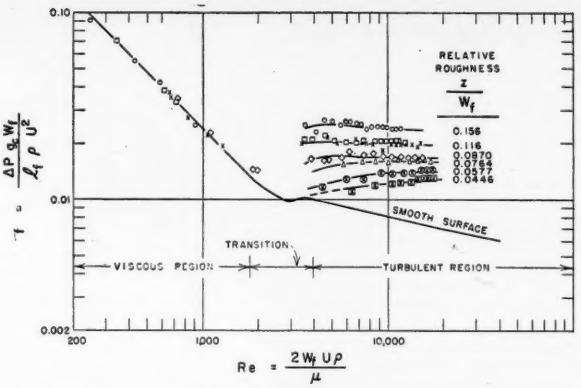

Fig. 5. Friction-factor–Reynolds-number relation for flow in rough-surface fractures.

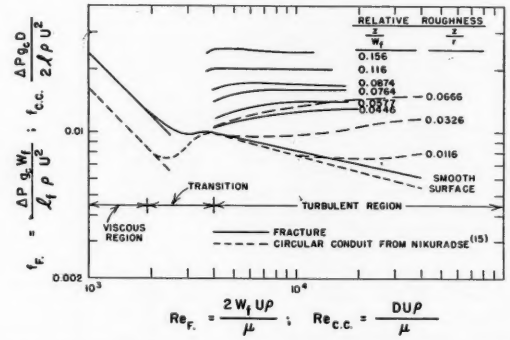

Fig. 6. Friction-factor–Reynolds-number relation for flow in fractures and circular conduits.

The values of the friction factor f calculated from flow data are higher than those calculated with Equation (11) in the Reynolds number range of 5 to 100, but the agreement is good at Reynolds numbers below or above this range. The higher values of the friction factor could be due to the flow discontinuity at the entrance to the sand pack. For Reynolds numbers less than 10 the kinetic energy effects can be neglected, which results in Equation (10) reducing to Equation (8). Also, for Reynolds numbers greater than 1,000 the viscous energy effects can be neglected and Equation (10) becomes the same as Equation (9). In the Reynolds number range of 10 to 1,000, both the viscous and kinetic energy effects must be considered, in which case only Equation (10) is adequate.

The sand-pack porosities used in the friction-factor calculations were those obtained from the correlation shown in Figure 8. The porosity ϵ_f exhibited by the sand in the fracture was as much as 1.4 times greater than the bulk porosity ϵ. The dependence of porosity on the ratio D_p/W_f is somewhat similar to that described by Furnas (*9*) for the wall effect in packed columns; however, in most cases the ratio D_p/W_f is greater in fractures that that reported by Furnas on columns. The largest size sand fraction used in this study was 20–35 mesh and the smallest was 120–200 mesh (U. S. sieve series). The bulk-sand porosity values ϵ ranged from 35 to 41 vol. %; the sand porosity in fractures ranged from 38 to 52 vol. % in fracture widths of 0.64 to 1.47 mm. In cases where D_p/W_f is less than about 0.1, ϵ_f and ϵ are the same. For D_p/W_f ratios above 0.1 it is necessary to know the value of ϵ_f. Provided that the true value for ϵ_f is used, the Ergun (*8*) equation appears adequate for flow calculations involving sand packs in fractures.

Figure 7 also allows comparison to be made of friction factor values calculated from flow data using a radial flow system of sand packs between glass plates with those values predicted by Equation (11). The data are limited, owing to the low differential pressures necessary with the apparatus. For the case of radial flow, l_f becomes the difference between the radius of the glass plates and the radius of the inlet. Also, the bulk velocity is based on the log mean flow area of the empty fracture, in which case

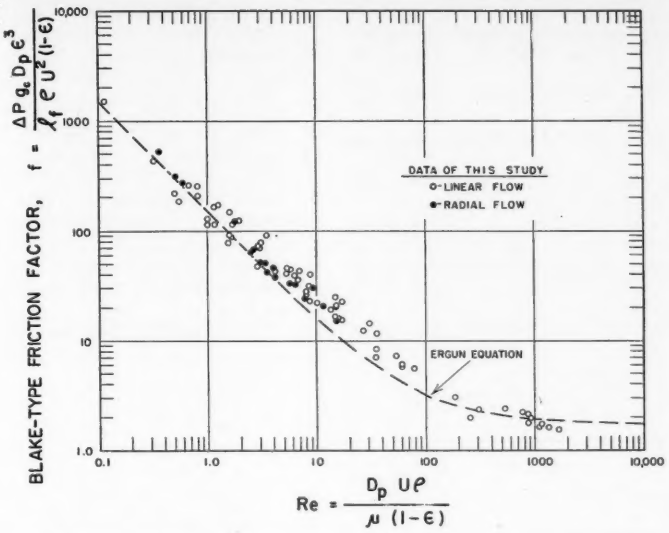

Fig. 7. Blake-type friction-factor–Reynolds-number relation for flow in fractures.

$$U = \frac{Q}{A_m} = \frac{Q}{W_f\left(\frac{2\pi[R - R_w]}{\ln \frac{R}{R_w}}\right)} \quad (15)$$

With these modifications the correlation parameters used are the same as Equations (13) and (14). As in the case of linear flow, the agreement between the friction factor calculated from flow data and predicted with Equation (11) is good; however, above *Re* of 5 the friction factor calculated from flow data is somewhat larger in the range of *Re* studied.

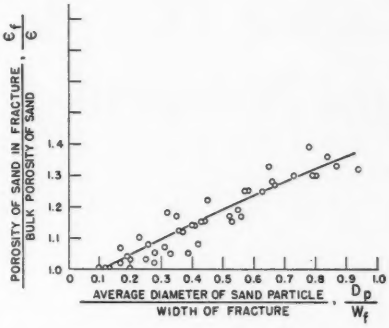

Fig. 8. Porosity–particle-diameter–fracture-width relation.

APPLICATIONS

One of the primary uses for the information presented in this investigation is in the engineering analysis of flow problems in fractured reservoirs. It is realized that values for some of the variables which are relatively easy to measure in the laboratory cannot be determined for an oil reservoir by the present methods of analysis; however, with the use of information presented here, useful approximations can be made for various reservoir problems involving fractures.

The "propping" of induced and widened fractures with sand has received considerable attention in recent years (*5*). The propping agent would rarely form a pack throughout the entire fracture; however, as a limiting case the flow calculations made on a sand pack in a fracture could serve as a model to describe the nature of flow that might be expected under certain reservoir conditions.

It is considered likely that the normal production rates from oil wells rarely create turbulent flow in planar fractures; however, during hydraulic well-treatment processes, and under some of the more unusual production conditions, it is probable that turbulent flow exists in the fractures in the vicinity of the well bore. As shown in Figure 5, surface roughness plays an important part in the flow calculations. A laboratory flow experiment employing both viscous and turbulent flow conditions with a formation core sample containing a fracture of known or measurable width could produce data useful in estimating surface-roughness characteristics of reservoir fractures.

SUMMARY AND CONCLUSIONS

The results reported in the literature cited in this paper together with the new data obtained from the study reported here show that fluid flow in fractures can be treated similarly to fluid flow in circular conduits and that satisfactory friction-factor correlations permitting engineering flow calculations for fractured systems result. The principal conclusions that may be drawn are

1. Viscous flow in planar fractures is limited to Reynolds numbers of less than 1,800. The surface roughness has no appreciable effect upon the resistance to flow when the flow is of a viscous nature.
2. Flow in planar fractures departs from viscous flow at a Reynolds number of about 1,800, but the flow does not become completely turbulent until a Reynolds number of about 4,000 is exceeded.
3. In the region of turbulent flow the effect of surface roughness becomes prominent. The extent to which the friction factor is controlled by the surface roughness is dependent on the relative surface roughness and the Reynolds number.
4. The flow in packed fractures can be treated similarly to flow in a packed column. The porosity exhibited by the sand pack in the fracture is dependent on the ratio of the particle diameter to fracture width. By use of an appropriate porosity value, flow calculations can be made adequately with the Ergun (*8*) equation.

ACKNOWLEDGMENT

The author wishes to express appreciation to Magnolia Petroleum Company for the permission to publish this manuscript and to express gratitude to his fellow workers for their constructive advice during the study and preparation of the manuscript.

NOTATION

A_m = log mean cross-sectional flow area
b = depth of fracture
C_1, C_2 = constants
D = diameter of circular conduit
D_p = average diameter of particles, if the particles are assumed to be spheres
f = friction factor, as defined by the appropriate equation for the existing conditions
g_c = mass-force conversion factor
l = length of circular conduit
l_f = length of fracture
ΔP = pressure differential (force units)
Q = volumetric flow rate
r = radius of circular conduit
R_w = radius of source of fluid
R = radius of sump for fluid
Re = Reynolds number, as defined by the appropriate equation for the existing conditions
U = bulk average velocity, based on empty conduit
W_f = width of fracture
z = height of surface roughness
z/r, z/W_f = relative surface roughness
ϵ = bulk porosity exhibited by a bed or sand pack as determined in a porosimeter
ϵ_f = porosity exhibited by sand pack in a fracture
μ = absolute viscosity of fluid
ρ = density of fluid

LITERATURE CITED

1. Bazin, H., *Mémoires à l'Académie des Sciences de l'Institute de France*, **32**, No. 6 (1902).
2. Blake, F. E., *Trans. Am. Inst. Chem. Engrs.*, **14**, 415 (1922).
3. Burke, S. P., and W. B. Plummer, *Ind. Eng. Chem.*, **20**, 1196 (1928).
4. Carman, P. C., *Trans. Inst. Chem. Engrs.*, **15**, 150 (1937).
5. Clark, J. B., *Trans. Am. Inst. Mining Met. Engrs.*, **186**, 1 (1949).
6. Darcy, H., *Mémoires à l'Académie des Sciences de l'Institute imperial de France*, **15**, 141 (1858).
7. Davies, S. J., and C. M. White, *Proc. Roy. Soc. (London)*, **119A**, 92 (1928).
8. Ergun, S. K., *Chem. Eng. Progr.*, **48**, 89 (1952).
9. Furnas, C. C., *U.S. Bur. Mines Bull.* 307 (1929).
10. Hopf, L., *Z. Angew. Math. u. Mech.*, **3**, 329 (1923).
11. Huitt, J. L., *Bull. Am. Assoc. Petroleum Geol.*, **38**, 159 (1954).
12. Kozeny, J., *Sitzber. Akad. Wiss. Wien, Mathnaturw. Kl.*, **136**, 271 (1927).
13. Lamb, Horace, "Hydrodynamics," 6 ed., Dover Publications, New York (1945).
14. Mises, R. V., "Elemente der Technischen Hydrodynamik," S. G. Teuber, Leipzig (1914).
15. Nikuradse, J., *Forsch. Gebiete Ingenieurw. Forschungsheft*, (Sept.–Oct., (1932); reprinted in *Petroleum Engr.*, **11**, No. 6, 164; No. 8, 75; No. 9, 124; No. 11, 38; No. 12, 83 (1940).
16. Page, F., Jr., W. H. Corcoran, W. G. Schlinger, and B. H. Sage, *Ind. Eng. Chem.*, **44**, 419 (1952).
17. Schiller, L., *Z. Angew. Math. u. Mech.*, **3**, 2 (1923).
18. Stanton, T. E., *Proc. Roy. Soc. (London)*, **85A**, 366 (1911).

Presented at A.I.Ch.E. Houston meeting.

Plate Efficiency with Chemical Reaction—Absorption of Carbon Dioxide in Monoethanolamine Solutions

ARTHUR L. KOHL

The Fluor Corporation, Ltd., Los Angeles, California

The effect of chemical reaction on plate efficiency has been given little attention in the determination of bubble-plate efficiencies, although it is of importance in many operations. A typical example is the absorption of carbon dioxide in monoethanolamine solutions.

The over-all Murphree gas-phase plate efficiency can be shown to be a function of $K_g(A/V)$ where A/V is the interfacial surface area formed per tray per unit volume of gas. In order to evaluate variations in tray efficiency due to factors influencing K_g, data available in the literature for the absorption of carbon dioxide in monoethanolamine were considered. These showed that the liquid film was controlling and that for a packed column at constant liquid rate the absorption coefficient could be satisfactorily expressed by an equation that resembles somewhat equations which have been developed for the effect of rapid second-order reactions on k_L. However, the observed effect of carbon dioxide partial pressure in the gas is not so great as the theoretical equations would predict.

By use of the equation mentioned above to predict K_g, satisfactory correlation of observed plate efficiencies is obtained for a commercial column over a considerable range of conditions. It appears that the correlation can be extended to other pressures, flow rates, and column designs by an evaluation of the effect of these variables on A/V and K_g.

The estimation of plate efficiencies has only recently been approached from a theoretical basis, and for the general cases of distillation and physical absorption some success has been noted. The effect on plate efficiency of chemical reaction in the liquid phase has apparently been given little attention, although a large number of industrial absorption operations depend upon processes of this type.

Methods of estimating plate efficiency based upon an attempted visualization of the actual bubbling action at a single point have been discussed by Geddes (*6*), West et al. (*20*), Chu (*2, 3*), and others. The problem of predicting the effect of chemical reaction upon absorption has been treated by Sherwood and Pigford (*14*); by Van Krevelen and Hoftijzer (*17*); and recently by Perry and Pigford (*12*), who used a digital computer to solve the diffusion equations for the case of second-order reactions. The ultimate answer to the calculation of plate efficiency in the presence of chemical reaction would be to determine the effect of the reaction on the liquid-film coefficient by means of a fundamental treatment and, subsequently, to relate both liquid and gas film coefficients to the plate efficiency through an accurate analysis of phenomena occurring in the bubble zone. Unfortunately,

it does not appear that this can be accomplished at the present time because of a lack of data on reaction kinetics and because of some fundamental inadequacies in the knowledge of what happens on bubble trays. It is therefore proposed that the problem be handled by an empirical technique.

The absorption of carbon dioxide by monoethanolamine solutions is an important commercial process particularly with regard to gas purification and dry-ice manufacture. In either application it is necessary to predict the number of plates required to effect the desired removal of carbon dioxide from the gas and to ascertain the degree of saturation which can be expected in the solution.

Equilibrium data for carbon dioxide over a typical aqueous monoethanolamine solution (15%) are presented in Figure 1. This chart is based on a cross plot of the data of Lyudkovskaya and Leibush (*8*), Mason and Dodge (*10*), and Reed and Wood (*13*). As can be seen for conditions encountered in the absorber, at solution concentrations below about 0.5 mole of carbon dioxide/mole of monoethanolamine and temperatures below about 150° F., the equilibrium partial pressure of carbon dioxide over the liquid is negligible. Stoichiometrically, 0.5 mole of carbon dioxide would be expected to react with 1 mole of monoethanolamine in water to form the compound monoethanolamine carbonate.

Although the liquid film resistance is apparently controlling in this system, gas-phase plate efficiency has been considered because the degree of carbon dioxide removal from the gas stream is normally more important than the solution concentration change per plate and because the gas-phase driving force can be estimated more readily. If it is assumed that the equilibrium at the interface is one of physical solubility, for which Henry's Law applies, and the concentration of molecular carbon dioxide in the body of the liquid is zero, the driving force in the liquid for unreacted carbon dioxide will be proportional to the carbon dioxide partial pressure.

BASIC EQUATIONS

The assumption of zero vapor pressure over the solution at equilibrium simplifies the efficiency equation. The equation for point efficiency on any tray becomes

$$E_{OG} = \frac{y_{n+1} - y_n}{y_{n+1}} \qquad (1)$$

where

E_{OG} = Murphree point efficiency based on gas
y_{n+1} = mole fraction CO_2 entering point on tray n (leaving $n + 1$)
y_n = mole fraction CO_2 leaving point on tray n

Integration of the basic rate equation can be shown to yield an equation of the form

$$\ln (1 - E_{OG}) = -\frac{K_g a P h}{N} \qquad (2)$$

where

K_g = over-all mass transfer coefficient
a = interfacial area per foot of depth
P = total pressure
h = height of contact zone
N = gas rate, moles per unit cross-sectional area

which may be simplified to

$$E_{OG} = 1 - e^{-\frac{K_g A R T_A}{V}} \qquad (3)$$

in which A equals ah, the interfacial area per tray, T_A is the absolute temperature, and V is the actual volumetric gas rate.

For the carbon dioxide–monoethanolamine system, the gas composition in equilibrium with the solution leaving each tray is essentially the same as it is with respect to the solution at any point on the tray, i.e., zero carbon dioxide. The Murphree vapor efficiency E_{MV} is therefore equal to the point efficiency E_{OG} expressed by the foregoing equations.

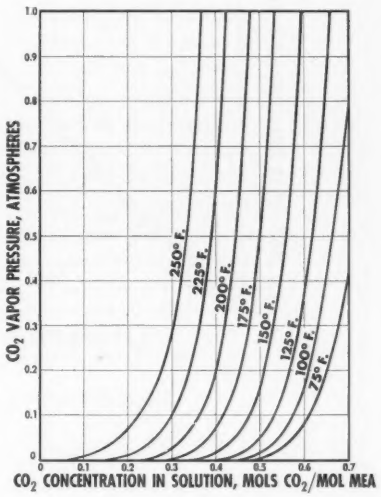

Fig. 1. Vapor pressure of carbon dioxide over 15% monoethanolamine (approx. 2.5*M*).

It is believed that A/V, the ratio of the area of surface formed to the actual volume rate of gas passed, is relatively constant for any given tray operating near design flow rates. For approximate efficiency estimates, it appears that an empirical correlation of A/V with physical properties of the system and operating characteristics of the tray is more satisfactory than an attempted theoretical analysis. With columns operating at the same pressure and employing approximately the same vapor velocity and tray design, it is convenient to assume that A/V is a constant. $K_g(A/V)$ can then be correlated much the same as $K_g a$ for packed towers.

The over-all coefficient K_g is related to the individual coefficients by

$$\frac{1}{K_g} = \frac{1}{k_g} + \frac{H}{k_L} \qquad (4)$$

where the Henry's Law constant H refers to physical absorption at the interface and k_L represents the coefficient for the transfer of molecular carbon dioxide away from the interface. Because of the chemical reaction occurring in the liquid, k_L is greater than would be predicted for simple physical absorption. However, the observed low plate efficiencies of 8 to 25% indicate that the liquid film is largely controlling, as columns operating with gas film controlling (absorption of ammonia, evaporation of water) give plate efficiencies of 80% and higher.

On the basis of observed efficiencies, it is estimated that the liquid-film resistance comprises from 85 to 95% of the total for efficiencies typically encountered in the carbon dioxide absorption units. For the purpose of developing an empirical correlation, it is therefore assumed that $1/K_g$ is essentially equal to H/k_L. It should be noted, however, that k_g becomes more important at higher tray efficiencies and this simplification would introduce an appreciable error for cases where the total tray efficiency exceeds about 25%.

EVALUATION OF K_g

Effect of Carbon Dioxide Concentration

The data of Shneerson and Leibush (*16*) are valuable in establishing the nature of the reaction between carbon dioxide and dilute amines. They show $K_g a$ for a packed column to decrease linearly with carbon dioxide concentration in the solution, approaching zero at concentrations equivalent to about 0.5 mole of carbon dioxide/mole of monoethanolamine (MEA). This effect was also noted by Comstock (*5*). These studies were made at atmospheric pressure with relatively low carbon dioxide partial pressures, conditions under which a concentration of 0.5 mole of carbon dioxide/mole of monoethanolamine is a fair approximation of equilibrium. The relation undoubtedly does not hold at very high carbon dioxide partial pressures, for which the equilibrium concentration may be 0.7 mole of carbon dioxide/mole of amine or even higher. It is therefore suggested that for high-pressure operations the effective amine concentration be considered proportional to the difference between the equilibrium concentration of carbon dioxide and the actual concentra-

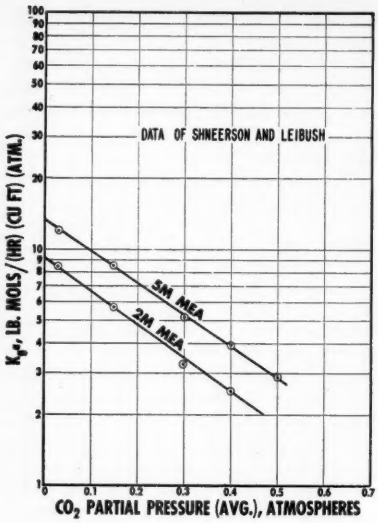

Fig. 2. Effect of carbon dioxide partial pressure on $K_g a$ in packed column.

tion of carbon dioxide in the body of the liquid ($C_e - C$).

Effect of Amine Concentration and Viscosity

With increased amine concentration, Shneerson and Leibush found $K_g a$ to increase up to 6 or 7 molar, then to decrease sharply. The latter effect is probably due principally to the viscosity increase, although it is expected that the decreased ionization of the amine at higher concentrations may also affect the transfer coefficient. In the region of concentrations normally used commercially (2 to 5 molar) $K_g a$ appears to vary directly with amine concentration when corrected for viscosity change according to the relationship $K_g a \sim M/\mu^{0.68}$ where M is the amine concentration. Viscosity data for lean monoethanolamine solutions are available in the literature(*1*). The presence of carbon dioxide in the solution increases the viscosity somewhat; however, no published data on the relationship are available. For estimating purposes, it was assumed that the solution viscosity increased about 0.3% for each volume of carbon dioxide absorbed per volume of solution—a relationship indicated by limited tests on a 30% solution.

Effect of Temperature

Shneerson and Leibush (*16*) conducted tests at several temperatures ranging from 77° to 167°F. and found that $K_g a$ increased with increased temperature up to 122°F. and leveled off or decreased in the range from 122° to 167°F. If the increase in the lower range is assumed to be due to viscosity change alone, it would be required that $K_g a$ be proportional to $1/\mu^{1.3}$.

This is the same exponent observed by Walter and Sherwood (*19*) for the effect of viscosity change due to temperature variation on H_L (height of a liquid-phase transfer unit) for the desorption of carbon dioxide from water in a plate column. It is quite probable that the effect due to increased temperature is the result of viscosity decrease, reaction-rate increase, and other physical changes.

The data of Shneerson and Leibush (*16*) were plotted as $K_g a \mu^{0.68}$ vs. T °F. to determine the function of temperature after removal of the effect due to viscosity. This plot indicated that $K_g a$ varies as $e^{0.0067T}$ at constant viscosity. This may be compared with $e^{-0.013T}$ reported by Sherwood and Pigford (*15*) as the effect of temperature on H_L. Their exponent, however, also includes the effect due to viscosity change with temperature. It should be pointed out that the foregoing relationship for effect of temperature on $K_g a$ in carbon dioxide absorption, using monoethanolamine solutions, was found to hold reasonably well up to about 125°F. Above this point, increased temperature was found actually to decrease $K_g a$ so that use of the relationship must obviously be limited accordingly.

It cannot be expected that viscosity will have exactly the same effect upon K_g in a plate column as it would upon $K_g a$ in a packed absorber. However, it is of interest to note that a for packed columns is not generally considered to vary with viscosity, and studies with bubble-cap absorbers (*15*) indicate that the interfacial area in such devices is also unaffected by viscosity. If, then, the principal effect of viscosity change is on diffusion in the liquid film, it can be expected that μ will have approximately the same exponent in its effect on k_L in either plate or packed columns.

Carbon Dioxide Partial Pressure

The packed-column absorption data also show a marked effect of carbon dioxide partial pressure on $K_g a$. A decrease in k_L with increased concentration of carbon dioxide at the interface is predicted by Sherwood and Pigford (*14*) for a rapid second-order irreversible reaction. If, for example, it is assumed that $D_A/D_B = 2$ where A refers to carbon dioxide and B refers to monoethanolamine, these authors show that if a rapid second-order reaction occurs,

$$k_L/k_L' = 1 + (1/2)(q/C_{A_i}) \quad (5)$$

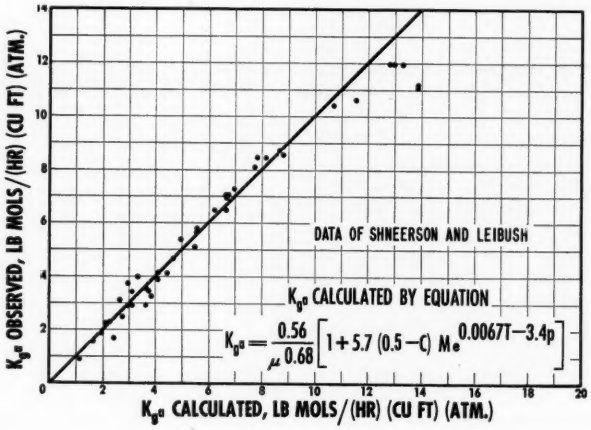

Fig. 3. $K_g a$ correlation for packed column.

It cannot be expected that viscosity will have exactly the same effect upon K_g in a plate column as it would upon $K_g a$ in a packed absorber. However, it is of interest to note that a for packed columns is not generally considered to vary with viscosity, and studies with bubble-cap absorbers (*15*) indicate that the interfacial area in such devices is also unaffected by viscosity. If, then, the principal effect of viscosity change is on diffusion in the liquid film, it can be expected that μ will have approximately the same exponent in its effect on k_L in either plate or packed columns.

Carbon Dioxide Partial Pressure

The packed-column absorption data also show a marked effect of carbon dioxide partial pressure on $K_g a$. A decrease in k_L with increased concentration of carbon dioxide at the interface is predicted by Sherwood and Pigford (*14*) for a rapid second-order irreversible reaction. If, for example, it is assumed that $D_A/D_B = 2$ where A refers to carbon dioxide and B refers to monoethanolamine, these authors show that if a rapid second-order reaction occurs,

$$k_L/k_L' = 1 + (1/2)(q/C_{A_i}) \quad (5)$$

to a close degree of approximation. In this equation k_L' represents the liquid-film coefficient if no reaction occurs, q refers to the concentration of B (unreacted monoethanolamine) in the body of the liquid, and C_{A_i} refers to the concentration of A (carbon dioxide) at the interface. For the carbon dioxide–monoethanolamine system, q is approximately equal to $2(0.5 - C)M$. According to Equation (5), at very low partial pressures of carbon dioxide it is possible for k_L to become so large that the gas film would become controlling, and at very high partial pressures the liquid-film coefficient would approach that for no reaction.

The absorption of carbon dioxide in aqueous monoethanolamine solutions apparently does not follow Equation (5) exactly, as the carbon dioxide partial pressure has not been found to have so great an effect on $K_g a$ as does the amine concentration in the region of partial pressures investigated. Instead of an

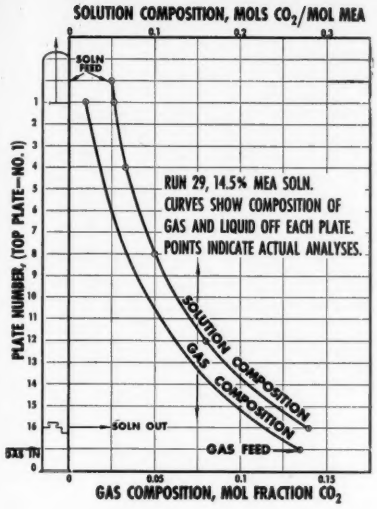

Fig. 4. Composition profile for commercial absorber.

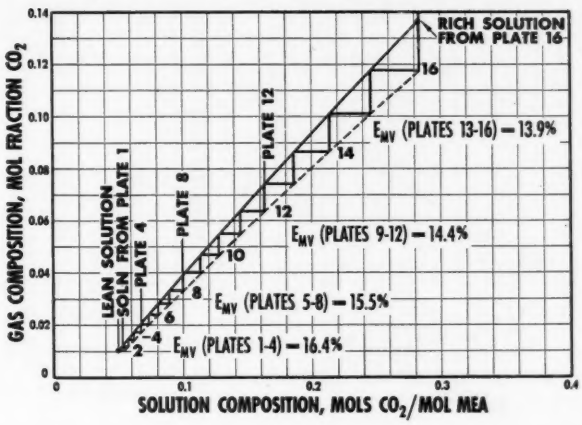

Fig. 5. Plate-efficiency diagram for run 29, solution 14.5 monoethanolamine, solution analyses at plates indicated.

approximately linear relationship with respect to $1/C_{A_i}$ (or $1/p$), $K_g a$ appears to vary with $e^{-3.4p}$, as shown in Figure 2. However, there is serious doubt that the coefficient would continue to decrease at the same rate at very high partial pressures of carbon dioxide, and so use of this equation appreciably above the range of the data may not be warranted. Insufficient data are available to prove or disprove the expression for absorption in bubble-tray equipment, but as the effect is apparently related to absorption through the liquid film, it seems reasonable to assume that a similar relationship holds.

Over-all Equation for $K_g a$

The various factors discussed above would yield an over-all equation for the absorption of carbon dioxide in aqueous monoethanolamine solutions in a packed tower at constant liquid rate of the form

$$K_g a = \frac{B(0.5 - C)Me^{0.0067T - 3.4p}}{\mu^{0.68}} \quad (6)$$

All the Shneerson and Leibush (*16*) runs for which sufficient data are available have been correlated by use of this equation, and B is indicated to be equal to 3.7. These data were obtained with a 1-in.-diam. column packed with 5- to 6-mm. glass rings at a liquid flow rate of 695 lb./(hr.)(sq. ft.) and for gas velocities varying from 0.09 to 0.55 ft./sec.

Somewhat better correlation of the data is obtained with the equation

$$K_g a = \frac{0.56}{\mu^{0.68}} [1 + 5.7(0.5 - C)M \cdot e^{0.0067T - 3.4p}] \quad (7)$$

A plot of the observed $K_g a$ vs. that calculated by this equation is given in Figure 3. Comparison of this equation with that given by Sherwood and Pigford (*14*) and described above for a rapid second-order irreversible reaction indicates that if the concentration of reactive amine q were reduced to zero (by M becoming 0 or by C becoming 0.5), $K_g a$ would be the same as for physical absorption, in this case equal to $0.56/\mu^{0.68}$.

Absorption in Plate Columns

For the case where E_{MV} is the same for each plate in a column and both operating and equilibrium lines are straight, an equation has been developed which enables the number of actual plates to be calculated (*9*). For the highly simplified case where the equilibrium line lies on the x axis ($m = 0$ and $y_e = 0$), the equation reduces to the expression

$$n = \frac{\ln (y_1/y_2)}{-\ln (1 - E_{MV})} \quad (8)$$

Combining with Equation (3) yields an expression for $K_g(A/V)$ in terms of the inlet and outlet gas composition

$$K_g\left(\frac{A}{V}\right) = \frac{\ln (y_1/y_2)}{nRT} \quad (9)$$

where

n = number of plates
y_1 = composition of the feed gas
y_2 = mole fraction of solute in gas leaving

Operating data from a 4-ft.-diam. commercial absorber have been analyzed by use of the foregoing equation. The column contained sixteen trays at 2-ft. spacing with fifteen rectangular caps per tray. The design employed for the caps and overflow weir resulted in an average slot submergence of about 3 in. during normal operation. Gas rate through the column varied from about 0.6×10^6 to 3.3×10^6 std. cu. ft./day with the majority of runs made at a gas flow rate of approximately 3×10^6 std. cu. ft./day. The lean-solution flow rate varied from 120 to 180 gal./min. with most runs at about 160 gal./min. As plate-efficiency calculations were based entirely on analytical data, exact flow rates were not measured during each sampling period; however, occasional checks indicated material balances within about 5%. For the run illustrated by Figures 4 and 5, for example, the gas flow to the column was indicated to be 2.89×10^6 std. cu. ft./day and the lean-solution rate 152 gal./min. (of 14.5% monoethanolamine). On the basis of the gas-composition change from 13.7 to 1.0% carbon dioxide and the aforementioned gas rate 40.8 moles of carbon dioxide was absorbed from the gas/hour. This may be compared with 42.3 moles/hour indicated absorption on the basis of the solution rate and composition change from 0.050 to 0.283 mole carbon dioxide/mole monoethanolamine. (*See* Figure 5.)

As most of the data were for a gas flow rate of approximately 3×10^6 std. cu. ft./day through this column, the factor A/V was taken as unity for this rate, and $K_g(A/V)$ values based upon Equation (9) were correlated on the basis of an equation of the general form of (7) above. Equation (9) is, of course, most nearly correct for small sections of the column in which

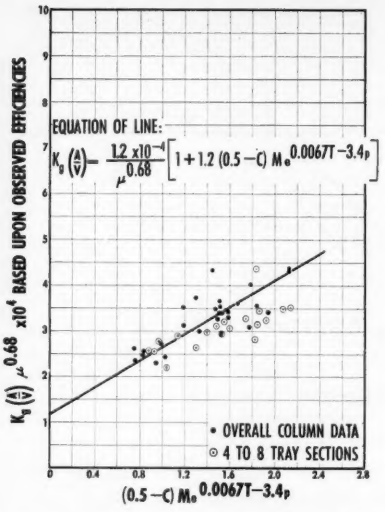

Fig. 6. Determination of $K_g(A/V)$ equation for carbon dioxide absorption in plate columns.

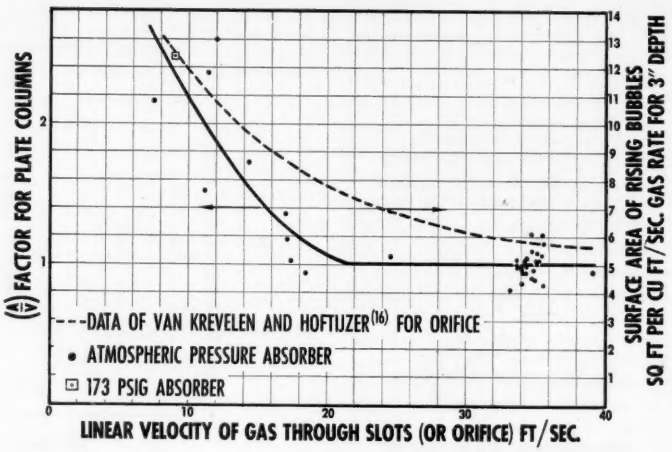

Fig. 7. Effect of gas velocity through slots on the interfacial area in bubble-plate columns.

it can be expected that the change in efficiency will not vary greatly. Available column-profile data were therefore considered first to determine the approximate efficiency range occurring throughout the column. A typical composition profile is shown in Figure 4. Because of the manner in which gas and liquid composition varied with column height, log mean values of these variables were used to express average conditions in column sections. A plate-efficiency diagram is shown in Figure 5 for a profile based upon solution analyses at three points in the column, plus inlet and outlet conditions. As can be seen, the efficiency variation was not very great throughout the entire column. This was due principally to the relatively small liquid-concentration change occurring in the test tower and is not generally true of plants of this type.

A study of the profile data indicated that for this particular operation over-all efficiencies could be used for correlation purposes. This would permit use of test data covering a much wider range of conditions. A summary of these data is presented in Table 1.* The temperature given for each run represents a simple average between the feed and exit solution temperatures. Solution viscosity at this average temperature was used for correlation purposes. $K_g(A/V)\mu^{0.68}$, based upon the observed efficiency, was first plotted against $(0.5 - C)M\ e^{0.0067T - 3.4p}$ for average conditions in the column to obtain the intercept and slope. This plot, which is given in Figure 6, indicated that $K_g(A/V)$ for these operations can best be expressed by the equation

$$K_g\left(\frac{A}{V}\right) = \frac{1.2 \times 10^{-4}}{\mu^{0.68}} \cdot [1 + 1.2(0.5 - C)Me^{0.0067T - 3.4p}] \qquad (10)$$

Points representing small sections of the column derived from profile data are also shown on the chart. As the profile points represent only five runs and because they are somewhat less certain, owing to the large effect of minor analytical errors on observed $K_g(A/V)$ for the column sections, the position of the line was based on the over-all column data. In order to use the data from a few tests in which the operating temperature was above the range for which the relationship $K_g \sim e^{0.0067T}$ was known to hold, it was assumed that the temperature effect had an equal reverse slope above 125°F. A corrected value for T was therefore used for these high-temperature runs, obtained by subtracting from 125°F. a figure equal to the number of degrees by which the actual temperature exceeded 125°F. This relationship is not included in the final correlation because of its uncertainty. Comparison of Equation (10) with the analogous one obtained for the packed-column data [Equation (7)] reveals that the portion of the equation which represents the influence of the reaction is appreciably smaller in the case of the plate columns. The reason for this is not known, although it is possible that the use of data representing several trays or the entire column, instead of point conditions, may have contributed to this effect.

*Table 1, as published, presents sample runs. Data for the complete series of forty-three runs may be obtained as document 4794 from the Photoduplication Service, American Documentation Institute, Library of Congress, Washington 25, D. C., for $1.25 for photoprints or 35-mm. microfilm.

Effect of Gas Rate

It was noted that at low gas velocities in the atmospheric-pressure carbon dioxide absorber appreciably higher efficiencies were obtained. The increased efficiency was considerably above what could be expected on the basis of decreased carbon dioxide concentration in the liquid. Data from a high-pressure column (which was designed for a lower gas velocity) also showed appreciably higher efficiency at design conditions than the low-pressure absorber operated at its design gas rate.

As bubble size and, in fact, the bubbling mechanism on the plate are greatly influenced by gas rate, it is expected that this would be an important variable. Although the data are inadequate for a satisfactory analysis, they show a definite trend which may be of value in utilizing the basic correlation for other columns. These data are plotted in Figure 7 as the A/V factor vs. the linear velocity of gas through the bubble-cap slots. The A/V factor was obtained by dividing $K_g(A/V)$, based on observed column efficiency, by the $K_g(A/V)$ obtained by the use of Equation (10). This, of course, results in an average A/V factor of 1.0 for the runs used as a basis for the equation.

For comparison purposes, a curve has been included on the figure which is based upon the data of Van Krevelen and Hoftijzer (*18*) for air bubbles formed at a single orifice 2.3 mm. in diam. submerged in water and in glycerol solutions. This curve indicates the effect of linear velocity through the orifice on the surface area of the rising bubbles per unit rate of gas flow. The values have been calculated for a 3-in. liquid depth to make the work more comparable with the commer-

Table 1A. Atmospheric-pressure Absorber (Sixteen Trays 48-in. I.D., 24-in. Tray Spacing)—Gas Rate Constant—Slot Velocity Approximately 35 Ft./Sec.

Run	CO_2 in gas y_1	CO_2 in gas y_2	E_{MV}, avg. observed, %	CO_2 in soln., moles/mole MEA In	CO_2 in soln., moles/mole MEA Out	MEA conc. molarity, M	Temp., °F., avg. in column	$K_g(A/V)$ observed, $\times 10^{-4}$	$K_g(A/V)$ calculated, $\times 10^{-4}$	E_{MV}, avg. calculated, %
1	0.0940	0.0190	9.5	0.068	0.244	1.73	92	2.49	2.39	9.16
6	0.0960	0.0140	11.3	0.079	0.300	1.53	127	2.82	3.13	12.49
11	0.0950	0.0085	14.0	0.135	0.256	2.70	108	3.54	3.24	12.52
16	0.0950	0.0080	14.3	0.119	0.219	3.60	104	3.76	3.73	14.18
21	0.1350	0.0185	11.6	0.046	0.274	2.16	109	3.00	3.11	12.07
26	0.1058	0.0060	16.2	0.053	0.230	2.21	147	4.06	3.91	15.89

Table 1B. Atmospheric-pressure Absorber—Profile Data—Gas Rate Constant—Slot Velocity Approximately 35 Ft./Sec.

Run	Plate section	CO_2 in gas y_1	CO_2 in gas y_2	E_{MV}, avg. observed, %	CO_2 in soln. mean conc., moles/mole MEA	MEA conc. molarity, M	Temp. (avg.), °F.	$K_g(A/V)$, observed $\times 10^{-4}$	$K_g(A/V)$, calculated $\times 10^{-4}$	E_{MV}, avg., calculated, %
29	1–4	0.0205	0.0100	16.40	0.058	2.37	133	4.16	5.09	19.8
	5–8	0.0403	0.0205	15.52	0.084	2.37	135	3.89	4.79	18.6
	9–12	0.0752	0.0403	14.37	0.132	2.37	137	3.57	4.56	17.9
	13–16	0.1370	0.0752	13.89	0.223	2.37	139	3.43	3.47	14.0
31	1–4	0.0260	0.0160	11.43	0.061	2.32	113	2.91	4.01	12.8
	5–8	0.0458	0.0260	13.18	0.090	2.32	118	3.36	4.16	16.1
	9–12	0.0818	0.0458	13.49	0.145	2.32	123	3.41	3.67	14.4
	13–16	0.1340	0.0818	11.61	0.246	2.32	127	2.89	2.88	11.6

Table 1C. Atmospheric-pressure Absorber—Gas Rate Variable

Run	CO_2 in gas y_1	CO_2 in gas y_2	E_{MV}, avg. observed, %	CO_2 in soln., moles/mole MEA In	CO_2 in soln., moles/mole MEA Out	MEA conc. M	Temp. (avg.), °F.	$K_g(A/V)$, observed $\times 10^{-4}$	Slot velocity, ft./sec.	(A/V), factor	$K_g(A/V)$, calculated $\times 10^{-4}$	E_{MV}, avg., calculated, %
35	0.0935	0.0025	20.2	0.084	0.111	1.75	90	5.65	7.5	2.60	6.79	22.9
37	0.0960	0.0050	16.8	0.093	0.195	1.79	97	4.55	14.4	1.53	4.04	15.0
40	0.1020	0.0100	13.5	0.148	0.234	3.32	103	3.54	24.6	1.00	3.34	12.7

Table 1D. High-pressure Absorber (Sixteen Trays 84-in. I.D., 24-in. Tray Spacing) 173 Lb./Sq. In. Gauge

Run	CO_2 in gas y_1	CO_2 in gas y_2	E_{MV}, avg., observed, %	CO_2 in soln., moles/mole MEA In	CO_2 in soln., moles/mole MEA Out	MEA conc., M	Temp. (avg.), °F.	$K_g(A/V)$, observed $\times 10^{-4}$	Slot velocity, ft./sec.	(A/V) factor	$K_g(A/V)$, calculated $\times 10^{-4}$	E_{MV}, avg., calculated, %
43	0.0641	0.003	17.5	0.204	0.529	2.34	115	4.57	9.0	2.33	4.32	16.5

cial-column data. In view of the wide divergence in conditions between the plate-column operations and the Van Krevelen and Hoftijzer (*18*) experiments, it is interesting to note that the same general shape of curve is obtained.

Further indications of the effect of gas velocity are presented by the data of West et al. (*20*), who show that the interfacial area for bubble-cap plates used in the desorption of oxygen decreased markedly with increased air rate.

It cannot be expected that results from the high-pressure column will be in close agreement with those from the atmospheric absorber, as the high-pressure plant operated on a gas stream which contained hydrogen sulfide in addition to carbon dioxide and attained a much higher degree of saturation of the solution. The position of this point with respect to the line may therefore be more of a coincidence than evidence of a good correlation.

By use of the curve shown on Figure 7 to correct (A/V) for all tests in the atmospheric column at gas rates appreciably different from design and for the test in the high-pressure column, $K_g(A/V)$ has been estimated for all runs and converted to E_{MV} by use of Equation (3). These values are compared to the observed E_{MV} calculated from the inlet and outlet gas compositions by use of Equation (8) in Figure 8.

Effect of Slot Submergence

In the commercial-column tests described herein, the slot submergence (height of liquid above the centers of bubble-cap slots) varied within a relatively narrow range (i.e., 3 to 4 in.) and so an accurate evaluation of the effect of this factor on efficiency was not possible. If the correlation were to be applied to columns of appreciably different design, however, it is apparent that the effect of slot submergence would have to be considered. Various investigators have studied this variable and in general agreed that increased submergence provides an increased efficiency. Walter and Sherwood (*19*) suggest a general equation in which the contact is assumed to be proportional to h (height of solution above slot centers). Geddes (*6*) used the height of liquid over the midpoint of the slot opening under operating conditions

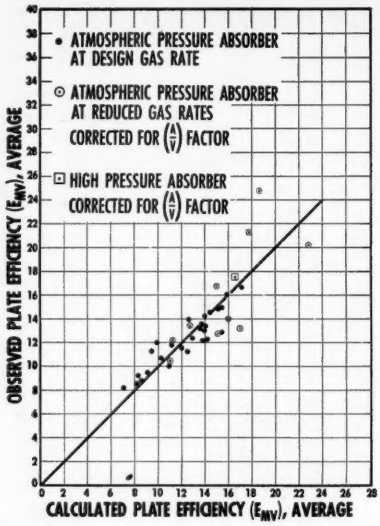

Fig. 8. Plate-efficiency correlation for carbon dioxide absorption in plate columns.

and assumed that the time of contact would be proportional to this height. Chu et al. (*4*) analyzed the data of Peavy and Baker (*11*) and determined a factor B for correcting over-all plate efficiencies for effective submergence. Their correlation leads to the conclusion that a zero effective slot depth (static submergence plus one-half slot height) would result in a plate efficiency equal to 87% of that calculated for a 0.7-in. submergence, and a 2.5-in. depth would result in an efficiency equal to 143% of the base value. In a more recent article by Chu et al. (*2*) it is pointed out that a substantial portion of the mass transfer appears to occur in the bubble-formation zone where the gas jets through the slots at high velocities. This would indicate a fallacy in assuming the interfacial area or the time of contact to be directly proportional to liquid height above the slots.

SUMMARY

For the absorption of carbon dioxide in aqueous solutions of monoethanolamine in bubble-plate columns, it is proposed that the Murphree vapor-phase efficiency E_{MV} be calculated from the equation

$$E_{MV} = 1 - e^{-K_g(A/V)RT_A}$$

$K_g(A/V)$ for the specific column tested, at a gas rate which results in a superficial velocity of about 35 ft./sec. through the bubble-cap slots, can be estimated from the equation

$$K_g\left(\frac{A}{V}\right) = \frac{1.2 \times 10^{-4}}{\mu^{0.68}} \cdot [1 + 1.2(0.5 - C)Me^{0.0067T - 3.4p}]$$

The indicated temperature effect holds only up to about 125°F.; so the equation should not be used above this value unless a suitable correction is applied. For high-pressure operations, it appears that the value $(0.5 - C)$, which indicates the fraction of amine unconverted, should be replaced by $(C_e - C)$ where C_e is the concentration in equilibrium with the gas.

The data indicate that $K_g(A/V)$ increases appreciably at decreased gas rates, presumably owing to an increase in A/V. The magnitude of the A/V correction at various gas velocities is indicated by a plot of the data which includes several gas rates in the atmospheric-pressure absorber and one operation at higher pressure.

The equation for calculating E_{MV} can be used for single plates or for groups of plates where concentration changes are not extreme. A simplified equation for calculating the number of plates required after E_{MV} has been estimated is

$$n = \frac{\ln (y_1/y_2)}{-\ln (1 - E_{MV})}$$

This assumes constant plate efficiency and no vapor pressure of carbon dioxide over the amine solution. If the plate efficiency varies appreciably throughout the column, a conventional graphical method may be employed.

ACKNOWLEDGMENT

The author wishes to express appreciation to The Fluor Corporation, Ltd., for permission to publish this work and to fellow workers in the Research Division who obtained much of the test data used.

NOTATION

a = interfacial area, sq. ft./(ft. of depth) (sq. ft. of tray) or sq. ft./cu. ft. of packing.
A = ah; contact area, sq. ft./sq. ft. of tray
B,B' = constants
C = concentration of carbon dioxide in the solution, moles/mole MEA
C_e = equilibrium concentration of carbon dioxide in solution
D = diffusivity
E_{OG} = Murphree point efficiency based on gas
E_{MV} = Murphree vapor efficiency for entire plate
h = height of contact zone, ft.
H = p/C, Henry's Law coefficient
k_g = gas-film coefficient, lb. moles/(hr.)(sq. ft.)(atm.)
K_g = over-all gas-film coefficient, lb. moles/(hr.)(sq. ft.)(atm.)
k_L = liquid-film coefficient
k_L' = liquid-film coefficient based upon physical absorption
m = y/x, slope of equilibrium line
M = amine concentration of solution (molarity, gram moles/liter)
n = number of plates
N = total gas rate, moles/(hr.)(sq. ft.)
p = partial pressure, atm.
P = total pressure, atm.
q = concentration of unreacted amine in solution
R = gas constant
T = temperature, °F.
T_A = absolute temperature, °R.
V = actual gas volume, cu. ft./(hr.)(sq. ft. of tray)
y = mole fraction carbon dioxide in gas
μ = viscosity, centipoises

Subscripts

g = gas
L = liquid
e = equilibrium
i = interface
1 = feed condition
2 = exit condition

LITERATURE CITED

1. Carbide and Carbon Chemicals Company, "Aliphatic Nitrogen Compounds," p. 24, New York (1952).
2. Chu, J. C., J. Forgrieve, and G. C. Papacosta, presented at Heat Transfer Symposium, A.I.Ch.E. Annual Meeting, St. Louis, Mo. (Dec. 3–16, 1953).
3. Chu, J. C., *Petroleum Processing*, p. 39 (January, 1951).
4. ———, J. R. Donovan, B. C. Boswell, and L. C. Fuhrmeister, *Petroleum Processing*, p. 154 (February, 1951).
5. Comstock, C. S., Ph.D. thesis, Yale University, New Haven, Conn. (1935).
6. Geddes, R. L., *Trans. Amer. Inst. Chem. Engrs.*, **42**, 79 (1946).
7. Gerster, J. A., W. E. Bonnet, and I. Hess, *Chem. Eng. Progr.*, **47**, No. 12, 621 (1951).
8. Lyudkovskaya, M. A., and A. G. Leibush, *J. Appl. Chem.* (*U.S.S.R.*), **22**, No. 6, 558 (1949).
9. Marshall, W. R., and R. L. Pigford, "Application of Differential Equations to Chemical Engineering Problems," Univ. Delaware, Newark (1947).
10. Mason, J. W., and B. F. Dodge, *Trans. Amer. Inst. Chem. Engrs.*, **32**, 27 (1936).
11. Peavy, C. C., and E. M. Baker, *Ind. Eng. Chem.*, **29**, 1056 (1937).
12. Perry, R. H., and R. L. Pigford, *Ind. Eng. Chem.*, **45**, 1247 (1953).
13. Reed, R. M., and W. R. Wood, *Trans. Amer. Inst. Chem. Engrs.*, **37**, 363 (1941).
14. Sherwood, T. K., and R. L. Pigford, "Absorption and Extraction," 2 ed., p. 317, McGraw-Hill Book Company, Inc., New York (1952).
15. *Ibid.*, p. 309.
16. Shneerson, A. L., and A. G. Leibush, *J. Appl. Chem.* (*U.S.S.R.*), **19**, No. 9, 869 (1946).
17. Van Krevelen, D. W., and P. J. Hoftijzer, *Chem. Eng. Progr.*, **44**, 529 (1948).
18. *Ibid.*, **46**, 29 (1950).
19. Walter, J. F., and T. K. Sherwood, *Ind. Eng. Chem.*, **33**, 493 (1941).
20. West, F. B., W. D. Gilbert, and T. Shimizu, *Ind. Eng. Chem.*, **44**, 2470 (1952).

Presented at A.I.Ch.E. New York meeting

A Semiempirical Solution for Local Heat Transfer Coefficients for Flow in Nonparallel Passageways

P. N. STEVENS and E. F. OBERT

Northwestern Technological Institute, Evanston, Illinois

A method, based upon the pertinent flat-plate heat transfer equation, is presented for computing the local heat transfer coefficients for a boundary layer subjected to streamwise velocity and pressure gradients. No extensive mathematical background is required as the complexity of a rigorous solution for this type of problem is avoided. The validity of the method for gases is demonstrated by comparison of the predicted coefficients with the experimental data for two widely different problems.

At the present time no good solution is available to the engineer for predicting the local heat transfer coefficients in a passageway with accelerated or decelerated flow. The empirical Colburn equation fails both qualitatively and quantitatively in many problems. Exact solutions must satisfy a number of fundamental relationships: the integral momentum equation, the energy equation, and the continuity equation. Too, assumptions must be made on the velocity and temperature profiles as well as approximations on skin friction and the relationship between heat and momentum transfer. Because of these complexities, it is doubtful whether an exact solution is feasible for many problems where cost or time is a factor.

It is the object of this paper to present a simple yet reliable method of analysis that can be readily handled by the engineer for a wide variety of applications. The method is based on the appropriate flat-plate equation for local heat transfer coefficients without pressure gradient—appropriate in the sense that the type of flow is similar to that of the analysis.

METHOD

1. Select from the literature a flat-plate equation which is known to be accurate for turbulent (or laminar) flow and for the fluid under consideration.

2. Extend the equation to include variable velocity by differentiation:

$$dh = \frac{\partial h}{\partial x}\,dx + \frac{\partial h}{\partial U}\,dU + \frac{\partial h}{\partial \rho}\,d\rho$$

For the turbulent-flow examples of this paper the flat-plate equation of Eckert (*1*) was selected:

$$St = \frac{Nu}{Re\,Pr} = \frac{0.0296/Re^{0.2}}{1 + [0.0296/Re^{0.2}]^{1/2}\left[5(Pr - 1) + 5\ln\frac{5Pr + 1}{6}\right]}$$

This equation can be arranged into the form

$$h = \frac{QU\rho}{Re^{0.2} + N\,Re^{0.1}}$$

The partial derivatives of h are as follows:

$$\frac{\partial h}{\partial x} = -\frac{Q\rho U}{x}\left[\frac{0.2\,Re^{0.2} + 0.1N\,Re^{0.1}}{[Re^{0.2} + N\,Re^{0.1}]^2}\right]$$

$$\frac{\partial h}{\partial U} = Q\rho\left[\frac{0.8\,Re^{0.2} + 0.9N\,Re^{0.1}}{[Re^{0.2} + N\,Re^{0.1}]^2}\right]$$

$$\frac{\partial h}{\partial \rho} = QU\left[\frac{0.8\,Re^{0.2} + 0.9N\,Re^{0.1}}{[Re^{0.2} + N\,Re^{0.1}]^2}\right]$$

3. When the leading-edge coefficient is infinite (the usual case), utilize the flat-plate equation to obtain an initial coefficient near the leading edge. The choice of this initial increment is arbitrary but should be as small as practical, say, 1/100 in.

4. Select increments throughout the passageway (10 steps are usually sufficient) and find h_2, etc.:

$$h_2 = h_1 + \frac{\partial h}{\partial x}\,\Delta x_{12} + \frac{\partial h}{\partial U}\,\Delta U_{12} + \frac{\partial h}{\partial \rho}\,\Delta \rho_{12}$$

(For the examples to follow all properties were evaluated at the mean local film temperature and flow conditions assumed to be isentropic.)

Note that the qualitative change in h can in part be rationalized by inspection of dh:

$$dh = \frac{\partial h}{\partial x}\,dx + \frac{\partial h}{\partial U}\,dU + \frac{\partial h}{\partial \rho}\,d\rho$$

In the convergent section of a nozzle the first two terms are significant, with the velocity term being predominant except near the leading edge, where the first term is of prime importance. The third term is relatively small until the region near the throat is reached, but then large negative values of this term cause the maximum coefficient to be realized immediately before the throat. After the throat the density term is the controlling factor and the coefficient rapidly decreases in value. These effects, of course, are further influenced by the pressure gradient, and this influence is neglected in this analysis.

COMPARISON WITH EXPERIMENTAL DATA

The proposed method was used to predict coefficients for two widely different flow problems recently investigated

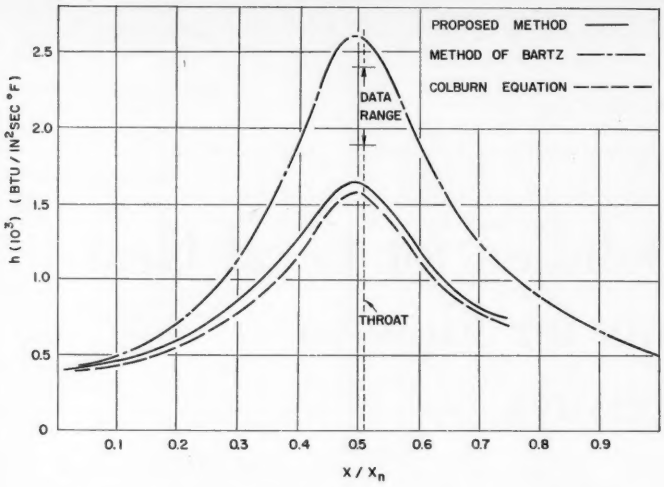

Fig. 1. Local heat transfer coefficients h for a nozzle with accelerated velocities (outlet velocity at mach 2).

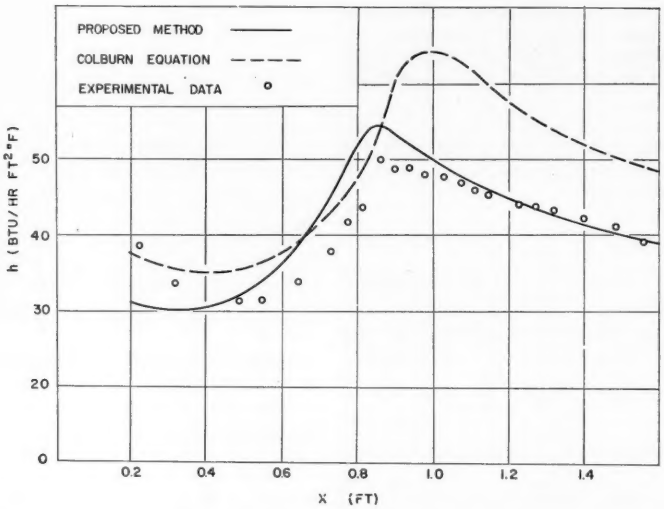

Fig. 2. Local heat transfer coefficients h for a flat plate with accelerated and decelerated subsonic velocities.

by Bartz (*2*) and by Seban and Doughty (*3*). In the Bartz problem the flow was accelerated to supersonic velocities with the pressure continually decreasing in the direction of flow (negative pressure gradient); in the Seban-Doughty problem the flow was accelerated to a subsonic velocity (negative pressure gradient) and then decelerated (positive pressure gradient).

Bartz made a rigorous, but complex, analytical solution for the flow of combustion gases at high temperature (4,000 °F.) through a convergent-divergent nozzle. Although not included in the paper, experimental data (*4*) were obtained for a nozzle which was the prototype of the analytical solution. The range of values of these data at the throat of the nozzle is shown in Figure 1, along with Bartz's predictions (his Case IIa) and those made by the relatively simple analysis of this paper. The proposed method and the Colburn equation yield results on the low side, while the results of Bartz's method* are on the high side of the experimental data. It would appear for this particular problem that the deviations of the two methods from the correct values are probably quite comparable.

Seban and Doughty experimentally determined local heat transfer coefficients over the surface of a flat plate which was located in the converging-diverging section of a wind tunnel. The experimental and analytical results for their run 99 are shown in Figure 2 along with values calculated by the methods of this paper (*5*). By the proposed method both qualitative and quantitative correlations are obtained with the experimental data.

The Colburn coefficients calculated by Seban Doughty (Figure 2) correlate reasonably well with their experimental data in the accelerated-flow region. The Colburn coefficients are in neither qualitative nor quantitative agreement with the experimental data over the whole flat plate.

It should be mentioned that the close quantitative correlation of the proposed method with the Seban-Doughty data is somewhat surprising. Qualitative agreement was expected from the differentiation procedure and step-by-step solution. But the flat-plate equations should not reflect strong pressure gradients as the data are for zero gradients. Thus the proposed method should predict values on the low side in the regions of accelerated flow and values on the high side in regions of decelerated flow. It is believed, however, that the results will be superior in most cases to those from the Colburn equation.

*Bartz has recently made (private communication) a second calculation which reduces his throat value to 2.35 (10^{-3}).

NOTATION

c_p = heat capacity at constant pressure
h = local heat transfer coefficient

$$N = [0.0296]^{1/2}\left[5(Pr - 1) + 5 \ln \frac{5Pr + 1}{6}\right]$$

Nu = Nusselt number
Pr = Prandtl number
Q = $0.0296\ c_p$

$$Re = \text{Reynolds number } \frac{\rho U_x}{\mu}$$

St = Stanton number
U = local-main-stream velocity
x = distance from the leading edge
x_n = nozzle length

Greek Letters

ρ = density
μ = viscosity

LITERATURE CITED

1. Eckert, E. R. G., "Introduction to the Transfer of Heat and Mass," p. 124, McGraw-Hill Book Company, Inc., New York (1950).
2. Bartz, D. R., *Trans. Am. Soc. Mech. Engrs.*, **77**, No. 8, 1235 (1955).
3. Seban, R. A., and Doughty, D. L., *Trans. Am. Soc. Mech. Engrs.*, **78**, No. 1, 217 (1956).
4. Barty, D. R., private communication (1955).
5. Doughty, D. L., private communication (1955).

Diffusion Coefficients in Hydrocarbon Systems

n-Heptane in the Gas Phase of the Ethane–*n*-Heptane and Propane–*n*-Heptane Systems

L. T. CARMICHAEL and B. H. SAGE, California Institute of Technology, Pasadena, California

Because little information is available concerning the behavior of hydrocarbons under conditions far from equilibrium, it appears desirable to obtain data for the diffusion coefficients of the lighter hydrocarbons in the gas phase.

The Maxwell diffusion coefficients of *n*-heptane in the gas phase of the ethane–*n*-heptane and propane–*n*-heptane systems were measured at temperatures from 100° to 220° F. and for pressures up to 60 lb./sq. in. The Fick diffusion coefficient was calculated as a function of state from these measurements.

The experimental results indicate that the interfacial resistance between the liquid and the gas phases into which the transport was taking place is small. It was found that pressure exerted a significant influence upon the Maxwell diffusion coefficient for both of the binary systems investigated. There is a marked decrease in the Maxwell diffusion coefficient with an increase in molecular weight of the stagnant component.

The evaluation of material transport in the gas phase as a result of a concentration gradient was placed on a surprisingly satisfactory basis by Maxwell (*12*) and Stefan (*18-21*). Chapman and Cowling (*7*) extended their treatment to include the effects of composition upon the diffusion characteristics of gaseous mixtures. Jost (*9*) reviewed the status of diffusion in gases, liquids, and solids. Kirkwood and Crawford (*10*) outlined the basic transport characteristics of homogeneous systems. A discussion of the application of diffusion coefficients was presented by Sherwood and Pigford (*17*). The relations of the several diffusion coefficients were recently reviewed (*13*) and it does not appear necessary to consider further the background of diffusion in gases beyond that associated with the paraffin hydrocarbons.

Wilke (*22*) reviewed the status of prediction of diffusion coefficients for the lighter gases and supplemented available correlations for gases at atmospheric pressure. Schlinger (*16*) established diffusion coefficients for *n*-heptane and *n*-hexane in air and reviewed the literature concerning the experimental determination of Maxwell diffusion coefficients. The coefficients for *n*-heptane in the gas phase of the methane–*n*-heptane system at pressures up to 60 lb./sq. in. are available (*5*) and measurements of the diffusion of *n*-hexane in the gas phase of the methane–*n*-hexane, ethane–*n*-hexane, and propane–*n*-hexane systems were reported (*6*). In each of these cases it was found that the Maxwell hypothesis, with either partial pressure or fugacity as the potential, did not fully describe the transport process even at pressures below 60 lb./sq. in. The present work is concerned with the measurement of the Maxwell diffusion coefficient for *n*-heptane in the gas phase of the ethane–*n*-heptane and the propane–*n*-heptane systems for temperatures from 100° to 220°F. and at pressures from 14 to 60 lb./sq. in. abs. Throughout this discussion and in the associated figures the pressures are reported in pounds per square inch absolute or pounds per square foot absolute.

METHODS AND APPARATUS

The experimental approach to this investigation involved an adaptation of the classical diffusion cell of Stefan (*18*). The gas phase filled the diffusion path and the *n*-heptane was introduced as a liquid into the lower part of the chamber through a fritted-glass disk. Steady state conditions were indicated by the constancy of the capillary depression within the fritted disk. The concentration of the *n*-heptane in the gas phase at the top of the diffusion cell was maintained at a steady value by circulation across the top of the cell of a gas phase which was at equilibrium with *n*-heptane liquid at 32° F.

The apparatus, which is rather complicated, has been described in detail (*4, 5*). Appropriate corrections were made for the end effects associated with the introduction of *n*-heptane through the fritted-glass disk and its withdrawal by gas circulation at the top of the cell. The methods for evaluation of these corrections have been described (*4*). The pressures were measured within 0.01 lb./sq. in. and the temperatures with an uncertainty of 0.01° F. relative to the international platinum scale. The estimated uncertainty in each of the variables pertinent to these measurements is available (*5*).

It has been shown (*16*) that for measurements of this kind the Maxwell diffusion coefficient may be evaluated from the following expression in which T refers to the temperature of the transport path:

$$D_{M,k} = \frac{\overset{\circ}{m}_k b_k T (l_G - l_c)}{Z\left(\frac{f_k^0}{P}\right) \ln\left(\frac{f_k^0 - f_{k,t}}{f_k^0 - f_{k,i} + b_k T r_{i,k} \overset{\circ}{m}_k}\right)} \quad (1)$$

Equation (1) is based upon an assumption that the gas phase is an ideal solution, and fugacity is chosen as the potential. It takes into account end corrections to the length of the diffusion path which amounted to less than 1.5% of the average transfer distance. The resistance in the interface shown in Equation (1) was found to be negligibly small and has not been presented in this discussion because with the accuracy of evaluation of this effect attainable its existence was uncertain. In any event the total influence of the resistance in the interface was in no case more than 1% of the total resistance to transport, and a first order correction was made for its influence as indicated in Equation (1).

If the gas phase is treated as a perfect gas, Equation (1) assumes the form

$$D_{M,k} = \frac{\overset{\circ}{m}_k b_k T (l_G - l_c)}{\ln\left(\frac{p_{i,t}}{p_{i,i} + b_k T r_{i,k} \overset{\circ}{m}_k}\right)} \quad (2)$$

If length corrections and interfacial resistance are neglected, Equation (2) assumes the conventional form

$$D_{M,k} = \frac{\overset{\circ}{m}_k b_k T l}{\ln\left(\frac{p_{i,t}}{p_{i,i}}\right)} \quad (3)$$

The values of the length correction were determined from experimental data already available (*4*). It was assumed that this correction was solely a function of the Reynolds number of the flow at the exit to the transport path. The diameter of the exit tubes was used as a characteristic length. In the present instance the effective transport length was described by (*5*).

$$l = l_G - 4.90 \times 10^{-4} \frac{\eta_r}{\eta} \overset{\circ}{m}_t \quad (4)$$

In Equation (4) the reference viscosity corresponds to that of pure methane at 100°F. and atmospheric pressure.* The viscosity at the state in question was determined from available information concerning the influence of pressure and temperature upon the behavior of methane (*15*). In estimating the viscosity of the gas phase no regard was taken of the effect of small quantities of *n*-heptane present in the recirculating gas.

*The dimensional constant 4.90×10^{-4} is expressed in (ft.)(sec.)/lb.

MATERIALS

The *n*-heptane employed for this study was obtained as research grade from the Phillips Petroleum Company. The air-free sample had a specific weight of 42.4229 at 77° F., which compares satisfactorily with a value of 42.417 reported by Rossini (*14*) for an air-saturated sample at the same temperature. The index of refraction for the *D* lines of sodium was found to be 1.3852, in comparison with a value of 1.38517 reported by Rossini for 77° F. It appears that the sample of *n*-heptane used in this investigation was relatively free of impurities and probably contained more than 0.998 mole fraction *n*-heptane.

TABLE 1. EXPERIMENTAL MAXWELL DIFFUSION COEFFICIENTS FOR *n*-HEPTANE

Pressure, lb./sq. ft.	Temperature transport path, °F.	Diffusion coefficient: Perfect gas, lb./sec.	Diffusion coefficient: Ideal solution, lb./sec.
	Ethane–*n*-Heptane		
2,393	100.56	0.0929	0.0951
3,620	100.56	0.0986	0.1002
2,429	99.96	0.1154	0.1173
2,226	160.60	0.1353	0.1397
2,287	160.50	0.1447	0.1496
3,019	160.61	0.1377	0.1422
7,223	160.02	0.1230	0.1289
4,402	160.01	0.1228	0.1271
7,353	160.02	0.1096	0.1143
5,113	190.00	0.1537	0.1617
7,791	190.05	0.1445	0.1533
4,422	189.99	0.1451	0.1556
5,992	219.98	0.1701	0.1834
8,482	220.05	0.1681	0.1806
5,071	220.03	0.1738	0.1779
	Propane–*n*-Heptane		
2,122	100.70	0.0623	0.0636
2,158	130.57	0.0829	0.0851
2,314	130.64	0.0881	0.0913
4,382	130.59	0.0655	0.0684
4,375	160.59	0.0831	0.0849
3,058	160.58	0.0945	0.0982
4,469	160.66	0.0778	0.0817
6,627	160.60	0.0660	0.0702
6,696	190.63	0.0838	0.0899
4,392	190.62	0.1038	0.1100
3,561	190.65	0.1117	0.1176
6,644	220.55	0.1256	0.1362
8,370	220.58	0.0945	0.1032
4,952	220.66	0.1137	0.1223
7,137	220.63	0.1130	0.1224

The sample of ethane utilized in the study of the ethane–*n*-heptane system was obtained from Phillips Petroleum Company as research grade and was reported to contain not more than 0.0006 mole fraction impurities. A mass spectrometric analysis of this sample of ethane indicated that the dried material contained less than 0.00028 mole fraction of material other than compounds containing two carbon atoms. Care was exercised to avoid contamination of the sample during introduction to the apparatus, but no purification of the ethane was made other than to dry it over anhydrous calcium sulfate.

The propane was also obtained from Phillips Petroleum Company as pure grade. This material was subjected to mass spectrometric analysis, and the dried sample was found to contain less than 0.0002 mole fraction of impurities. The impurities present were compounds containing four carbon atoms. Before introduction into the diffusion apparatus, this material was carefully dried by passage over anhydrous calcium sulfate at pressures in excess of 100 lb./sq. in.

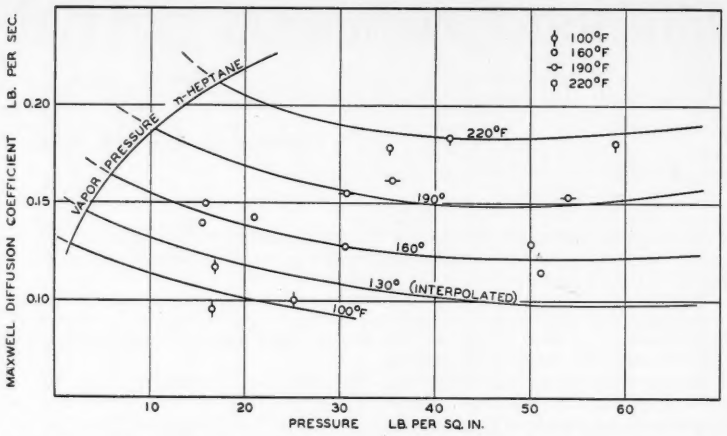

Fig. 1. Effect of pressure upon the Maxwell diffusion coefficient for *n*-heptane in the gas phase of the ethane–*n*-heptane system.

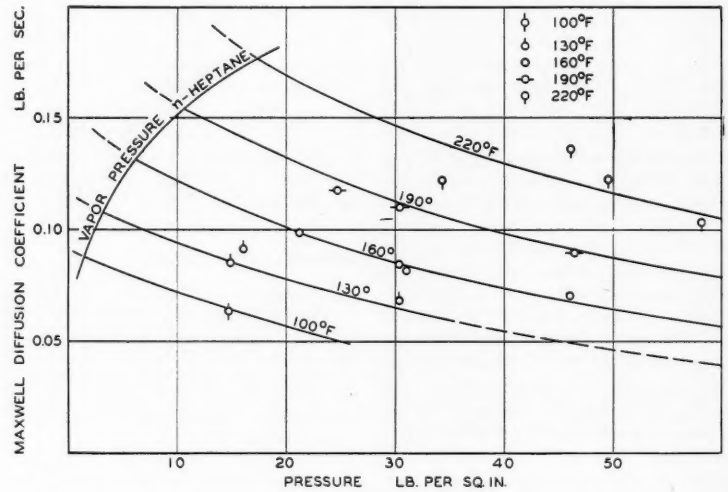

Fig. 2. Effect of pressure upon the Maxwell diffusion coefficient for *n*-heptane in the gas phase of the propane–*n*-heptane system.

EXPERIMENTAL RESULTS

In the investigation of the Maxwell diffusion coefficient for *n*-heptane in the ethane–*n*-heptane and in the propane–*n*-heptane systems, the minimum pressure studied was fixed by approach to the vapor pressure of *n*-heptane where uncertainties as to the behavior at the interface became important. As a result of the relatively high rate of diffusion of ethane and propane into the *n*-heptane liquid some difficulties were experienced from the transport of ethane and propane through the fritted-glass disk at the higher pressures. For example, it was necessary to limit the measurements at 100° F. to pressures below 25 lb./sq. in. Throughout the temperature interval investigated it was not possible to make measurements at pressures much below twice the vapor pressure of *n*-heptane at the temperature in question.

The results of the experimental measurements with the ethane–*n*-heptane and the propane–*n*-heptane systems are available (*3*). Each measurement of diffusion coefficients required approximately 14 hr. for its completion. The information available (*3*) is sufficient to establish the Maxwell diffusion coefficients of *n*-heptane in these systems when taken with the collateral thermodynamic properties of the gas phase, the vapor pressure, and fugacity of *n*-heptane. The Maxwell diffusion coefficients were calculated from the available data (*3*) on the basis of Equations (1) and (2) and are recorded in Table 1. The difference in the Maxwell diffusion coefficients computed on the basis of ideal solutions and of perfect gases is not significant at the lowest temperature but becomes of significant interest at the higher temperatures.

The fugacity and compressibility factor of *n*-heptane and the compressibility factors of ethane and propane were obtained by application of the Benedict equation of state (*1, 2, 8*). The vapor pressure of *n*-heptane

Table 2. Maxwell Diffusion Coefficients for *n*-Heptane in the Ethane–*n*-Heptane System

Temperature, °F.	Pressure, lb./sq. in. 14.696	20	30	40	50	60
100	0.1070*	0.1010	0.0920			
130	0.1250	0.1179	0.1081	0.1019	0.0980	0.0979
160	0.1468	0.1385	0.1280	0.1235	0.1220	0.1220
190	0.1789	0.1690	0.1565	0.1500	0.1484	0.1520
220	—	0.2050	0.1901	0.1840	0.1840	0.1869

*Maxwell diffusion coefficients expressed in lb./sec.

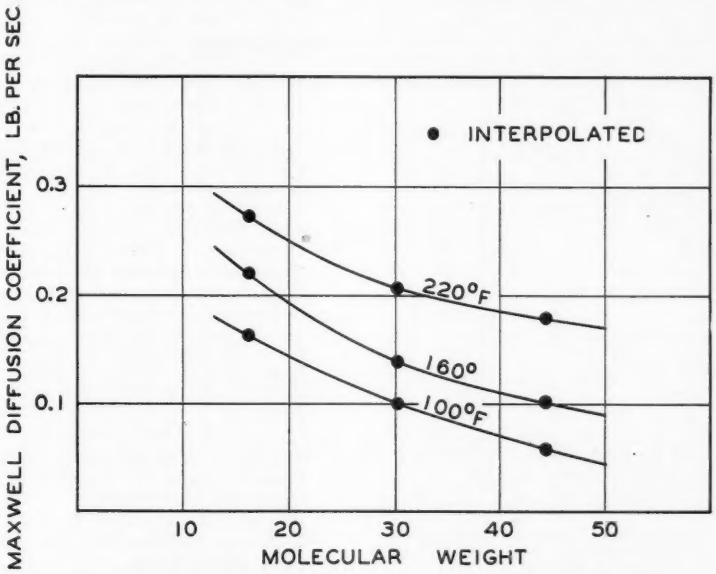

Fig. 3. Effect of molecular weight of stagnant component on diffusion coefficients for *n*-heptane.

was taken from a critical review of Rossini (*14*), supplemented by the experimental measurements of Young (*23*). The values of vapor pressure employed were associated with the temperature of the interface. This interfacial temperature differs slightly from that of the transport path. The composition of the gas phase at the interface and in the condenser was estimated from ideal solutions (*11*) and fugacity data calculated from the Benedict equation of state (*2*). It was predicated upon the existence of local equilibrium (*10*).

The experimental results for the Maxwell diffusion coefficients for *n*-heptane in the ethane–*n*-heptane system are shown in Figure 1. The behavior at 130° F. was interpolated from measurements at the other temperatures. The standard deviation of the experimental data shown from the smoothed curves of Figure 1 was 0.00686 lb./sec. and the corresponding average deviation without regard to sign was 0.00565 lb./sec. Smoothed values of the Maxwell diffusion coefficients for *n*-heptane in the gas phase of the ethane–*n*-heptane system are given in Table 2. These data were interpolated from the experimental results shown in Figure 1. The minima shown in the curves of Figure 1 resulted from fitting a three-coefficient curve to the data by least squares methods. The existence of this minimum may be open to some question, but this representation yields a much smaller standard deviation than does a linear presentation.

The experimental measurements upon the transport of *n*-heptane in the gas phase of the propane–*n*-heptane system are shown in Figure 2. In this case measurements were obtained at five temperatures evenly spaced between 100° and 220° F. The experimental data indicate a progressive decrease in the Maxwell diffusion coefficients with an increase in pressure for this system. The standard deviation of the measurements shown in Figure 2 and recorded in a part of Table 1 from the smoothed curve was 0.00692 lb./sec. The corresponding average deviation without regard to sign was 0.00447 lb./sec. The data for 130° F. were extended in Figure 2 to pressures somewhat above the range of the experimental measurements. The added uncertainty in this region has been indicated by a dashed curve. Likewise, the curves have been extended to pressures below the vapor pressure of *n*-heptane to indicate that the boundary of the heterogeneous region is not a limitation of the region of pressure and temperature in which the Maxwell diffusion coefficients may be employed. Smoothed values of the Maxwell diffusion coefficients for *n*-heptane in the gas phase of the propane–*n*-heptane system are shown in Table 3.

It should be emphasized that throughout the analysis of the experimental data it was assumed that the Maxwell hypothesis is descriptive of the transport of *n*-heptane at a specified pressure and temperature throughout the composition interval encountered in the apparatus. It is probable that some improvement in the description of the experimental results could have been obtained by use of the methods suggested by Chapman and Cowling (*7*), but such refinements were not justified in the present instance because of the uncertainties in the primary measurements. As more is learned concerning the transport characteristics of the hydrocarbons of intermediate molecular weight, corrections for the effect of composition upon the Maxwell diffusion coefficients can be made. The experimental data available (*3*) permit the reader to make such calculations if they should be of interest. Likewise a comparison with the predicted effect of pressure (*7*) upon the Maxwell diffusion coefficient can well await the accumulation of additional experimental facts over a wider range of pressure than was studied in the present instance.

Available information concerning the diffusion of *n*-heptane in the gas phase of the methane–*n*-heptane system (*5*) together with the information presented here permits the effect of the nature of the stagnant component on the transport characteristics of this paraffin hydrocarbon to be estimated. Figure 3 presents interpolated values of the Maxwell diffusion coefficients at 20 lb./sq. in. for *n*-heptane in the gas phase of the methane–*n*-heptane, ethane–*n*-heptane, and the propane–*n*-heptane systems. The points shown are the experimental data for each of the several binary systems interpolated to a pressure of 20 lb./sq. in. The data indicate a rather marked decrease in the Maxwell diffusion coefficient with an increase in the molecular weight of the stagnant component. This effect is more pronounced at the lower temperatures. The behavior depicted in Figure 3 for *n*-heptane is similar to that found for *n*-hexane in the corresponding binary systems (*6*).

TRANSPORT CHARACTERISTICS

For perfect gases the Fick diffusion coefficient is related to the Maxwell diffusion coefficient in the following way (*5, 13*):

$$D_{F,k} = \left(\frac{n_i}{n_i}\right) \frac{D_{M,k}}{P} \qquad (5)$$

Equation (5) was utilized to compute values of the Fick diffusion coefficient for *n*-heptane. These are available (*3*) for the ethane–*n*-heptane and the propane–*n*-heptane systems, respectively. The variation in composition with position in a transport path may be determined from Equation (2). The values of the Fick diffusion coefficient were calculated from the foregoing expression as a function of composition and pressure on the assumption that the Maxwell diffusion coefficient was independent of composition. The Fick diffusion coefficients are a marked function of composition, pressure, and temperature of the phase at the point at which the transport takes place. The effect of temperature on the product of pressure and the Fick diffusion coefficient for *n*-heptane is shown in Figure 4. The behavior of *n*-heptane in the methane–*n*-heptane system (*5*) was included for comparison. There is a progressive decrease in the Fick diffusion coefficient

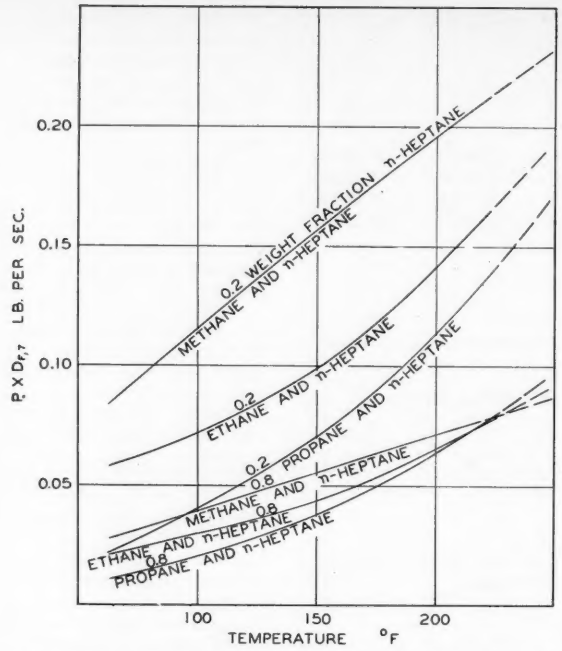

Fig. 4. Fick diffusion coefficients for *n*-heptane in the gas phase at 20 lb./sq. in.

with an increase in molecular weight of the stagnant component.

The coefficients for the components of an ideal solution are related by the following expression:

$$D_{F,i} = \frac{\sigma_k^0}{\sigma_i^0} D_{F,k} \qquad (6)$$

By use of Equation (6) the values for the Fick diffusion coefficients of ethane and propane in the systems studied were computed and are available (*3*).

ACKNOWLEDGMENT

This work is a contribution from Project 37 of the American Petroleum Institute at the California Institute of Technology. Jacques Bodes assisted with the experimental work, Betty Kendall carried out the calculations, and Elizabeth McLaughlin contributed to the preparation of the manuscript, which was reviewed by W. N. Lacey.

NOTATION

b_k = specific gas constant of component k, ft./°R.

$D_{F,k}$ = Fick diffusion coefficient of component k, sq. ft./sec.

$D_{M,k}$ = Maxwell diffusion coefficient of component k, lb./sec.

f_k = fugacity of component k, lb./sq. ft.

f_k^0 = fugacity of component k in pure state, lb./sq. ft.

l = effective transport length, ft.

l_c = effective correction to gross transport length, ft.

l_G = gross transport length, ft.

ln = natural logarithm

$\overset{\circ}{m}_k$ = weight rate of transport of component k, lb./(sq. ft.)(sec.)

$\overset{\circ}{m}$ = total weight rate of transport, lb./sec.

n_k = weight fraction of component k

η_k = mole fraction of component k

p_k = partial pressure of component k, $(P\eta_k)$, lb./sq. ft.

P = pressure, lb./sq. ft. abs.

r_i = interfacial resistance, sec./ft.

T = thermodynamic temperature, °R.

Z = compressibility factor of gas phase

η = absolute viscosity of gas phase, (lb.)(sec.)/sq. ft.

σ_k = specific weight of component k, lb./cu. ft.

Table 3. Maxwell Diffusion Coefficients for *n*-Heptane in the Propane–*n*-Heptane System

Temperature, °F.	Pressure, lb./sq. in. 14.696	20	30	40	50	60
100	0.0645*	0.0569				
130	0.0860	0.0780	0.0650	0.0549		
160	0.1119	0.1010	0.0854	0.0740	0.0648	0.0569
190	0.1459	0.1329	0.1130	0.0982	0.0880	0.0789
220	—	0.1696	0.1471	0.1302	0.1161	0.1055

*Maxwell diffusion coefficients expressed in lb./sec.

Superscript

0 = pure substance

Subscripts

i = conditions at interface
j = stagnant component
k = diffusing component
r = reference state
t = conditions at exit of transfer section

LITERATURE CITED

1. Benedict, M., G. B. Webb, and L. C. Rubin, *J. Chem. Phys.*, **8**, 334 (1940).
2. ———, and Leo Friend, *Chem. Eng. Progr.*, **47**, 419, 449, 571, and 609 (1951).
3. Carmichael, L. T., and B. H. Sage, Document 4833, Am. Doc. Inst., Photoduplication Service, Library of Congress, Washington, D. C. (1956).
4. Carmichael, L. T., H. H. Reamer, and B. H. Sage, Document 4611, Am. Doc. Inst., Photoduplication Service, Library of Congress, Washington, D. C. (1955).
5. ———, and W. N. Lacey, *Ind. Eng. Chem.*, **47**, 2205 (1955).
6. Carmichael, L. T., B. H. Sage, and W. N. Lacey, *A.I.Ch.E. Journal*, **1**, 385 (1955).
7. Chapman, S., and T. G. Cowling, "The Mathematical Theory of Non-Uniform Gases," Cambridge University Press, Cambridge, Eng. (1939).
8. Connolly, T. J., S. P. Frankel, and B. H. Sage, *Am. Inst. Elec. Engrs. Misc. Paper*, 50-259 (1950).
9. Jost, W., "Diffusion in Solids, Liquids, Gases," Academic Press, Inc., New York (1952).
10. Kirkwood, J. G., and B. Crawford, Jr., *J. Phys. Chem.*, **56**, 1048 (1952).
11. Lewis, G. N., *J. Am. Chem. Soc.*, **30**, 668 (1908).
12. Maxwell, J. C., "Scientific Papers," Vol. 2, Cambridge University Press, Cambridge, Eng. (1890).
13. Opfell, J. B., and B. H. Sage, *Ind. Eng. Chem.*, **47**, 918 (1955).
14. Rossini, F. D., *et al.*, "Selected Values of Physical and Thermodynamic Properties of Hydrocarbons and Related Compounds," Carnegie Press, Pittsburgh (1953).
15. Sage, B. H., and W. N. Lacey, *Trans. Am. Inst. Mining Met. Engrs.*, **127**, 118 (1938).
16. Schlinger, W. G., H. H. Reamer, B. H. Sage, and W. N. Lacey, "Report of Progress-Fundamental Research on Occurrence and Recovery of Petroleum, 1952–1953," Am. Petroleum Inst., pp. 70–106.
17. Sherwood, T. K., and R. L. Pigford, "Absorption and Extraction," McGraw-Hill Book Company, Inc., New York (1952).
18. Stefan, J., *Ann. Phys.*, **41**, 725 (1890).
19. ———, *Sitzber. Akad. Wiss. Wien, Math. Naturw. Kl., Abt. IIb*, **63**, 63 (1871).
20. *Ibid.*, **65**, 323 (1872).
21. *Ibid.*, **83**, 943 (1881).
22. Wilke, C. R., and C. V. Lee, *Ind. Eng. Chem.*, **47**, 1253 (1955).
23. Young, S., *Sci. Proc. Roy. Dublin Soc.*, **12**, 374 (1910).

Application of Bernoulli's Equation to Buoyant Systems

B. F. RUTH and D. R. BOYLAN

Iowa State College, Ames, Iowa

The various forms of Bernoulli's equation as customarily written express static pressure energy in terms of absolute pressure, thereby restricting their direct application to systems situated *in vacuo*. It is shown here that recognition (1) of the universal presence of a fluid outside all systems over which Bernoulli's equation is written, and (2) of the practical necessity of measuring pressure within such systems as gauge pressures relative to the pressure of the exterior fluid leads to a more general set of equations and to a concept of buoyant static pressure and potential energies, as opposed to strictly absolute values.

Failure properly to distinguish between these two types of energy quantities may result in error and confusion in the application of the various forms of Bernoulli's equation.

The terms in the Bernoulli equation as generally written in hydraulics are often referred to as *heads* since the units are commonly expressed as *feet*. This concept of fluid columns standing to various heights is valuable and appropriate in applications to the flow of incompressible fluids. However, when it is applied to compressible fluids considerable error may be introduced. It is the purpose of this paper to present a more rigorous concept of the terms in Bernoulli's equation which will be appropriate for all fluids under any conditions.

The integrated form of Bernoulli's equation

$$pv + \frac{V^2}{2g_c} + Z = \text{constant} \quad (1)$$

is a consequence of Newton's laws of motion and was developed at least fifty years before Helmholtz unambiguously stated the First Law of Thermodynamics. The equation is, however, a restricted form of the First Law and can be derived from the general energy equation (*1*). An analysis of the units and character of the terms of the general energy equation will, therefore, be applicable to the Bernoulli equation.

The general energy equation is written, according to accepted practice, as

$$Z_1 + U_1 + p_1v_1 + V_1^2/2g_c + Q = Z_2 + U_2 + p_2v_2 + V_2^2/2g_c + Ws \quad (2)$$

The terms of this equation are energy terms and must be expressed in equivalent units, i.e., foot pounds force per pound mass. This can be accomplished by writing (2) as

$$Z_1\left(\frac{g}{g_c}\right) + JU_1 + p_1v_1 + V_1^2/2g_c + JQ = Z_2\left(\frac{g}{g_c}\right) + JU_2 + p_2v_2 + V_2^2/2g_c + W_s \quad (3)$$

where J is the mechanical equivalent of heat (778 ft. lb. force/B.t.u.), g is the local acceleration of gravity (ft./sec.^{2}), and g_c is the dimensional constant in Newton's law [32.1740 (lb. mass) (ft.)/(lb. force)(sec.^{2})]. Combining Equation (3) with the first and second law and introducing the degree of reversibility F gives, in consistent units,

$$\frac{g}{g_c}(Z_2 - Z_1) + \int_{p_1}^{p_2} v\,dp + \frac{(V_2^2 - V_1^2)}{2g_c} = -JF - W_s \quad (4)$$

If this equation is multiplied by g_c/g, a form of Bernoulli's equation results which includes friction and in which the units of each term are simply feet.

$$(Z_2 - Z_1) + \left(\frac{g_c}{g}\right)\int_{p_1}^{p_2} v\,dp + \frac{(V_2^2 - V_1^2)}{2g} = -\left(\frac{g_c}{g}\right)JF - \left(\frac{g_c}{g}\right)W_s \quad (5)$$

Equation (5) contains the ratio g_c/g, which relates Newton's gravitational constant g_c to the local acceleration of gravity. For certain applications this ratio is unity, and the equation is commonly used without regard to the magnitude of the ratio. For general application, however, the equation as written in (5) must be used.

For isothermal flow and small changes in absolute pressures, Equation (4) becomes

$$(g/g_c)(Z_2 - Z_1) + (p_2 - p_1)v_{avg} + \frac{(V_2^2 - V_1^2)}{2g_c} = -JF - W_s \quad (6)$$

The symbol p in the foregoing equations represents absolute pressure, a quantity customarily evaluated by adding Bourdon gauge pressures or manometer readings in pounds force per square feet to the barometric pressure expressed in the same units. Since the difference of two absolute pressures thus evaluated is the same as the difference between the original gauge pressures or the difference indicated upon a manometer, the pressures conveniently used in practice are gauge pressures.

In the application of Equations (1) through (6) the almost universal presence outside the system of some buoyant fluid such as air is generally neglected. This practice produces an error, as the term Δp, the difference of absolute pressures, is no longer exactly equal to ΔP, the difference in gauge pressures. The error is small when incompressible fluids or liquids are involved or when systems over which the equation is written contain no elevation change. For compressible fluids such as gases or for cases where the system contains an elevation change, the error can become so large as to yield quite inaccurate and even absurd results. This is illustrated in the following example.

Illustration 1

Problem. A cylindrical brick chimney 108 ft. tall (measured from the center line of the breeching) and 7.5 ft. in diameter develops a draft of 0.600 in. of water at the base of the chimney (barometer normal, atmospheric temperature 62°F.) when the furnace it serves is fired at such a rate as to produce 1.715 moles/sec. of stack gas having an average molecular weight of 30.2 and an average temperature of 500°F.

It is necessary to double the steam-generating capacity by installation of a second identical furnace and boiler. Rather than build another chimney, it is proposed to conduct the gases from the second furnace into the breeching of the first by means of a Y connection, as illustrated in Figure 1, and by installing an induced-draft fan at the base of the chimney to compensate for the reduction in natural draft. What will be the theoretical power consumption of such a fan?

Solution. Writing the Bernoulli equation as commonly used between *d* and *e* of Figure 1 for the original furnace (no friction loss in the breeching assumed) gives

$$\left(\frac{g}{g_c}\right)\Delta Z + \frac{\Delta V^2}{2g_c} + v\Delta P = -JF - W_s$$

If $W_s = 0$ and it is assumed that $V_1 = V_2$ and that $g/g_c = 1.0$

$$\Delta Z + v\Delta P + JF = 0$$

or with

$$JF = \Delta H_f = \frac{2fLV^2}{g_cD},$$

The original manuscript was conceived and written by Dr. B. F. Ruth. His death on January 1, 1954, left this and other manuscripts unfinished and unpublished. Dr. Boylan has rewritten in part and revised the original manuscript.

$$(Z_2 - Z_1) + \frac{(P_2 - P_1)}{\rho_{avg}} + \Delta H_f = 0$$

$$Z_2 = 108 \text{ ft.}$$

$$Z_1 = 0$$

$$P_2 = 0 \text{ gauge pressure}$$

$$P_1 = -\frac{0.600 \times 62.3}{12}$$

$$= -3.115 \text{ lb./sq. ft.}$$

$$\rho_{avg} = \frac{30.2}{359} \times \frac{492}{960}$$

$$= 0.0431 \text{ lb./cu. ft.}$$

$$\Delta H_f = -108 - \left(\frac{3.115}{0.0431}\right)$$

$$= -108 - 72.3 = \frac{2fLV^2}{g_c D}$$

$$= -180.3$$

$$f = -\frac{180.3 g_c D}{2LV^2}$$

$$= -\frac{180.3 \times 32.17 \times 7.5}{2 \times 108 \times (27.2)^2}$$

$$= -0.273,$$

which is absurd as f is negative.

DERIVATION OF MODIFIED EQUATIONS

The modification needed to make Bernoulli's equation as generally used in its various forms applicable under all conditions is derived as follows.

The level of the mercury well of a conveniently situated barometer may be considered as the datum of elevation and the static pressure of the atmosphere at this level as the datum of pressure; the absolute pressures within a system at elevations Z_1 and Z_2 may be expressed as

$$p_1 = P_1 + B - Z_1(g/g_c)\rho_0 \quad (7)$$

$$p_2 = P_2 + B - Z_2(g/g_c)\rho_0 \quad (8)$$

where ρ_0 is the average density of the outside fluid between the datum and elevations Z_1 and Z_2, B is the barometric pressure at the elevation datum, and P_1 and P_2 are the pressure differences between system fluid and outside fluid measured at the elevations Z_1 and Z_2. Representing the quantities $(P_1 + B)$ and $(P_2 + B)$ by the symbols p_1' and p_2' and substituting into Equation (3) gives, upon rearrangement,

$$Ju_1 + Z_1(g/g_c)(1 - \rho_0 v_1) + p_1'v_1 + V_1^2/2g_c + JQ = Ju_2 + Z_2(g/g_c)(1 - \rho_0 v_2) + p_2'v_2 + V_2^2/2g_c + W_s \quad (9)$$

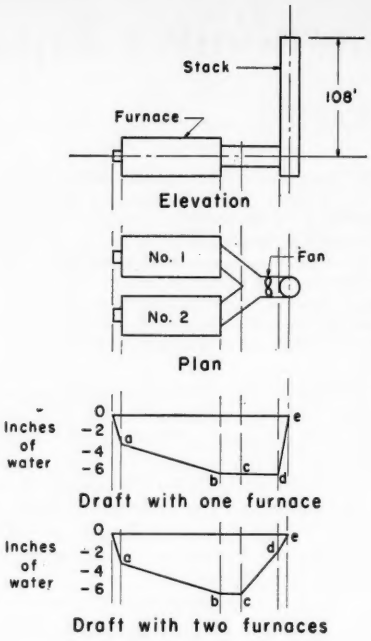

Fig. 1. Furnace arrangement.

From Equation (9) the corresponding mechanical-energy-balance equation is obtained as

$$Z_1(1 - \rho_0 v_1)(g/g_c) + V_1^2/2g_c - W_s - \int_{p_1'}^{p_2'} v\,dp - JF = Z_2(1 - \rho_0 v_2)(g/g_c) + V_2^2/2g_c \quad (10)$$

If it is assumed that the variation of v is linear with Z, Equation (10) becomes, for isothermal flow and small changes in the absolute pressure,

$$(Z_2 - Z_1)(g/g_c)(1 - \rho_0 v_{Z_{avg}}) + (V_2^2 - V_1^2)/2g_c + (P_2 - P_1)v_{avg} = -JF - W_s \quad (11)$$

as $(p_2' - p_1')$ is identically $(P_2 - P_1)$.

The specific volume of the system fluid in the potential energy difference term has been written as $v_{Z_{avg}}$ to indicate that it is not necessarily the same quantity as v_{avg} in the static pressure energy term but is instead the arithmetic average value of v over only that portion of a system in which the elevation change from Z_1 to Z_2 takes place. Strictly speaking, of course, Bernoulli's equation when applied to gases should never be written over the entire length of a complicated system. The continual change in specific volume and velocity from point to point in a complex system makes it much safer to apply the theorem in its various forms in a series of steps, solving for intermediate values of pressure, density, and velocity before and after each important change in velocity, temperature, or elevation. Such a procedure, however, is quite laborious.

When the density ρ_0 of the outside fluid approaches zero, $(P_1 + B_1)$ and $(P_2 + B_2)$ approach p_1 and p_2, and the term $(Z_2 - Z_1)(g/g_c)(1 - \rho_0 v_{Z_{avg}})$ approaches $(Z_2 - Z_1)(g/g_c)$, showing that Equations (9), (10), and (11) are fundamentally the same as Equations (3), (4), and (6) but are directly applicable to any fluid under any conditions. The previous illustration can now be simply solved by use of Equation (11) and the convenient gauge pressure difference.

Applying Equation (11) to illustration 1, where it is assumed that $V_1 = V_2$, $W_s = 0$, and $g/g_c = 1.0$ as before

$$(Z_2 - Z_1)(1 - \rho_0 v_{Z_{avg}}) + \frac{\Delta P}{\rho_{avg}} + JF = 0$$

$$\rho_0 = \frac{29}{359} \times \frac{492}{522} = 0.0762 \text{ lb./cu. ft.}$$

$$V = \frac{1.715 \times 30.2}{0.0431} \times \frac{4}{(7.5)^2\pi}$$

$$= 27.2 \text{ ft./sec.}$$

$$(108 - 0)\left(1 - \frac{0.0762}{0.0431}\right) + \frac{(0 + 3.115)}{0.0431} + \Delta H_f = 0$$

$$-\Delta H_f = -\frac{2fLV^2}{g_c D}$$

$$= (108 - 191) + 72.3$$

or

$$\Delta H_f = 83 - 72.3 = 10.7$$

and

$$f = \frac{10.7 \times g_c \times D}{2LV^2}$$

$$= \frac{10.7 \times 32.17 \times 7.5}{2 \times 108 \times (27.2)^2}$$

$$f = 0.0162$$

Now

$$Re = \frac{Dv\rho}{\mu}$$

$$= \frac{7.5 \times 27.2 \times 0.0431}{0.028 \times 0.000672}$$

$$= 467{,}000$$

The roughness factor f/D, therefore, is 0.04 to 0.05, a condition where f is independent of Re. For the new furnace the velocity doubles but $f = 0.0162$ and the new draft at the base of the furnace is

$$-\frac{\Delta P}{\rho_{avg}} = \frac{P_1 - P_2}{\rho_{avg}}$$

$$= (Z_2 - Z_1)(1 - \rho_0 v_{Z_{avg}}) + \Delta H_f$$

$$\frac{P_1 - 0}{0.0431} = (108 - 0)(1 - \rho_0 v_{Z_{avg}})$$

$$+ 0.0162 \times \left(\frac{54.4}{27.2}\right)^2 \times 662$$

$$= -83 + 42.9 = -40.1$$

$$P_1 = -0.0431 \times 40.1$$

$$= -1.73 \text{ lb./sq. ft.}$$

Writing Equation (11) from c to d in Figure 1 gives

$$\frac{(\Delta V)^2}{2g_c} + v_{avg}\Delta P + W_s = 0$$

where $\Delta Z = 0$

$$-W_s = \frac{(V_d^2 - V_c^2)}{2g_c} + \frac{P_d - P_c}{\rho_{avg}}$$

$$= \frac{(54.4)^2 - (27.2)^2}{2 \times 32.17}$$

$$+ \frac{(-1.73 + 3.115)}{0.0431}$$

$$= 34.5 + 32.1$$

$$= 66.6 \frac{\text{ft. lb. force}}{\text{lb. mass}}$$

Therefore, the theoretical hp. =

$$\frac{66.6 \times 1.715 \times 30.2 \times 2}{550} = 12.6 \text{ hp.}$$

In transforming the sum of the static pressure and potential energy terms from the form

$$pv + Z(g/g_c) \qquad (12)$$

$$= [B + P - Z(g/g_c)\rho_0]v + Z(g/g_c)$$

to

$$pv + Z(g/g_c) \qquad (13)$$

$$= (B + P)v + Z(g/g_c)(1 - \rho_0 v)$$

all that has been done, in effect, is to refer the static-pressure-energy term to an elevation datum as well as to a pressure datum and the potential energy term to a density or pressure datum, as well as an elevation datum. The result is to increase the absolute static-pressure potential energy from the value pv that it actually has at elevation Z to the slightly larger value it assumes when referred to the elevation $Z = 0$, where the absolute pressure is $p + Z(g/g_c)\rho_0$. Similarly, the potential head term is decreased from what it would be in a vacuum to the value $Z(g/g_c)(1 - \rho_0 v)$ that it actually has relative to an exterior fluid of density ρ_0. For this reason, the terms $(B + P)v$ and $Z(g/g_c)(1 - \rho_0 v)$ may be thought of, respectively, as buoyant static pressure and potential energies, in recognition of the effect of the external fluid medium. In the same way the energy-difference terms $(P_1 - P_2)v_{avg}$ and $(Z_1 - Z_2)(g/g_c)(1 - \rho_0 v_{Z_{avg}})$ may be termed *buoyant static pressure* and *potential energy differences* to distinguish them from the absolute differences $(p_1 - p_2)v_{avg}$ and $(Z_1 - Z_2)(g/g_c)$ of a system *in vacuo*.

While the use of the term *head* is still retained in speaking of the various terms of Bernoulli's equation, it is better to regard the units of head as comprising foot pounds of force per pound of mass, and not simply as feet of column height. With this approach and the recognition of buoyant static and potential heads as the effective and more realistic forces responsible for flow in a submerged system, the Bernoulli equation may be applied to all types of flow.

When dealing with heating and ventilating problems, most engineering text books and handbooks avoid or at least reduce error in the application of Equation (4) by suggesting that the potential-head-difference term be ignored. It is obvious from Equation (11) that when the system fluid is air at atmospheric pressure and temperature this recommendation does lead to an exact answer. When the density of the system fluid is greater or less than that of the outside fluid, the result is no longer exact although usually much closer to the correct value than it would be were the term $(Z_2 - Z_1)(g/g_c)$ to be included. It is apparent, however, that such a recommendation is entirely empirical and gives better results only because the term $(1 - \rho_0 v_{avg})$ is small, and not because the quantity $(Z_2 - Z_1)(g/g_c)$ is necessarily negligible. As another example, the following problem, given in a familiar text book (*2*), will be considered.

Illustration 2

Problem. Air at 70°F. is heated to 170°F. in a horizontal heater, thereby increasing its velocity from 20 ft./sec. at station 1 to 23.8 ft./sec. at station 2. The absolute pressure at station 1 is given as normal barometer; that at station 2 as 1 in. of water less. After the net heat input to the air in the heater is computed as 24.003 B.t.u./lb. of air, the question is raised as to whether the heat input would have been materially different had the heater exit been arranged vertically with the air leaving the apparatus at an elevation 10 ft. above the inlet.

Solution. The solution given is $(Z_2 - Z_1)/J = 10/778 = 0.0129$ B.t.u./lb. of air, additional heat input required.

However, as the gas passing through the vertical section has a density of 0.0690 lb./cu. ft. as compared with a density of 0.075 lb./cu. ft. for the outside air, it is clear that, other quantities remaining as before, the additional heat input is in reality given by

$$(Z_2 - Z_1)(g/g_c)(1 - \rho_0 v_{avg})/J$$

$$= (10 - 0)(1 - 0.075/0.0690)/778$$

$$= -0.00112 \text{ B.t.u./lb.; i.e.,}$$

the necessary heat input is actually smaller in the vertical than in the horizontal apparatus.

NOTATION

- B = absolute pressure of external buoyant fluid at zero datum of elevation (barometric pressure in the case of air), lb. force/sq. ft.
- D = pipe diameter, ft.
- F = heat input as a result of friction, B.t.u./lb. mass
- f = Fanning friction factor, dimensionless
- g = local acceleration of gravity, ft./sec.^{2}
- g_c = dimensional constant in Newton's law, 32.1740 (lb. mass) (ft.)/(lb. force)(sec.^{2}).
- J = mechanical equivalent of heat, 778 ft. lb. force/B.t.u.
- L = length of a conduit or pipe, ft.
- p = absolute pressure at elevation Z, lb. force/sq. ft.
- p' = absolute pressure at elevation Z referred to zero datum elevation. Buoyant absolute pressure, lb. force/sq. ft., = $(P + B)$
- P = gauge pressure at elevation Z. Pressure difference between system fluid and external fluid at elevation Z, lb. force/sq. ft.
- Q = heat added to the system, B.t.u./lb. mass
- U = internal energy, B.t.u./lb. mass
- V = average linear velocity of fluid flow, ft./sec.
- v = specific volume of system fluid, cu. ft./lb. mass
- v_{avg} = arithmetic average specific volume between stations 1 and 2, cu. ft./lb. mass
- $v_{Z_{avg}}$ = arithmetic average specific volume over section of system containing either an abrupt or gradual change in elevation, cu. ft./lb. mass
- W_s = external work performed by the system, ft. lb. force/lb. mass
- Z = elevation, ft.
- ρ = $1/v$, density, lb. mass/cu. ft.
- ρ_0 = average density of fluid outside a system, between the datum $Z = 0$ and elevations Z_1 and Z_2, lb. mass/cu. ft.

Subscripts

- 1 = upstream section
- 2 = downstream section

LITERATURE CITED

1. Coulson, J. M., and J. F. Richardson, "Chemical Engineering," vol. 1, pp. 22–24, McGraw-Hill Book Company, Inc., New York (1954).
2. McAdams, W. H., "Heat Transmission," 3d ed., p. 147, McGraw-Hill Book Company, Inc., New York (1954).

COMMUNICATIONS TO THE EDITOR

Vapor-liquid Equilibrium for the Benzene-acetone System

LAWRENCE N. CANJAR and THOMAS E. LONERGAN

Carnegie Institute of Technology, Pittsburgh, Pennsylvania

There are many conflicting data in the literature on the vapor-liquid–equilibrium phase relationships for the system benzene-acetone. Figure 1 illustrates the disagreement among the different investigators who have studied the problem. Composition and temperature data have been obtained by Soday and Bennett (*4*), Reinders and De Minjer (*3*), Othmer (*2*), Tallmadge and Canjar (*5*), and most recently by Canjar, Horni, and Rothfus (*1*). The last two investigations were carried out in this laboratory.

Activity coefficients were calculated by use of the expression

$$\gamma_i = \frac{y_i}{x_i}\frac{P}{P_i^0} \qquad (1)$$

and the data cited above. The logarithm of the ratio of activity coefficient of acetone to activity coefficient of benzene is plotted vs. mole fraction of acetone in Figure 1.

It will be noted that there is wide disagreement not only among all the investigators but also in the two works carried out in this laboratory. The first work, by Canjar and Tallmadge (*5*), was carried on for the primary purpose of obtaining integral isobaric heats of vaporization. The vapor-liquid-equilibrium data were obtained as a by-product of the experimental measurements. The second work, by Canjar, Horni, and Rothfus (*1*), was specifically designed for the determination of precise vapor-liquid–equilibrium data to be used in the study of a ternary system. In spite of this the former came closer to satisfying the thermodynamic consistency test

$$\int_0^1 \log \frac{\gamma_1}{\gamma_2}\, dx_1 = 0 \qquad (2)$$

(*Continued on page 14J*)

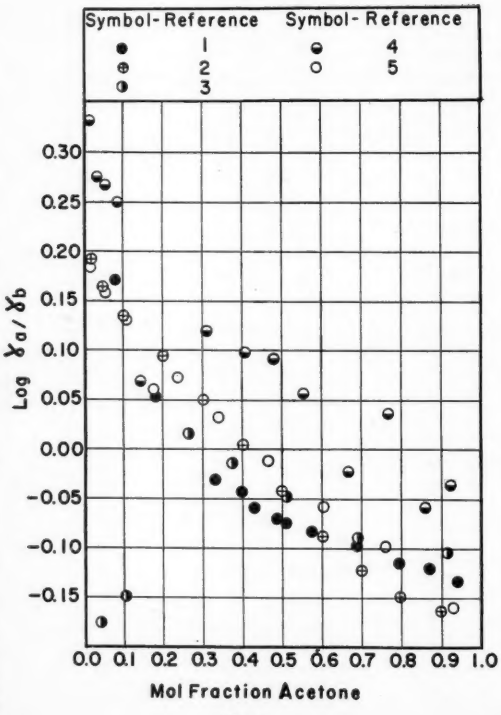

Fig. 1.

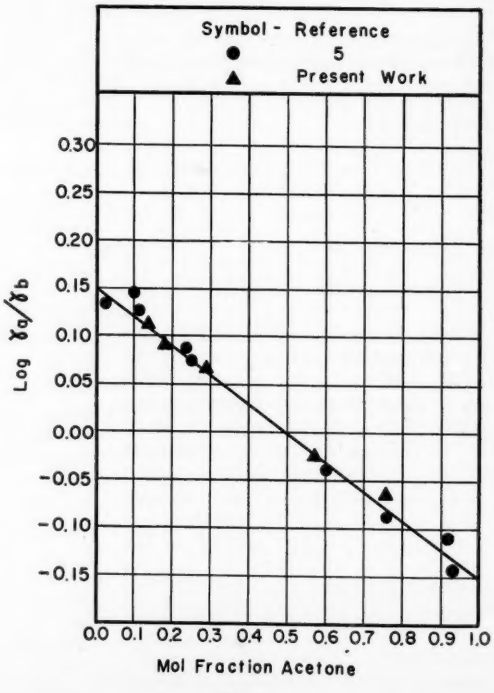

Fig. 2.

If you are concerned with:

Reactor development...
Atomic energy projects...
Nuclear problems...

This new data book will help you

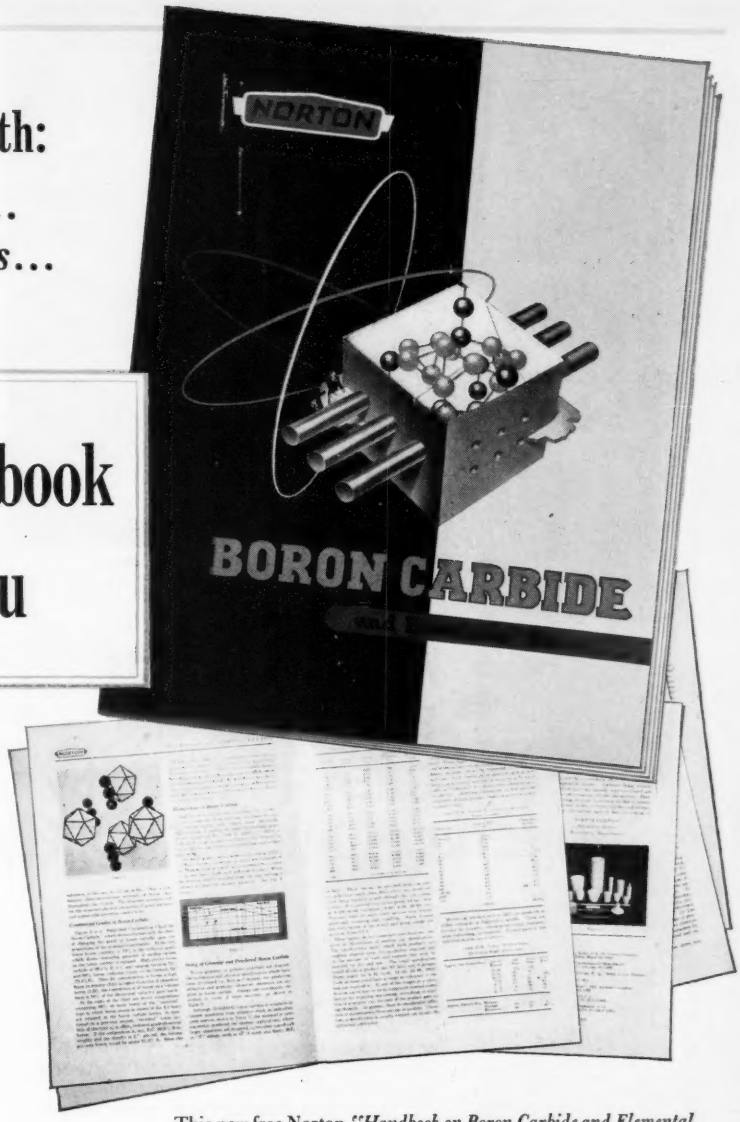

This new free Norton *"Handbook on Boron Carbide and Elemental Boron"*, is a valuable reference, containing both fundamental data and practical information. Printed in colors with many charts and tables it will serve as a useful and permanent addition to the reference files of those concerned with atomic energy and related fields.

In nuclear science and engineering the importance of the neutron absorption reaction of the boron isotope B^{10} is well recognized.

Now, for the first time, available data on the development of numerous stable, boron-rich materials have been compiled and coordinated by Norton in one convenient reference book.

This book is the *"Handbook on Boron Carbide and Elemental Boron"* — a compact source of technical information on materials made by Norton for use in the atomic energy field.

A partial list of the table of contents includes: *Boron for neutron absorption... Technical grade boron... Properties of boron... Commercial grades of boron carbide... Radiation damage to boron carbide... Bonded boron carbide (carbon, silicate, plastic, metal)... Boron nitride... Metal borides.* These and many other subjects are fully described and illustrated with tables, charts and photographs.

A Quarter-Century of Experience

Work in Norton laboratories on boron compounds began some 25 years ago. This included the development of NORBIDE* boron carbide, the hardest material yet produced commercially. Norton facilities for producing NORBIDE wear-resistant articles and abrasive have been expanded to supply boron carbide in numerous forms for atomic energy applications.

Recent Norton development has been aimed at improving the quality, increasing the production and reducing the costs of various boron-rich products. As a result, Norton now produces these materials to highest purity standards, at prices ranging between one-half and one-tenth of former pricing.

Other Norton Electric Furnace Products

of special interest to nuclear engineers include ALUNDUM* fused alumina, CRYSTOLON* silicon carbide, MAGNORITE* magnesium oxide, FUSED ZIRCONIA and various refractory carbides, oxides and nitrides.

Besides being the basic ingredients of the famous Norton Refractory R_x's — refractories *engineered and prescribed* for the widest range of conventional applications — these high-melting materials are finding many new and valuable uses in atomic energy projects.

They are all described in the new Norton handbook. For your free copy, write to NORTON COMPANY, Refractories Division, 671 New Bond St., Worcester 6, Massachusetts.

NORTON
REFRACTORIES
Engineered... Rx... Prescribed
Making better products... to make your products better

*Trade-Marks Reg. U. S. Pat. Off. and Foreign Countries.

(*Continued from page 280*)

than the latter. To resolve this discrepancy the system acetone and benzene was studied again by means of the apparatus described in (*1*). Preparation and purity of chemicals were also the same as described in (*1*). The results of this remeasurement are given in Figure 2, where they are compared with the original data of Canjar and Tallmadge, with which they are essentially in agreement. The Canjar-Tallmadge data given in Figure 1 represent smoothed temperature-composition data. The plot was taken from reference *1*.

The explanation of the disagreement between this work and the previous work obtained in the same laboratory by Canjar, Horni, and Rothfus (*1*) will help future investigators using the Othmer still. Our early experience with the Othmer stills indicated that high boiling or heat-input rates gave erratic and scattered results. Lower boiling rates on the other hand gave extremely precise and reproducible results. Therefore low boiling rates were used in the earlier investigation (*1*). In the present work it was found that the temperature in the Othmer still increased asymptotically with the rate of vapor boil-up. A boil-up rate of 120 ml./hr. yielded essentially a maximum temperature reading with no evidence of entrainment. The data given in Figure 2 were obtained with this rate. Unfortunately other investigators did not report their boil-up rates, and comparison is impossible.

The final data for the system acetone-benzene can be given by the relationship (strictly valid only for a system pressure of 1 atm.)

$$\log_{10} \gamma_i = 0.15(1 - x_i)^2 \qquad (3)$$

where γ_i, activity coefficient, is given by relationship (1) and vapor pressures of the pure components are given by the following:

Acetone

$$\log_{10} P_{atm.} = 4.14366 - \frac{1{,}161.0}{224.0 + t°\text{C.}} \qquad (4)$$

Benzene

$$\log_{10} P°_{atm.} = 4.02484 - \frac{1{,}211.033}{220.790 + t°\text{C.}} \qquad (5)$$

LITERATURE CITED

1. Canjar, L. N., E. C. Horni, and R. R. Rothfus, *Ind. Eng. Chem.*, **48**, 427 (1956).
2. Othmer, D. F., *loc. cit.*, **25**, 614 (1933).
3. Reinders, W., and C. H. De Minjer, *Rec. Trav. Chim.*, **59**, 369 (1940).
4. Soday, F. J., and G. W. Bennett, *J. Chem. Ed.*, **7**, 1336 (1930).
5. Tallmadge, J. A., and L. N. Canjar, *Ind. Eng. Chem.*, **46**, 1279 (1954).

BOOKS

Automatic Process Control for Chemical Engineers. Norman H. Ceaglske. John Wiley and Sons, Inc., New York (1956). 228 pages. $6.75.

A welcome addition to the number of texts already published on the subject of automatic control is this book by Professor Ceaglske. Perhaps the only misleading statement in the entire book is the title, which would seem to limit the readers to those with a chemical engineering background. It is true that the author designed this text primarily for the chemical engineer, and more specifically for the chemical engineering undergraduate student, but the reviewer feels that this book could serve equally as well as a source of valuable information for all practicing engineers whose knowledge of automation is mainly descriptive.

Professor Ceaglske has been associated with teaching the subject of automatic control to chemical engineering students since 1936 (presently as professor of chemical engineering at the University of Minnesota) and is of the opinion that the majority of courses taught today tend to retard progress in this important field. In an attempt to correct this, he presents a clear interpretation of the developments in automatic control theory over the past 20 years. The subject matter was compiled from the undergraduate courses taught by Professor Ceaglske and therefore deals with many elementary topics; however, the graduate student or the process engineer in industry would be well advised to read this introductory text before trying to master more advanced books.

The first two chapters give a brief history of automatic control; a descriptive treatment of various instruments, processes, and control systems; and the necessary terminology. The remainder of the book is divided into five parts, each of which covers a specific phase of the mathematical analysis. The control systems considered have been restricted to those having linear response, expressed by differential equations of the first and second order only. As prerequisites the author assumes a senior standing in chemical engineering, including a working knowledge of differential equations. The Laplace transform has been used throughout the book to solve the differential equations.

Chapters 3 and 4 are devoted to the derivations of the needed equations, and the solutions to these equations, for the majority of the control systems under study. The response of these systems or parts of the systems to the three standard inputs—the step change, the ramp input, and the sinusoidal input—has also been derived. The transient analysis and the frequency response of control systems have been fully discussed and explained in Chapters 5 and 6. As a concluding section the author has dealt with the analysis and preliminary design factors of some simple control systems. To demonstrate further the theoretical principles in this text the author has included a number of illustrative examples and has also presented a list of typical problems at the end of each chapter for solution by the reader.

RICHARD M. CLARKE

An Outline of Atomic Physics. Third edition. O. H. Blackwood, T. H. Osgood and A. E. Ruark. John Wiley and Sons, Inc., New York (1955). 501 pages. $7.50.

Those who are familiar with the two earlier editions of this book, published in the thirties, will welcome this new edition. Considerable revision and the addition of much new material have served to make this book on atomic physics an excellent introductory text for those students who desire a general knowledge of the modern particulate approach to matter, both atomic and nuclear. The book is an outgrowth of a course directed not to physics students but rather to any others having a year's work in college physics and a desire to know more about the concepts and methods of modern physics.

Approximately half of the book is devoted to the understanding of atomic phenomena, including X rays, atomic and molecular structure, radiation, and spectra, and an introduction to the solid state. The authors are to be especially commended in the manner in which they introduce and use the concepts of quantum mechanics. The discussions are not so oversimplified as to lose all meaning; rather they are introduced as needed, in a logical and quantitative manner, with the appropriate background of classical theory and the explanation of its breakdown. In fact, these sections provide an excellent introduction to quantum mechanics and could well be assigned as preliminary reading to a student about to engage in a more quantitative and mathematical course in quantum mechanics.

The remainder of the book is devoted to nuclear physics, including sections on nuclear structure and transmutations, elementary particles, cosmic rays, and a brief discussion of the applications of nuclear energy. The last chapter provides a brief introduction to the theory of relativity, although those portions of special relativity, such as the relativistic mass increase, are introduced earlier as needed. In fact, much of the material introduced in the earlier editions near the end of the book as special topics has been worked into the body of the text. For example, the uncertainty principle in the new edition is discussed in the chapter on waves associated with material particles, where the De Broglie relation and much of quantum mechanics are introduced.

This reviewer's major criticism is that the authors, perhaps irked as students by "beyond the scope of this text" statements, seem to feel that there is little that cannot be explained within their scope, at least qualitatively. A case in point is their five-paragraph coverage of the general theory of relativity, transferred unchanged from the earlier editions. Not only are their statements and interpretations of the principle of equivalence confusing but their choice of experimental verification, the results of which they state as conflicting, seems ill-conceived. The red shift, the evidence for which seems more conclusive, would have been just as easy to explain. The new section on magnetic susceptibilities will also probably be confusing to the student.

Except for such minor shortcomings as these, the book is excellent, should be quite teachable, and in addition should be

pleasant reading for those who wish a refresher in the field.

Introductory Nuclear Physics. Second edition. David Halliday. John Wiley and Sons, Inc., New York (1955). 493 pages.

The first edition of Professor Halliday's book, published in 1950, won immediate favor with many students then studying nuclear physics at the upper undergraduate and beginning graduate levels and with their instructors. Among its few competitors the book was distinguished for the wide breadth of material surveyed and for the clarity with which the many topics were presented.

Although the number of books on nuclear physics has grown rapidly since 1950, the second edition of *Introductory Nuclear Physics* should hold much of the popularity of its predecessor. It is still frankly an introductory text, covering the broad field of basic nuclear physics briefly and clearly. Topics include cosmic rays, subnuclear particles, and molecular beams, for example, as well as the standard fare of nuclear decays and radiations, particle detection, accelerations, reactions, fission, etc. The arrangement of the material has been improved over the first edition, and the early introduction of new chapters on elements of quantum mechanics and two-nucleon systems should be helpful to the reader. The reviewer recommends the book not only for pedagogical purposes, but also for the library of the nonspecialist in nuclear physics who wishes to have readily available one book in which clear, concise answers to his questions can probably be found.

GEORGE F. PIEPER

Electrons, Atoms, Metals and Alloys. William Hume-Rothery. Revised edition. Philosophical Library, New York (1955). 387 pages. $10.00.

This book, originally published in 1948, represents an attempt to teach modern concepts of atomic structure and the theory of the crystalline state of matter by means of a dialogue between a "Young Scientist" and an "Older Metallurgist." The latter, who took his degree in the period 1910-1920, is unable to keep up with modern advances in metallurgy and seeks the help of a member of the newer generation who brings him up to date in these matters. Topics covered begin with an introduction to quantum mechanics and proceed through the theory of atomic structure, free-electron theory of metals, Brillouin zone theory, ferromagnetism, and the theory of alloy formation. Also included are short sections on the theory of plastic deformation and the structure of the nucleus, both of which have been modified in this new edition as a result of recent developments.

Hume-Rothery states that the book is intended primarily for industrial metallurgists who wish to become acquainted with modern physical theories of metals and alloys and the dialogue form was chosen to make the material more palatable to such readers. How successful he has been in this objective is hard to say. Undoubtedly, a review of this book would best be given by an "Older Metallurgist" who has tried his hand at this novel form of education. It is hard to believe, however, that the few in this category who would have the perseverance to read this book

from start to finish would not also be able to attack the same material in the more conventional form. As for the graduate student studying the theory of metals and alloys, there is no doubt that another book by the same author ("Atomic Theory for Students of Metallurgy," The Institute of Metals, 1952), which covers essentially the same subject matter in conventional text-book form, would be a far more useful volume. Nevertheless, the present book may provide one who has already been exposed to the subject matter with a pleasant way to review the material and to increase his physical insight into the principles of quantum theory.

A. S. NOWICK

Nuclear and Radiochemistry. Gerhart Friedlander and Joseph W. Kennedy. John Wiley and Sons, Inc., New York (1955). 468 pages. $7.50.

This book is a new, revised edition of the widely used *Introduction to Radiochemistry*, written primarily as a text book of a graduate or senior undergraduate course in radiochemistry. The book is divided into thirteen chapters. It begins with a general survey of radioactivity, nuclear structure, and the elementary principles and methods for studying nuclear reactions. The rate equations of radioactive transformations are then derived and applied to a number of problems. This section is followed by an elementary but instructive survey of nuclear states and the related radioactive processes and a discussion of the interaction of radiation with matter with many useful applications. The theory and methods for the detection and measurement of radiation are then taken up in the three consecutive chapters. A brief but well-written review of radioactivity applied to chemistry is given in Chapter 11. Two new chapters have been added to this edition: Chapter 12 gives a survey of the design and operation of nuclear reactors, and Chapter 13 contains a stimulating discussion on some cosmic problems, viz., the production of energy in stars, cosmic rays, geo- and cosmochronology, and the genesis of the elements.

The effectiveness of presentation and the clarity of discussion which characterized the earlier edition is maintained in the present book. The list of references at the end of each chapter has been revised and expanded. An up-to-date table of nuclides is given in Appendix G. The isotopic masses listed in this table should be very useful and convenient for computations regarding nuclear reactions. Answers to most of the exercises are given. These exercises are often as instructive as the text itself and were included by the authors as an integral part of the course. Undoubtedly, *Nuclear and Radiochemistry* will continue to be the most widely used text book of introductory radiochemistry for many years to come.

J. H. WANG

Thermodynamics from the Classic and Generalized Standpoints. Joseph Louis Finck. Bookman Associates, New York (1955). 224 pages. $7.50.

This book is of interest to advanced students and those engaged in research in thermodynamics and applied fields. It is clearly written, well organized, and does not

contain any difficult mathematics. The result of the author's own work in the field, which has extended over many years, the book represents an attempt to extend the range of applicability of thermodynamics particularly to include metastable states.

The first part of this two-part book is devoted to classic thermodynamics, of which the treatment is excellent. It covers, with emphasis on its difficulties and limitations, the most important concepts in the field, such as the equation of state; the law of conservation of energy; temperature; entropy; the Kelvin-Planck and Clausius principles; and the general thermodynamic system of Gibbs.

The second part is a presentation of generalized thermodynamics. The author's basic postulate is that a thermodynamic system has more degrees of freedom than are usually assigned; by virtue of this metastable states may be incorporated into the equation of state, enlarging the scope of this equation and the scope of thermodynamics. Agreement of the generalized point of view with the laws of conservation of energy and the Kelvin-Planck and Clausius principles is demonstrated and is followed by a discussion of systems in which energy is dissipated, of systems in which energy changes occur under equilibrium and nonequilibrium conditions, and of phenomena at low temperature and absolute zero.

A discussion of the potential character of entropy leads to the conclusion that entropy is not a function of state in a system of more than two independent variables and that this demands new criteria of equilibrium and stability of systems. Near the end of the book the enthalpy and latent heat are calculated for ammonia and water from an explicit equation by use of pressure, volume, and temperature as the independent variables. The agreement is excellent for ammonia and good for water.

The author is to be complimented for a thought-provoking work.

HOWARD LITTMAN

Reader Reaction

HEAT TRANSFER

The introductory paragraph of the article "Heat Transfer to Water in an Annulus" by Miller, Byrnes, and Benforado, published in the December issue of the *Journal*, contains a statement which I fear might mislead someone into repeating old research. The statement that "... literature contains only a limited amount of data for annular flow heat transfer ..." seems hardly appropriate to me when the proper paragraph in "Perry" [J. H. Perry, "Chemical Engineers' Handbook," McGraw-Hill Book Company, Inc., New York] lists about nine articles, in the bibliographies of which will be found at least thirty other references to similar work.

The general tone of these articles parallels the conclusions reported in this article, to the effect that the conventional equation underpredicts the coefficient, but further research would show that the divergence is not neatly relatable to any physical dimension.

ALAN S. FOUST

BETHLEHEM, PENNSYLVANIA

A.I.Ch.E. JOURNAL INDEX OF ADVERTISERS

Advertising Offices

New York 36—Lansing T. Dupree, Adv. Mgr.; John M. Gaede, Asst. Adv. Mgr.; Paul A. Jolcuvar, Dist. Mgr.; Donald J. Stroop, Dist. Mgr.; 25 W. 45th St., Columbus 5-7330.

Chicago 11—Richard R. Quinn, Dist. Mgr., 612 North Michigan Ave., Room 507, Superior 7-0385.

Cleveland 15—Eugene B. Pritchard, Dist. Mgr., 1836 Euclid Ave., Superior 1-3315.

Pasadena 1—Richard P. McKey, Dist. Mgr., 465 East Union St., Ryan 1-8779.

Dallas 28—Richard E. Hoierman, 2831 El Capitan Drive, DA7-3630.